#5

AVAILABLE TO THE PUBLIC

CR-73439

FINAL REPORT

Prepared By

LOCKHEED MISSILES & SPACE COMPANY

For

NATIONAL AERONAUTICS AND SPACE ADMINISTRATION • AMES RESEARCH CENTER

CR-73439
AVAILABLE TO THE PUBLIC

SOLAR POINTING AEROBEE ROCKET CONTROL SYSTEM

(SPARCS)

FINAL REPORT

November 1969

Prepared under Contract NAS 2-3500 by

LOCKHEED MISSILES & SPACE COMPANY
Sunnyvale, California

LMSC-A972158

for

NATIONAL AERONAUTICS AND SPACE ADMINISTRATION
AMES RESEARCH CENTER

CONTENTS

ILLUSTRATIONS

Section 1
INTRODUCTION

1.1 PROGRAM OBJECTIVES

Lockheed Missiles & Space Company participation in the Solar Pointing Aerobee Rocket Control System (SPARCS) program began in October 1965 upon receipt of a NASA/Ames Research Center request for proposal for the development of a solar-pointing attitude control system for the Aerobee 150 sounding rocket. The system was to be specifically tailored to the needs of solar scientists who wanted to utilize the Aerobee as a platform for sun-oriented experiments. Improvements over existing solar-pointing systems were desired in several areas, the foremost of which was pointing accuracy. Reductions in control system size and weight, to accommodate larger more precise experimental equipment on the payload-limited Aerobee, were also of prime importance. In addition, a system which would be less expensive, more reliable, and simpler to operate than existing systems was desired. Finally, to maximize utilization of the new system, it was essential that it be available in early 1968 during the predicted peak in the 11-year cycle of solar flare activity.

Several aspects of the control system design and function of SPARCS were specified in the RFP. The Aerobee rocket (Fig. 1-1), which consists of a boost engine, sustainer engine, payload section, and nose cone, is spin-stabilized during the powered flight portion of the ascent trajectory. After sustainer engine burnout, the attitude control functions would be acquired by SPARCS, which was to be housed in a control insert in the payload section. (The Aerobee payload section, sometimes referred to in this report as the SPARCS vehicle, is shown in Fig. 1-2) The SPARCS control task was to point the longitudinal axis of the rocket toward the sun and to provide roll stabilization about that axis during the 4 to 5 minutes of ballistic flight above the Earth's atmosphere. The SPARCS control function was to be divided into four phases: despin, coarse acquisition of the sun, fine acquisition, and fine pointing. The attitude reference for the last two phases was to come from a specially designed Fine Sun Sensor (FSS).

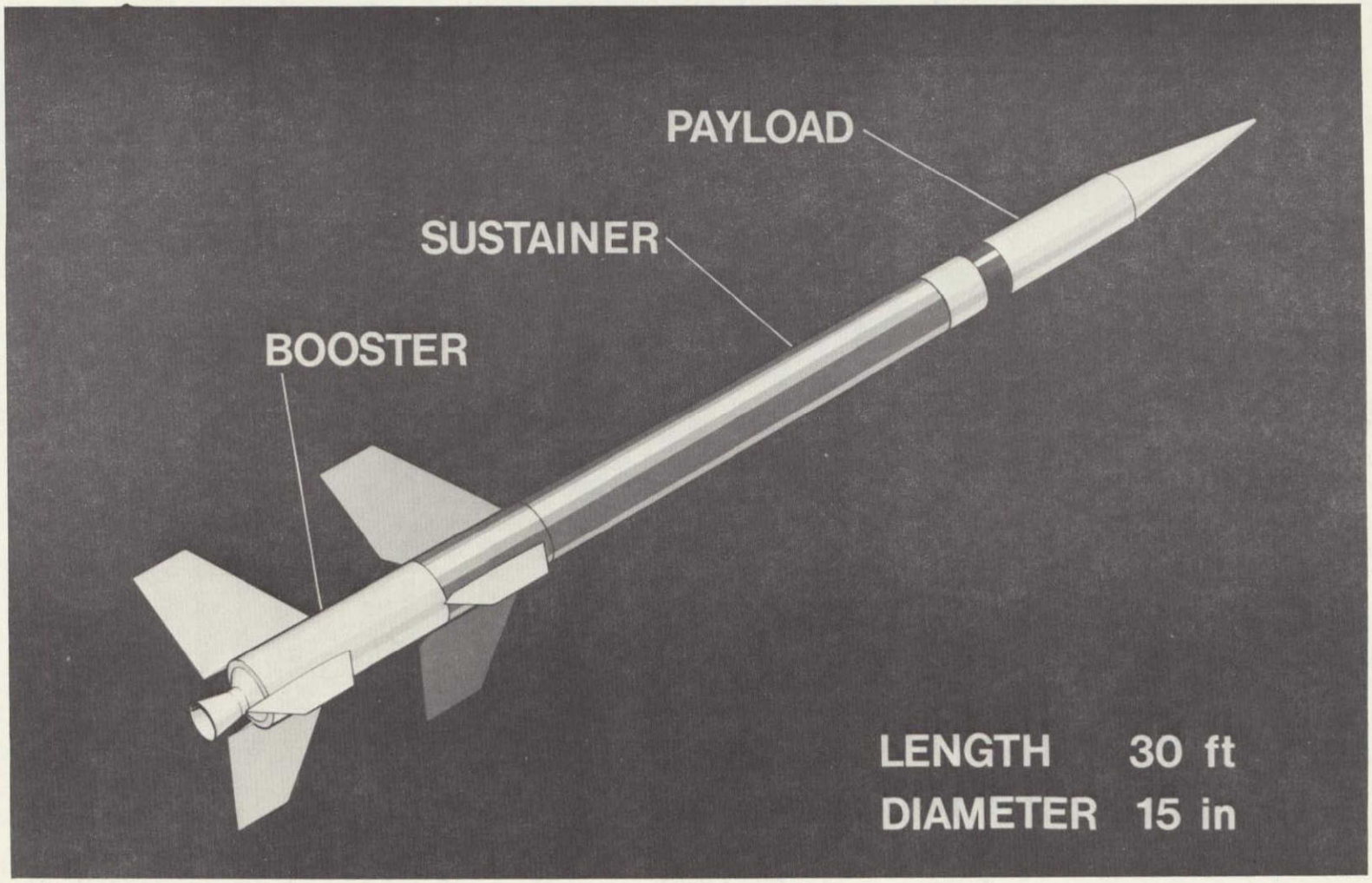

Fig. 1-1 Aerobee Rocket and Payload

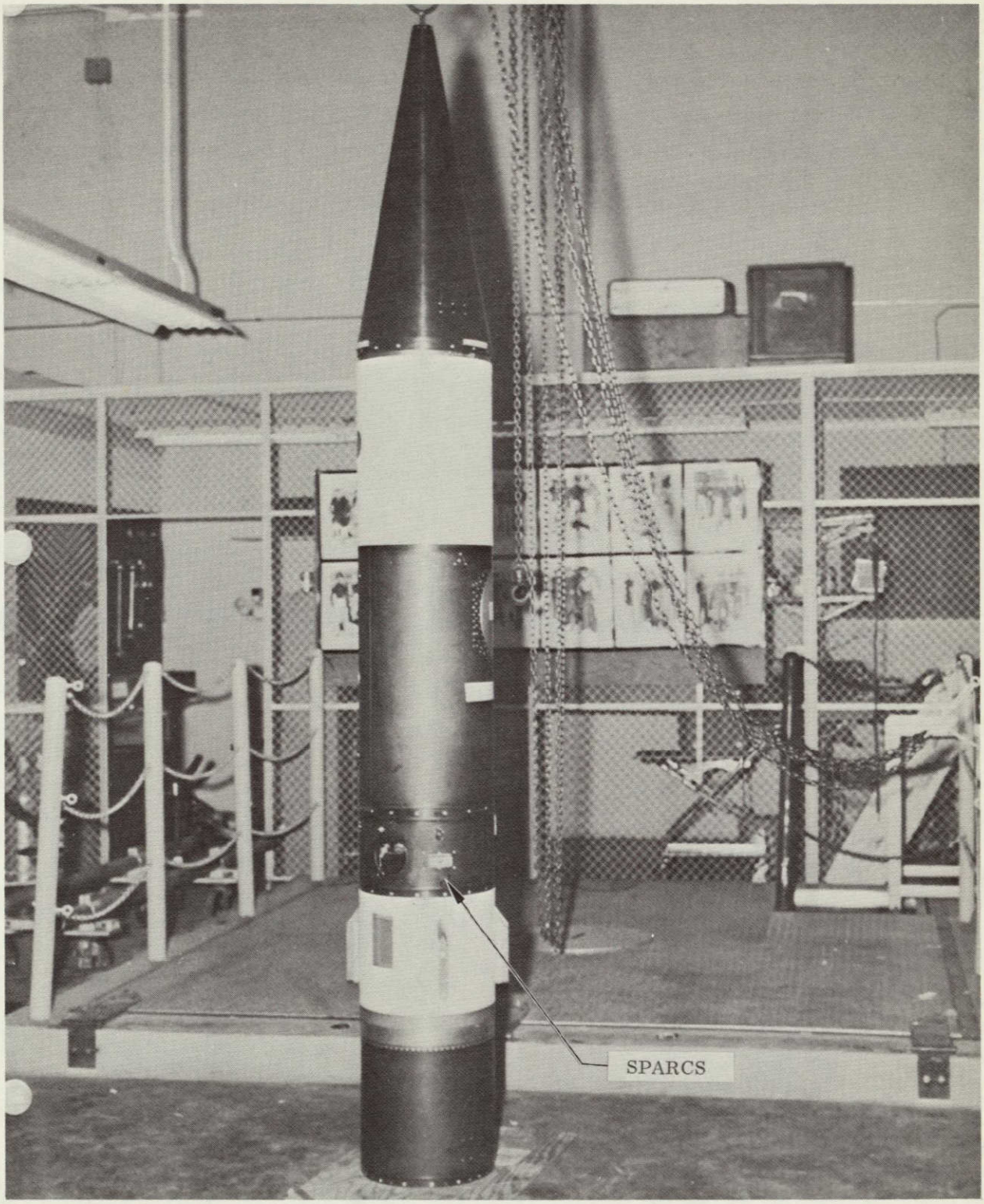

Fig. 1-2 SPARCS Vehicle

The performance and design objectives specified in the contract are given in Table 1-1. The major hardware items called for were the SPARCS unit, the FSS, and the associated ground equipment necessary for field preparation of the SPARCS system prior to a flight.

Table 1-1

SPARCS PERFORMANCE AND DESIGN REQUIREMENTS

		Marginally Acceptable	Target	Goal	SPARCS 0 Flight Test Results	Typical SPARCS I Flight Results
Pitch and Yaw Performance						
Absolute Accuracy	(arc sec)	±30	±15	±5	±8.9	not measured
Drift	(arc sec)	±5	±2	±0.5	±10	not measured
Jitter Amplitude	(arc sec)	±10	±4	±1	±9	±1
Jitter Rate	(arc sec/sec)	±20	±8	±2	±10	±2
FSS Noise (rms)	(arc sec)	1	0.4	0.1	<0.1	<0.1
Roll Reference						
Absolute Accuracy	(deg)	±5	±2	±0.5	±2.6	±2.0
Drift	(deg)	±0.6	±0.24	±0.06	±0.25	not measured
Jitter Amplitude	(deg)	±0.6	±0.24	±0.06	±0.07	±0.03
Jitter Rate	(deg/sec)	±1.2	±0.48	±0.12	±0.04	±0.04
Design						
Weight	(lb)	60	40	30	40.5	41
Insert Length	(in.)	12	8	4	9	9

1.2 SYSTEM DESCRIPTION

The SPARCS conceptual design was accomplished during the period between the receipt of the RFP and the contract award. The control system is unique in that neither rate gyros nor an inertial platform are used for payload despin or sun acquisition. Direction cosines to the solar vector and to the Earth's magnetic vector are measured by solar cells and a two-axis magnetometer. Attitude errors and vehicle rates are electronically computed from these sensors and used as inputs for the control system.

Although the control formulation in the general case is complete, implementation has been greatly simplified by tailoring the system to the solar-pointing mission. Roll control is provided by the magnetometer, which may be biased to select the final roll orientation. A nonimaging Fine Sun Sensor (FSS), which has a high resolution around null and good stability over the mission life, is used for fine pointing. Control torques are provided by cold-gas jets, which are driven by pulse modulation circuitry to provide linear control during acquisition and small impulses for fine pointing.

SPARCS is a self-contained system and only the payload is controlled. The payload and rocket are separated a short time after burnout, after which the SPARCS control sequence is divided into two phases: The first phase, payload despin and solar acquisition, utilizes a direction cosine approach. The second phase, fine pointing, utilizes the specially developed FSS.

Not only is the complete control system lighter in weight and more reliable than systems utilizing inertial devices, but the necessity for careful handling, extensive testing, anc complex prelaunch updating required by gyros and an inertial platform is eliminated. With the exception of the pneumatic hardware, the system has no moving parts.

All of the SPARCS components are located in the payload section, as shown in Figs. 1-3 through 1-6. This arrangement has several advantages. First, it enables the payload section to be separated from the sustainer after cutoff, which minimizes the pointing errors introduced by vehicle flexure and eliminates experiment contamination by sustainer gases. Second, the entire SPARCS can be recovered with the payload and

can be reused after refurbishing. Thus the cost per flight is substantially reduced. Finally, because the SPARCS is independent of the rocket, it is possible to adapt it to several control gases (nitrogen, freon, argon, and helium). This allows the experimenter to minimize the contamination caused by control jet exhaust.

The relative location of SPARCS with respect to the test payload is illustrated in Fig. 1-6. The insert houses the electronics, pneumatics, power supply, and the Coarse Sun Sensor (CSS). The FSS is located in the forward end of the experiment section for adequate viewing and convenient alignment with the solar experiment. The magnetometer sensing heads are located on the aft end of the recovery package to minimize the effects of magnetic disturbances.

The system has an insert length of 9 inches and weighs approximately 40 pounds. Analog simulation has indicated that for longitudinal pointing (pitch and yaw motion), a limit cycle of ±1 arc sec is achievable. Air bearing tests have demonstrated a ±5-arc-sec limit cycle. In roll, the payload may be oriented to any direction selected prior to liftoff with absolute accuracy of better than 5 deg and a limit cycle of ±0.06 deg, which is adequate for most purposes.

The experiment axis will be pointed to the radiometric center of the sun within 40 sec after the initiation of control. This can be achieved from attitude errors as large as 90 deg and with normal Aerobee vehicle rates. Larger initial attitude errors or rates require longer time.

At the present time, there are three SPARCS configurations: SPARCS 0, SPARCS I, and SPARCS II. The first three SPARCS were fabricated to a SPARCS 0 configuration, and on 19 March 1968 one of these systems successfully demonstrated the feasibility of the SPARCS concept by acquiring the sun and achieving fine pointing. A pitch and yaw absolute pointing error of less than 10 arc sec was achieved; this represents a state-of-the-art advance. Corresponding jitter amplitudes of 12 arc sec peak-to-peak for pitch and yaw and 5 deg peak-to-peak for roll were recorded.

Subsequent to the 19 March 1968 flight, all systems were modified into the SPARCS I configuration. SPARCS I has demonstrated jitter amplitudes of 1 arc sec peak-to-peak in pitch and yaw and is capable of acquiring the sun under conditions that would have been considered outside the SPARCS 0 launch window capabilities.

Summaries of the SPARCS 0 and SPARCS I flights are given in Section 2.

The improved SPARCS II is a completely new configuration, which is less expensive to fabricate, launch, and refurbish. Also, it is expected to achieve pitch and yaw jitter amplitudes of less than 0.5 arc sec peak-to-peak and is lighter in weight and shorter in length than SPARCS 0 or SPARCS I. The first SPARCS II flights are scheduled for 1970.

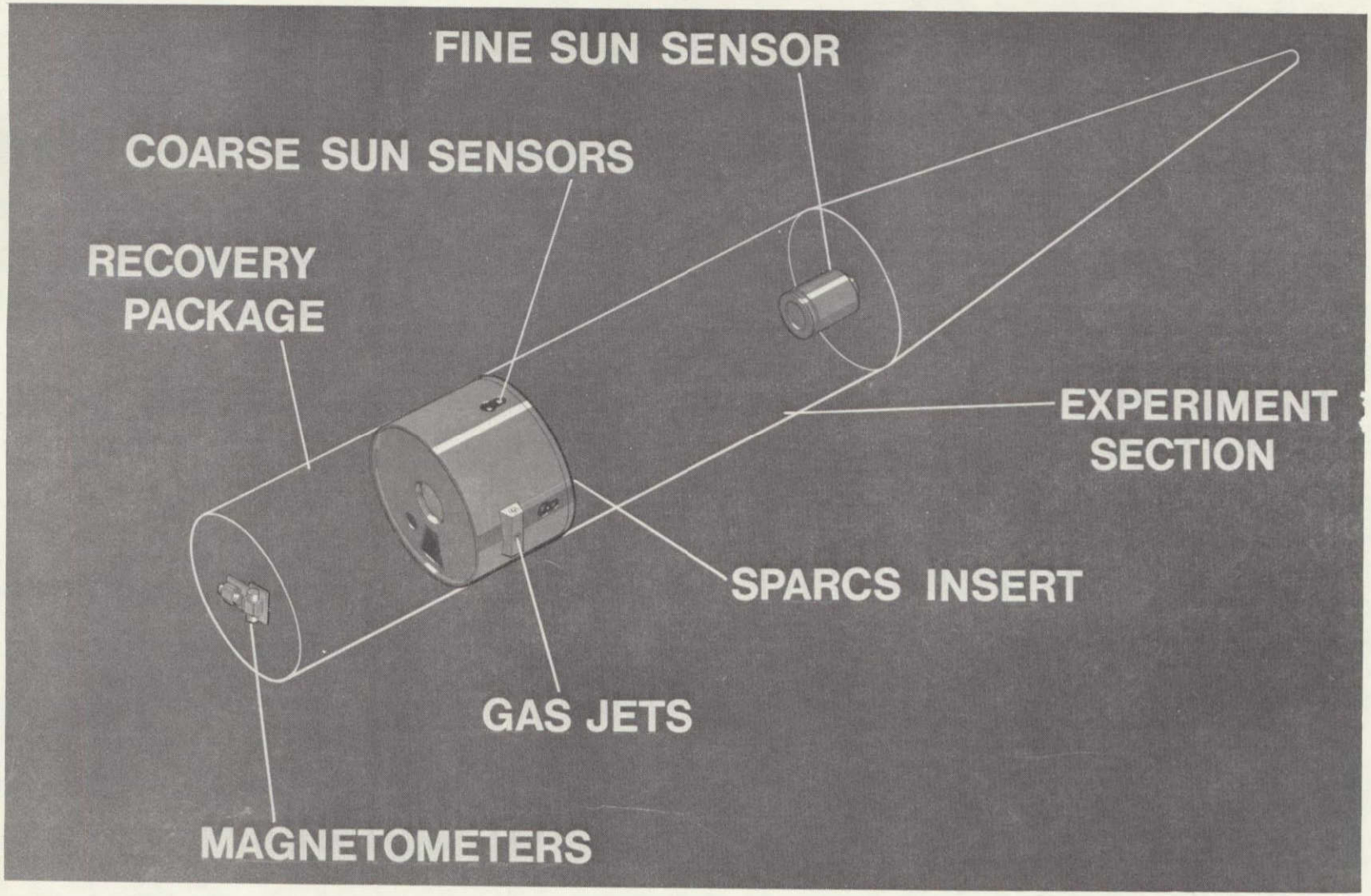

Fig. 1-3 SPARCS Location Geometry

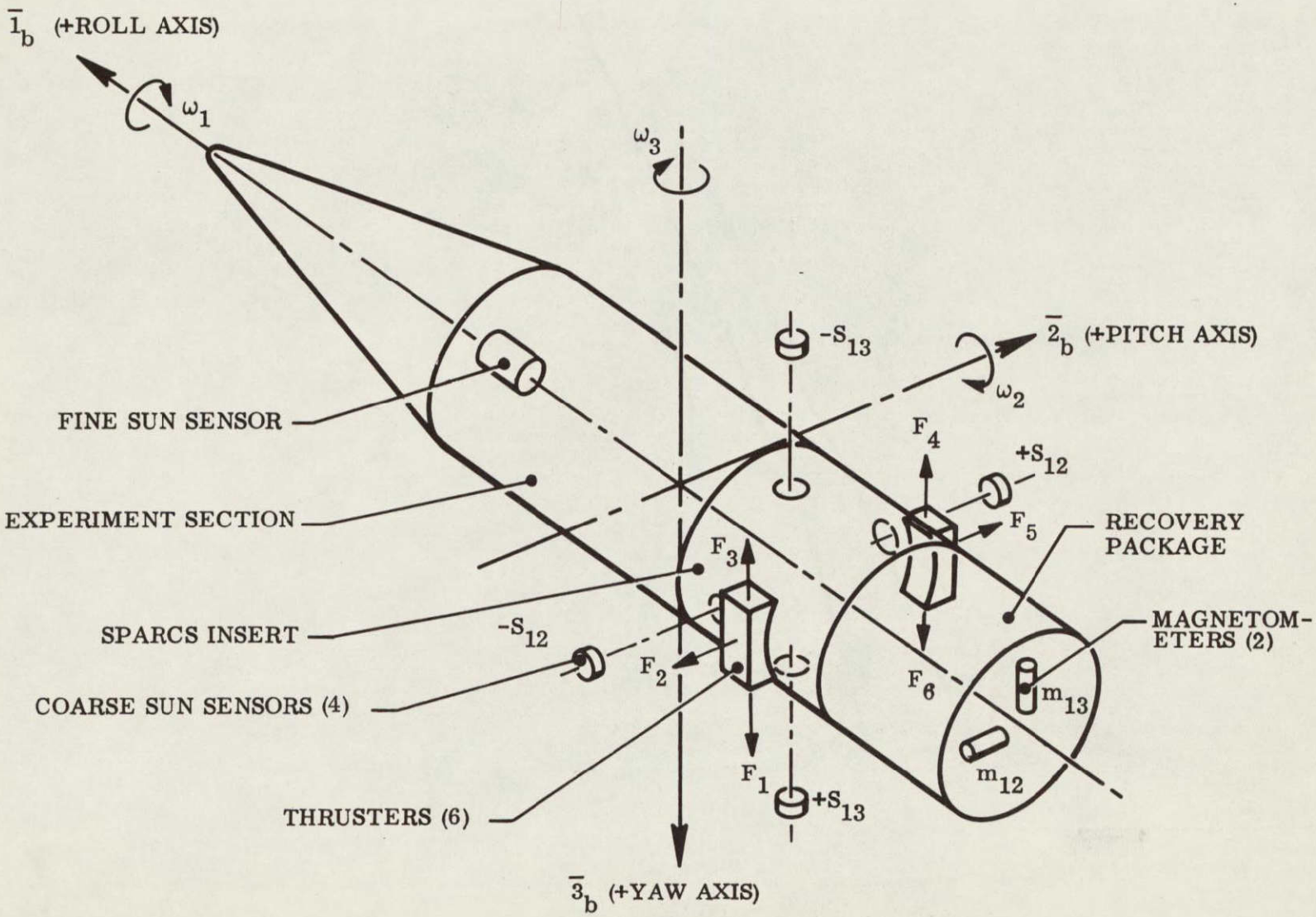

Fig. 1-4 Sensor and Thruster Locations

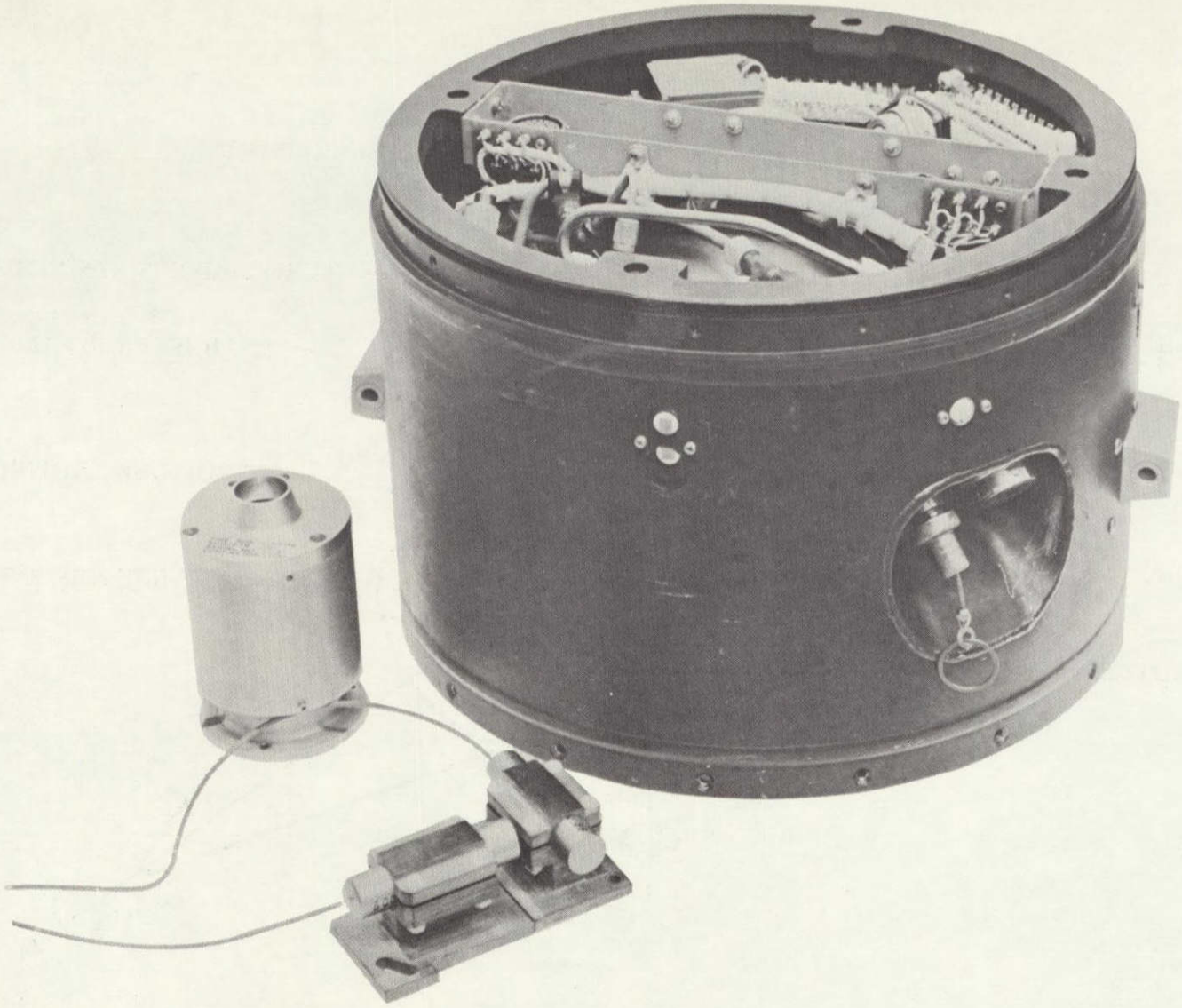

Fig. 1-5 SPARCS 0 With Fine Sun Sensor and Magnetometer Probes

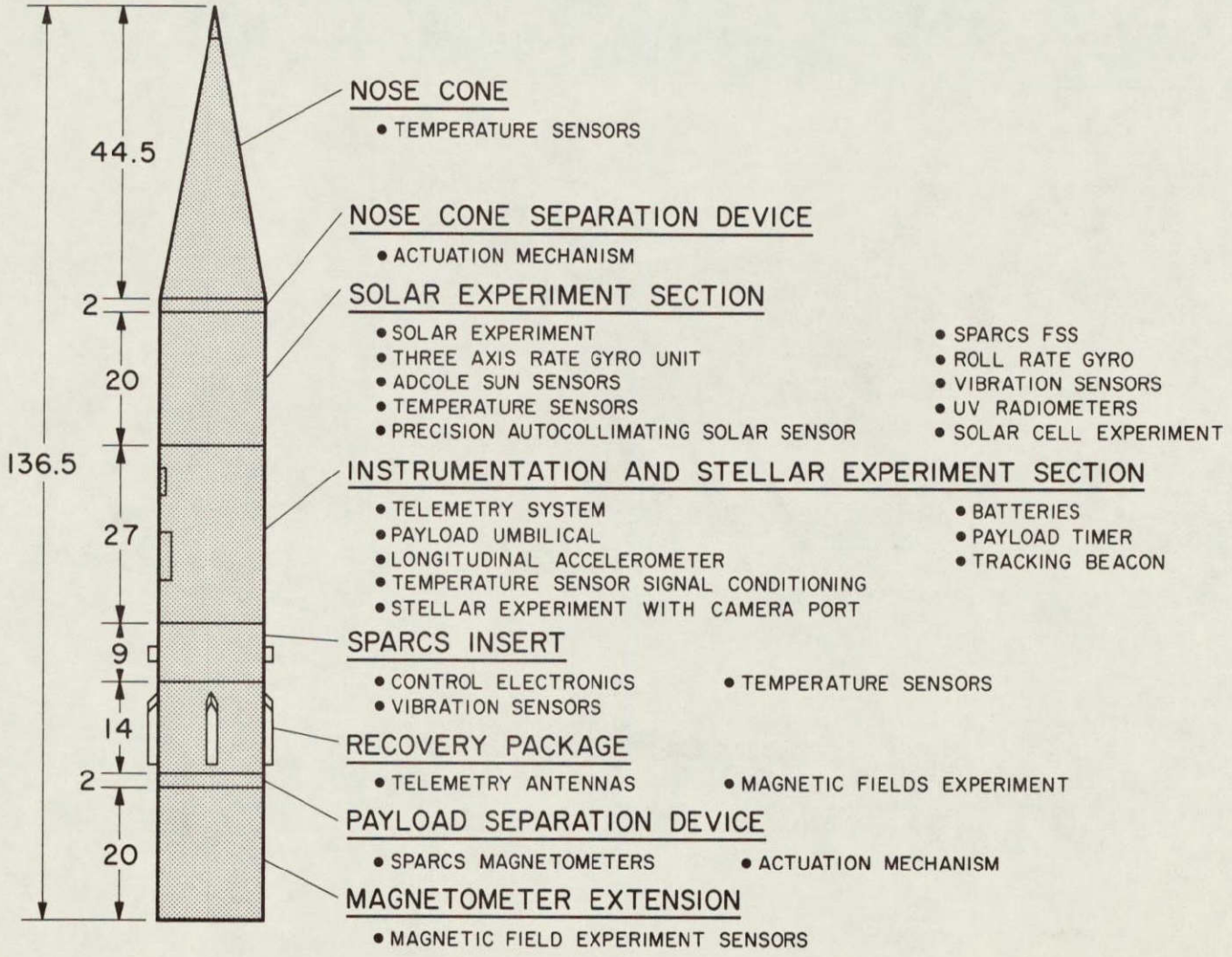

Fig. 1-6 Payload Configuration

Section 2
FLIGHT TEST RESULTS

A summary of the SPARCS 0 and SPARCS I flight histories is given in Table 2-1. Detailed discussions of the two SPARCS 0 flights and a representative SPARCS I flight (April 1969 launch of SPARCS I, S/N 106) are presented in the following paragraphs.

2.1 FIRST FLIGHT TEST – SPARCS 0, S/N 103

The first SPARCS flight took place at White Sands Missile Range (WSMR), New Mexico, on 10 December 1967. The flight was launched with Aerobee 4.201 and utilized the SPARCS unit S/N 103. Although SPARCS did not achieve an arc-second limit cycle, the flight demonstrated the capability of a gyroless control system, which computes attitude and rate signals from sensors, to despin a payload and acquire the sun.

Liftoff of the Aerobee rocket was at 1500 hours MST. Despin was accomplished in 6.56 sec after SPARCS was enabled from an initial spin rate of 790 deg/sec. The Course Sun Sensor (CSS) and the associated Earth shine compensation unit performed as designed, eliminating the effect of Earth shine on course acquisition. Also, the payload was pointed to the sun in the expected manner to within the field-of-view of the Fine Sun Sensor (FSS) for fine acquisition.

Due to a wiring error in the interface between the FSS and SPARCS, the pitch and yaw channels were cross coupled, resulting in instabilities from which the system was not capable of recovering. However, sun presence indications which occurred several times during the flight demonstrated that the concept of a magnetometer roll control system was valid. During the time that the system was pointing at the sun, the roll attitude stabilized with a limit cycle of approximately ±2 deg about a value approximately 6 deg from the desired roll angle.

Table 2-1

SUMMARY OF SPARCS 0 AND SPARCS I FLIGHTS

Date	Experiment	Comments
SPARCS 0		
10 Dec 1967	4.201 – First Flight Test; SPARCS S/N 103	Proved the unique SPARCS concept of gyroless attitude control.
19 Mar 1968	4.202 – Second Flight Test; SPARCS S/N 102	Performed as designed. Stability of 16 arc sec peak-to-peak achieved.
SPARCS I		
8 Jun 1968	4.134 – Apollo Telescope Mount Test, Payload A, for Dr. Tousey of Naval Research Laboratory; SPARCS S/N 105	Payload separation device failed, preventing opportunity for SPARCS to perform. Payload and SPARCS destroyed.
12 Feb 1969	4.135 – Apollo Telescope Mount Test, Payload B; SPARCS S/N 104	SPARCS performed as expected, achieving stability of better than 2 arc sec peak-to-peak. Experiment failed to return data.
8 Apr 1969	4.282 – American Science and Engineering X-ray Experiment; SPARCS S/N 106	SPARCS performed as designed, achieving stability of better than 2 arc sec peak-to-peak. Experiment returned excellent data
6 Sep 1969	4.234 – Naval Research Laboratory Experiment for Dr. Garrett; SPARCS S/N 103 (refurbished)	Rocket broke up at +3.8 sec, preventing SPARCS operation. SPARCS and experiment destroyed.
24 Sep 1969	4.294 – University of Colorado Experiment for Dr. Rense; SPARCS S/N 101	SPARCS achieved stability of 2 arc sec peak-to-peak. Acquisition time was excessive, due to SPARCS intermittent circuit. Experiment failed to return data.
4 Nov 1969	4.136 – Reflight of the Apollo Telescope Mount Test, Payload A; SPARCS S/N 104 (refurbished)	SPARCS and experiment performed well; stability of 2 arc sec peak-to-peak achieved.
4 Nov 1969	4.283 – Reflight of the American Science and Engineering Payload; SPARCS S/N 106 (refurbished)	SPARCS and experiment performed well; stability of 3 arc sec peak-to-peak achieved.

The pneumatic system performed as expected during the flight, and the gas remaining in the tank at the completion of coarse acquisition would have been adequate for fine pointing had the FSS been properly phased. However, the low pressure regulator was set to the design value of 155 psi. This setting was discovered to be too high during tests conducted as part of the failure review following the flight. In this review, the thrust characteristics of the SPARCS nozzles with Freon propellant were measured in a vacuum, and it was demonstrated that the nozzles provided a greater thrust than originally calculated. The higher thrust would have initially caused the system to be unstable in the fine pointing mode, and thus the predicted arc-second fine pointing would not have been achieved until the tank pressure had decayed due to gas usage. For satisfactory limit cycle performance, the low pressure regulator should have been set to 60 psi.

2.2 SECOND FLIGHT TEST – SPARCS 0, S/N 102

The second SPARCS flight test was conducted at WSMR on 19 March 1968. This flight was made with Aerobee 4.202 and utilized SPARCS unit S/N 102. The primary objective of the SPARCS program was achieved at T+126.2 sec (407,400 ft) when the fine pointing phase of flight began. During the 200 sec that SPARCS was in the fine pointing mode, pitch jitter varied from ±4 to ±16 arc sec peak-to-peak (p-p) and yaw jitter varied from ±8 to ±20 arc sec p-p, with an uncertainty of ±1.6 arc sec in the measurements. The roll jitter during the same period was never greater than 0.133 deg p-p, and at times was as low as 0.033 deg p-p.

Absolute pointing accuracy, as observed at T+130 sec, was 3.3 arc sec in pitch and 8.3 arc sec in yaw when measured from the radiometric center of the sun; the absolute error of the combination was 8.9 arc sec. Drift during flight occurred primarily in yaw and was approximately 9.7 arc sec for a period of 180 sec (from T+130 sec to T+310 sec). Pitch and yaw errors were determined by a pair of sun sensors (Precision Autocollimating Solar Sensors, PASS) which were mounted on the same surface as the SPARCS FSS. The measurements were verified by white-light solar pictures from a Questar telescope-Nikon camera combination. The resultant pointing accuracy represents an advance in the state-of-the-art for a solar pointing sounding rocket.

Absolute roll pointing accuracy during the limit cycle control was 9 deg clockwise from the roll angle selected by the experimenter (203.5 deg clockwise from the North Ecliptic Pole). A stellar camera, which was to measure roll attitude with respect to a star field, did not yield data because the camera door failed to eject during the flight. However, over 200 white-light pictures of the sun were taken and were of sufficient quality to record the position of several suspots which, when compared with ground photographs from Sacramento Peak Observatory, yielded the desired roll attitude. (These pictures were also used to verify the pitch and yaw pointing values.)

The roll absolute pointing error could have been caused by one, or a combination, of the following events:

a. An input selector switch on the AGE checkout console was turned to the magnetometer input for pitch and yaw; this caused an unscheduled input into the test coils which resulted in an erroneous null and/or calibration factor for the roll angle.

b. The roll angle calibration was checked prior to flight under the launch tower where the steel structure could have produced a field which was not linear. An error due to the inaccurate roll calibration could have amounted to approximately 7.5 deg of pointing error.

Liftoff occurred at 0915 hours MST and was followed by sustainer burnout at T+50.7 sec (112,000 ft), nose cone separation at T+69.8 sec (203,700 ft), and payload separation at T+75.1 sec (227,100 ft). The observed roll rate was 960 deg/sec both before and after separation, but the lateral rate increased from 1.3 to 7.0 deg/sec and the cone angle increased from 1.6 to 8.8 deg as a result of separation. This was probably due to the shift in the c.g. of the launch configuration to the new c.g. of the payload or to unequal separation forces. The angle to the sun at this time was 58 deg.

SPARCS was enabled at T+79.7 sec (246,000 ft) with an angle to the sun of 72 deg, which was the maximum angle observed until loss of control much later in the flight. The lateral rate increased to 7.6 deg/sec and the cone angle increased to 9.6 deg just prior to enabling. Despin required 7.0 sec.

At T+90.5 sec (289,900 ft), the first indication of sun presence from the mode sensor occurred momentarily but was lost, probably because the lateral rate was too great for the system to overpower within the narrow field-of-view of the mode sensor (+10 deg). Sun acquisition occurred at T+107.3 sec (349,000 ft) and was not lost until the aerodynamic disturbances overcame the controlling forces at T+351.7 sec on the downward leg of the trajectory. SPARCS switched into the fine mode at T+119.4 sec (387,800 ft) with the FSS in control of the experiment.

During payload integration, the low pressure regulator was replaced because it could not be adjusted to the 60 psi required to achieve an arc-second limit cycle for the flight. The required value of 60 psi was determined by pneumatic and analog computer tests following the first test flight (par. 2.1). A spare unit was suitably modified and substituted.

The condition of SPARCS when recovered was good, as shown in Fig. 2-1. One CSS was broken, but the insert was otherwise operational. The FSS required relapping of the base pads to bring them within 15 arc sec of the reference optical surface.

2.3 SPARCS I FLIGHTS

A summary of all SPARCS I flights through 4 November 1969 is given in Table 2-1. More detailed information on the first flight of SPARCS S/N 106, which is typical of the SPARCS I flights, is presented here.

Liftoff of Aerobee 4.282 from the WSMR was at 1000 MST, 8 April 1969. The payload was a high resolution, X-ray grazing incidence from American Science and Engineering. The experiment returned excellent X-ray photographs and met all the flights objectives.

Fine pointing was achieved at T+121 sec at 426,000 ft. Fine pointing stability was excellent, varing in pitch and yaw from 1.4 to 3.0 arc sec peak-to-peak (p-p) during any 20-sec period. Roll stability was better than 0.1 deg p-p. The pitch/yaw absolute pointing requirement of better than ±2 arc min was also achieved. Roll absolute pointing was within 1 deg as determined from sun spot data.

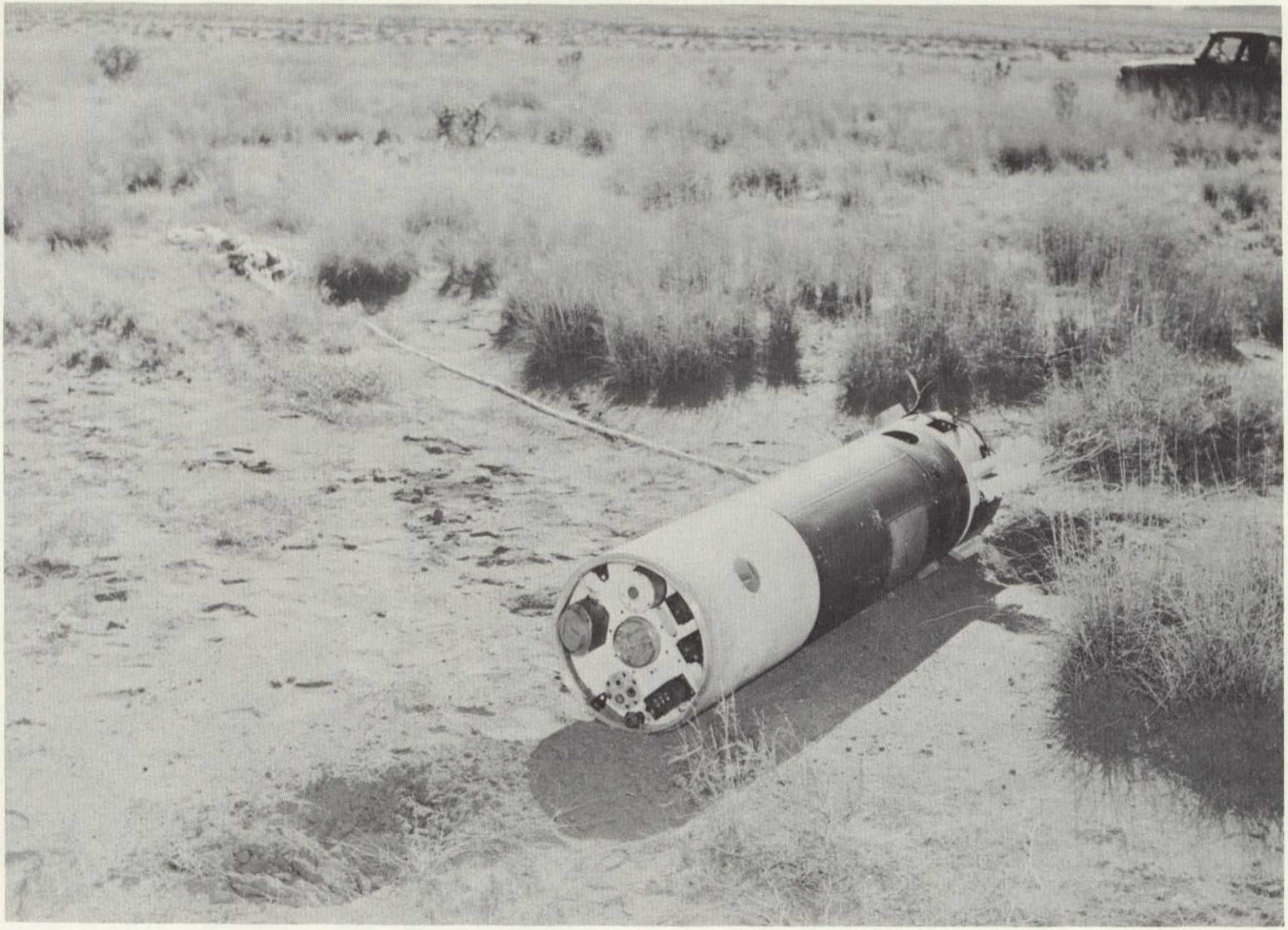

Fig. 2-1 Recovered Payload

Nose cone and payload separation occurred by T+75 sec (250,000 ft), and SPARCS was enabled at T+80 sec (317,000 ft). Despin from an initial roll rate of 2.74 rps required 11 sec, due to the large roll moment of inertia. The FSS indicated sun presence at T+103 sec, and fine pointing was achieved by T+117 sec (413,000 ft). Fine pointing continued until T+325 seconds (327,000 ft), when the experimenter covered the FSS for reentry and recovery.

Detailed information on all SPARCS I flights is available from the post-launch reports. These reports contain payload information, flight summary, pointing information, and discussions of any flight anomilies or special features. Figure 2-2 illustrates typical fine pointing behavior for a SPARCS I flight. It can be seen that the jitter is less than 2 arc sec p-p for the period shown.

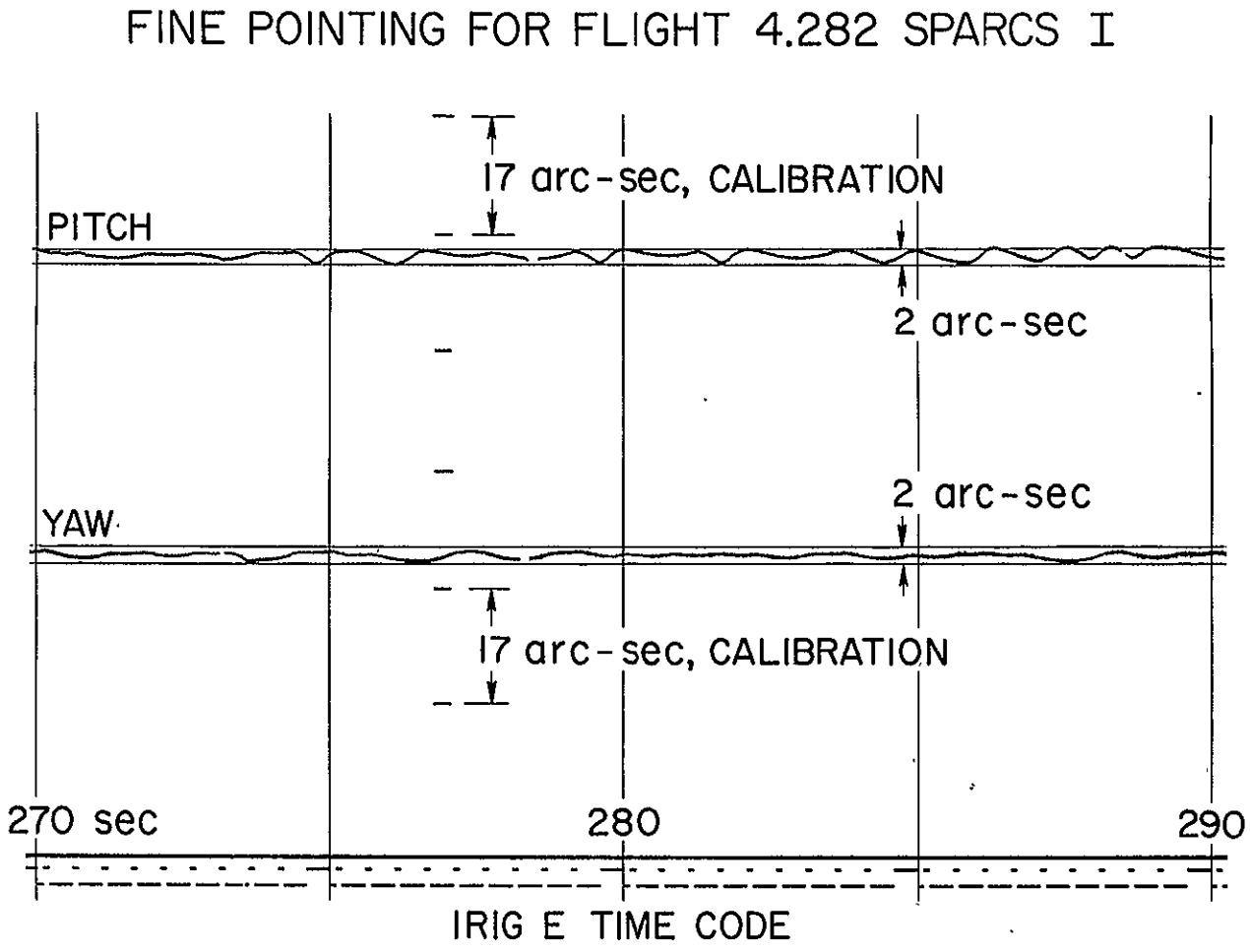

Fig. 2-2 Typical Limit Cycle Performance (SPARCS I)

Section 3

SYSTEM DESIGN

3.1 REQUIREMENTS

The objectives of the SPARCS design was to provide a solid-state system to despin and point an Aerobee 150 type payload toward the sun with an arbitrary preset roll angle about the payload-sun line. The performance goals are listed in Section 1, Table 1-1. A payload weight range of 100 to 350 pounds was originally specified in the contract; however, this was subsequently changed to a range of 200 to 350 pounds. All of the payloads are essentially pencil-shaped, with characteristics as given in Table 3-1 below. The lever arms shown in the table represent distances from the payload center of mass to the SPARCS thrusters.

Table 3-1

PAYLOAD DESIGN CHARACTERISTICS

Parameter	Payload Weight Range			
	200-lb	250-lb	300-lb	350-lb
Pitch and Yaw Inertias (slug-ft^2)	20.9	36.1	55.1	62.7
Roll Inertia (slug ft^2)	1.1	1.4	1.7	2.0
Pitch/Yaw Lever Arm (ft)	1.51	2.04	2.55	2.91
Roll Lever Arm (ft)	0.625	0.625	0.625	0.625

At separation, the payload is spinning about its longitudinal axis at a nominal rate of 2 rev/sec with this axis oriented arbitrarily with respect to the sun. Transverse rates up to a maximum of 5 deg/sec may be present due to separation disturbances. Other disturbances were to be computed as part of the design effort.

3.2 CONTROL THEORY

Selection of the method of control is based largely on the choice of error sensors and control torque mechanization. Since the objective is to point the payload toward the sun, sun sensors were chosen as the primary error detection devices. Because of the conflicting requirements of high accuracy near null and the necessity of acquisition from any angle, separate sensors for the two modes were used. Silicon solar cells, whose field-of-view is a full hemisphere, were chosen for the wide angle sensors. Four such cells provide measurement of the direction cosines between the vehicle transverse axes (axes $\bar{2}_b$ and $\bar{3}_b$) and the vehicle-sun line. These four cells, referred to as Coarse Sun Sensors (CSS), are mounted as shown in Section 1, Figs. 1-3 and 1-4. A Lockheed-developed Fine Sun Sensor (FSS), described in detail in Appendix C, provides the high-accuracy, narrow-field sensing required for fine pointing.

When control is initiated, cold-gas jets despin the payload and simultaneously precess the payload longitudinal axis toward the sun. The despin signal is derived by summing and demodulating the outputs of the CSS units and the magnetometers. The precession signal is formed by differentiating the proper CSS output signal (see Appendix A).

Preference is initially given to despin and this operation will usually occur before the sun is acquired. When the despin signal falls below a preset threshold, the attitude errors about all three axes are used for the completion of acquisition. During this phase, the gas jets are driven by pulse modulation circuitry and act as linear components, resulting in the applied thrust being proportional to the error signal.

Sun sensors furnish sufficient information for pointing the longitudinal axis toward the sun; however, three-axis control requires another independent error measurement. The Earth's magnetic field was selected as a reference source for this purpose. Two magnetometers (Figs. 1-3 and 1-4) measure the direction cosines between the vehicle's transverse axes and the Earth's field. The coordinate system used to describe the vehicle attitude is shown in Fig. 3-1, where the vector $\bar{1}_s$ is in the direction of the sun and $\bar{1}_m$ is aligned with the magnetic field. Two sets of right-hand orthogonal reference axes are constructed from these two vectors as follows. Vectors $\bar{2}_s$ and $\bar{2}_m$ are

coincident and normal to the plane determined by $\bar{1}_s$ and $\bar{1}_m$ and are positive in the direction $\bar{1}_s \times \bar{1}_m$. Vectors $\bar{3}_s$ and $\bar{3}_m$ are chosen to complete the set of sun and magnetic reference axes, respectively. The output of magnetometer m_{12} is a measure of the direction cosine between the $\bar{1}_m$ and $\bar{2}_b$ axes.

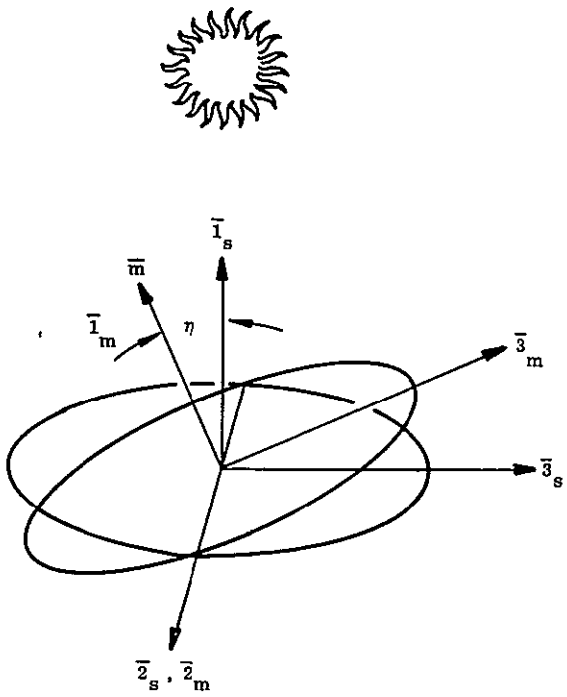

Fig. 3-1 Coordinate System

The basic control system produces control torques proportional to error, plus error rates for all three axes. It is clear that the vehicle longitudinal axis will point toward the sun when S_{12} and S_{13} are zero, and these signals are therefore used for yaw and pitch, respectively. If m_{12} is used as the roll error signal, a roll angle of zero will result. If m_{13} is used, the final roll angle will be -90 deg. A suitable combination of m_{12} and m_{13}, set before launch, permits any desired roll angle.

Lead networks on the position signal provide adequate damping for all axes. Because of the need to despin, an additional computed spin rate signal is required in roll. The detailed control theory, including spin rate computation, is discussed in Appendix A.

3.3 DESIGN CONSIDERATIONS

Some of the basic considerations which influenced the SPARCS design and/or method of operation are discussed in the following paragraphs.

3.3.1 Disturbance Torques

In investigating external disturbance torques that might act on the vehicle, it was found, that aerodynamic torques represent the only significant source of disturbance and can initially overpower the control torques. Thus separation of the payload and activation of the control system is delayed until the aerodynamic torques are well below the control level. By the time acquisition is completed, a sufficiently high altitude is achieved so that aerodynamic torques are negligible.

3.3.2 Albedo

Because of the Earth's albedo, pointing as determined by the coarse solar cells will not be toward the center of the sun but will be biased toward the Earth. If uncompensated, this bias can be sufficiently large that the sun will not be in the field-of-view of the FSS. A set of recessed solar cells are therefore placed near the CSS main cells and are used to partially chancel the bias, as discussed in Appendix D, par. D.1 . This reduces the bias to a point where switching to the FSS is always possible.

3.3.3 Eta Angle

The suitability of the SPARCS method of three-axis control and the magnitude of the magnetometer signals at null are strongly dependent on eta (η) , the angle between the sun line and the magnetic field. Although this dependency primarily affects the roll gain and the spin rate computation as eta approaches 180 deg, the reliability of sun acquisition is also affected. Since it was considered desirable to hold the number of prelaunch settings to a minimum, the system design represents the best compromise over the expected eta range (approximately 90 deg to 170 deg).

3.3.4 Pneumatics

A high level of thrust is required in order to despin in a relatively short time. However, because pulsed valves require a certain minimum pulse width for reliable operation, a high thrust level is not compatible with the need to achieve low vehicle rates during fine pointing. At least two thrust levels are therefore required. The required low thrust is achieved by lowering the supply pressure to a single set of thrusters. Since lowering the thrust also decreases the thruster gain, this gain change is compensated by increasing the electronic gain.

3.4 OPERATING MODES

A SPARCS flight profile and a block diagram of the SPARCS I control system are presented in Figs. 3-2 and 3-3. A description of the system's three principal operating modes is given by the following sequence of events:

Despin. Upon activation of control, a despin signal is derived by summing and demodulating the CSS and magnetometer outputs. The despin signal in turn is used to activate a pair of pitch/roll thrusters, which cause the vehicle to despin. During this time, the yaw signal from the CSS (together with the pitch signal which is coupled into yaw) causes the yaw thrusters to fire alternately at the spin frequency, moving the spin axis toward the sun.

Coarse Acquisition. When the spin rate is reduced to the point where the pitch/roll thrusters are no longer saturated by the spin rate signal, attitude errors as determined by the CSS produce simultaneous acquisition of the pitch and yaw axes to a point where the sun presence is detected by the mode sensor. (The mode sensor is part of the FSS and has an approximate 10-deg field-of-view about the longitudinal axis.) During coarse acquisition, the roll axis is controlled by a rate signal only. When the mode sensor indicates sun presence, the roll position signal from the magnetometers is switched into the roll axis to cause roll acquisition.

Fine Mode Acquisition. The sun enters the field-of-view of the FSS when the error angle between the vehicle longitudinal axis and the solar vector is approximately 14 deg. At an error angle of 10 deg, the sun presence indicator is

triggered and the CSS is switched out of the control loop and the gas jet thrust level is reduced. The switching logic requires a sun presence indication for 6 sec and, simultaneously, an indication that despin has occurred. This ensures that the vehicle rates are low and that acquisition is nearing completion.

The switching reduces the thrust level from 2.4 lb to 0.27 lb, removes the CSS from the control loop, and connects the FSS low gain channel. When the FSS indicates an error of approximately 0.5 deg, the system electronic gains are increased for fine pointing. The pitch and yaw axes are controlled by the FSS and the roll axis is controlled by the magnetometer. Valve modulation is used to obtain low limit cycle rates and low susceptibility of the system to noise. Fine pointing continues until the reentry aerodynamic torques overpower the system and cause the payload to tumble.

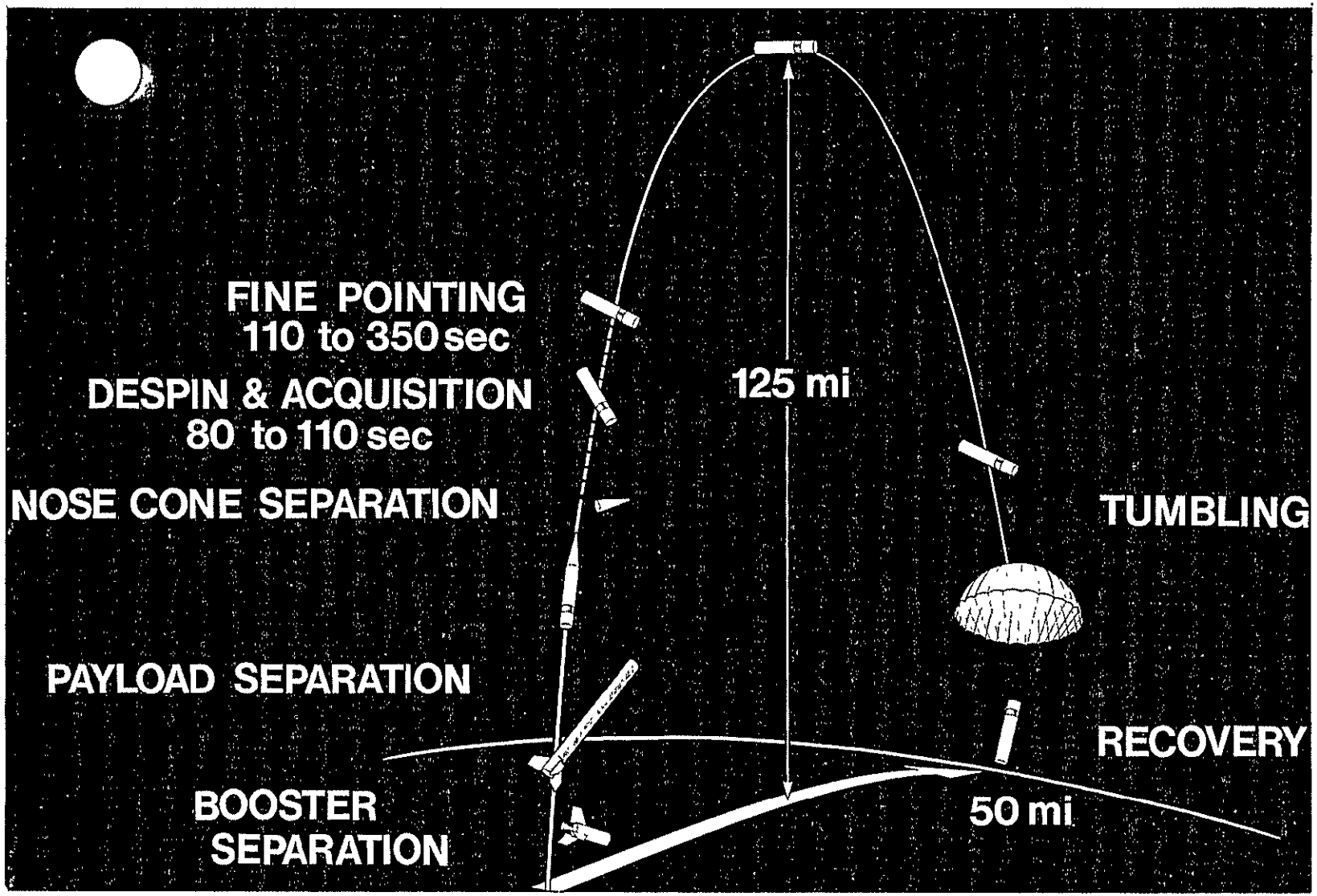

Fig. 3-2 SPARCS Flight Profile

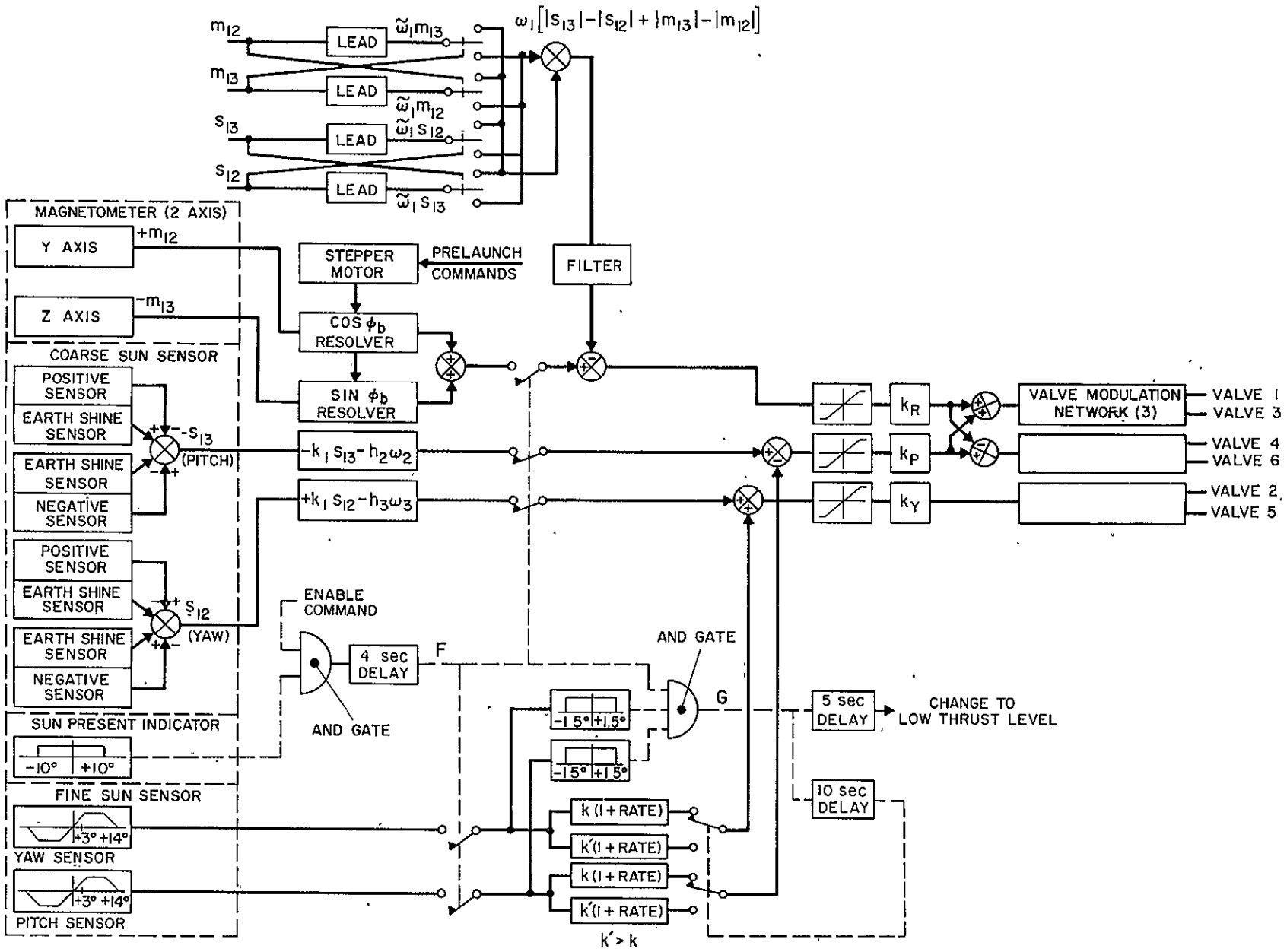

Fig. 3-3 SPARCS I Block Diagram

Section 4
SYSTEM DEVELOPMENT AND TEST PROGRAM

The principal tools used in SPARCS analysis, development, and testing were an analog computer simulation and an Air Bearing Vehicle (ABV). A digital simulation was occasionally employed, primarily to check the validity of results obtained from the analog simulation.

4.1 ANALOG COMPUTER SIMULATION

The analog simulation hardware consisted of an Applied Dynamics Model 256 analog computer, patchboards programmed for the simulation, two 8-channel strip recorders, and a Fine Sun Sensor (FSS) simulator. Equations for the vehicle dynamics, control system electronics, pneumatics, and attitude sensors were simulated in sufficient detail to ensure that nonlinear effects were accurately represented. Because of the unusual characteristics of the FSS response, an FSS simulator was used in place of an analog simulation. This simulator consisted of an array of four solar cells upon which the image of an oscilloscope dot was focused to simulate the relative motion of the sun.

Equations for both the coarse and fine control modes were included in such a way that the transition between modes could be simulated. The vehicle dynamics in the coarse mode were simulated by a three-degree of freedom dynamically coupled set of equations. Originally, a Euler angle transformation was used to determine vehicle attitude and direction cosines; however, the accuracy of the simulation was then related to the magnitude of the pitch angle and the results became invalid for pitch angles approaching 90 deg. These equations were replaced later by Euler parameter simulation and the problem was eliminated. In the fine mode, the vehicle dynamics were simulated by a set of single-axis, dynamically uncoupled, small-angle rotational equations.

The purpose for which the analog simulation was used changed during the course of the program. In the early stages of the analysis and design effort, analog simulation was used extensively to establish the basic control system design. The control system electronics were simulated and studies were carried out to determine nominal parameter values for the entire system. When a design evolved which met the SPARCS performance requirements, a breadboard control electronics package was fabricated. This was then tied into the analog simulation to verify that the hardware duplicated the behavior of the simulated electronics. Later, some of the actual SPARCS flight units were tied into the simulation for checkout and comparison with ABV tests. In addition, proposed design modifications which showed promise on the ABV were then tested on the analog simulation over a wide range of initial conditions.

Many computer runs of completed designs were made during the course of the program, showing that the contract goals on acquisition and pointing performance could be reached theoretically.

4.2 MOTION SIMULATOR FACILITY ABV TESTS

The Motion Simulator Facility used during SPARCS development consisted of an ABV (Fig. 4-1), a solar simulator (Fig. 4-2), an albedo simulator, a set of magnetic field coils, and a number of 8-channel strip recorders.

The ABV was built specifically for the SPARCS program and was designed to match as closely as possible the inertia properties of nominal Aerobee 150 payloads. Magnetic field coils were arranged around the entire test facility so that a field vector of arbitrary orientation could be produced. A rate gyroscope mounted on the ABV was used to check the rate signals generated by the SPARCS control electronics.

The ABV incorporated the breadboard electronics of the original SPARCS 0 design. For the early ABV tests, it was necessary to use substitute hardware for the FSS and the pneumatics subsystem because the flight hardware was not yet available. The substitute FSS, which was called the Intermediate Sun Sensor (ISS), is discussed in Appendix F.

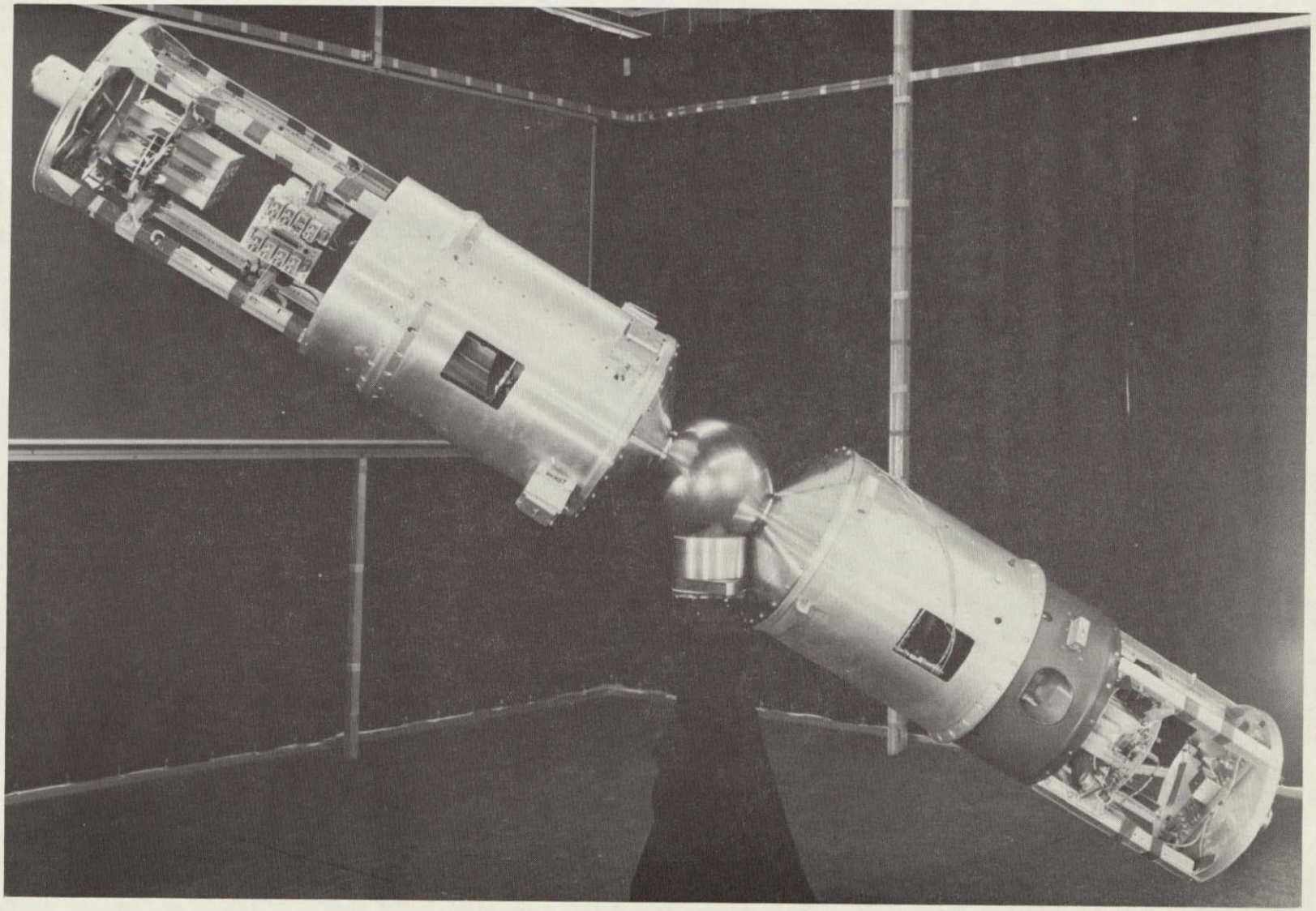

Fig. 4-1 Air Bearing Vehicle

Fig. 4-2 Solar Simulator

The ABV fulfilled three essentially distinct functions during the course of the SPARCS program. The SPARCS 0 design was basically established on the analog simulation, and the ABV was used primariliy as a testing device to verify the design (although minor modifications were introduced as a result of ABV tests). When further modifications leading to SPARCS I were considered, the ABV was used as a design tool for performing tests of the breadboarded changes. When such modifications proved promising, they were then subjected to extensive testing on the analog simulation. Finally, the ABV was used for qualification and acceptance testing of all complete SPARCS units.

Difficulties were experienced in three areas during the initial ABV testing:

a. The acquisition pattern on the analog-designed system allowed the ABV to hit the ±30 deg pitch limits on the support structure, which invalidated the acquistion.

b. The coarse acquisition was not positive enough to produce repeatable results in the presence of ABV disturbance and minor sensor anomalies.

c. The low pressure of the fine mode produced a thrust that was too low to hold the ABV in the fine control null position against the force of mass unbalance and other small torques.

To overcome these difficulties as soon as possible, minor design changes (including increasing the fine mode pressure level) were incorporated into the breadboard system without further analog analysis. When a breadboard design evolved which improved the ABV performance to within the contract requirements, an etched circuit electronics package was fabricated. This development package, plus the first flight hardware FSS and pneumatics, were then installed on the ABV for further development tests. The flight equipment thrust had been designed at a lower level than determined by the ABV breadboard tests because the flight payloads were smaller than the ABV. However, the tests were completed successfully by using the flight hardware and making minor changes in circuit values.

Appendix A
CONTROL THEORY DETAILS

Appendix A
CONTROL THEORY DETAILS

The SPARCS final design is the result of an extensive development program. The desired coarse mode control, as presented in the proposal, was considered to require an excessive amount of equipment; studies performed during the development showed that numerous simplifications could be made which would still yield satisfactory performance. In addition, new concepts were incorporated in the design as the development progressed. The principal considerations and the various configurations that lead to the present SPARCS design are discussed in this appendix.

A.1 SENSOR AND THRUSTER CHARACTERISTICS

The objective of the SPARCS mission is to stabilize the payload in all three axes, with the longitudinal axis pointing toward the sun with a high degree of accuracy. This must be achieved with the vehicle initially spinning about its longitudinal axis and with this axis at an arbitrary initial orientation. Wide-angle sensors capable of detecting an error at any attitude are therefore required. Silicon solar cells and a three-axis magnetometer, mounted as shown in Fig. A-1, were initially chosen to fulfill this requirement. These sensors can measure the direction cosines between each of the three vehicle axes and the vehicle-sun line and magnetic field direction, respectively. Since the solar cells (Coarse Sun Sensors, CSS) are not capable of providing the high accuracy that is required, a narrow-angle Fine Sun Sensor (FSS) mounted in the nose of the vehicle is also included. Control torques are provided by a set of six pulsed cold-gas thrusters.

To despin the vehicle and point it near the sun in the allotted time, a relatively high level of thrust is required. This thrust level, coupled with the minimum pulse width allowable for reliable thruster performance, is inconsistent with the requirements for high accuracy and low rates after acquisition. A lower thrust level is therefore needed after coarse acquisition and is accomplished by lowering the pressure of the gas which feeds the thrusters.

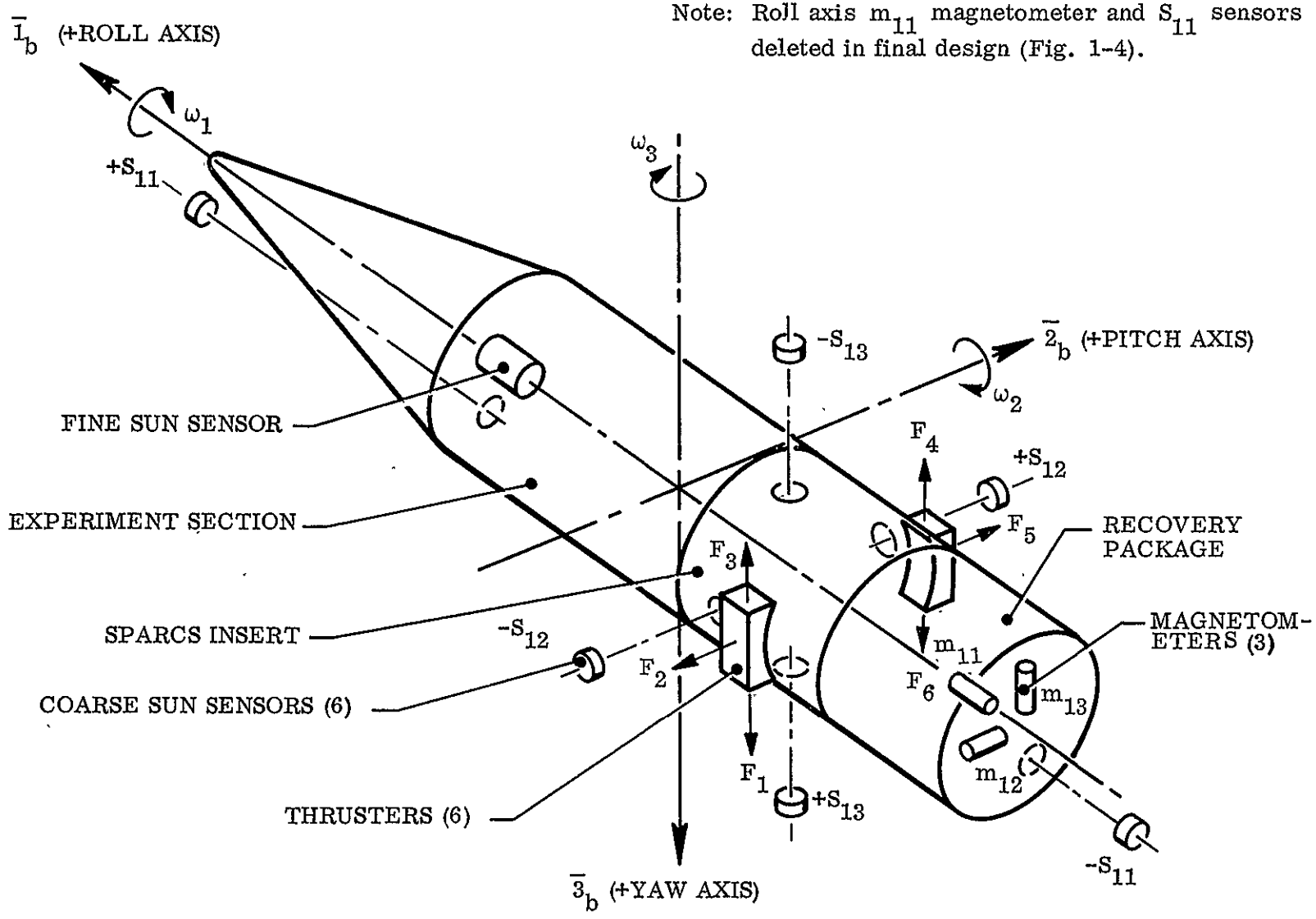

Fig. A-1 Sensor and Thruster Locations

As shown in Fig. A-1, the magnetometers are mounted so that their sensitive axes are aligned along the principal body axes. Each of the six CSS units is mounted with the plane normal to its surface aligned with a body axis. In this manner the three direction cosines between the body axes and the sun line can be measured, as well as the direction cosines between the body axes and the magnetic field direction. This system provides sufficient information to completely define the vehicle attitude at any time. The thrusters are capable of providing moments about any of the three body reference axes. Valves 2 and 5, driven by a single pulsing network, provide yaw torques. The remaining four valves are coupled to provide both pitch and roll torques. Valves 1 and 3 are driven by one pulsing network and Valves 4 and 6 by another. Pitch and roll control torque commands are combined at the inputs to the two pulsing networks in such a manner that Valves 1 and/or 4 provide positive roll torques, and Valves 3 and/or 4 provide positive pitch torques.

A.2 SEQUENCE OF EVENTS

The sequence of events used to achieve the fine pointing mode is as follows. Upon activation of control, despin and coarse acquisition are achieved using the magnetometers and CSS units to provide control signals. When the vehicle is pointing approximately toward the sun, a condition detected by the narrow field-of-view FSS mounted in the nose of the vehicle, the CSS units are switched out and only the FSS and magnetometers remain as error sensors. The control gas pressure is reduced and the pitch and yaw channel gains are increased, leading finally to fine pointing mode limit cycle motions about all three axes.

A.3 COORDINATE SYSTEM

The coordinate system used to describe the sensor outputs and vehicle motion is shown in Fig. A-2. The system consists of three sets of three orthogonal axes. One set contains one axis which points in the direction of the sun. A second set contains one axis which is coincident with the direction of the Earth's magnetic field. The third set has one axis along the longitudinal axis of the vehicle. Unit vectors in these three directions are designated $\overline{1}_s$, $\overline{1}_m$, and $\overline{1}_b$, respectively. Unit vectors $\overline{2}_s$, and $\overline{2}_m$ are coincident and aligned in the direction of $\overline{1}_s \times \overline{1}_m$, with $\overline{3}_s$ and $\overline{3}_m$ completing sets of

right-handed orthogonal axes. Similarly, units vectors $\overline{2_b}$ and $\overline{3_b}$ are chosen as any two-body fixed vectors, completing a right-handed orthogonal set with vector $\overline{1_b}$.

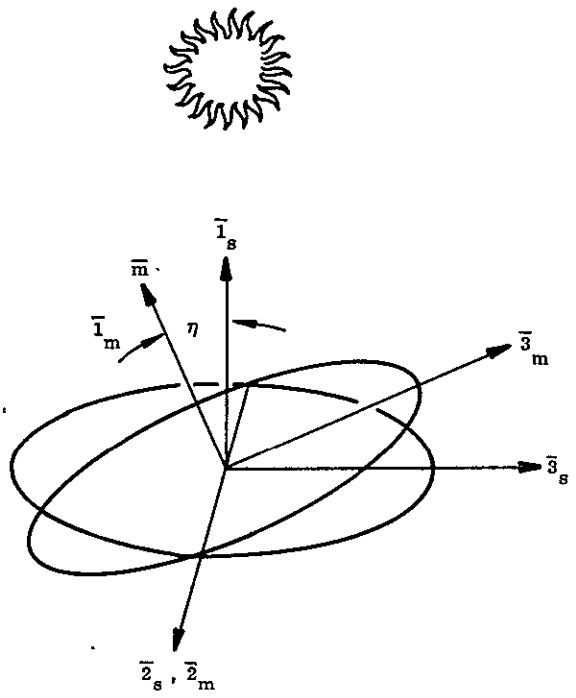

Fig. A-2 Coordinate System

A list of the symbols used in equations and elsewhere in this appendix is given in Table A-1.

Table A-1

APPENDIX A SYMBOLS

$\overline{1}_b$, $\overline{2}_b$, $\overline{3}_b$	vehicle coordinate system
$\overline{1}_m$, $\overline{2}_m$, $\overline{3}_m$	magnetic coordinate system
$\overline{1}_s$, $\overline{2}_s$, $\overline{3}_s$	solar coordinate system
3_g	roll null axes
CSS	Coarse Sun Sensor
F_i	cold gas thrust levels (i = 1 · · · 6)
FSS	Fine Sun Sensor
h_1 , h_2 , h_3	damping gains (control equation)
K	unspecified system gain
k_1 , k_2	attitude error gains (control equation)
k_r , k_p , k_y	control loop gains (roll, pitch, yaw)
M_c	control torque
M_r , M_p , M_y	control torques (roll, pitch, yaw)
m_{ij}	direction cosines (vehicle to magnetic coordinate systems)
S_{ij}	direction cosines (vehicle to solar coordinate systems)
δ_r , δ_p , δ_y	error signals (roll, pitch, yaw)
η	angle between vehicle sun line and magnetic field vector
ϕ_b	selected roll null angle
ϕ , θ, ψ	Euler angles
ω_1 , ω_2 , ω_3	vehicle rates about axes 1 , 2 , 3

A.4 CONTROL EQUATIONS

The reference system (Fig. A-2) is defined by the solar vector and the Earth's local magnetic field vector. The two vectors may not be coincident, and the angle between them, η, is assumed to lie between 30 deg and 150 deg (170 deg for SPARCS I). Control for values outside this range requires longer acquisition times and results in degraded roll performance.

The control law for the pitch and yaw axes is:

$$\bar{1}_b \times \bar{1}_s = 0 \tag{A1}$$

An additional term, for roll control, could be:

$$\bar{3}_b \times \bar{3}_s = 0 \tag{A2}$$

However, this would not allow an arbitrary choice of roll angle because the vehicle axis, $\bar{3}_b$, would always be coincident with $\bar{3}_s$ when the control law is satisfied. A new vector, $\bar{3}_g$, is defined which is free to rotate in the $\bar{2}_b$, $\bar{3}_b$ plane; the roll term then becomes:

$$\bar{3}_g \times \bar{3}_s = (\bar{3}_b \cos \phi_b + \bar{2}_b \sin \phi_b) \times \bar{3}_s = 0 \tag{A3}$$

The roll angle which satisfies the control law is determined by ϕ_b.

To satisfy the above control law for any arbitrary vehicle attitude, a torque proportional to the attitude error must be applied:

$$M_c = k_1 (\bar{1}_b \times \bar{1}_s) + k_2 \left[(\bar{3}_b \cos \phi_b + \bar{2}_b \sin \phi_b) \times \bar{3}_s\right] \tag{A4}$$

where k_1 and k_2 are gain constants chosen to optimize the system.

The transformation between the vehicle axis and the solar reference axis is

$$\begin{bmatrix} \bar{1}_s \\ 2_s \\ 3_s \end{bmatrix} = \begin{bmatrix} S_{11} & S_{12} & S_{13} \\ S_{21} & S_{22} & S_{23} \\ S_{31} & S_{32} & S_{33} \end{bmatrix} \begin{bmatrix} \bar{1}_b \\ 2_b \\ 3_b \end{bmatrix} = S^T \begin{bmatrix} \bar{1}_b \\ 2_b \\ 3_b \end{bmatrix} \tag{A5}$$

and Eq. (A4) may be written in component form with damping terms added for stability:

$$\begin{aligned} M_r &= -k_2 (S_{32} \cos \phi_b - S_{33} \sin \phi_b) + \text{roll damping} \\ M_p &= -k_1 S_{13} + k_2 S_{31} \cos \phi_b + \text{pitch damping} \\ M_y &= k_1 S_{12} - k_2 S_{31} \sin \phi_b + \text{yaw damping} \end{aligned} \tag{A6}$$

A.4.1 Attitude Terms

The terms S_{12} and S_{13} are the direction cosines between the solar vector and the vehicle $\bar{2}_b$ and $\bar{3}_b$ axes, respectively. Since the output of a solar cell is approximately equal to the cosine of the incident light, S_{12} and S_{13} may be measured in this manner.

The terms S_{32} and S_{33} are the direction cosines between the $\bar{3}_s$ coordinate axis and the $\bar{2}_b$ and $\bar{3}_b$ axes, respectively. These quantities cannot be measured directly but may be computed from the output of the magnetometer and sun sensors.

The transformation between the vehicle axis and the magnetic axis is

$$\begin{bmatrix} \bar{1}_m \\ 2_m \\ 3_m \end{bmatrix} = \begin{bmatrix} m_{11} & m_{12} & m_{13} \\ m_{21} & m_{22} & m_{23} \\ m_{31} & m_{32} & m_{33} \end{bmatrix} \begin{bmatrix} \bar{1}_b \\ 2_b \\ 3_b \end{bmatrix} = m^T \begin{bmatrix} \bar{1}_b \\ 2_b \\ 3_b \end{bmatrix} \tag{A7}$$

The solar and magnetic coordinate axes are related by the η rotation about the $\bar{2}_s$, $\bar{2}_m$ axis (Fig. A-2).

$$\begin{bmatrix} \bar{1}_m \\ 2_m \\ 3_m \end{bmatrix} = \begin{bmatrix} \cos\eta & 0 & -\sin\eta \\ 0 & 1 & 0 \\ \sin\eta & 0 & \cos\eta \end{bmatrix} \begin{bmatrix} \bar{1}_s \\ 2_s \\ 3_s \end{bmatrix} = \eta \begin{bmatrix} \bar{1}_s \\ 2_s \\ 3_s \end{bmatrix} \tag{A8}$$

When Eqs. (A5), (A7), and (A8) are combined

$$\eta \; S^T = m^T \tag{A9}$$

and solving for the S_{3j} terms,

$$\left.\begin{aligned} S_{31} &= \left[S_{11}\cos\eta - m_{11}\right]/\sin\eta \\ S_{32} &= \left[S_{12}\cos\eta - m_{12}\right]/\sin\eta \\ S_{33} &= \left[S_{13}\cos\eta - m_{13}\right]/\sin\eta \end{aligned}\right\} \tag{A10}$$

Since m_{11}, m_{12}, and m_{13} are the direction cosines between the magnetic field vector and the vehicle coordinate axes, they may be measured by the magnetometer. Now S_{32} and S_{33} are expressed in terms of measurable quantities, and the roll component of the control law becomes

$$M_r = \frac{-k_2}{\sin\eta}\left[(S_{12}\cos\eta - m_{12})\cos\phi_b - (S_{13}\cos\eta - m_{13})\sin\phi_b\right] + \text{roll damping} \tag{A11}$$

The attitude terms of the control equation [Eqs. (A6) and (A11)] are now completely defined in terms of the measurable quantities S_{12}, S_{13}, m_{12}, and m_{13}; the angle η which is known prior to launch; and φ_b, the arbitrarily chosen roll angle.

A.4.2 Vehicle Rate Computation

Damping signals are provided by vehicle rates computed from the direction cosine outputs of the sun sensors and the magnetometer. They are derived by differentiating Eq. (A5) and noting that $\dot{\bar{1}}_s = \dot{\bar{2}}_s = \dot{\bar{3}}_s = 0$, since these reference axes constitute an inertial reference system. The results are

$$\begin{aligned}
\omega_1 &= \dot{S}_{12}S_{13} + \dot{S}_{22}S_{23} + \dot{S}_{32}S_{33} = -\dot{S}_{13}S_{12} - \dot{S}_{23}S_{22} - \dot{S}_{33}S_{22} \\
\omega_2 &= \dot{S}_{13}S_{11} + \dot{S}_{23}S_{21} + \dot{S}_{33}S_{31} \\
\omega_3 &= -\dot{S}_{12}S_{11} - \dot{S}_{22}S_{21} - \dot{S}_{32}S_{31}
\end{aligned} \tag{A12}$$

The alternate expressions for ω_2 and ω_3, though available, are not used and are therefore not included.

Since all S_{1j} terms may be directly measured by the solar cells, and the expressions for the S_{3j} terms are derived in Eq. (A10), only the S_{2j} terms must be computed.

From Fig. A-2, $\bar{2}_s = \bar{3}_s \times \bar{1}_s$, and when substitutions are made from Eq. (A5), the results are

$$\left.\begin{aligned}
S_{21} &= S_{32}S_{13} - S_{33}S_{12} \\
S_{22} &= S_{33}S_{11} - S_{31}S_{13} \\
S_{23} &= S_{31}S_{12} - S_{32}S_{11}
\end{aligned}\right\} \tag{A13}$$

A.4.3 Complete Control Law Equation

The complete control equation may be written:

$$\left.\begin{aligned} \delta_r &= \frac{-k_2}{\sin\eta}\left[(S_{12}\cos\eta - m_{12})\cos\phi_b - (S_{13}\cos\eta - m_{13})\sin\varphi_b\right] - h_1\omega_1 \\ \delta_p &= -k_1 S_{13} + k_2 S_{31}\cos\phi_b - h_2\omega_2 \\ \delta_y &= k_1 S_{12} - k_2 S_{31}\sin\phi_b - h_3\omega_3 \end{aligned}\right\} \quad \text{(A14)}$$

where h_1, h_2, and h_3 are gain constants chosen to provide proper damping.

The δs represent the control errors and have replaced the Ms of Eqs. (A6) and (A11). In the actual system, the control torques are applied to the vehicle as a function of the control errors by a valve modulation circuit. When δ is very large, the system saturates and operates in a bang-bang mode. During acquisition, the input signal decreases and a transition occurs during which the torque is proportional to δ. For the fine pointing mode, the system delivers a small impulse whenever the jet is fired.

The control torques may be redefined in terms of the six control jets which are arranged as shown in Fig. A-1.

$$\left.\begin{aligned} M_r &= (F_1 + F_4) \quad \text{or} \quad -(F_3 + F_6) \\ M_p &= (F_3 + F_4) \quad \text{or} \quad -(F_1 + F_6) \\ M_y &= F_5 \quad \text{or} \quad -F_2 \end{aligned}\right\} \quad \text{(A15)}$$

The yaw channel is completely independent, whereas the pitch and roll channels share thrusters. Error signals are combined to drive the control jets as follows:

$$\left.\begin{aligned} F_1 \text{ (or } -F_3) &= k_r\delta_r + k_p\delta_p \\ F_4 \text{ (or } -F_6) &= k_r\delta_r - k_p\delta_p \\ F_2 \text{ (or } -F_5) &= -k_y\delta_y \end{aligned}\right\} \quad \text{(A16)}$$

Roll and pitch error signals are summed in the ratio of k_r to k_p; and by varying this ratio, preference may be given to one error signal over the other. Acquisition times are improved by increasing the influence of the roll error signal at the expense of the pitch error signal so that $k_r > k_p$.

A.4.4 Simplifications

The formulation of the control system as depicted in Eq. (A14) is not simple to implement electronically, since it requires 15 multipliers and 20 summing amplifiers (Fig. A-3). Although this system will provide control from any initial attitude or rate (provided, of course, that the gas supply is not exhausted first), this capability is not required for SPARCS. The following five simplifications were made to Eq. (A14) and satisfactory system operation was verified with each simplification prior to implementation:

a. Elimination of the S_{31} terms in the δ_p and δ_y equations
b. Elimination of the S_{12} and S_{13} terms in the δ_r equation
c. The substitution of $\dot{S}_{13}$ for ω_2 in the δ_p equation
d. The substitution of $\dot{S}_{12}$ for ω_3 in the δ_y equation
e. The substitution of $(\dot{S}_{12} + \dot{m}_{12})$ sign $(S_{13} + m_{13}) - (\dot{S}_{13} + \dot{m}_{13})$ sign $(S_{12} + m_{12})$ for ω_1 in the δ_r equation

When these simplifications are incorporated, the equations in (A14) become:

$$\delta_r = \frac{k_2}{2}\left(m_{12}\cos\phi_b - m_{13}\sin\phi_b\right) + h_1\left((\dot{S}_{12} + \dot{m}_{12})\ \text{sign}\ (S_{13} + m_{13}) - (\dot{S}_{13} + \dot{m}_{13})\ \text{sign}\ (S_{12} + m_{12})\right)$$

$$\delta_p = -k_1 S_{13} - h_2 \dot{S}_{13} \qquad \text{(A17)}$$

$$\delta_y = k_1 S_{12} - h_3 \dot{S}_{12}$$

and $k_2 = 0$ when $S_{12} + S_{13} \geq \epsilon\ 0$, where ϵ is a small value.

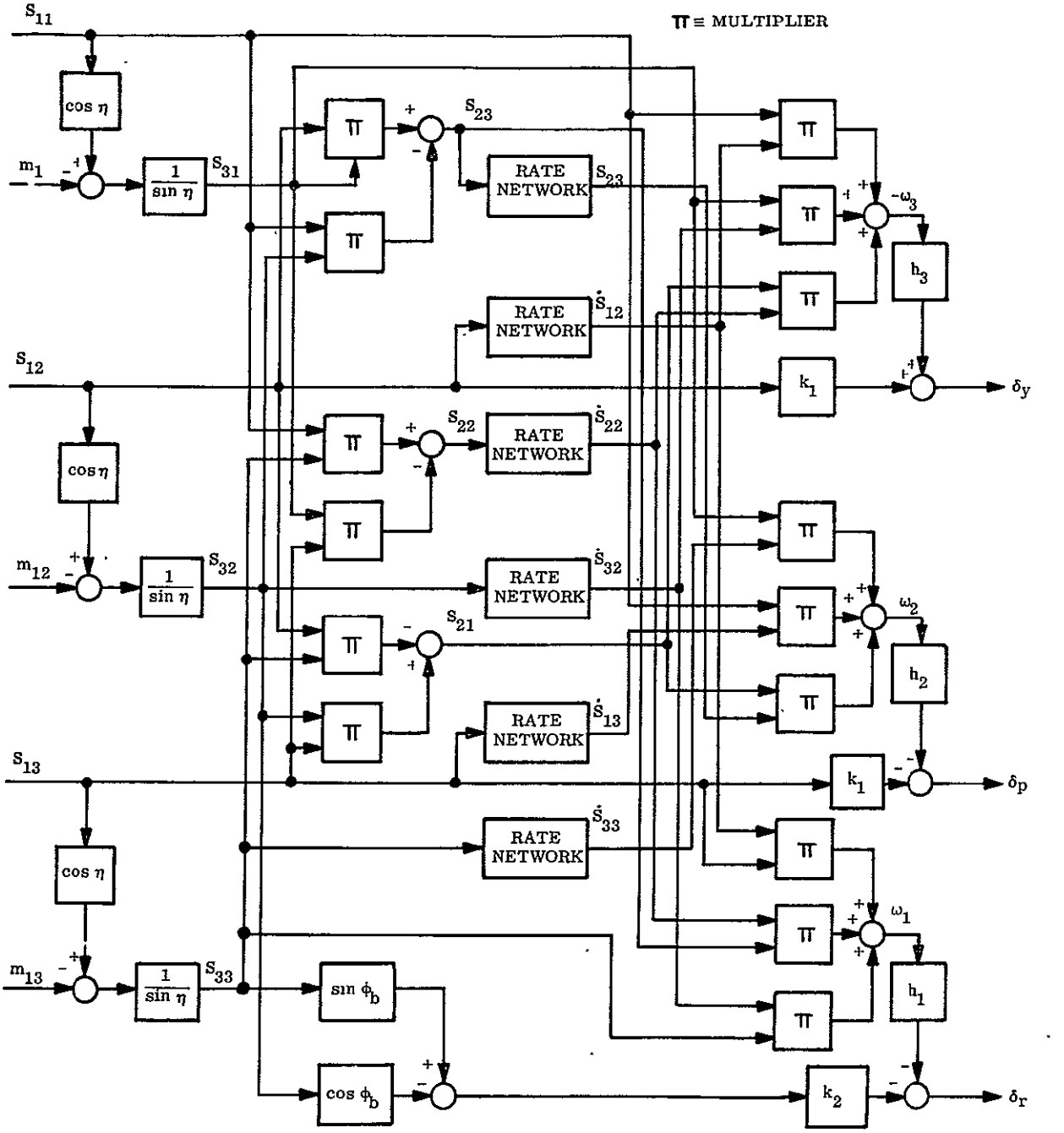

Fig. A-3 Control System Before Simplification

The mathematical justification of these simplifications follows:

1. S_{31} terms in the δ_p and δ_y equations of (A14) result from the roll position of the control law, and are not required to satisfy the pitch and yaw control law, Eq. (A1). If the direction cosine matrix in Eq. (A5) is written in terms of Eulerean angles, nonclassical rotation (Fig. A-4), $S_{31} = -\sin\theta$, which is zero when Eq. (A1) is satisfied. When Eq. (A1) is not satisfied, $S_{31} \neq 0$; however, the lack of this steering information has no effect on sun acquisition.

2. Simplifications 2 and 3 result from a hardware limitation: the pitch and roll channels use the same gas jets, Eq. (A15). Since the vehicle is initially spinning (ω_1 large), gas consumption is minimized if ω_1 is reduced to zero prior to torquing the system to satisfy Eq. (A1). Since roll attitude is unimportant until Eq. (A1) is satisfied, the gas jets are made to respond primarily to δ_p and δ_y once ω_1 is reduced to a small value. Once Eq. (A1) is satisfied, $S_{12} = S_{13} = 0$. Thus these terms contribute nothing to the δ_r equation of (A14). Hence they were eliminated.

   The hardware implementation for SPARCS I includes an inhibit on the roll attitude signal until Eq. (A1) is satisfied; $k_2 = 0$ when $S_{12} + S_{13} \geq \epsilon > 0$, and thus the basis for the above simplification is valid. Because this inhibit was not implemented in SPARCS 0, sun acquisition was not possible for some initial conditions.

3. Since the despin requirement must be given priority for gas consumption considerations, h_1 is sufficiently large so that $h_1\omega_1$ predominates over all other δ_r and δ_p terms, and jets F_3 and F_6 are held on until ω_1 is reduced to a small value. By the time δ_p is able to affect sun acquisition, the yaw jets (F_2 and F_5), which were active during despin, will have reduced the vehicle-sun line so that pitch motion occurs essentially in a plane. ω_2 in Eq. (A12) is approximately equal to $\dot{S}_{13}$, as $S_{11} \cong 1$ and both S_{21} and S_{31} are approaching zero.

4. The yaw jets F_2 and F_5 are used to precess the vehicle toward the sun prior to the completion of despin ($\omega_1 = 0$). A precession signal proportional to $\omega_1 S_{13}$ is desired because as ω_1 becomes small, both the precession effect and signal are proportionally decreased. If it can be shown that $\dot{S}_{12} \cong \omega_1 S_{13}$, then replacing ω_3 in Eq. (A14) with $\dot{S}_{12}$ would give the proper signal during despin and (using the same arguments for $\dot{S}_{13} \cong \omega_2$) the proper damping signal for the yaw channel during acquisition. When the direction cosine matrix is written in terms of Eulerian angles, nonclassical rotation:

$$S_{12} = S\phi\, S\theta\, C\psi - C\phi S\psi \quad (S = \text{sine};\ C = \text{cosine}) \tag{A18}$$

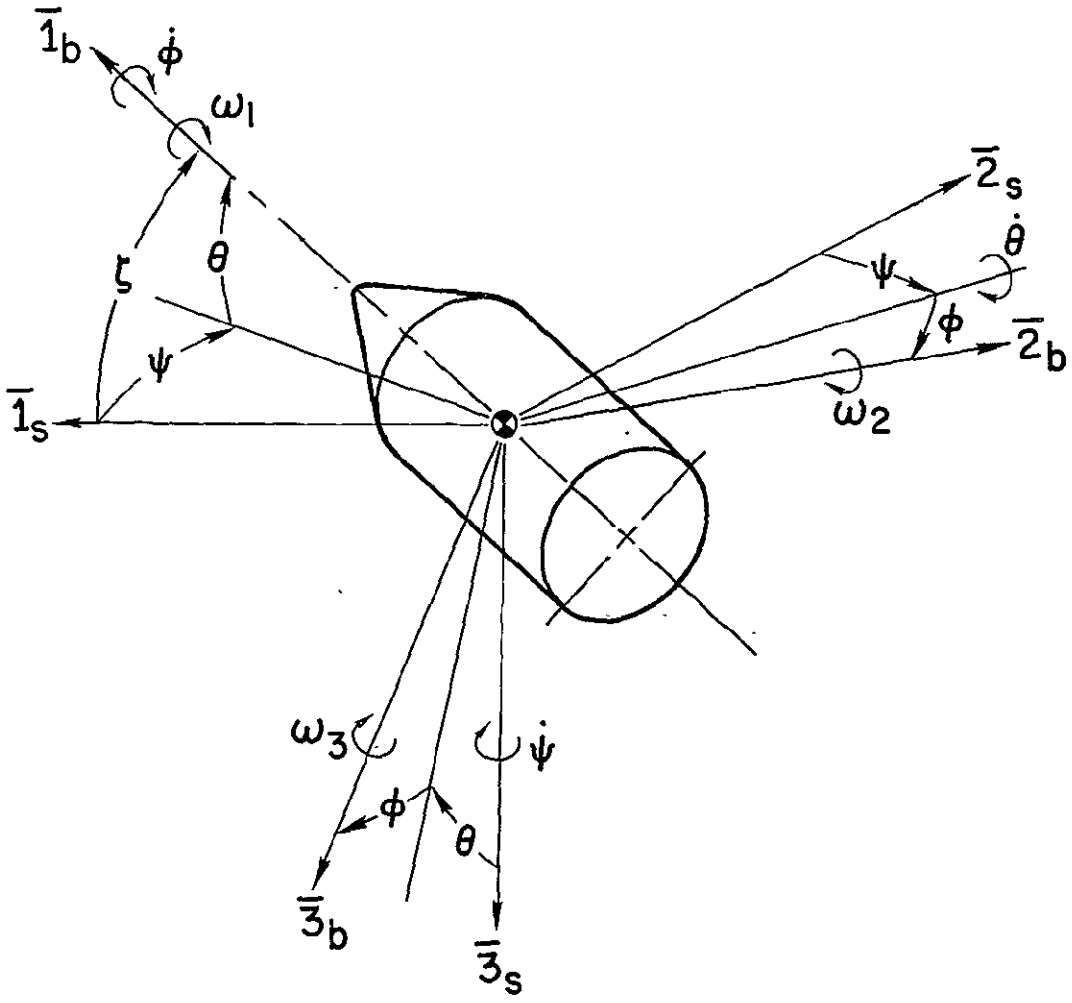

Fig. A-4 Euler Angles

and differentiating and recombining into direction cosines:

$$\dot{S}_{12} = \dot{\phi}\, S_{13} + \dot{\theta} S_{11} S\phi - \dot{\psi} S_{22}$$

The desired equation is achieved if

$$\dot{\phi} >> \dot{\theta} \text{ and } \dot{\psi} \text{ and } \omega_1 \cong \dot{\phi}$$

and these conditions are characteristic of a rocket payload spinning about its minimum moment of inertia. The precession rate is related to the spin rate by

$$\omega_p = \frac{I_1 \omega_1}{I_2} \cos \xi \tag{A19}$$

(where ξ = cone angle) since $I_1 << I_2$, $\omega_p << \omega_1$ for any ξ. Also, $\dot{\theta}$ and $\dot{\psi} \cong \omega_p$, and $\dot{\phi} = \omega_1 + \dot{\psi} \cos \theta$. Now combining inequalities $\omega_1 >> \dot{\psi}$, which implies $\dot{\phi} \cong \omega_1 >> \dot{\theta}$ and $\dot{\psi}$. Therefore $\dot{S}_{12} \cong \omega_1 S_{13}$ and $\dot{S}_{12}$ provide both the proper precession signal and the yaw damping signal.

5. The simplified method of deriving ω_1 follows directly from Eq. (A12). If both expressions for ω_1 are combined to form $2\omega_1$ and all S_{ij}'s are expressed in terms of S_{1j} and M_{1j},

$$\begin{aligned} 2\omega_1 = {} & \dot{S}_{12} S_{13} + 1/S\eta^2 \left\{ (\dot{S}_{13} m_{11} + S_{13} \dot{m}_{11} - \dot{S}_{11} m_{13} - S_{11} \dot{m}_{13}) (S_{11} m_{12} - S_{21} m_{11}) \right. \\ & \left. + (\dot{S}_{12} C_\eta - \dot{m}_{12}) (S_{13} C_\eta - m_{13}) \right\} - \dot{S}_{13} S_{12} - 1/S\eta^2 \left\{ (\dot{S}_{11} m_{12} \right. \\ & + S_{11} \dot{m}_{12} - \dot{S}_{21} m_{11} - S_{21} \dot{m}_{11}) (S_{13} m_{13} - S_{11} m_{13}) \\ & \left. + (\dot{S}_{13} C_\eta - \dot{m}_{13}) (S_{12} C_\eta - m_{12}) \right\} \end{aligned} \tag{A20}$$

All terms resulting from $\dot{S}_{22} S_{23}$ and $\dot{S}_{23} S_{22}$ are fourth order products of direction cosines, which are small compared with the other terms and are neglected. Combining terms:

$$\begin{aligned} 2\omega_1 = {} & 1/S\eta^2 \left[\dot{S}_{12} S_{13} - C_\eta (\dot{S}_{12} m_{13} + S_{13} \dot{m}_{12}) + \dot{m}_{12} m_{13} \right] \\ & -1/S\eta^2 \left[\dot{S}_{13} S_{12} - C_\eta (\dot{S}_{13} m_{12} + S_{12} \dot{m}_{13}) + \dot{m}_{13} m_{12} \right] \end{aligned} \tag{A21}$$

Adding a term so each [ ] may be factored and then combining terms,

$$2\omega_1 = 1/S\eta^2 \left[(\dot{S}_{12} + \dot{m}_{12})(S_{13} + m_{13}) - (\dot{S}_{13} + \dot{m}_{13})(S_{12} + m_{12}) - (1+C_\eta)\left((\dot{S}_{12}m_{13} + \dot{m}_{12}S_{13}) + (\dot{S}_{13}m_{12} + \dot{m}_{13}S_{12})\right)\right] \quad (A22)$$

Since most SPARCS launches will occur when 150 deg $\leq\eta\leq$170 deg, $\cos\eta \geq -1/2$ and $(1 + \cos\eta) \leq 1/2$. Neglecting all terms multiplied by $(1 + \cos\eta)$ leads to an acceptable approximation. Since $1/2\ S\eta^2$ is a gain term, it may be combined with the gain constant, h_1;

$$\omega_1 = h_1 \left\{(\dot{S}_{12} + \dot{m}_{12})(S_{13} + m_{13}) - (\dot{S}_{13} + \dot{m}_{13})(S_{12} + m_{12})\right\} \quad (A23)$$

To avoid the use of multipliers, the gain of the position terms is made large compared to the rate terms so that they are always at their positive or negative limits. Then

$$\omega_1 = h_1 \left\{(\dot{S}_{12} + \dot{m}_{12})\ \text{sign}\ (S_{13} + m_{13}) - (\dot{S}_{13} + \dot{m}_{13})\ \text{sign}\ (S_{12} + m_{12})\right\} \quad (A24)$$

For SPARCS 0, an even simpler expression for ω_1 resulted from neglecting all the cross-product terms of Eq. (A21); then

$$\omega_1 = \dot{S}_{12}\ \text{sign}\ S_{13} - \dot{S}_{13}\ \text{sign}\ \dot{S}_{12} + m_{12}\ \text{sign}\ \dot{m}_{13} - m_{13}\ \text{sign}\ m_{12} \quad (A25)$$

This expression follows by showing that $\dot{S}_{13} = -\omega_1 S_{12}$, $\dot{m}_{12} = \omega_1 m_{13}$, and $\dot{m}_{13} = -\omega_1 m_{12}$. In the same way, $\dot{S}_{12} = \omega_1 S_{13}$ and by noting that S_{12} sign $S_{13} \cong \omega_1 S_{13}$ and sign $S_{13} \cong \omega_1 |S_{13}|$, and when combined with other similarly derived expressions,

$$\dot{S}_{12}\ \text{sign}\ S_{13} - \dot{S}_{13}\ \text{sign}\ S_{12} + \dot{m}_{12}\ \text{sign}\ m_{13} - \dot{m}_{13}\ \text{sign}\ m_{12} \cong \omega_1 \left[|S_{13}| - |S_{12}| + |m_{13}| - |m_{12}|\right] \quad (A26)$$

Division by the term in [ ] was not implemented; as a result, system sensitivity to the magnitude of the magnetic field and solar intensity at the completion of despin is increased, so that the magnitude of ω_1 is less certain. This was instrumental in restricting system performance when $\eta \geq 150$ deg.

A.5 FINAL MECHANIZATION

The resulting mechanization of the control law with all the simplifications included is shown in Fig. A-5. Analog studies and air bearing tests have shown that acquisition times will be less than 40 seconds with initial attitude errors as large as 90 deg, angular rates as large as 5 deg/sec about the transverse axis, and spin rates of 2.5 rps.

A.5.1 Fine Pointing Mode

Pointing accuracy in the fine mode is primarily a function of the Fine Sun Sensor (FSS) and magnetometer characteristics. The cross coupling due to vehicle dynamics may be neglected, and all channels are independent except for the sharing of thrusters in pitch and roll.

The FSS is a nonimaging type that permits solar energy to fall on a quad array of cells. Because of its nonimaging characteristics, the sun's energy is not concentrated and the effects of cell mismatch and local irregularities are consequently reduced. The incident energy is further reduced by the use of a mask which obscures part of the cells near null (Fig. A-6). The required gain around null is achieved by electronic amplification. Although the choice of cell arrangement yields highly cross coupled output signals, system performance is not significantly affected and around the null the cross coupling is negligible.

A.5.2 Roll Bias Angle

If a single-axis magnetometer were placed in a plane perpendicular to the payload longitudinal axis, roll null would occur when the projection of the Earth's magnetic field vector was perpendicular with the sensor. If the sensor were free to rotate in this plane, any roll null could be commanded. The SPARCS roll control works essentially the same way. A two-axis magnetometer is aligned with the 2_b and 3_b axis, respectively. With the vehicle pointing at the sun, Eq. (A17) defines the roll control signal and $(m_{12} \cos \phi_b - m_{13} \sin \phi_b)$ defines a new roll null axis which lies in an

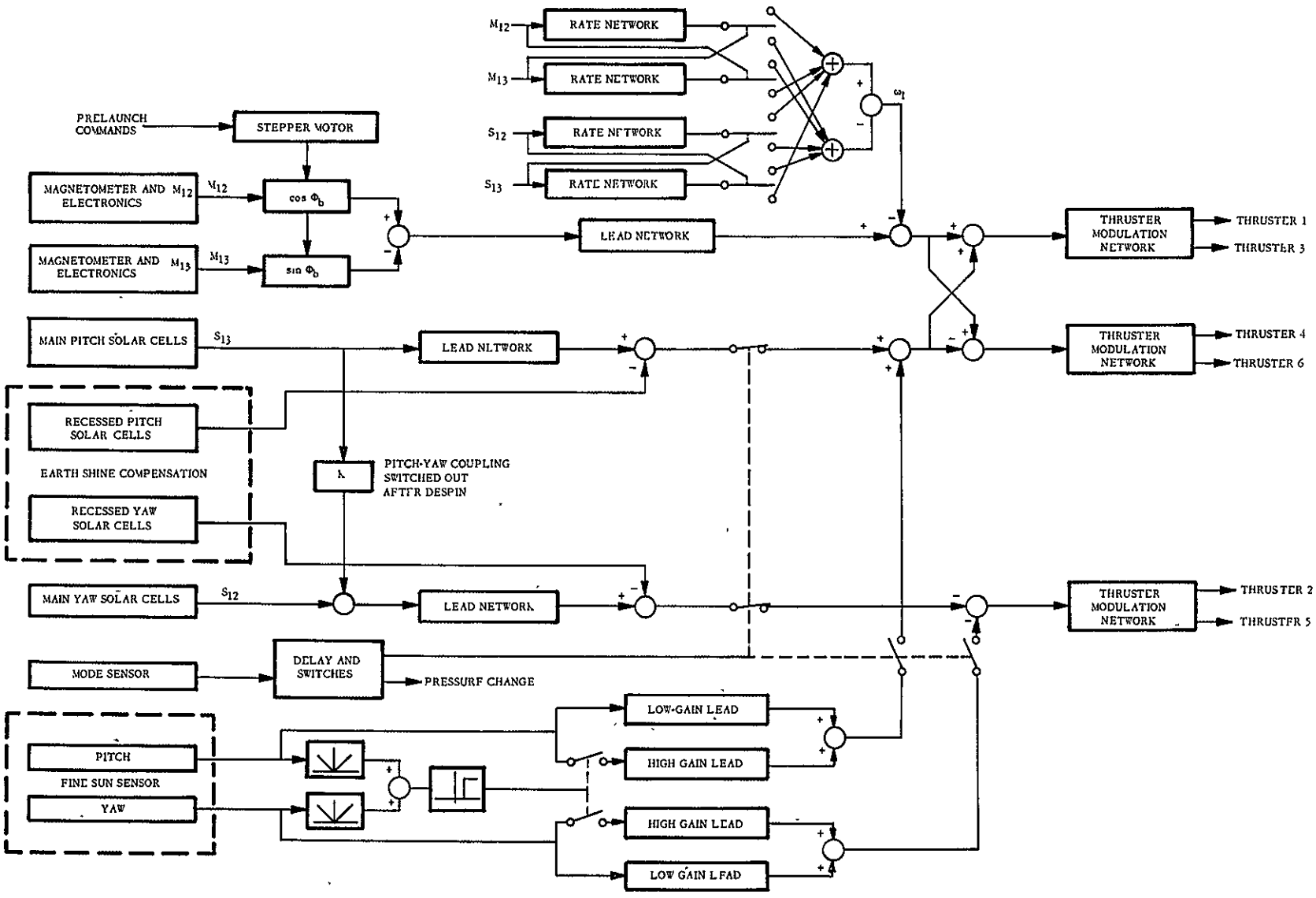

Fig. A-5 SPARCS 0 Block Diagram

angle ϕ_b from the m_{12} or $\bar{2}_b$ axis (Fig. A-6). Roll null is achieved only when the $\bar{3}_g$ axis and the projection of $\bar{I}_m$ into the $\bar{2}_b$, $\bar{3}_b$ plane are coincident. Thus, specifying ϕ_b determines the roll null angle.

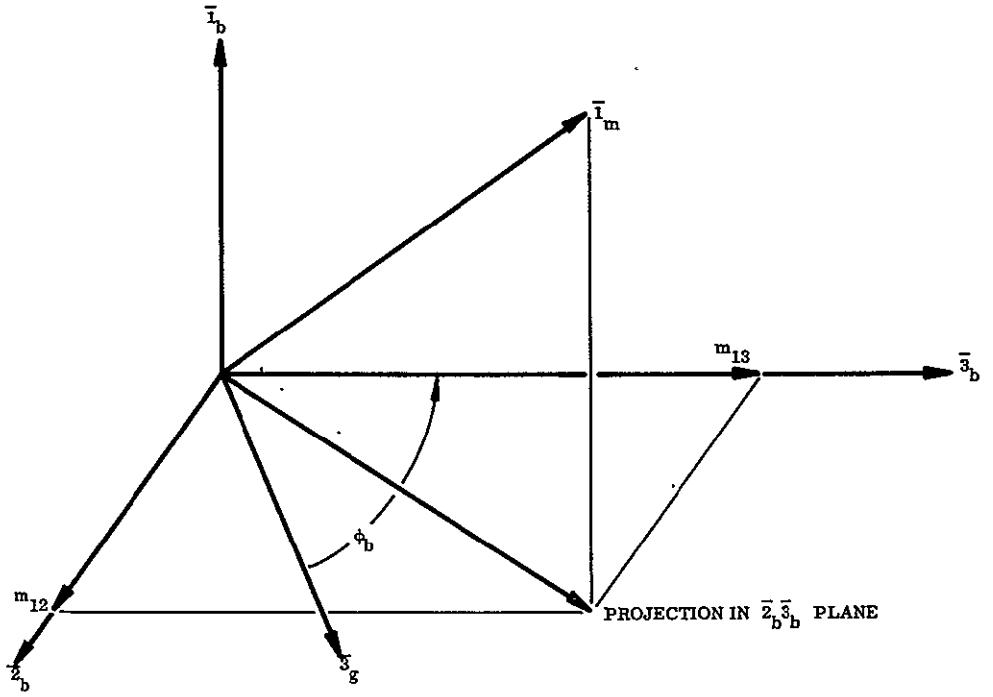

Fig. A-6 Roll Command Angle, ϕ_b

A.5.3 Hardware Implementation

In theory, SPARCS I operates in a similar manner as the SPARCS 0 system shown in Fig. A-5; only the hardware implementation differs (as discussed in Appendix D). The sequence of events from initiation of control to the fine pointing mode is as follows:

Despin. At the initiation of control, the signal produced by the spin rate computation circuitry will be very large (sufficient to saturate two pitch/roll thrusters)

and will cause the vehicle to despin. During despin, the yaw channel, using the Coarse Sun Sensor (CSS) signals, will produce a motion of the spin axis in a direction generally toward the sun.

Coarse Acquisition. When the spin rate has been reduced to a small value, the spin rate signal will no longer cause valve saturation; consequently, both pitch and roll will be active through their respective coarse position control loops. Pointing near the sun (possibly offset a few degrees because of the Earth's albedo,) will thus be accomplished in the coarse mode.

Fine Control Mode. The narrow field-of-view FSS detects when the longitudinal axis is within 10 deg of the sun. When the sun has remained within this 10-deg field-of-view for a period of 6 sec (indicating that coarse acquisition has been completed), the pneumatics are switched to the low pressure regulator and the valve thrust is reduced to a low level. Two seconds later, the FSS low gain channel is switched in and the CSS cells are switched out. After the pitch and yaw errors as measured by the FSS have been reduced to less than 0.5 deg., the high gain channel is switched in, leading to the fine pointing mode. The vehicle remains in this mode until overcome by aerodynamic forces on its return to Earth.

Appendix B
SYSTEM STUDIES

Appendix B
SYSTEM STUDIES

B.1 ENVIRONMENTAL DISTURBANCE TORQUE STUDY

Design of the SPARCS attitude control system requires a knowledge of the environmental torques acting on the vehicle after sustainer separation. The methods by which these torques (aerodynamic, solar, magnetic, and gravity gradient) were calculated and the results of the torque analyses are discussed in the following paragraphs. The symbols used in these discussions are listed in Table B-1.

B.1.1 Payload Vehicle Configuration

Two payload vehicles, representing extremes in SPARCS payload weights, were chosen for this study. Both vehicles, obtained from Ref. 1 and shown in Fig. B-1, are cone-cylinder configurations with a maximum diameter of 15 in. and a 10-deg half-angle conical forebody. The 200-lb and 350-lb payload vehicles are represented by configurations using cylinder fineness ratios (ℓ/d) of 3.07 and 7.00, respectively. The protuberances on the aft end of the vehicle (Fig. B-1) are quadraloop antennas.

B.1.2 Continuum Flow Aerodynamic Coefficients

The SPARCS vehicle nominal launch trajectories of Ref. 1 show that the Aerobee launch rocket achieves hypersonic speed before sustainer engine cutoff and payload separation. Consequently, only hypersonic aerodynamic characteristics have been determined for the SPARCS payload sections in continuum flow. Ref. 2 was used for calculating normal and axial force coefficients (C_N and C_A, respectively). Newtonian flow characteristics were assumed in all cases. Velocity and density magnitudes, V and ρ, respectively, were obtained from the nominal 200- and 350-lb payload trajectories of Ref. 3. Maximum rolling moments were found to be 0.655 ft-lb for the 350-lb vehicle and 0.295 ft-lb for the 200-lb configuration. A zero rolling moment represents vehicle symmetry with respect to the velocity vector.

Table B-1

ENVIRONMENTAL TORQUE STUDY SYMBOLS

C_A	axial force coefficient $= \dfrac{F_A}{1/2\ \rho V_\infty^2 S_{ref}}$
C_N	normal force coefficient $= \dfrac{F_N}{1/2\ \rho V_\infty^2 S_{ref}}$
C_l	rolling moment coefficient $= \dfrac{F_{na}}{1/2\ \rho V_\infty^2 S_{ref}}$
C_m	moment coefficient $= \dfrac{M}{1/2\ \rho V_\infty^2 d\ S_{ref}}$
d	maximum vehicle diameter (reference length) = 15 in.
F_A	axial force, lb
F_N	normal force, lb
$\overline{H}$	magnetic field strength vector
H	magnitude of $\overline{H}$, gauss
$\overline{\overline{I}}$	vehicle moment of inertia tensor
I	pitch and yaw moment of inertia, slug-ft^2
I_x	vehicle moment of inertia about axis of symmetry, slug-ft^2
K_n	Knudsen number
L	characteristic length, ft
ℓ	cylinder length, ft
ℓ_c	cone length, ft
ℓ_{tot}	total vehicle length, ft
ℓ/d	fineness ratio
M	moment or torque, ft-lb
$\overline{m}$	magnetic dipole strength vector

Table B-1 (Cont.)

m	magnitude of $\overline{m}$, pole-cm
P_s	solar radiation pressure, 0.97×10^{-7} psf
$\overline{R}$	radius vector from Earth's center to vehicle mass center
R	magnitude of $\overline{R}$, ft
RM	rolling moment, ft-lb
S_{ref}	reference area (vehicle maximum cross section), ft^2
V_∞	free stream velocity, fps
α	body angle of attack, deg
δ	nose cone half-angle, deg
θ	angle between vehicle axis of symmetry and local horizontal, deg
λ	mean molecular free path, ft
μ	Earth's gravitational constant, ft^3/sec^2
ρ	atmospheric density, $slugs/ft^3$

Subscripts

fm	free molecule
g	gravity gradient
m	magnetic dipole
s	solar radiation

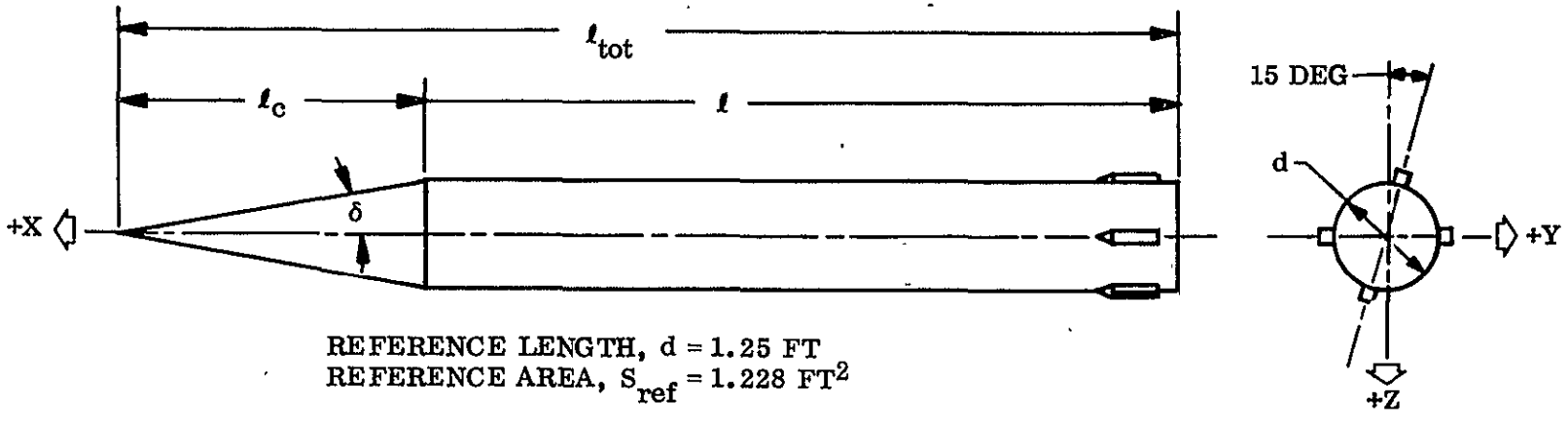

REFERENCE LENGTH, d = 1.25 FT
REFERENCE AREA, S_{ref} = 1.228 FT^2

200-LB PAYLOAD VEHICLE

δ = 10 DEG
ℓ_c/d = 2.833
ℓ/d = 3.07
ℓ_{tot} = 7.37 FT

350-LB PAYLOAD VEHICLE

δ = 10 DEG
ℓ_c/d = 2.833
ℓ/d = 7.00
ℓ_{tot} = 12.29 FT

Fig. B-1 SPARCS Nominal Vehicle Configuration

The magnitudes of the aerodynamic pitching and rolling moments depend on the time of separation from the sustainer, since aerodynamic torques are a function of vehicle velocity and air density (altitude). Fig. B-2 shows the magnitudes of the aerodynamic moments in pitch and roll for payload separation 66 sec after launch. The data represents conditions for the first 15 sec after separation and before nose cone ejection. They were calculated using the trajectory data for the earliest possible separation time and the programmed pitch maneuver from Ref. 3. The effect of altitude differences at separation are evident by the order of magnitude differences between torques acting on the two payload configurations. The 200-lb payload ($\ell/d = 3.07$ configuration) is separated at 222,500 ft and experiences maximum pitching and rolling moments of 0.36 and 0.0023 ft-lb, respectively. The heavier payload, represented by the $\ell/d = 7.0$ cylinder, experiences a maximum torque of 5.9 ft-lb in pitch and 0.014 ft-lb in the roll direction. The rolling moments for both configurations are well within the capabilities of the SPARCS control limits. However, the magnitude of the pitching moment experienced by the $\ell/d = 7.0$ vehicle may approach or exceed the capability of the control system. If this is the case, a delay in separation time can be used to reduce the pitching moment to below one ft-lb.

B.1.3 Free Molecule Flow Aerodynamic Coefficients

At relatively low altitudes (below approximately 266,000 ft), the atmosphere is sufficiently dense to be considered a continuous medium. As altitude increases, however, the atmosphere becomes less dense, causing flow characteristics to change and air molecules to have less influence on one another. The assumption of a continuous medium becomes invalid and the vehicle enters a transition flow region. As altitude continues to increase, the density is reduced to a point where the molecules which impinge on a vehicle surface are not influenced by the molecules which are reflected or re-emitted from the surface. This condition is defined as free molecule flow and is affected not only by low density, but also by the size of the vehicle. The condition of noninfluence is included in the parameter known as the Knudsen number, K_N, defined as follows:

$$K_N = \lambda/L \qquad \text{(B1-1)}$$

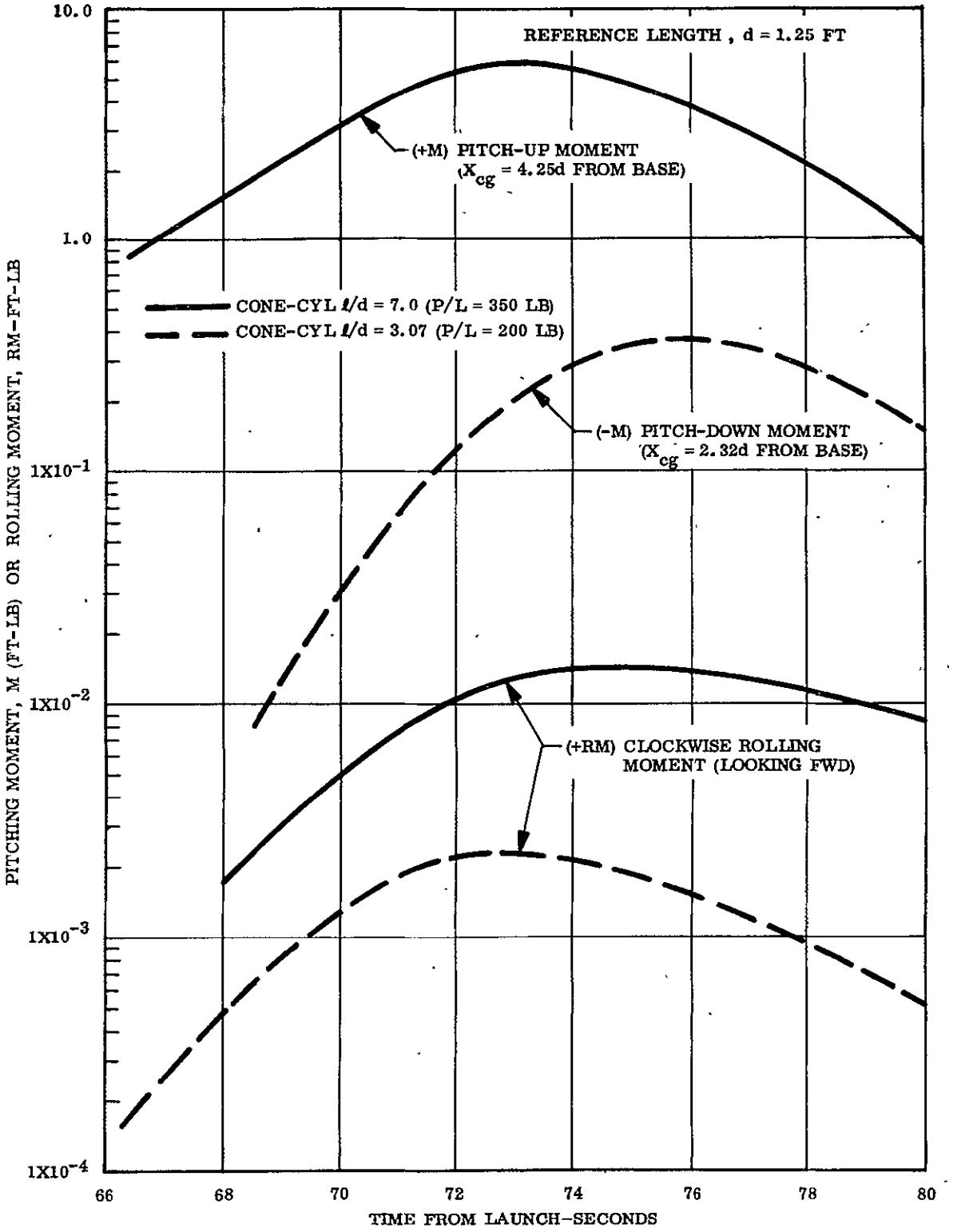

Fig. B-2 Aerodynamic Pitching and Rolling Moments During Payload Separation

where λ is the molecular mean free path and L is the characteristic length. The different flow regimes are defined by the magnitude of the Knudsen number in the following manner:

Continuum flow	$K_N \ll 1$ (0 - 300,000 ft)
Free molecule flow	$K_N \gg 1$ (>400,000 ft)
Transition flow	Intermediate values of K_N (300,000 ~ 400,000 ft)

where transition is defined as the region where flow characteristics change from one condition to the other.

In free molecule flow, the aerodynamic coefficients are functions of the geometry of the vehicle in question and the molecular speed ratio, S , which is defined as the ratio of the vehicle velocity to the mean molecular speed. Force and moment coefficient calculations were made using the exact free molecule flow theory, based on principles of kinetic theory of gasses. A detailed discussion of this method is given in Ref. 4, where expressions for the force and moment coefficients are evaluated for certain elementary shapes.

The moment coefficients were taken about the volume centroids of the cylinders. Actual forces and moments may be obtained from the following expressions.

$$
\begin{aligned}
F_{A_{fm}} &= C_{A_{fm}} \left(1/2\ \rho\ V_\infty^2\ S_{ref}\right) \\
F_{N_{fm}} &= C_{N_{fm}} \left(1/2\ \rho\ V_\infty^2\ S_{ref}\right) \\
M_{fm} &= C_{M_{fm}} \left(1/2\ \rho\ V_\infty^2\ d\ S_{ref}\right)
\end{aligned}
\qquad \text{(B1-2)}
$$

where ρ is the atmospheric mass density, V_∞ is the relative wind speed, and S_{ref} and d are the reference area and length upon which the aerodynamic coefficients are based. The data are based on the nominal design trajectories of Ref. 1.

Maximum pitch-yaw torque expected in the free molecular flow region is 4×10^{-4} ft-lb at an attitude of 400,000 ft. Figure B-3 presents roll torque curves showing the expected worst case variation from entrance into the molecule flow region (400,000 ft) to apogee.

B.1.4 Solar Radiation Forces and Disturbance Torques

Both Maxwell's equations of electrodynamics and Einstein's theory of relativity show that radiation involves momentum transfer in addition to energy transfer. Radiation impinging on an opaque surface causes a pressure on that surface as a result of the radiation momentum transferred to the surface. Radiation forces and torques are obtained by integrating this pressure over the surface of the spacecraft.

A detailed analysis of radiation forces on opaque bodies is given in Ref. 5. The method of analysis consists of computing the momentum transfer to an arbitrary surface due to both impinging and reflected radiation. The analysis includes the effect of surface reflectance and direction of reflection. Numerical tables are also included in Ref. 5 for force and torque computation for several simple geometric shapes.

Force and moment coefficients have been computed for the 200- and 350-lb payload cylinders. As before, the moment center was selected as the volume centroid of the body. Calculation of forces and torques were made using the following relationships:

$$\begin{aligned} F_{N_s} &= P_s S_{ref} C_{N_s} \\ F_{A_s} &= P_s S_{ref} C_{A_s} \\ M_s &= P_s d S_{ref} C_{m_s} \end{aligned} \qquad \text{(B1-3)}$$

where P_s is the solar radiation pressure in the region of the earth ($= 0.97 \times 10^{-7}$ psf). Curves showing solar torque about a transverse vehicle axis (pitch, yaw) as a function of angle of attack are presented in Fig. B-4. Negligible roll torque existed because of the high degree of symetry of the vehicle about the roll axis.

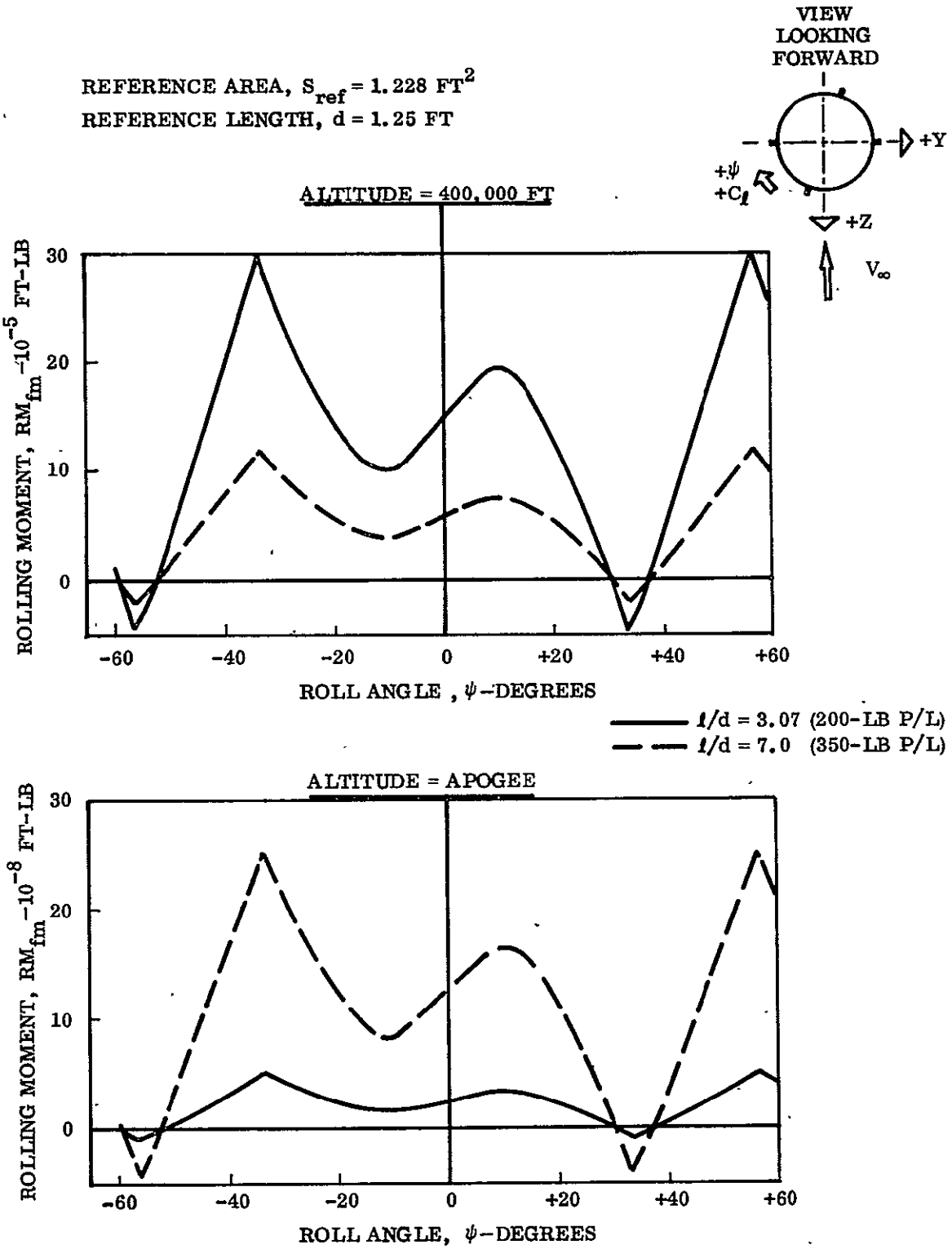

Fig. B-3 Payload Rolling Moment Characteristics at 90-Degree Angle of Attack in Free Molecule Flow

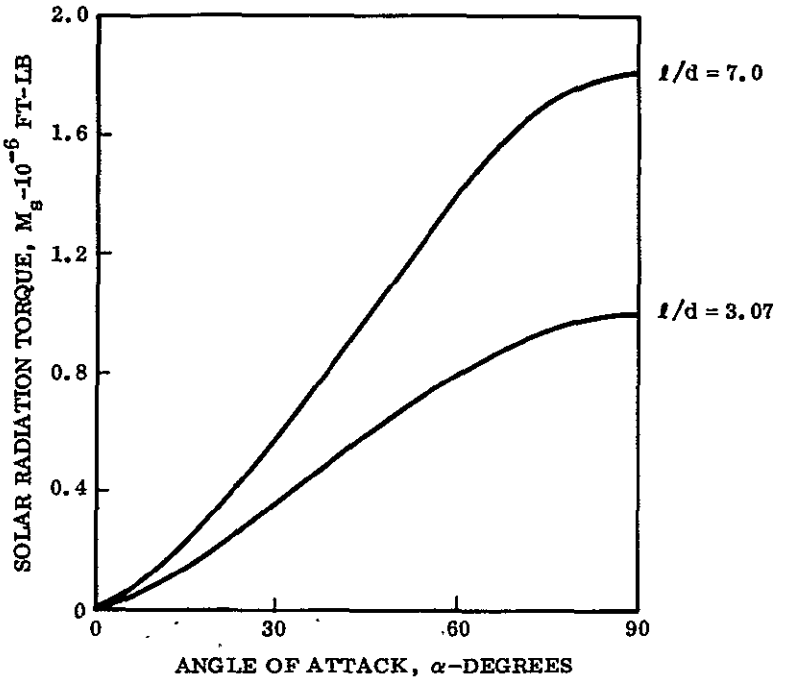

Fig. B-4 Variation of Solar Torque With Angle of Attack for Two Payload Cylinders

B.1.5 Magnetic Dipole Torque

A magnetic dipole when placed in a magnetic field results in a torque given by

$$\overline{M} = \overline{m} \times \overline{H} \qquad \text{(B1-4)}$$

where $\overline{m}$ is the magnetic dipole strength and $\overline{H}$ is the magnetic field strength. The value of $\overline{m}$ may be due to a combination of permanent magnets and/or electric current loops, since it is the effective value of $\overline{m}$ for the whole vehicle which produces the vehicle torque. The direction and magnitude of the Earth's magnetic field, $\overline{H}$, varies with position and altitude.

For the SPARCS vehicle, measurements show that the magnitude of $\overline{m}$ may be as large as 1000 pole-cm for the complete vehicle. For typical launch conditions, the magnitude of $\overline{H}$ is approximately 0.4 gauss. Thus, the maximum expected magnetic dipole torque is about

$$M_m = mH = 400 \text{ dyne} - \text{cm} = 2.95 \times 10^{-5} \text{ ft-lb}$$

The direction of this torque is normal to the plane formed by the vectors $\overline{m}$ and $\overline{H}$.

B.1.6 Gravity Gradient Torque

Gravity gradient torques occur as a result of the variation of the gravitational force per unit mass across the finite dimensions of the vehicle. Particles closer to the Earth are attracted more strongly than those farther away, resulting in a net torque about the vehicle center of mass. An analysis of this phenomena is given in Ref. 6.

Assuming principal axes with equal pitch and yaw moments of inertia, the magnitude of the gravity gradient torque is given by

$$M_g = 3\mu/R^3 \left(I - I_x\right) \cos\theta \sin\theta \qquad \text{(B1-5)}$$

where μ is the Earth's gravitational constant, R is the radial distance between the Earth and satellite mass centers, I and I_x are the pitch and roll moments of intertia, and θ is the angle between the vehicle roll axis and the local vertical. The maximum value of this torque occurs when θ = 45 deg, which may easily occur for typical launch conditions. For the SPARCS vehicle, I = 76.6 and I_x = 2.6 slug-ft^2, which results in a maximum torque of

$$M_g = 1.65 \times 10^{-4} \text{ ft-lb}$$

The vector representing this torque lies in the local horizontal plane and is normal to the axis of symmetry of the SPARCS vehicle. No gravity gradient roll torque exists, because of vehicle symmetry.

B.1.7 Results and Conclusions

The results of this study indicate that maximum aerodynamic pitching moments of approximately 6 ft-lb may be experienced when the SPARCS cone-cylinder configuration

is separated from the sustainer 66 sec after launch and the pitch program maneuver is initiated before nose cone ejection. A delay in separation to 70 sec, with a simultaneous ejection of the nose cone, reduces the maximum aerodynamic pitching moment to less than 0.5 ft-lb. Maximum pitching moments expected in the free molecule flow regime are on the order of 4×10^{-4} ft-lb at an altitude of 400,000 ft. Maximum solar radiation, gravity gradient, and magnetic dipole torques are 1.8×10^{-6}, 1.65×10^{-4}, and 2.95×10^{-5} ft-lb, respectively. Aerodynamic roll torques can reach a maximum of 0.0145 ft-lb during hypersonic flight and 30×10^{-5} ft-lb as the vehicle enters the free molecule flow regime. Both moments continue to decrease as altitude increases.

B.2 VEHICLE SUN LINE-MAGNETIC FIELD VECTOR ANGLE STUDY

The SPARCS sun line vector and the Earth's magnetic intensity vector define an attitude reference plane for the SPARCS vehicle. These two vectors may not be coincident and must make an angle of between 30 deg and 150 deg (10 deg and 170 deg for SPARCS I) to ensure rapid sun acquisition times and accurate vehicle roll positioning. In addition to the above launch requirement, the sun must be at least 18 deg above the horizon to guarantee that the SPARCS vehicle will not be looking at the sun through the Earth's atmosphere and thus see a refracted image of the sun. The variation of the η angle (the angle between the sun line and magnetic intensity vectors) with time of day and day of the year is determined in this section; the locus of acceptable SPARCS launch times is also established.

B.2.1 Determination of the Magnetic Field Direction

The Earth's magnetic field intensity vector, $\bar{H}$, was determined from a spherical harmonic expansion of the gradient of the Earth's magnetic potential. The coefficients of the terms of this expansion were determined by Tanselay and Kantzleben and may be found in Ref. 7. Most of the readily available information on the Earth's magnetic field variation is based on surface observations. These include (1) secular variations requiring hundreds of years to produce a change of a few percent (less than 100 γ/year*) and (2) transient variations which have periods ranging from a fraction of a second to several years. Due to the first effect, the Earth's dipole moment has decreased by about 7 percent (Ref. 8) in the past 100 years but is now slowly increasing.

Transient phenomenon is ordinarily divided into a regular and irregular variation. It is customary that each month five days be designated as quiet days and five days be designated as disturbed days, based on the worldwide records gathered by the DeBilt-Holland Magnetic Center. Station records show a fairly smooth and regular variation of the field over each 24-hour period. The solar quiet day variation measures anywhere from 10 to 200 γ, depending upon the component being measured and location of the reporting station. Irregular variations are caused by magnetic storms and can account for

*The gamma (γ) is used interchangeably as a unit of magnetic induction (10^5 γ = 1 gauss) or magnetic intensity (10^5 γ = 1 oersted).

variations of 500 γ or more, lasting several days. However, these variations cause a temporary angular shift in the magnetic field of less than one degree.

Since this variation is small in comparison to the rapid change in η due to the motion of H relative to the sun vector, the magnetic field was considered stationary relative to the Earth in this study. The magnetic field direction as a function of altitude for White Sands, New Mexico, (latitude 32.4°N and longitude 106.3°W) is shown in Fig. B-5. Since the altitude variation in the field direction is small, the ground level value of dip (-60.350°) and declination (+12.355° E) was used in the η angle computation.

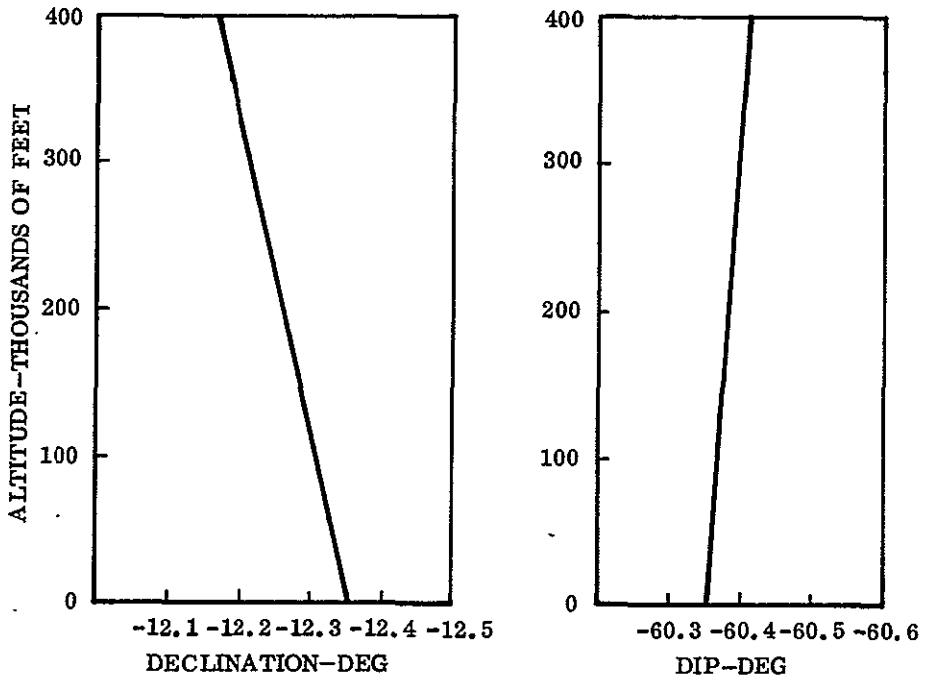

Fig. B-5 Earth Magnetic Field for White Sands, N.M.

B.2.2 Sun Line Vector Determination

The direction of the sun line vector with respect to an Earth fixed inertial reference frame changes only as a function of the position of the Earth in its orbit around the sun. The inertial reference frame utilized is defined in Section B.3 (Fig. B-9) of this

appendix (the $\bar{1}_I$ axis is in the direction of the north ecliptic pole with the $\bar{2}_I$ axis toward the vernal equinox). Thus, in this reference frame, the sun line vector rotates about the $\bar{1}_I$ axis in the $\bar{2}_I - \bar{3}_I$ plane once per year. The angle that the sun line makes with respect to the $\bar{2}_I$ axis in the $\bar{2}_I - \bar{3}_I$ plane is called the celestial longitude of the true sun, λ_s. The angle λ_s does not change linearly with time of the year because of the eccentricity of the Earth's orbit; however, λ_s may be calculated to an accuracy of ±0.05 deg by adding a small sinusoidal term to a linear time term as shown in Eq. (B3-8) in Section B.3.

B.2.3 Eta Angle Computation

The angle η between the sun line vector and the Earth's magnetic intensity vector was computed from the scalar or dot product of these two vectors for 1967:

$$\eta = \cos^{-1}\left(\bar{1}_s \cdot \bar{1}_m\right) \qquad \text{(B2-1)}$$

where $\bar{1}_s$ is the unit vector in the local direction of the sun, and $\bar{1}_m$ is the unit vector in the local direction of the magnetic field.

The components of the unit vectors $\bar{1}_s$ and $\bar{1}_m$ are expressed in the Earth fixed inertial reference frame shown in Section B.3 (Fig. B-11). The details of determining the components of $\bar{1}_s$ and $\bar{1}_m$ in this reference frame are explained in Section B.3.

Then

$$\bar{1}_s \cdot \bar{1}_m = S_{1_I} m_{1_I} + S_{2_I} m_{2_I} + S_{2_I} m_{2_I} \qquad \text{(B2-2)}$$

Figure B-6 shows the 1967 seasonal variation in η for noon mountain standard time at White Sands, New Mexico. Note that the maximum values of η (η closest to 180 deg) occur close to the equinoxes, since the magnetic vector at White Sands is nearly parallel to the equatorial plane and directed into the Earth. The daily variation in η for the first quarter of 1967 is shown in Fig. B-7 and is typical of the variation for that entire year. The curve for any day of the year may be obtained by interpolation and by using the noon values in Fig. B-6 as a reference.

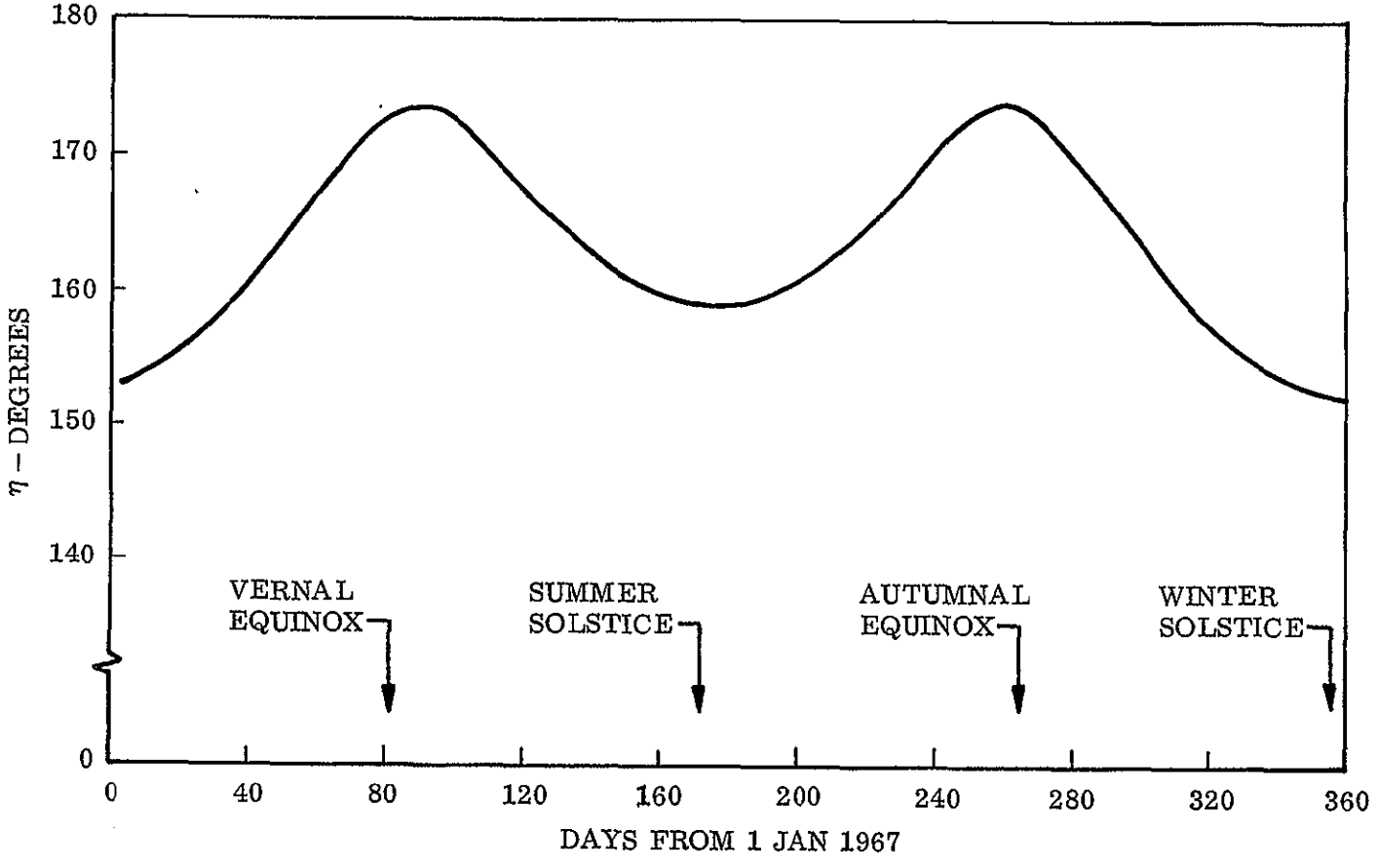

Fig. B-6 Seasonal Variation of η at Noon, White Sands, N.M., for 1967

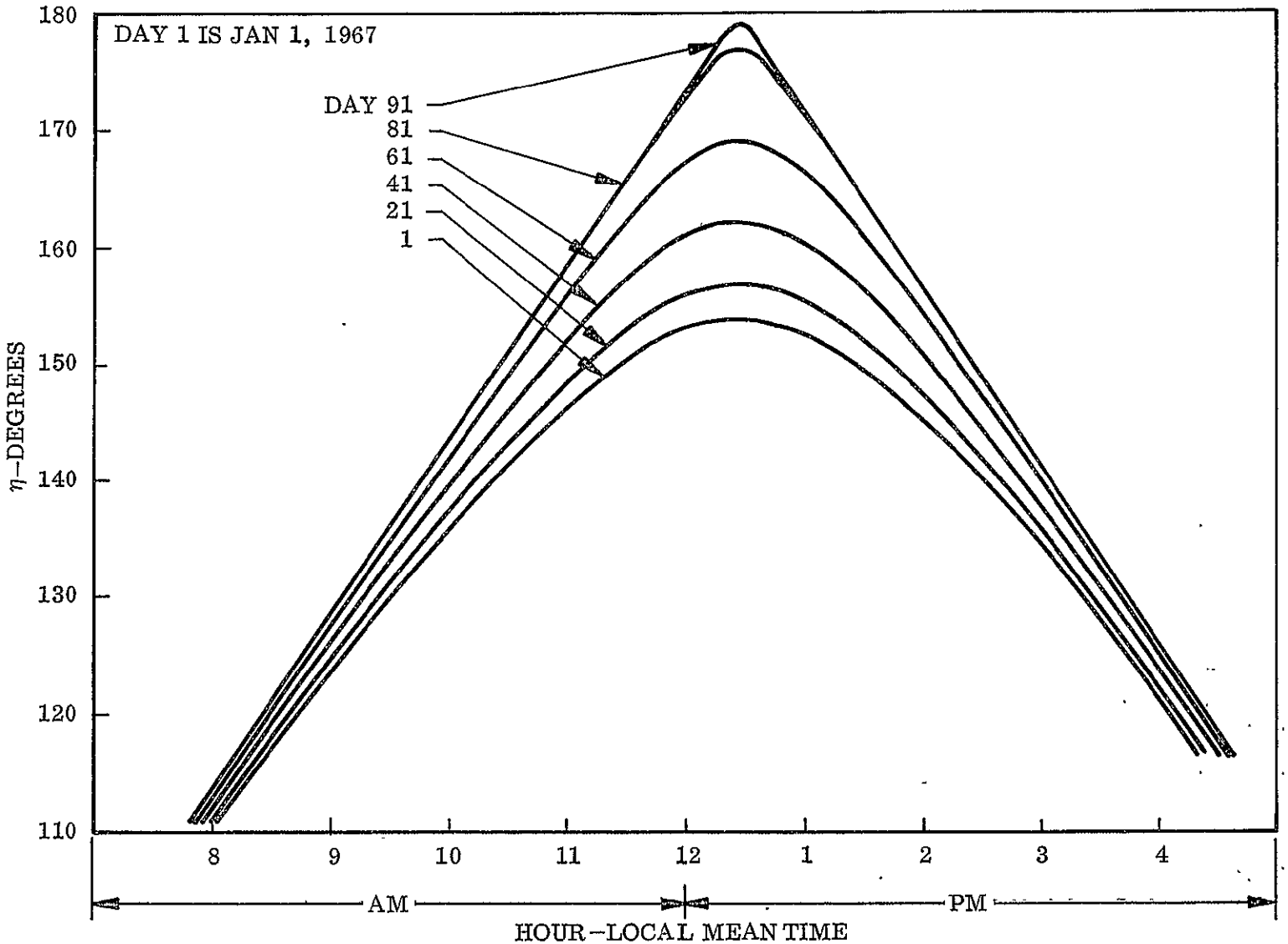

Fig. B-7 Daily Variation of η Limits at White Sands, N.M., for 1967

Figure B-8 shows the locus of constant η angles for time of day versus day of the year in 1969. Also shown is the sun line locus for the sun on the horizon and 18 deg above the horizon. The cross-hatched area of the graph indicates the time during which 30 deg $< \eta \leq$ 150 deg and the sun line inclination is greater than 18 deg. The η = 160 deg and 170 deg curves are also noted.

B.2.4 Conclusions

This analysis has shown that acceptable launch window times exist at White Sands every day of the year. Since the sun line vector's time history is approximately the same each year (1/2-day carryover to leap year and precession and nutation of the Earth have been ignored) and the predictable secular change in the magnetic field varies slowly, the data presented in this section should be valid for many years in determing approximate SPARCS launch window requirements at White Sands.

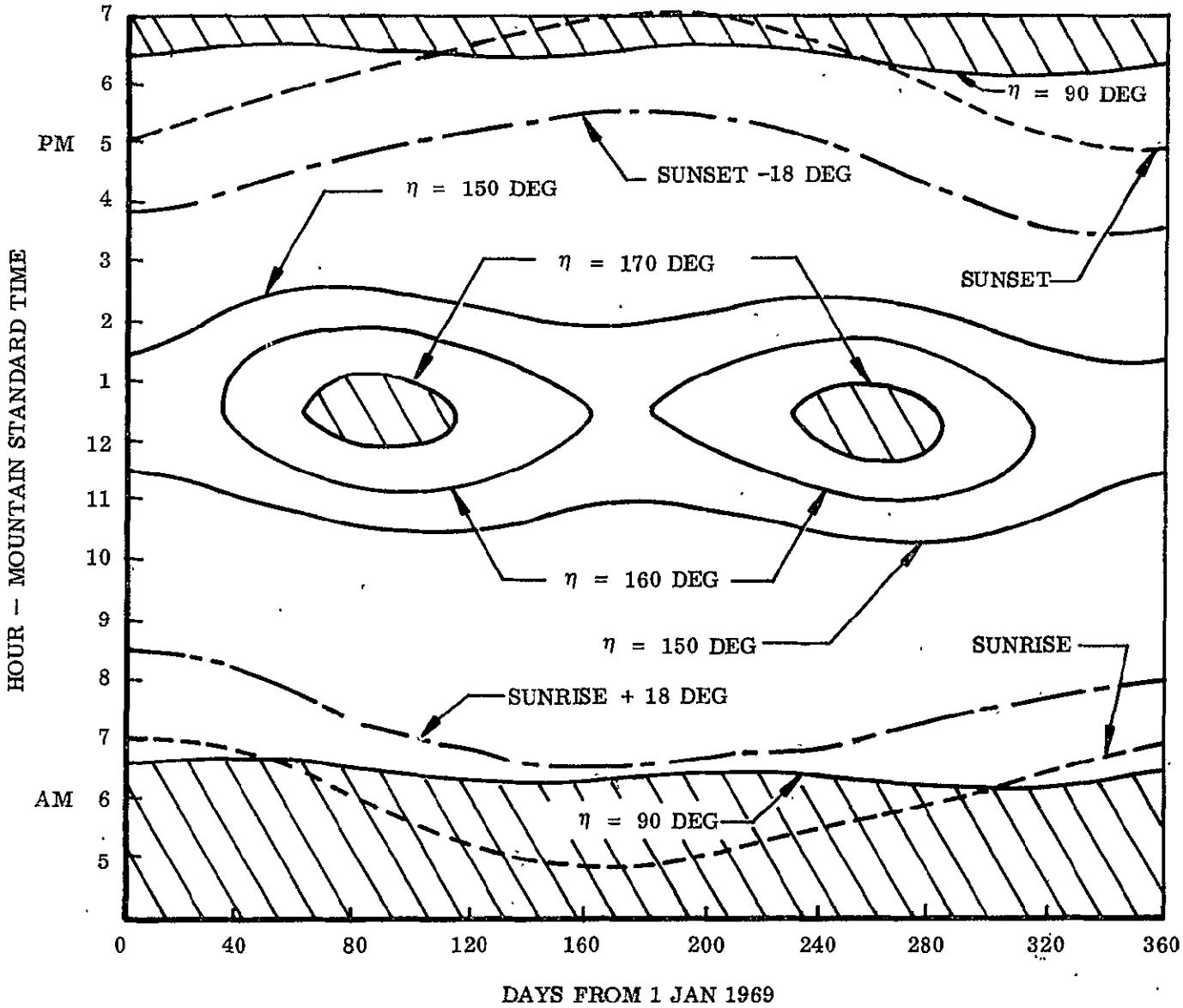

Fig. B-8 Summary of η Limits at White Sands, N.M., for 1969

B.3 VEHICLE NULL ROLL REFERENCE ANGLE STUDY

A typical mission requires the SPARCS payload to be oriented with respect to the solar and magnetic field vectors. In the desired orientation, the longitudinal vehicle axis is aligned with the solar vector, $\bar{S}$, and a transverse body axis is positioned at a desired roll angle, ϕ_D, from the north ecliptic pole (N.E.P.). Since roll control is afforded by sensing the roll angle with respect to the magnetic field vector, $\bar{H}$, it is necessary to relate ϕ_D to $\bar{H}$. This is accomplished by utilizing an angle, ϕ_N, designated as the null roll reference angle, which relates $\bar{S}$, $\bar{H}$, and the N.E.P. The expressions required to determine ϕ_N as a function of launch site and time are developed in this section. Typical results from a computer determination of ϕ_N for White Sands, N.M., for the year 1967 are determined. Also determined are the corrections to ϕ_N required due to the change in $\bar{H}$ with range and altitude during the mission.

B.3.1 Method of Analysis

The important geometrical quantities and relationships are illustrated in Fig. B-9. The null roll reference angle ϕ_N is the angle from the N.E.P. to the η plane* measured in a plane perpendicular to the sun line vector with the positive sense of the rotation defined as a clockwise rotation from the N.E.P. when looking toward the sun. The η angle was defined in Section B.2 as

$$\eta = \cos^{-1} (\bar{S} \cdot \bar{H})$$

$$0 \text{ deg} \leq \eta \leq 180 \text{ deg} \qquad \text{(B3-1)}$$

where

$\bar{S}$ is the unit vector in the local direction of the sun

$\bar{H}$ is the unit vector in the local direction of the Earth's magnetic field

*The η plane is the plane formed by the sun line and magnetic field vectors (see Section B.2).

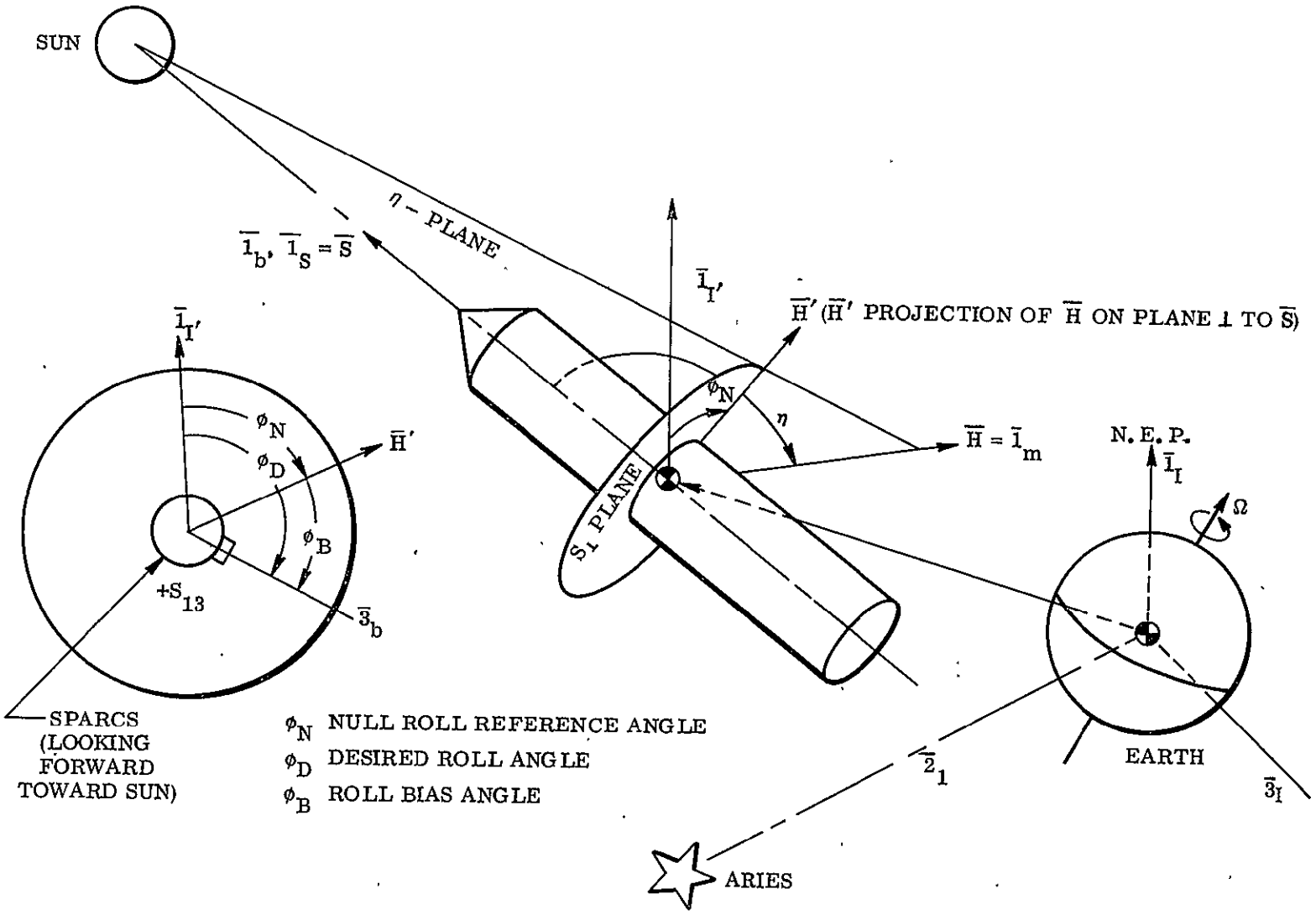

Fig. B-9 Illustration of Null Roll Reference Angle ϕ_N

A plane, S_1, is defined which is perpendicular to $\bar{I}_S$ and which contains the vector $\bar{S} \times \bar{H}$, the vector $\bar{I}_{I'}$, which is the projection of $\bar{I}_I$ onto S_1, and the angle ϕ_N. ϕ_N may now be defined as

$$\phi_N = \cos^{-1}\left[\frac{\bar{S} \times \bar{H}}{\sin \eta}\right] \cdot \bar{I}_{I'}\Bigg] - 90 \text{ deg} \qquad \text{(B3-2)}$$

The sign ambiguity in Eq. (B3-2) is resolved by the following table:

Sign $(\bar{H} \cdot \bar{I}_{I'})$	Sign $(\bar{S} \times \bar{H} \cdot \bar{I}_{I'})$	ϕ_N
+	-	0 deg $< \phi_N <$ 90 deg
-	-	90 deg $< \phi_N <$ 180 deg
-	+	180 deg $< \phi_N <$ 270 deg
+	+	270 deg $< \phi_N <$ 360 deg

In order to evaluate Eq. (B3-2) for ϕ_N it is necessary to express the components of the various unit vectors in a common reference frame. The frame chosen is the inertial frame shown attached to the Earth in Fig. B-9.

The local direction of the magnetic field is given in terms of dip and declination angles (θ_M and ψ_M respectively). The components of a unitary Earth field specified relative to the north, east, down reference frame is given by the following transformation:

$$\begin{aligned} H_N &= \cos \theta_M \cos \psi_M \\ H_E &= \cos \theta_M \sin \psi_M \\ H_O &= - \sin \theta_M \end{aligned} \qquad \text{(B3-3)}$$

A rotation about the $+\bar{2}_E$ vector through an angle equal to the latitude of the point of interest (λ_E) yields the components in terms of the Earth (E) axis system shown in Fig. B-10. Finally, the components of $\bar{H}$ are obtained in the desired inertial frame by

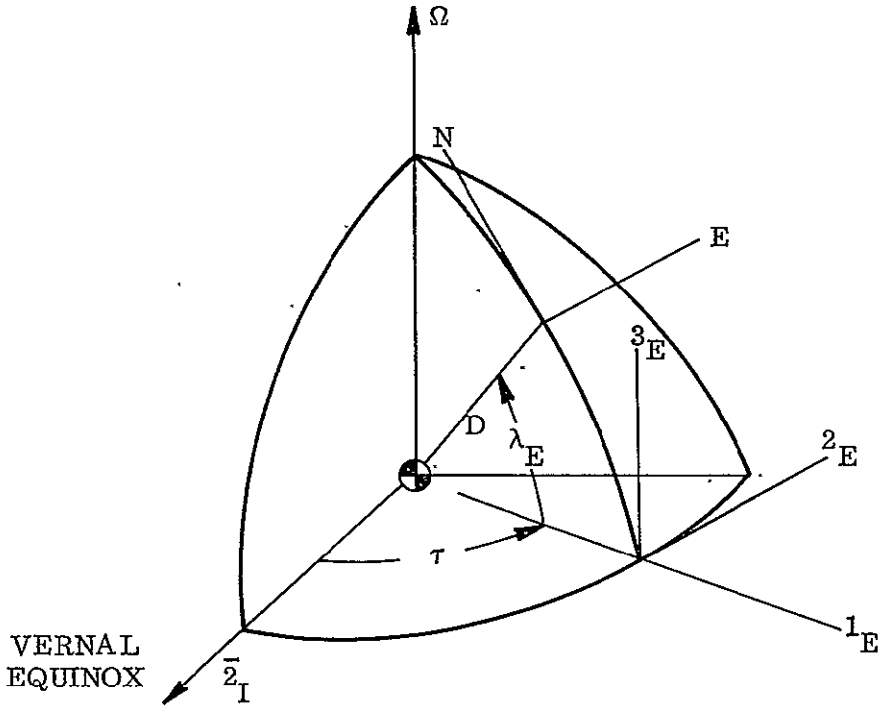

Fig. B-10 North, East Down Reference Frame Shown Relative to Earth Reference Frame

rotating the E frame about the $-\bar{3}_E$ vector through an angle equal to the right ascension (τ) of the point of interest followed by a rotation about the displaced $+\bar{1}_E$ vector through an angle equal to the inclination of the Earth's north pole with the N.E.P. (see Fig. B-11). Thus the components of the unitary Earth magnetic field $\bar{H}$ in the desired inertial frame shown in Fig. B-11 are given by the following expression:

$$\begin{bmatrix} H_{1_I} \\ H_{2_I} \\ H_{3_I} \end{bmatrix} = \begin{bmatrix} \cos\epsilon & 0 & -\sin\epsilon \\ 0 & 1 & 0 \\ \sin\epsilon & 0 & \cos\epsilon \end{bmatrix} \begin{bmatrix} 1 & 0 & 0 \\ 0 & \cos\tau & -\sin\tau \\ 0 & \sin\tau & \cos\tau \end{bmatrix} \begin{bmatrix} \cos\lambda_E & 0 & -\sin\lambda_E \\ -\sin\lambda_E & 0 & -\cos\lambda_E \\ 0 & 1 & 0 \end{bmatrix} \begin{bmatrix} H_N \\ H_E \\ H_D \end{bmatrix} \quad \text{(B3-4)}$$

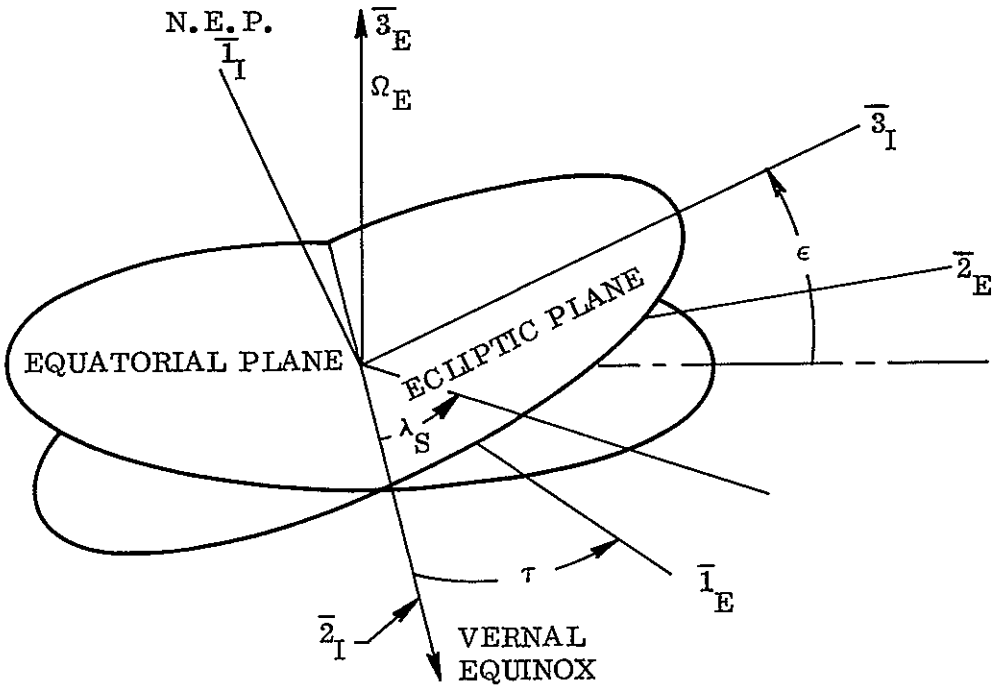

Fig. B-11 Inertial Reference Frame Shown Relative to Earth Reference Frame

The angle τ, which varies as a function of time due to the rotation of the Earth, was determined from the following formula:

$$\tau = \tau_o + \Omega \ (24d + H_{LT} + H_B) \qquad \text{(B3-5)}$$

where

τ_o	value of τ at zero hours Greenwich Mean Time (GMT) on 31 December 1966 (deg)
Ω	Earth's rotation rate (rad/hr)
d	days from 31 December 1966
H_{LT}	hour of the day (local time)
H_B	number of hours local time is behind Greenwich time

The initial value of τ was determined from the following formula:

$$\tau_o = \lambda'_{ms_o} - 180 \text{ deg} + \tau_E \qquad \text{(B3-6)}$$

where

λ'_{ms_o}	right ascention of the mean sun at zero hours GMT on 31 December 1966
τ_E	longitude of the point of interest

The relationship between the quantities given in Eq. (B3-6) is shown in Fig. B-12. This equation makes use of the fact that the right ascension of Greenwich is exactly 180 deg less than that of the mean sun at zero hours GMT.

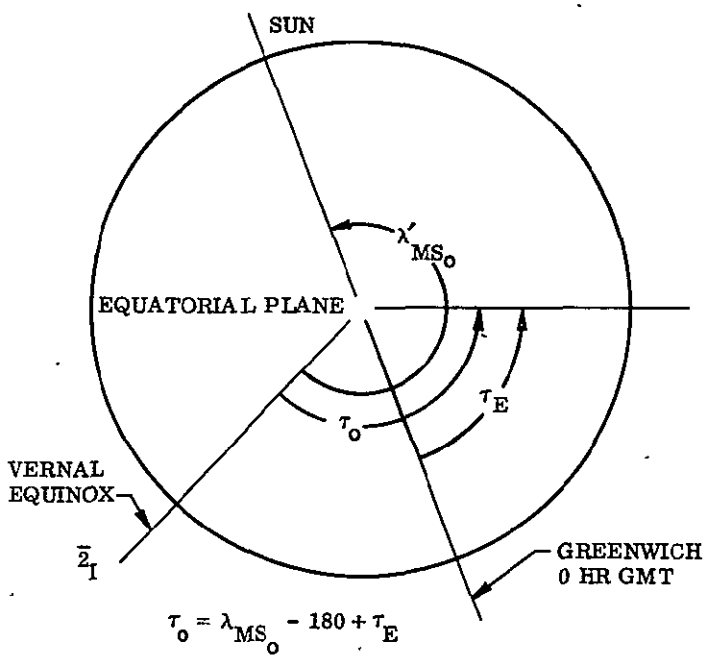

Fig. B-12 Relationship Between Right Ascension of the Mean Sun λ_{ms} and τ_o

The components of a unit sun vector $\bar{1}_s$ in the inertial frame are given by

$$\begin{pmatrix} S_{1_I} \\ S_{2_I} \\ S_{3_I} \end{pmatrix} = \begin{pmatrix} 0 \\ \cos \lambda_s \\ \sin \lambda_s \end{pmatrix}$$

where λ_s is the celestial longitude (measured in the plane of the ecliptic from the vernal equinox) of the true sun (see Fig. B-11). The following expression for λ_s is accurate to within ± 0.05 deg of the ephemeris value for 1967.

$$\lambda_s = -1.4145 + 0.017203d + 0.03345 \sin [0.017203 (d-3)] \qquad \text{(B3-8)}$$

A computer algorithm was constructed which solves Eq. (B3-2) for ϕ_N using Eqs. (B3-1), (B3-4), and (B3-7). The results for White Sands for the hours between 7 a.m. and 6 p.m. for the entire year 1967 are shown in Fig. B-13. The following location and direction of $\bar{H}$ was assumed for White Sands:

τ_E = 106.3° W longitude

λ_E = 32.226° N geocentric latitude

ψ_M = 12.355° magnetic declination

θ_M = -60.350° magnetic dip

B.3.2 Range and Altitude Corrections To ϕ_N

The null roll reference angle ϕ_N changes with range and altitude during the mission. This change in ϕ_N with time from launch is due to the change in orientation of the η plane which is caused by a change in the direction of $\bar{H}$. The variation in magnetic dip and declination angles with time from launch for nominal SPARCS trajectories is shown in Fig. B-14. Since the field is only known to an accuracy of 0.2 deg, these curves were judged to be adequately approximated by the straight lines shown. Thus the direction of $\bar{H}$ was assumed to change linearly and continuously with time.

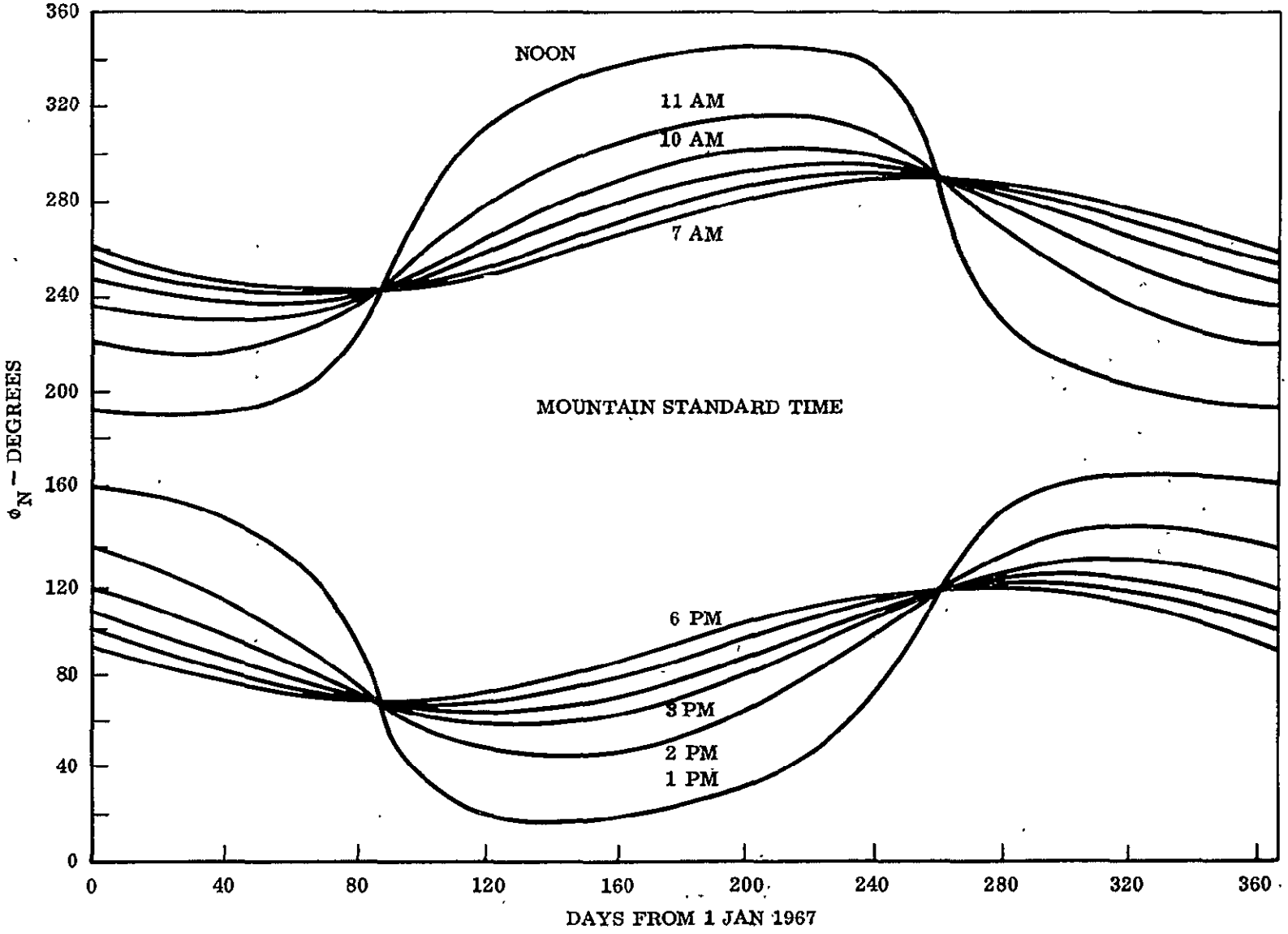

Fig. B-13 Variation in Null Roll Reference Angle, ϕ_N, at White Sands, N.M., for 1967

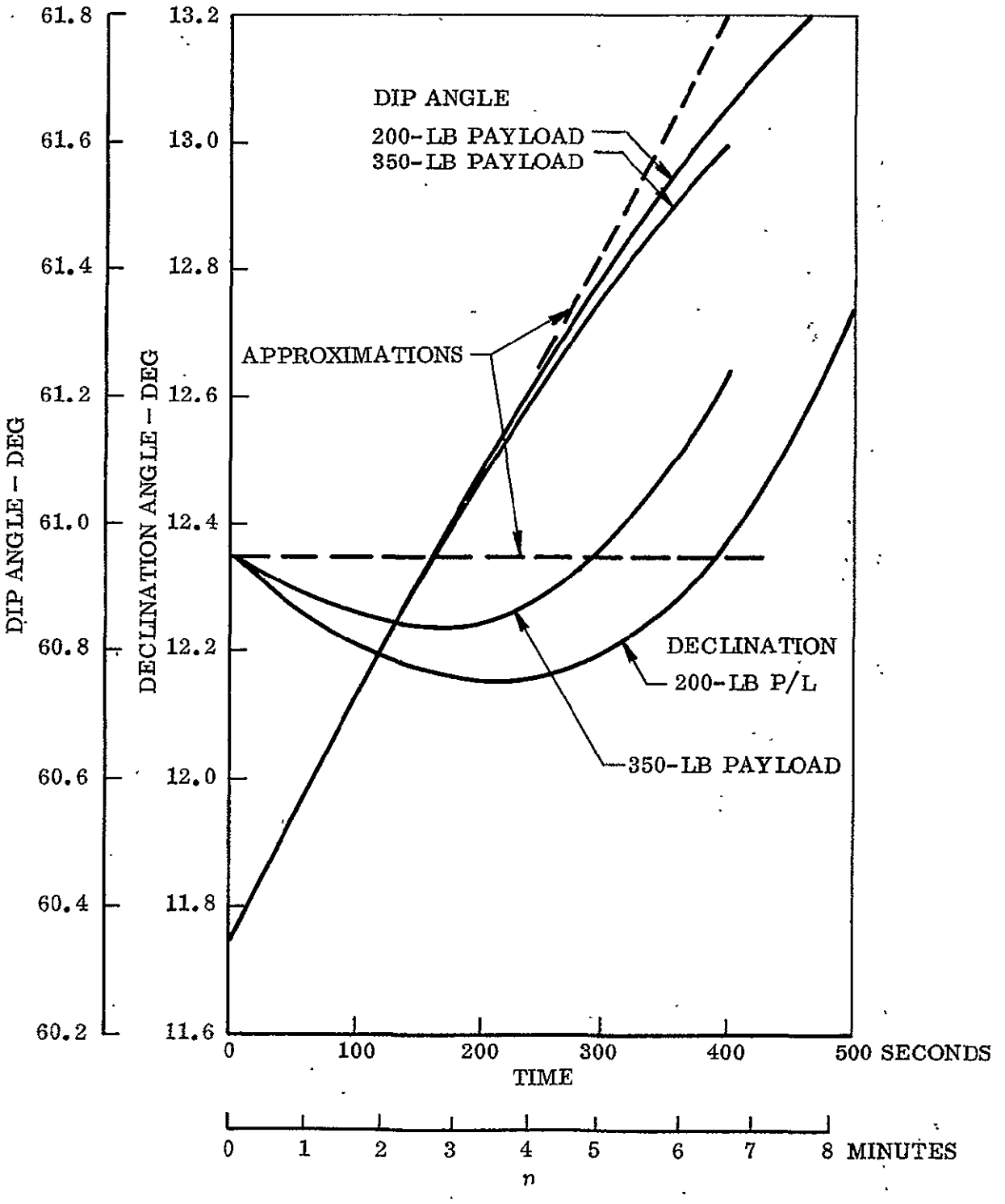

Fig. B-14 Variation in Magnetic Field Direction Components Versus Time for SPARCS Launched North From White Sands

If the direction of $\overline{H}$ changes linearly with time, the orientation of the η plane will change linearly and continuously with time. The rate at which the η plane changes orientation for given flight trajectories is a function of the initial orientation of the plane, and consequently the day and time of day of the launch. Figure B-15 shows typical curves for $\Delta \phi_N / \Delta t$ for the nominal SPARCS trajectories (200 to 350-lb payload launched north from White Sands).

The desired roll angle ϕ_D with respect to the N.E.P. (shown in Fig. B-9) is given by

$$\phi_D = \phi_N(t) + \phi_B(t) \tag{B3-9}$$

Therefore, in order to keep the value of ϕ_D constant, $\dot{\phi}_B$ must be equal and of opposite sign to $\dot{\phi}_N$. Then, using the $\Delta \phi_N / \Delta t$ curve at the assigned launch time, the required change in the roll bias angle during the flight is given by the following equation:

$$\frac{\Delta \phi_B}{\Delta t} = - \frac{\Delta \phi_N}{\Delta t} \tag{B3-10}$$

B.3.3 Conclusions

The null roll reference angle ϕ_N was found to be a function of launch site and launch time. In addition, ϕ_N was found to vary approximately linearly with time from launch for nominal trajectories from White Sands, New Mexico, and the rate of change was found to be dependent on the time of the launch.

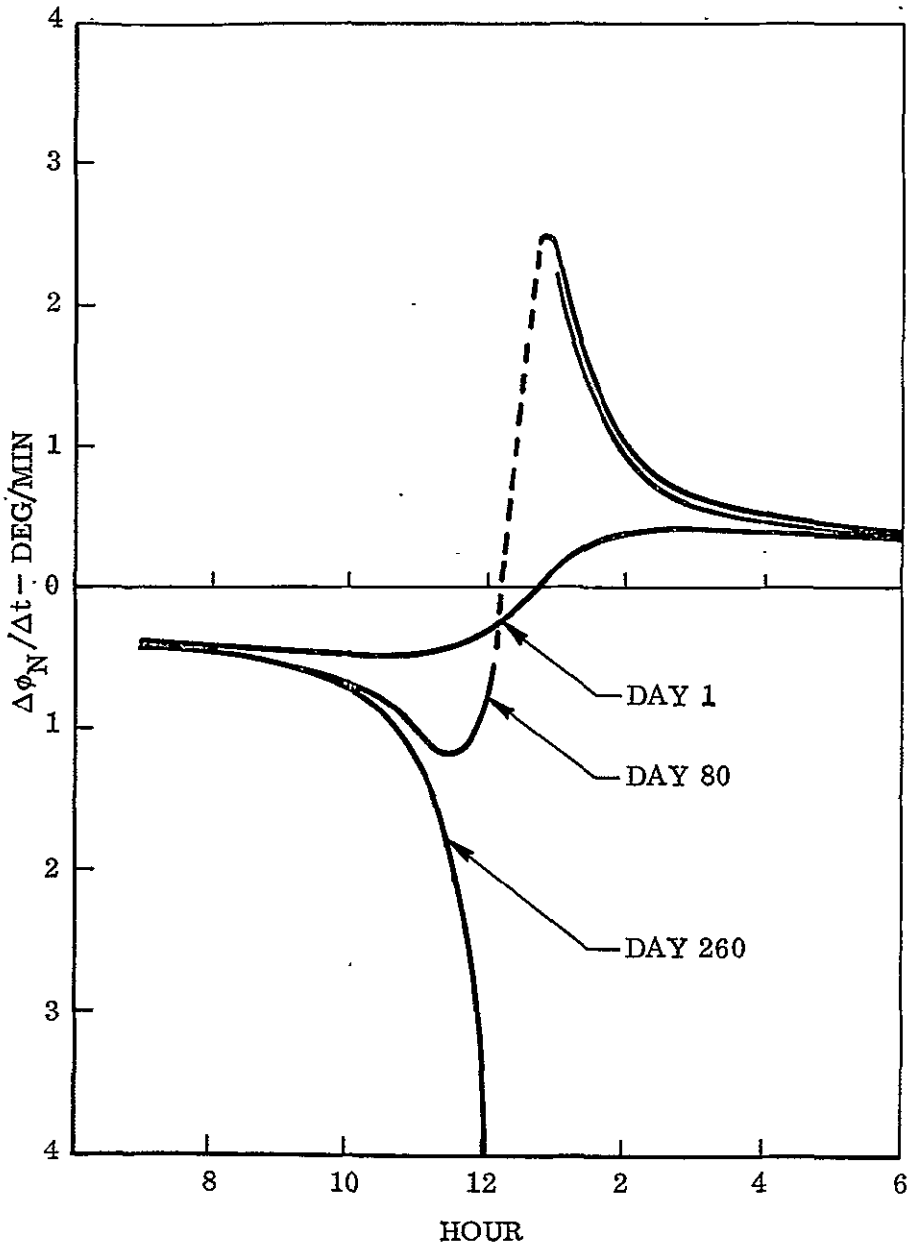

Fig. B-15 Typical Curves for $\Delta\phi_N/\Delta t$

B.4 ALBEDO COMPENSATION STUDY

Since the Earth reflects solar radiation, the Coarse Sun Sensors (CSS), which are used for coarse acquistion of the sun from any initial attitude, receive light energy from both the sun and the Earth. A study has shown that for the extreme value (0.6) of the Earth's albedo near White Sands, New Mexico, the coarse mode pointing error can be as much as 25 deg. The fine pointing mode is not affected by the Earth light (albedo) because the narrow field-of-view of the Fine Sun Sensor (FSS) excludes albedo radiation; however, initiation of the fine mode requires the coarse acquisition mode to bring the sun to within the circular field-of-view of the FSS (half-cone angle 15 deg max). Since the albedo-caused coarse mode pointing error can be larger than the FSS field-of-view, some means of improving the performance of the coarse mode was required. This section investigates the magnitude of the albedo, discusses several methods for reducing coarse mode steady-state pointing error, and evaluates the method selected for SPARCS.

B.4.1 Effect of Earth Shine on Vehicle Pointing Error

The effect of the albedo on the final vehicle direction will depend upon the magnitude of the Earth's reflected radiation and the geometry of the situation. The SPARCS CSS units are used in pairs mounted on opposite sides of the vehicle, the output being differenced to obtain a signal for the control system. The final pointing direction from such a pair of uncompensated cells is established when the output due to the sun on one cell of the pair exactly cancels the output due to the Earth shine on the other cell. The pointing error (E) is defined as the angle between the vehicle longitudinal axis and the direction to the sun. Figure B-16 shows the geometry for such a situation.

The voltage difference for the indicated pair of cells due to solar radiation is equal to $K_S \cos\alpha$, where K_S is a proportionality constant. The voltage difference due to the Earth's radiation is proportional to $(K_{Sr} K_S \cos\lambda \cos\psi_S)$, where K_{Sr} is the

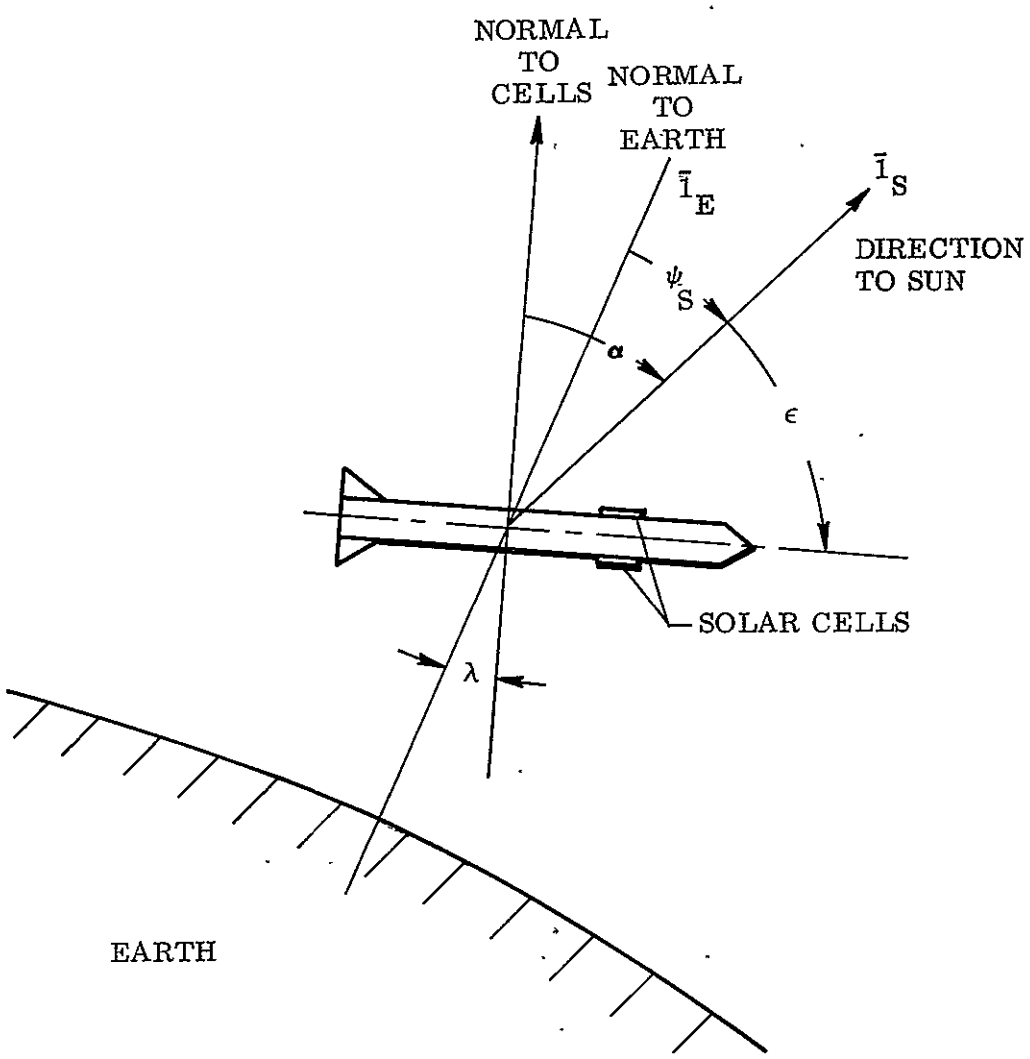

Fig. B-16 Pointing Error Geometry

albedo or the solar reflectivity for the portion of the Earth in question. * From the geometry indicated in Fig. B-16, the solar radiation output of the CSS primary cells can be written (since $\alpha + \epsilon = 90$ deg):

$$(E_{pr})_{sun} = K_s \sin \epsilon \quad .$$

The Earth shine output of the CSS primary cells can be shown to be:

$$(E_{pr})_{earth} = -K_s \alpha \sin (\epsilon + \psi_s) \cos \psi_s$$

A steady-state condition exists when the sum of these outputs equal zero. From which

$$\epsilon = \tan^{-1} \left[\frac{\alpha}{2} \quad \frac{\sin 2 \psi_s}{(1 - K_{sr} \cos^2 \psi_s)} \right]$$

This result is shown in Fig. B-17 for several values of K_{sr}.

B.4.2 Affect of Albedo on the Fine Sun Sensor

The SPARCS mission is to point the payload at the center of the solar disc with an accuracy on the order of several seconds of arc. The FSS has the required accuracy about null and a field-of-view which is limited to ± 15 deg. Consequently, when the sun is higher than 15 deg above the horizon, Earth shine will not significantly affect the FSS during the final acquisition phase. A flight restriction on the Aerobee for these missions is that the sun must be at least 18 deg above the horizon.

B.4.3 Earth Shine Compensation Methods

Several methods of compensating Earth shine effects on the CSS cells have been studied, as outlined in the following paragraphs.

*The conservative assumption is made that the cell has the same response to reflected radiation as it does to direct radiation.

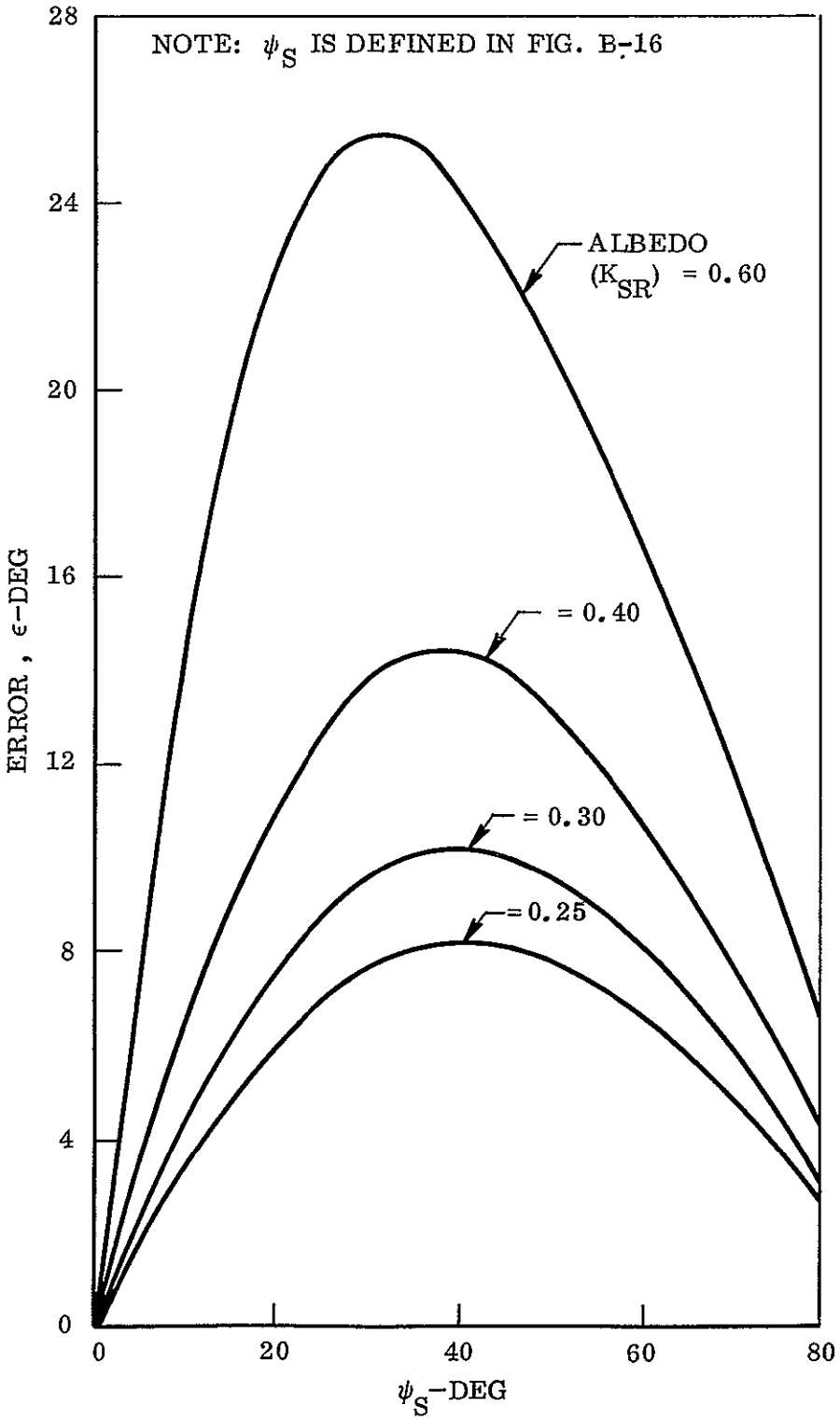

Fig. B-17 Coarse Sun Sensor Error Angle (Uncompensated)

One method considered is based on the selective reflectance and absorption of sunlight by the atmosphere and the Earth. The spectral response of the CSS cell is shown in Fig. B-18. It is seen to cover a broad spectrum, with response shifted toward the infrared. The distribution of flux emitted by the sun and the distribution of flux reaching the Earth is shown in Fig. B-19. Since there are several narrow regions of high atmospheric absorption that are within the CSS spectral response, it appears that the CSS cells could be made insensitive to Earth shine if a proper filter could be devised. However, such a filter could be a considerable undertaking because the wavelength bands of absorption are very narrow. Consequently, this method was rejected.

A second method considered was to take advantage of the polarization of light due to the atmosphere. Figure B-20 shows the degree of polarization for two solar zenith angles. While the figure shows that the atmosphere does have considerable effect on sunlight polarization, it is also shown to be highly dependent upon the solar zenith angle and the angle of observation, which would make the polarization effect very difficult to apply.

The method proposed for SPARCS is to mount a secondary cell next to each CSS primary cell and to difference the output. The secondary cell is shaded so that it will not receive the direct sunlight when the vehicle's controlled axis is within a predetermined angle of the sun. In this vehicle attitude, the primary cell will receive flux from both the Earth and the sun, and the secondary cell will receive flux from the Earth only. The difference will be the desired quantity, namely, a signal proportional to the flux from the sun. Although any shading of the secondary cell from the sun will also cause some shading from the Earth shine, this can be minimized by careful design. When the vehicle is at a large angle with respect to the sun, both the primary and secondary cells will have the same incident solar flux, and the differenced signal will be zero. For this reason, the maximum output of the secondary cell is limited to a lesser value than the primary cell output, ensuring a signal directing the controlled axis toward the sun.

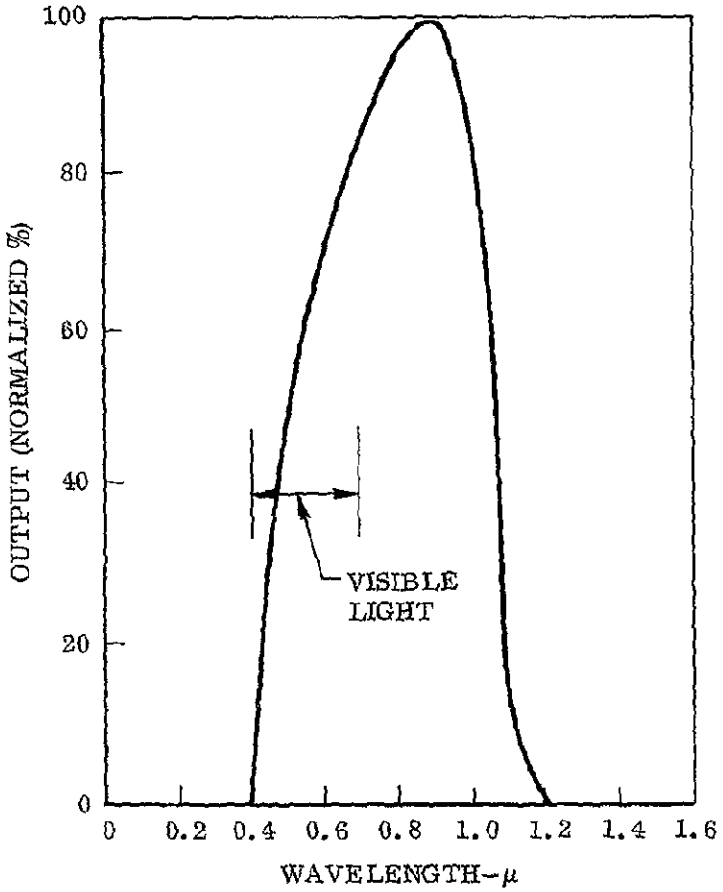

Fig. B-18 CSS Solar Cell Response

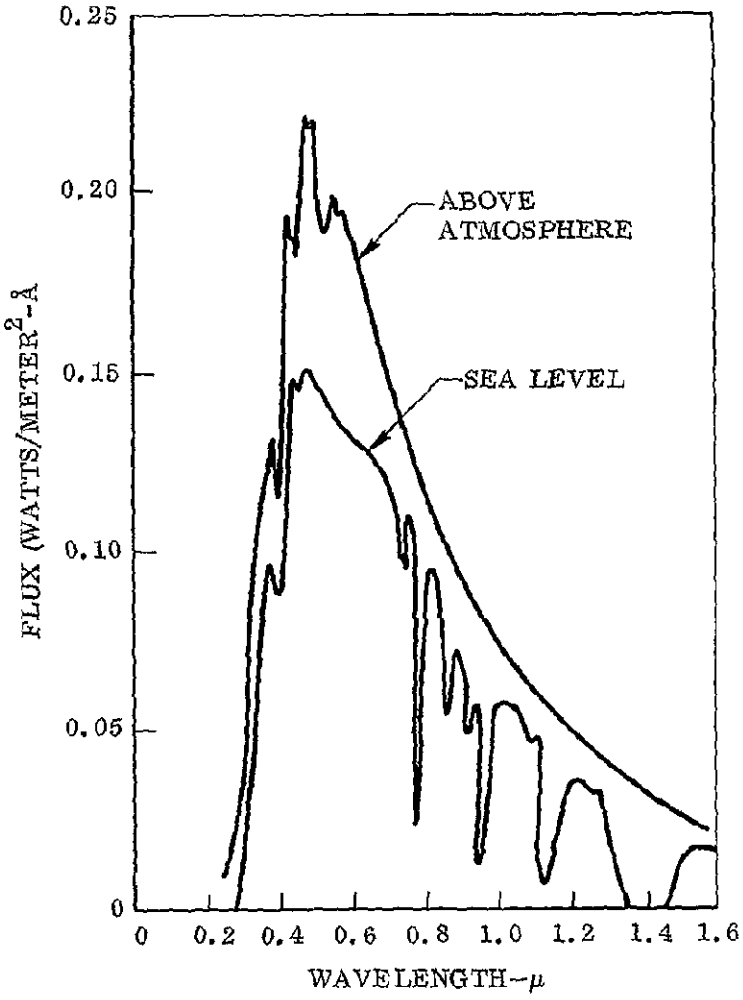

Fig. B-19 Solar Spectral Distribution

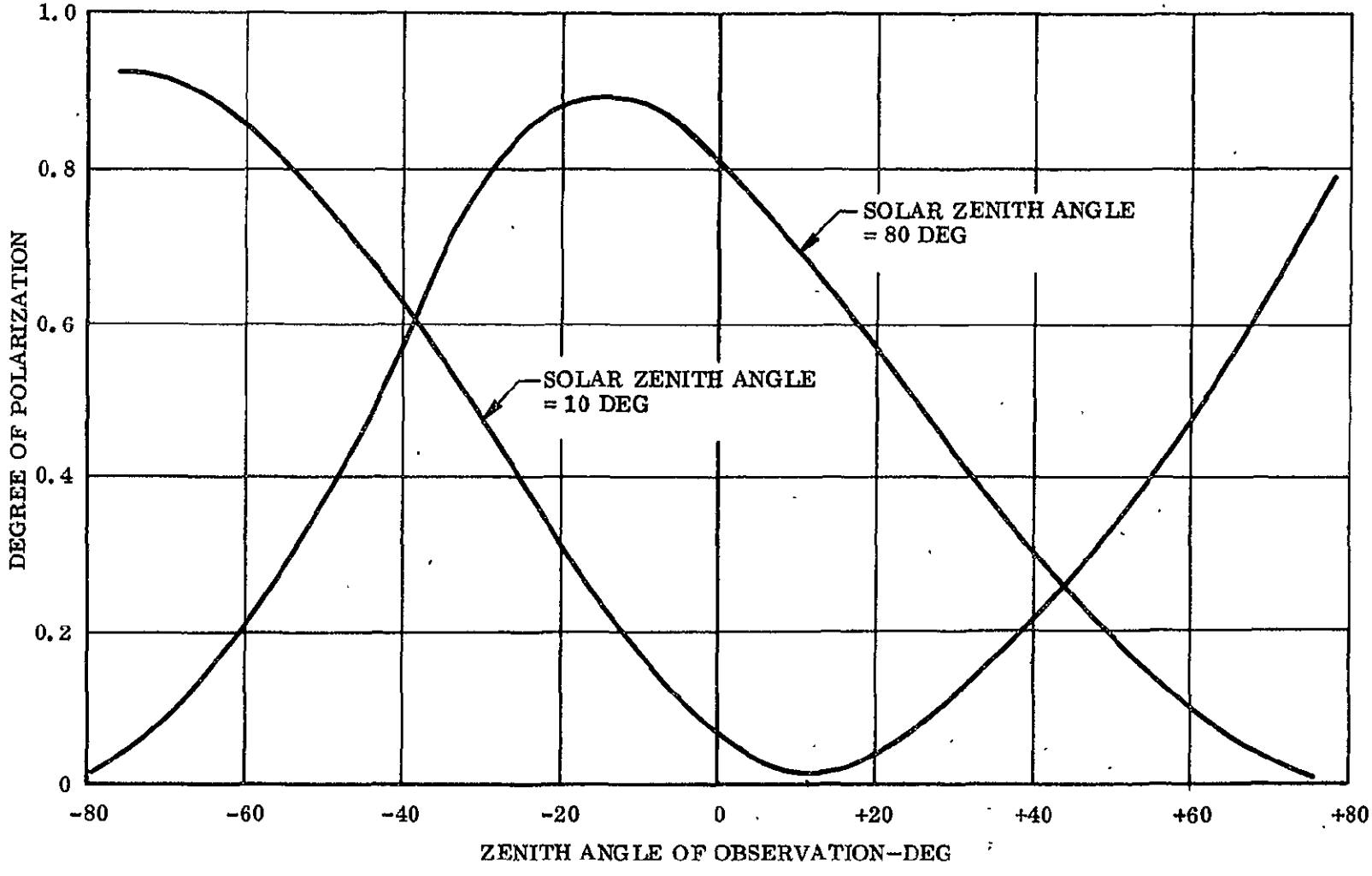

Fig. B-20 Distribution and Degree of Atmospheric Polarization

B.4.4 Experimental Verification of the Secondary Cell Method

A crude but conservative experiment was conducted to verify the CSS secondary cell concept. The experiment was performed with the same type of solar cell that will be used on SPARCS. The output as a function of angle of incidence was obtained for both a flush (unshaded) and a recessed (shaded) cell in simulated sunlight and earthlight. A "sun gun" of the type used for indoor motion picture photography was used in a specially constructed light box. A circular translucent screen was placed between the sun gun and the cell to give a diffuse light source and simulate the Earth's reflected light. The distance between the cell and the screen was adjusted so that the angle subtended by the periphery of the screen would be equal to the angle subtended by the horizon at a 100-nautical-mile altitude.

Figure B-21 shows the response to earthlight of the flush and recessed cells, respectively. The difference between the curves is the percent of full-scale output due to albedo, and is shown in Fig. B-22. The maximum error is seen to be about 30 percent of the full-scale output. In other words, the crudely shaded cells could eliminate 70 percent of the albedo effect and could obviously be made more efficient by a more refined design.

The secondary cell outputs were attenuated by a gain of 0.8 to ensure positive control for small solar incidence angle when both the primary and secondary cells could "see" the sun. The net effect was an increase in albedo error to 34 percent of the uncompensated value. Therefore, an assumed maximum albedo of 0.8 would effectively be reduced to 0.272. Figure B-17 shows that this effective albedo would allow coarse acquisition to within a half-cone angle of 9 deg (i.e., to within the field-of-view of the FSS).

B.4.5 Air Bearing Vehicle Tests

For the Air Bearing Vehicle (ABV) earth shine tests, a large screen was diffusely illuminated with sunlight focused by Fresnel lenses. By this method, the simulated

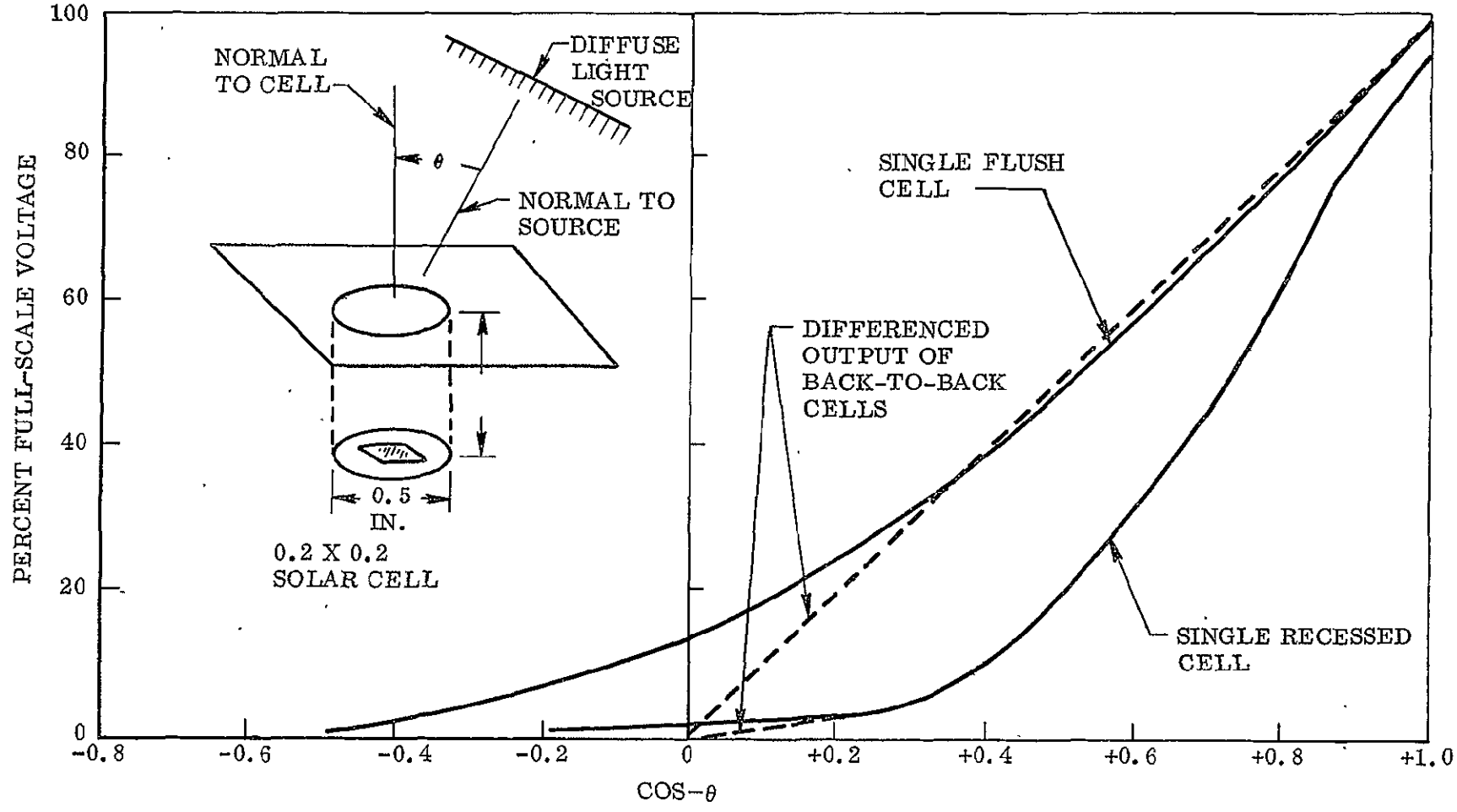

Fig. B-21 Response of Flush and Recessed Solar Cells in Simulated Earthlight

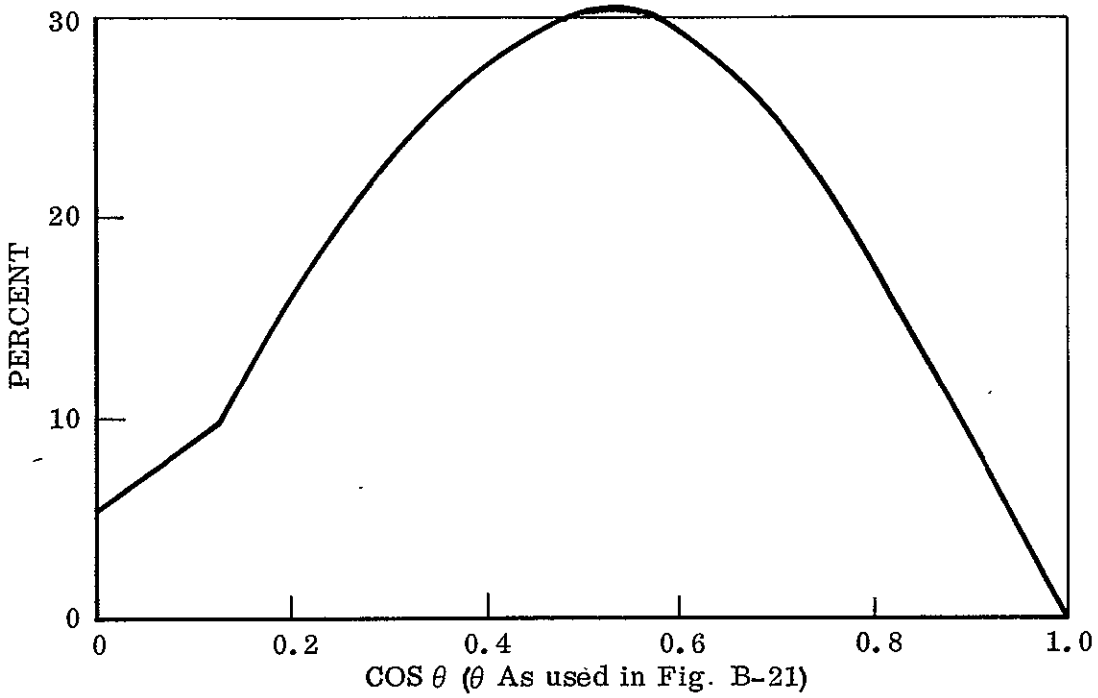

Fig. B-22 Percent Full-Scale Voltage Error Due to Albedo (After Compensation)

albedo could be set to any value up to 100 percent of the simulated sun input. The system was able to acquire the sun in the presence of earth shine for all values of simulated albedo which did not exceed the simulated sun signal on the CSS cells.

B.4.6 Conclusions

A method of albedo compensation has been devised that does not depend upon the magnitude of the albedo, or any prior knowledge about the characteristics of the emergent radiation, but uses the fact that the sun's rays are collimated, whereas the radiation reflected from the Earth is diffuse and emanates from a large area. The system employed does not restrict the field-of-view of the primary sensors and will allow acquisition of the sun from all initial attitudes and all values of albedo. Further, the system will ensure a final pointing error of less than 9 deg.

B.5 SUSTAINER-PAYLOAD SEPARATION STUDY

The flight sequence of events of the Aerobee-SPARCS vehicle differs from that of other high-altitude research programs using the Aerobee 150 sounding rocket in that the payload and associated equipment are separated from the forward end of the rocket after sustainer engine burnout. Thus after separation only the payload is rotated to a sun-oriented attitude for the remainder of the flight. The possibility of collision between the expended sustainer rocket and the ejected payload section is a matter of some concern in this type of flight programming. This section presents the results of a separation study for typical SPARCS payload weights separated at various times and with various velocities. The study was conducted using a computer program that determined the aerodynamic forces, acting on both the payload (with SPARCS) and the sustainer after separation, and calculated the resulting trajectories of the separated bodies.

B.5.1 Discussion

The Aerobee-SPARCS vehicle separation study was performed using a point mass trajectory computer program capable of utilizing varying vehicle aerodynamic characteristics. Using the design trajectories of Ref 1 for initial conditions (shown in Fig. B-23), it was assumed that the 200- and 350-lb payloads were separated from the sustainer rocket at 65 or 80 sec after launch with separation velocities of 2.5, 5.0, 7.5 or 10.0 ft/sec. Immediately after separation, the payload was programmed with a 30-sec pitch maneuver to 90 deg relative to its inertially referenced attitude at separation. The pitch program simulated a rapid rotation of 76 deg in the first 15 sec, at which time the nose cone was separated. A fine correction of 14 deg was made during the remaining 15 sec, and the resulting estimated angle of attack history of the payload was then calculated.

Ascent trajectories were calculated from separation to apogee for both payloads and for each set of separation conditions. These were compared to sustainer ballistic trajectories at zero angle of attack to ensure conservative separation distances. Payload sustainer aerodynamic characteristics were obtained from Ref 2 and are shown in

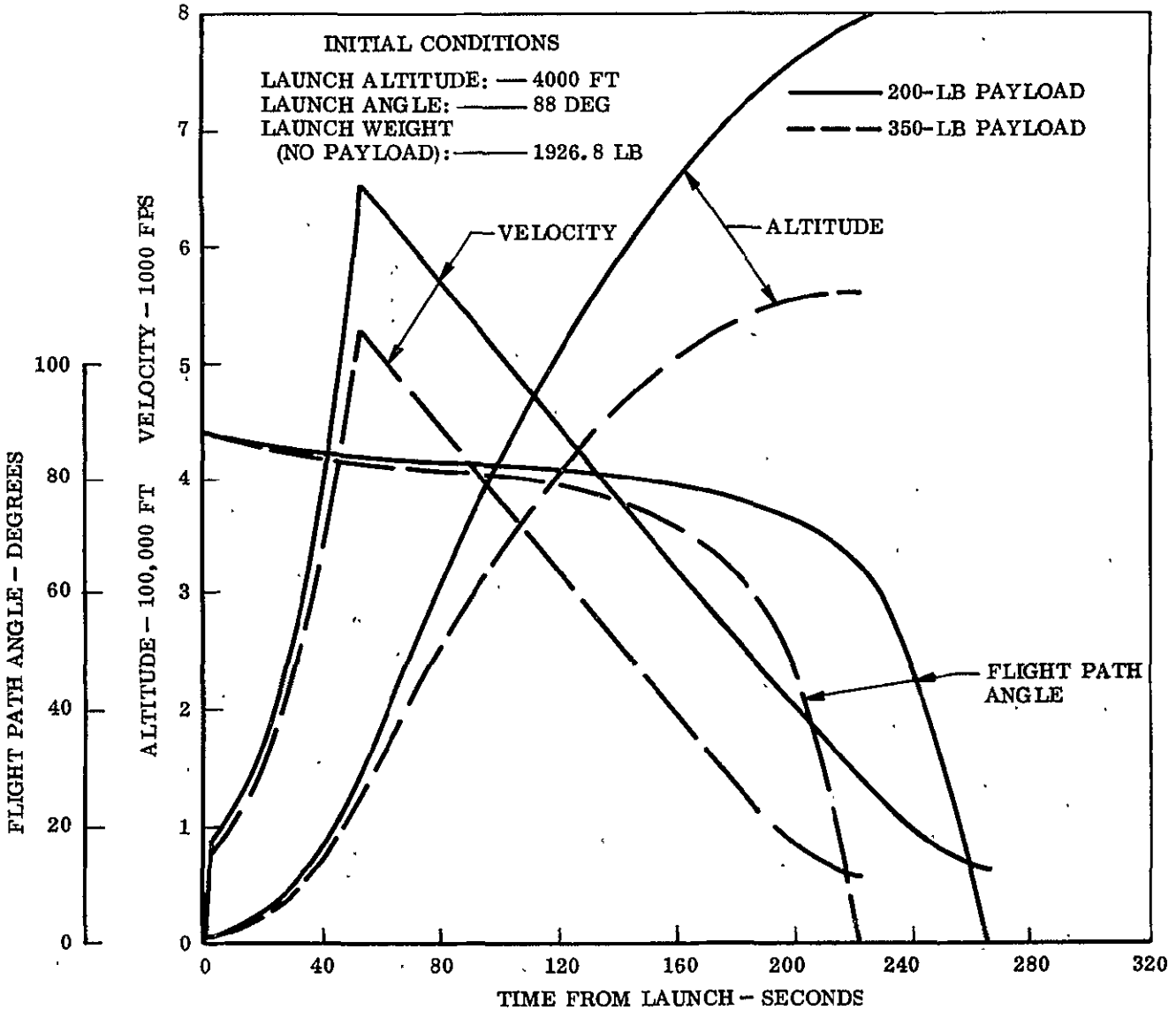

Fig. B-23 Design Trajectories for Aerobee 150 Vehicle With 200- and 350- Pound Payloads

Section B.1 of this appendix. These data consider continuum flow conditions below 300,000 ft, free molecule flow data above 400,00 ft, and estimated transition characteristics between the two flow regimes.

The results of the separation study during the first 30 sec after separation are shown in Figs. B-24 through B-27 for various payload weights, separation velocities, and separation times.. Separation distances were calculated by comparing the displacement of the vehicles from their point of separation.

Figure B-24 shows the total separation distances for the 200-lb payload separated 65 sec after launch. The near vertical ascent trajectory of the launch vehicle at the time of payload separation resulted in altitude differences and small in-track separations. Cross-track separation occured due to the Earth's rotation and the fact that two bodies are leaving the "sensible" atmosphere at different times, thereby allowing aerodynamic characteristics of the vehicles to be effective over different time periods. Since vehicle separation occurs at an altitude of 222,508 ft, or near the upper limit of the continuum flow regime, drag forces acting on the two bodies are significant for a short period of time only. The relative velocity between the payload and sustainer increases during this time and then is constant as the bodies move through transition to free molecule flow regimes.

When the separation time of the 200-lb payload is changed to 80 sec after launch, cross-track separation approaches zero because the two bodies are out of continuum flow at payload ejection and are therefore subject to negligible effects from the atmosphere. The total separation curves shown in Fig. B-25 show virtually no drag effects, as is indicated by the linearity of the curves. For all practical purposes, when the payload is separated 80 sec after launch, total separation disturbances for the first 30 sec can be approximated by

$$\Delta S = V_{sep} (t - t_o)$$

where V_{sep} = separation velocity, $(t - t_o)$ = time from separation.

Figure B-26 shows the sustainer-payload separation distances for a 350-lb payload with a separation time of 65 sec. Payload ejection for this configuration occurs at a much lower altitude (187, 181 ft), and the drag difference between the two vehicles has a significant effect on both altitude and cross-track separations. The relative velocity between the two bodies also shows the increased drag effects. As the two vehicles move apart during the first 8 to 10 sec, the higher drag sustainer begins to fall quickly behind the payload. As the payload body pitches upward, however, its drag increases; this decreases the relative velocity between the two bodies and allows the sustainer to begin catching up until both pass out of continuum flow into transitional and free molecule flow. As before, when this occurs the relative velocities become constant and the separation distance increases linearly with time for at least the first 30 sec.

Increasing separation time of the heavier payload to 80 sec after launch again has the effect of reducing the influence of the atmosphere and therefore the aerodynamic characteristics on vehicle separation. The separation distances shown in Fig. B-27 are almost linear with time, indicating very small drag effects. The relative velocity increases only by 0.1 ft/sec after 30 sec.

B.5.2 Conclusions

The results of the two-body collision study indicate that both the 200-and 350-lb SPARCS payloads can be separated from the sustainer rocket at 65 or 80 sec after launch with velocities as low as 2.5 ft/sec without danger of the two bodies colliding. Payload ejection at lower altitudes, corresponding to earlier separation times, results in more rapid separation of the payload and sustainer due to the greater drag of the sustainer. Delaying payload ejection until 80 sec eliminates the effect of vehicle aerodynamics on the two bodies, and separation distances become a function of the initial separation velocity only.

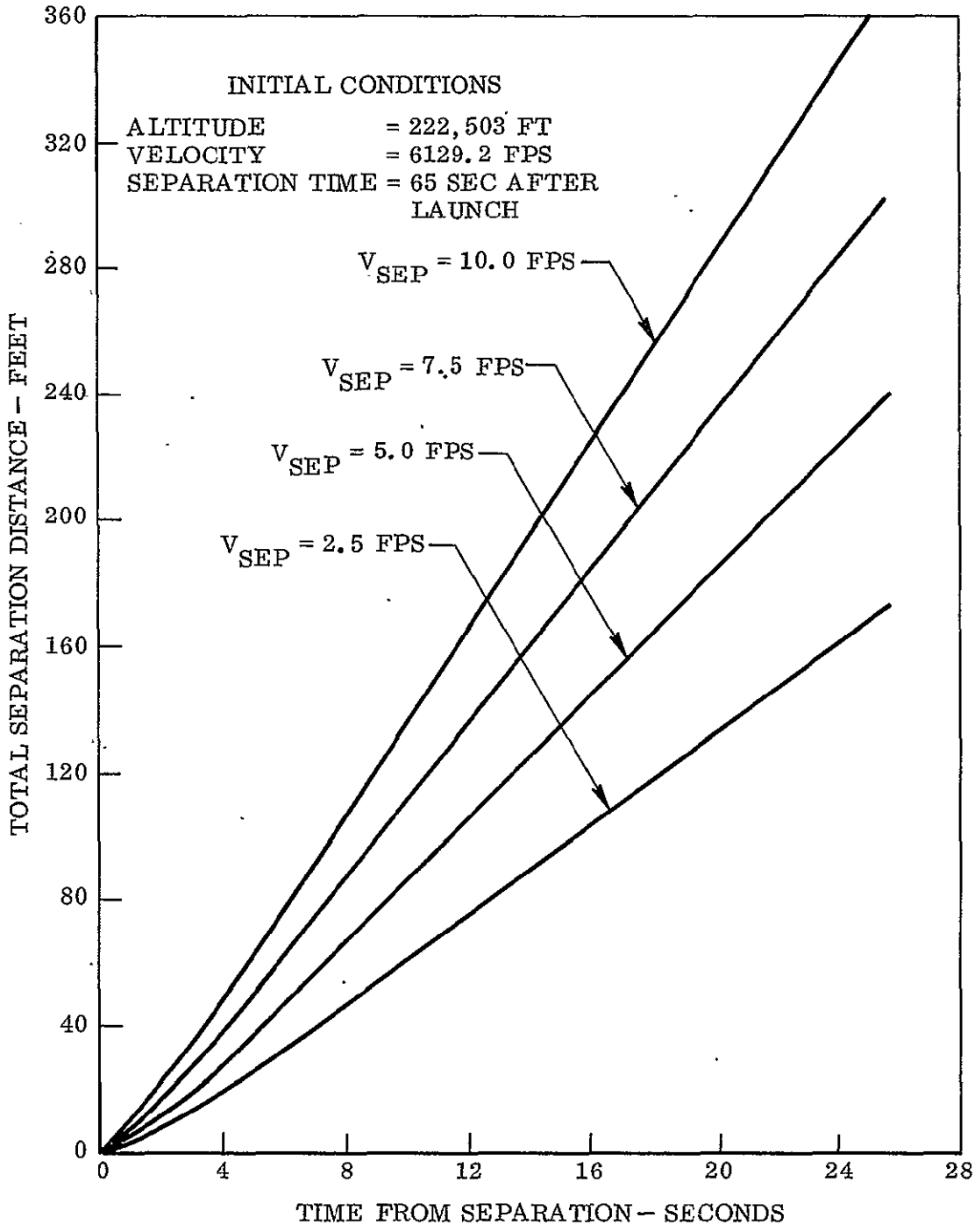

Fig B-24 Total Separation Distance Versus Separation Time – 200-lb Payload, 65 Sec After Launch

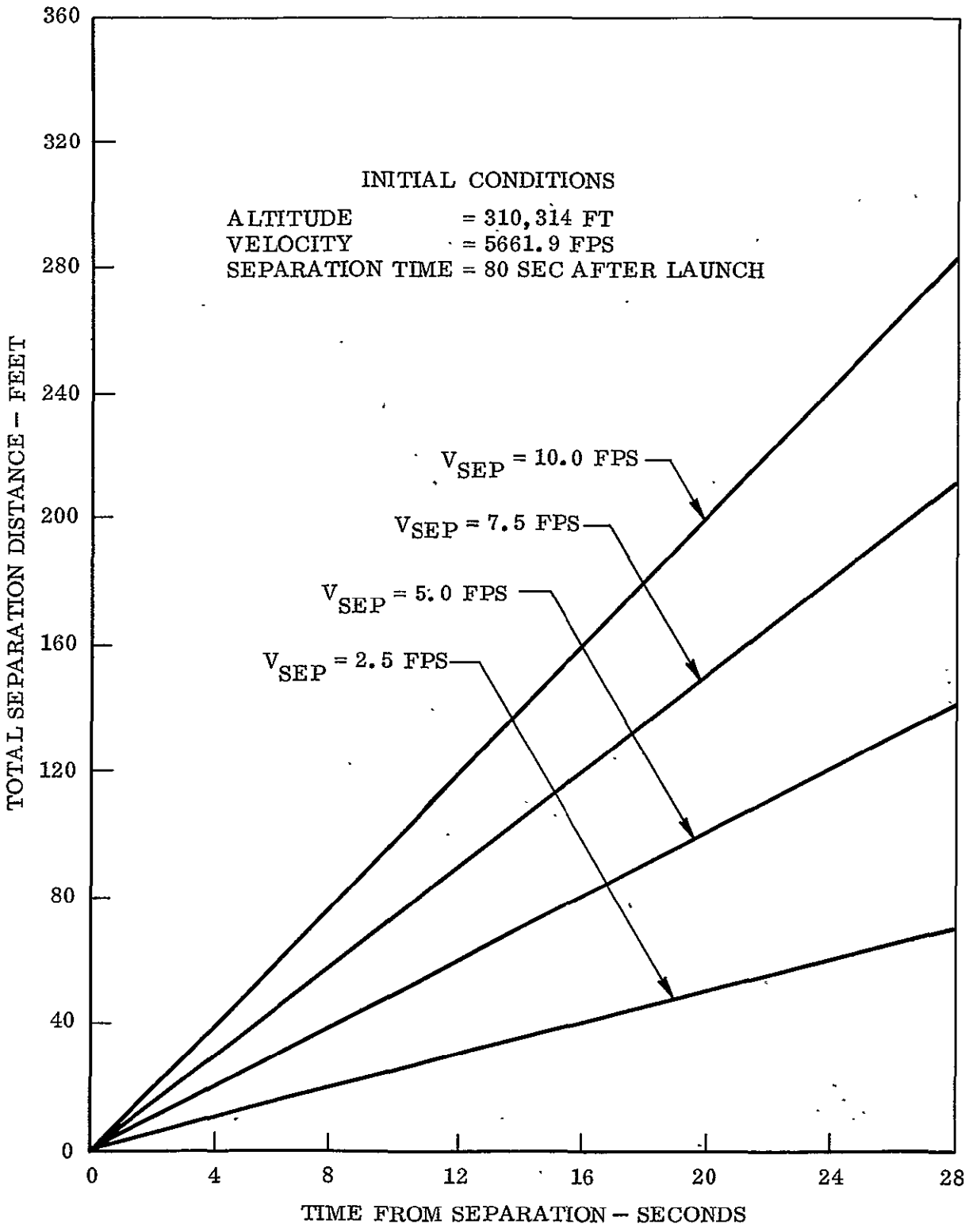

Fig B-25 Total Separation Distance Versus Separation Time – 200-lb Payload, 80 Sec After Launch

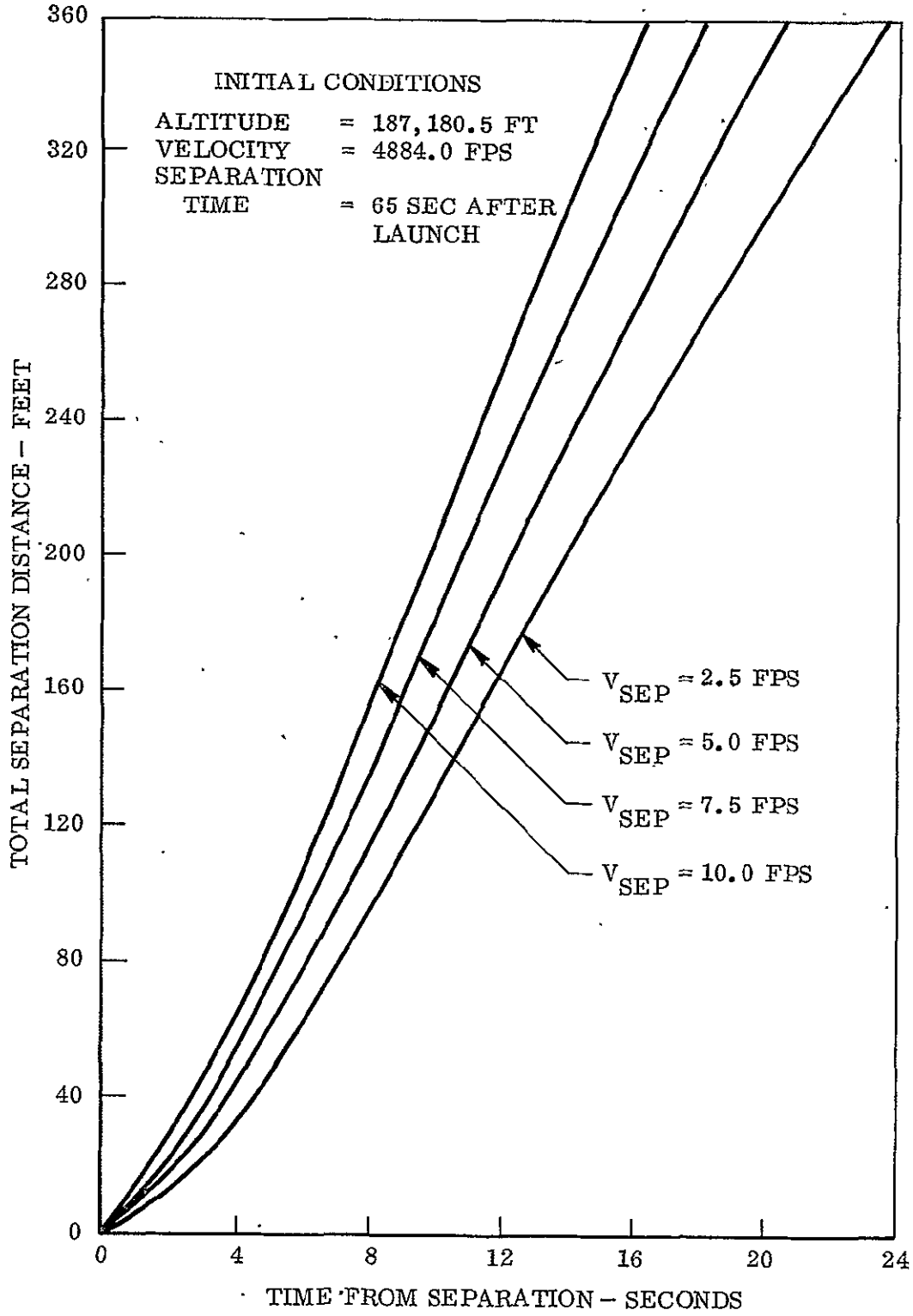

Fig B-26 Total Separation Distance Versus Separation Time – 350-lb Payload, 65 Sec After Launch

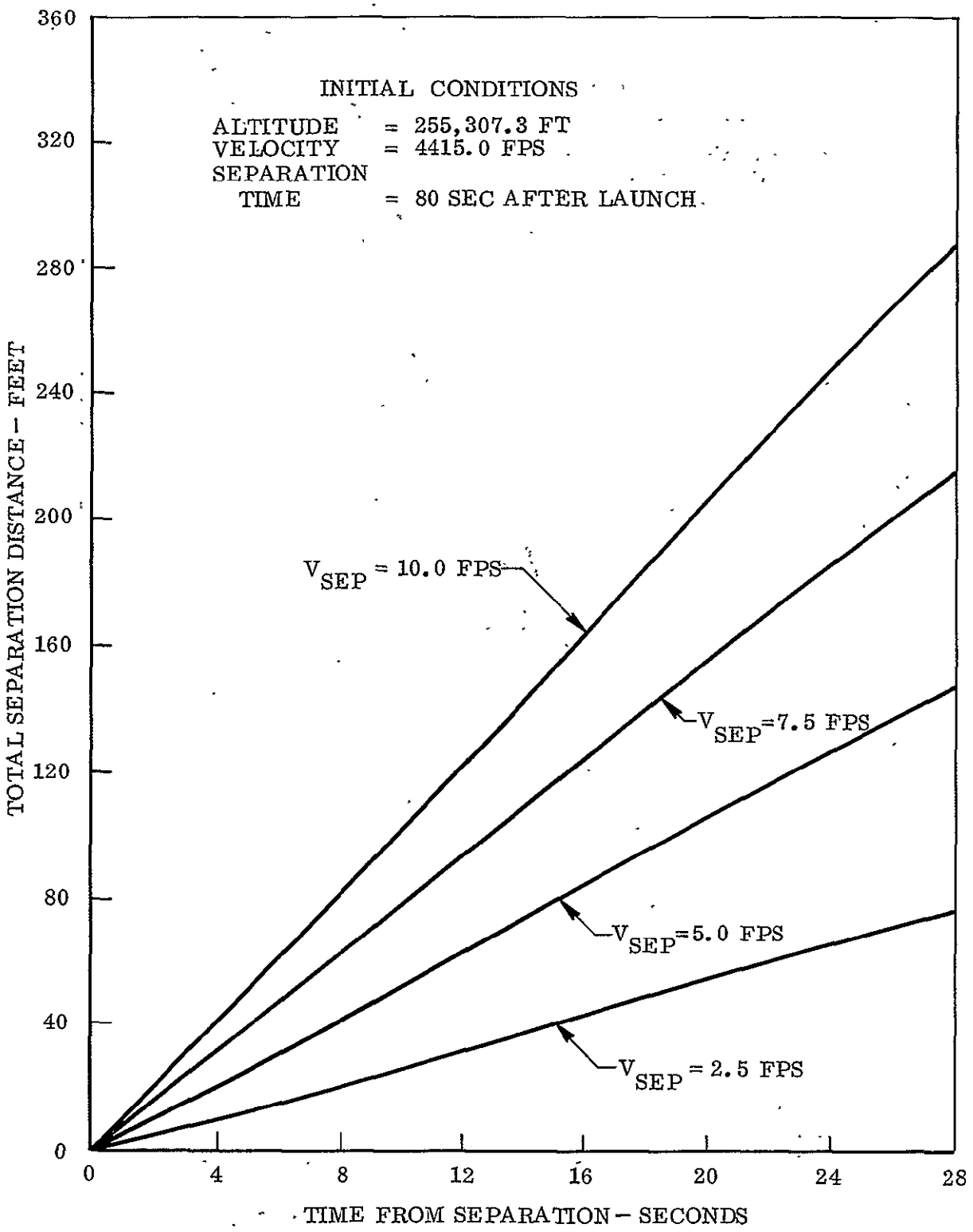

Fig. B-27 Total Separation Distance Versus Separation Time — 350-lb Payload, 80 Sec After Launch

Appendix C
FINE SUN SENSOR

Appendix C

FINE SUN SENSOR

The SPARCS Fine Sun Sensor (FSS) provides precise pitch and yaw attitude information to the system when it is operating in the fine control mode. Initially, it was planned that the FSS would be a subcontract item. However, before the end of the first three months of the contract, the plans for its development were changed because of NASA disapproval of the existing vendor facility and because of disagreement between NASA and the vendor on certain terms of the contract. Because of cost considerations, LMSC elected to make the FSS in-house rather than buy it from an alternate vendor.

C.1 REQUIREMENTS

The performance requirements for the SPARCS which are directly applicable to the FSS are listed below (values are given in arc seconds).

	Goal	Target	Minimum Acceptable	Second Test Flight Results
Absolute Accuracy	5	15	30	9
Drift	0.5	.2	5	3.5
Noise	0.1	0.4	1.0	<0.1

These requirements are for the pitch and yaw axes only. Although the values given are for the entire system, the FSS is the principal contributor to the listed errors.

Other requirements which served as major constraints in the design of the FSS include:

Maximum Diameter	3.5 in.
Maximum Length	6.0 in.
Maximum Weight	3.0 lb
Reference Optical Surface (ROS)	within 15 arc sec of mounting surface

Electrical Null Alignment	within 15 arc sec of reference surface
Electrical Bias Alignment	±30 arc sec (minimum)
Electrical Bias Adjustment Precision	0.1 arc sec
Electrical Output Slope	1.2 mV/arc sec (±10 percent)

The design environmental conditions for the FSS were more severe than those for the basic Aerobee 150 hardware because the FSS is mounted on the payload structure under the nose cone. It is thus subjected to structural amplification of rocket vibration and nose cone heating. The principal conditions were:

Vibration (maximum between 60 and 160 Hz)	15 g's
Shock	30 g's, 6 ms
Temperature	50^{o} to 130^{o}F

Initially, the temperature requirement was for a 50^{o}F change during flight. However, calculations showed this condition to be highly unlikely and acceptance tests drift measurements are made simulating the calculated worst-case conditions, where the vehicle skin in close proximity to the FSS was heated to 300^{o}F.

C.2 FSS DESCRIPTION

The FSS is a photoelectric device located on the forward end of the payload section. It furnishes pitch and yaw attitude information to SPARCS by generating signals which are proportional to the pointing error between the FSS electrical null and the radiometric center of the sun.

Figures C-1 and C-2 show the main components of the sensor. The reference optical surface (ROS) is a polished aluminum surface that is an integral part of the main housing. After the housing has been machined, the surface is polished and overcoated with silicon monoxide. The base mounting pads are then lapped so that the mounting surface is parallel (within 5 arc sec) to the reference surface. The electrical null axis is aligned to the ROS, which should be used when the FSS is aligned to an experiment.

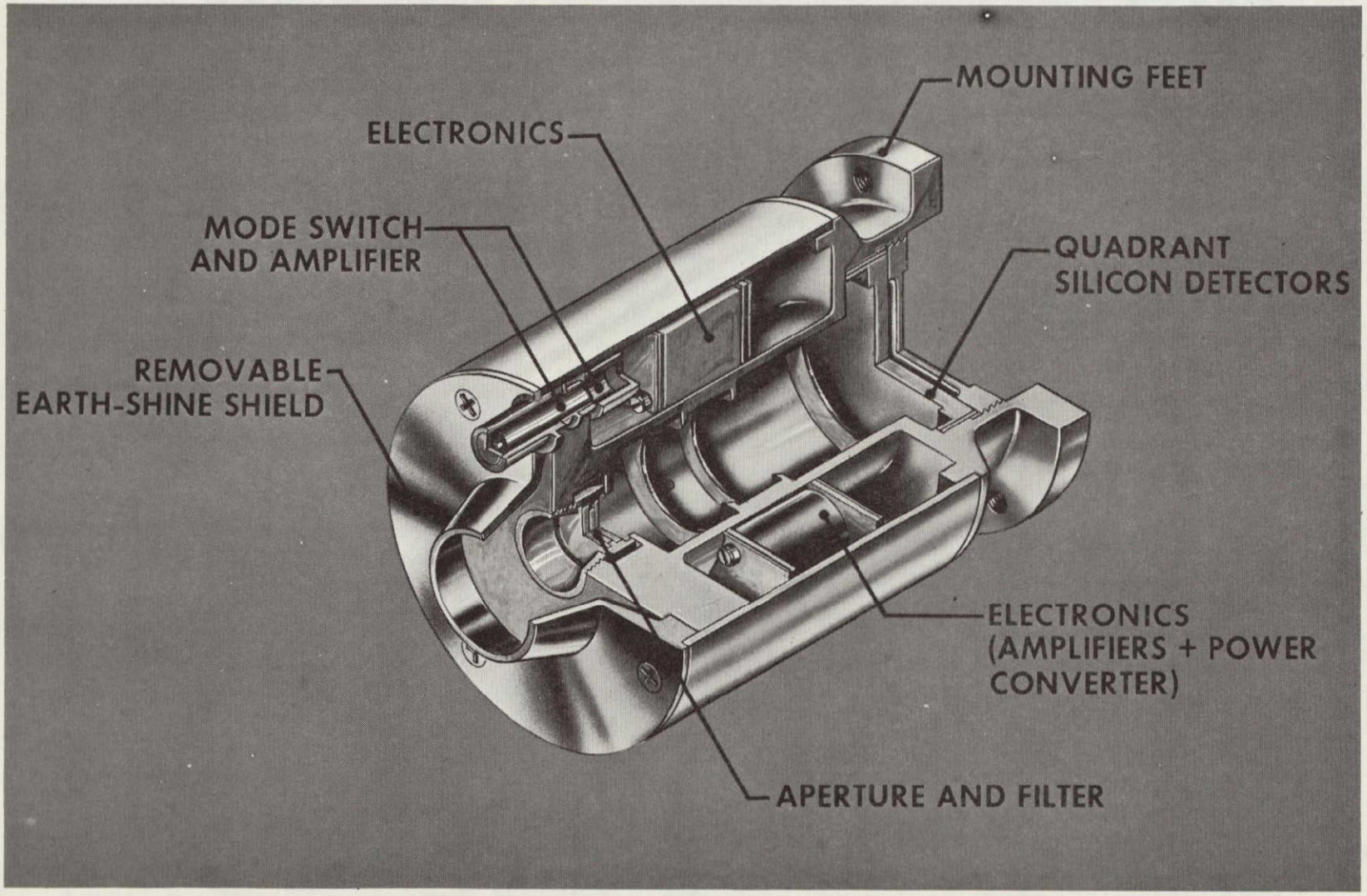

Fig. C-1 Fine Sun Sensor (FSS) Assembly

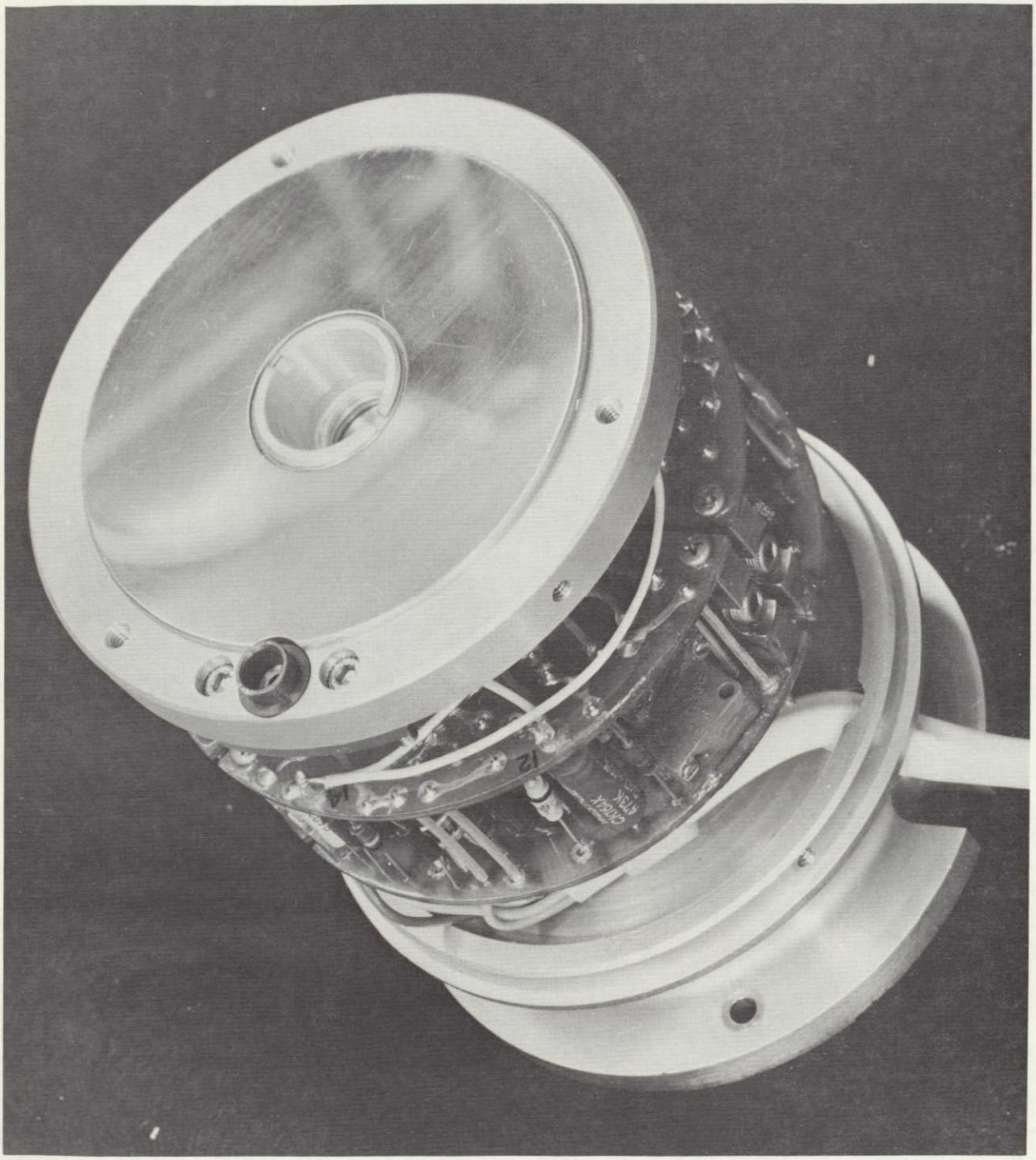

Fig. C-2 FSS Electronics

The aperture filter has a 0.300-in.-diameter clear aperture and an approximately square bandpass between 0.6 and 0.9 μ. The spectral response of the silicon detectors was limited to reduce the drift in the short circuit current due to temperature changes. LMSC tests and vendor data showed that the spectral responsivity of the cell shifted toward the long wavelengths (red end) as the temperature increased. The bandwidth was selected so that the decreased sensitivity on the blue end balanced the increased sensitivity on the red end. The FSS was calibrated and tested with a solar simulator that used a tungsten filament bulb which peaks in the near infrared (~1.0 μ) and has much less radiation than the sun.

The detector assembly is a quadrant array of four silicon n-on-p cells, similar to solar cells. Opposite cells are connected back to back to give an error signal proportional to the difference in radiation falling on each cell. The cells are connected to a low-input impedance amplifier so that they are operating in the short circuit mode, thereby minimizing temperature drift effects in the silicon cells. One pair of cells is connected to the pitch channel; the other pair is connected to the yaw channel.

The electronics consists of a military grade μA709 differential amplifier and associated equalizing components. A lab set resistor is used for feedback to set the gain of the sensor to 1.2 mV output per arc second error (near null). Provisions have been included to offset the electrical output of the FSS to compensate for small errors (up to 30 arc sec in each direction) when the FSS is aligned to the experiment.

A mode sensor, which has a circular field of view of 10.5 deg, is used by the control system to switch electronic gains and thrust levels when the sun is within the FSS main field-of-view. The mode sensor consists of two apertures, a small silicon detector, and an amplifier. The output changes from less than 1V to greater than 8V when the sun comes within the mode sensor field-of-view.

C.2 ANALYSES AND DESIGN

C.2.1 Sensor Geometry

As shown in Fig. C-3, the FSS geometry is defined by a circular aperture 0.3 inch in diameter and located 3.0 inches from an array of four silicon detectors. The adjacent edges of the detectors in the array are masked by a precision photoetched pattern, consisting of four narrow opaque strips which extend from a circular central blockage to the edges of the detectors. The mask thus actually defines the inner edges of the detector "active" areas and eliminates the need for precision alignment of the four individual detectors.

The enlarged view in the lower half of Fig. C-3 illustrates the relative sizes of the central blockage and circles of illumination at the detection plane (defined by the mask) when the sun is at one astronominal unit (AU). The small circle of illumination outlines the regions which receive illumination from the entire sun, the annulus between the large and small circles of illumination represents the regions which receive illumination only from part of the sun, and the area outside the larger circle represents the region which receives no illumination.

It is desirable to have the focal length (distance between the aperture and the detector) as long as possible for high system sensitivity. However, the over-all diameter of the sensor is dictated by the field-of-view (minimum ±12 deg), and the focal length of 3 inches and a 0.3-inch aperture were selected to meet this requirement. This made the FSS approximately 5 inches long, 1 inch less than the maximum allowable length. The FSS diameter, including the cover attaching screws, was just under the allowable 3.5-inch diameter.

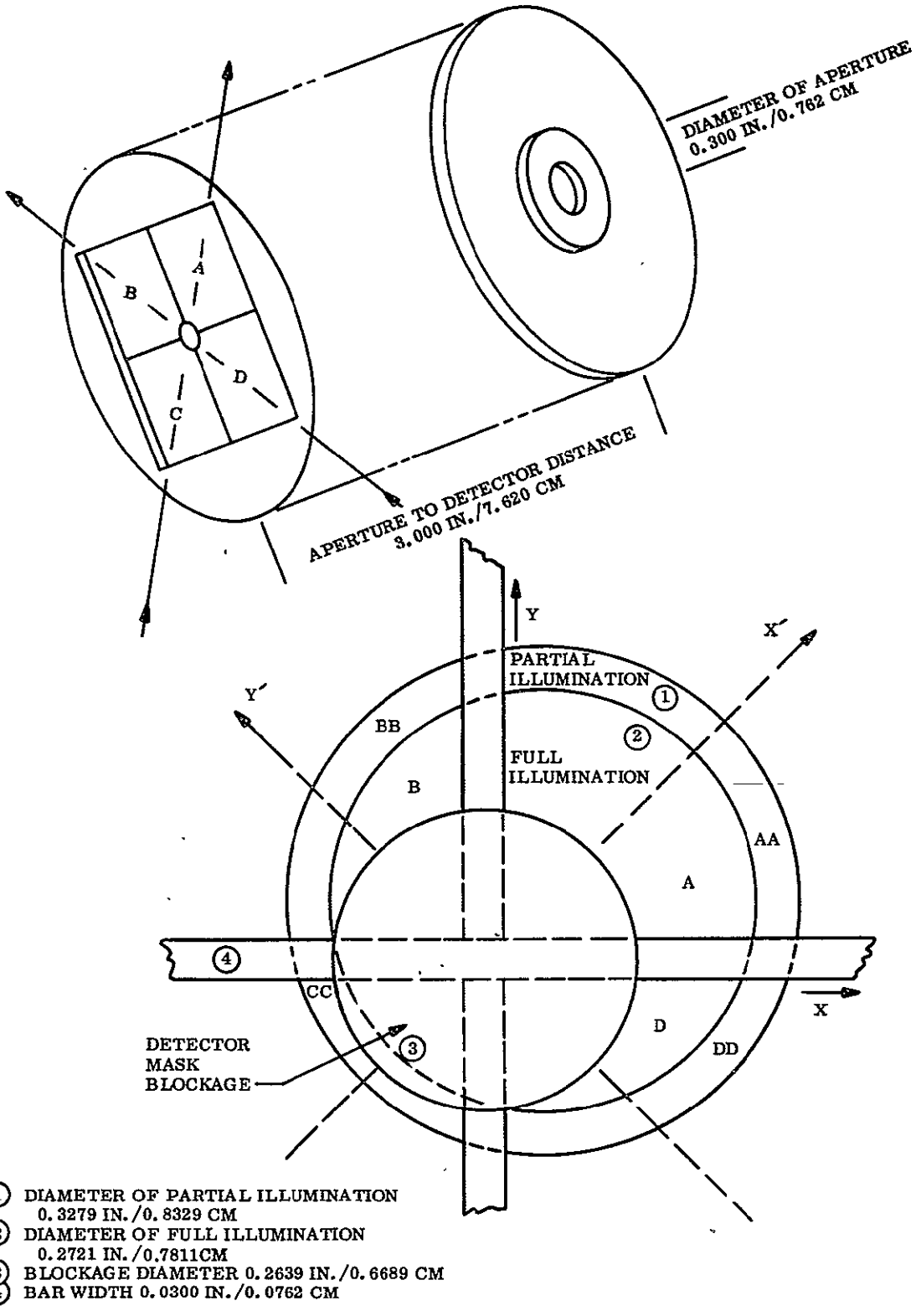

(1) DIAMETER OF PARTIAL ILLUMINATION
0.3279 IN./0.8329 CM
(2) DIAMETER OF FULL ILLUMINATION
0.2721 IN./0.7811CM
(3) BLOCKAGE DIAMETER 0.2639 IN./0.6689 CM
(4) BAR WIDTH 0.0300 IN./0.0762 CM

Fig. C-3 FSS Detection Geometry

C.2.2 Small Angle Characteristics

A computer program was written to investigate the slope, linearity, and cross coupling of the sensor near null (within 4 arc min). To simplify the program, which was intended to provide only rough-order-of-magnitude results, the following assumptions were made:

a. The sun is a uniform radiation disk.
b. The image of the sun forms a circle on the detector.
c. The penumbra of the sun's image is a $\cos^2$ distribution.

The first assumption leads to small errors because the sun has limb darkening, which is a function of wavelength as well as distance from the center of the sun. The second assumption leads to errors because the shadow of the sun in the detector plane is an ellipse for off-axis angles. The third assumption is in error because the integrated area of a circle crossing a circle (the sun crossing the detector mask as depicted in Fig. C-3) is not a $\cos^2$ function. The magnitude of this error was calculated and found to be less than 0.9 percent. When limb darkening was included, the error was reduced to approximately 0.3 percent. Because these errors were small, the $\cos^2$ approximation was used in the computer program.

The program calculated the illuminated areas on the detectors as illustrated in Fig. C-3. As the sun moved off axis (+X for the case shown), the areas marked A, B , C , D , AA , BB , CC and DD were calculated. Note that C equals 0 because the sun has moved far enough off null so that the detector mask blockage obscures the fully illuminated portion of the image of the sun. The differential area (A + AA) minus (C + CC) was then calculated for off-axis errors of 2 , 4 , 8 , 16 , 32 , 64 , 128 and 256 arc sec. This process was repeated for various blockage diameters and also for one case in which there was a fixed 10-sec error in the perpendicular axis.

Some of the numerical results obtained are summarized in Table C-1. The differential areas correspond to one arc sec of motion when viewing the real sun and simulated sun (3.2 times the real sun diameter), respectively. The linearity values are based on the difference between 64 times the signal at 2 arc sec and the signal at 128 arc sec.

Table C-1

COMPUTER PROGRAM RESULTS

Blockage Radius (cm)	Real Sun		Simulated Sun	
	Differential Area (10^{-4} cm^2)	Error in Linearity (deg/deg)	Differential Area (10^{-4} cm^2)	Error in Linearity (deg/deg)
0.24584	*0.3412	+0.0004	*0.3411	-0.0017
0.33447	*0.3412	+0.0000	0.2865	-0.0148
0.35663	0.3228	-0.0021	0.2461	-0.0078
0.36771	0.2703	-0.0020	0.2227	-0.0016
0.37879	0.1940	+0.0003	0.1979	+0.0047
0.38987	0.1112	+0.0042	0.1720	+0.0156
0.40095	0.0417	+0.1484	0.1457	+0.0281
0.41203	0.0035	+0.3185	0.1197	+0.0484

*Detector mask blockage smaller than full illumination ellipse (see Fig. C-3).

The results show that the linearity error is small for all cases; however, it increases rapidly when the blockage on the detector gets larger than the aperture on the filter. The blockage and the aperture are the same size when the blockage radius is 0.150 inch (0.381 cm).

The blockage radius selected was 0.33447 because the original computer runs showed that the output from the real sun had the same area as the output from the simulated sun. A subsequent check revealed that the program computed minus areas because of the limits of the integration, when in fact a zero area should have been used, i.e., Area C in Fig. C-1. This can lead to errors in sensor calibration with a simulated sun, as shown by comparing the differential area values for real and artificial conditions in Table C-1. The error may be taken into account during calibration, or the blockage diameter may be made smaller than the fully illuminated sun or approximately the same size as the aperture on the filter.

The cross coupling was less than 0.001 percent for cross-axis offsets of 10 arc sec and the cross coupling slope change increases to 10 percent for a 1-deg offset in the cross axis. Cross coupling effects for larger angles are described in the following paragraph.

C.2.3 Large Angle Characteristics

The FSS performance in terms of absolute accuracy, linearity, and slope is critical only over an angular range of a few minutes from null. A knowledge of the wide angle output of the FSS is important, however, in order to properly predict the acquisition capability. Since high precision is not required for these data, a graphical integration technique was used. The detector and mask were drawn at a scale of 5 inches per centimeter, and the circles of illumination for the sun "image" were then drawn with the center displaced at one-degree intervals in pitch and yaw. The illuminated area on each detector was then measured mechanically, using a planimeter for 86 unique cases. Partially illuminated areas were given an estimated weight, W , which was 0.5 for most cases. The areas of full illuminations were given a weight of one and were summed with the weighted areas of partial illumination. The results for pitch and yaw combinations from zero to 8 deg are presented in Fig, C-4.

The FSS was used to observe the real sun at air mass = 1 (approximately) from the LMSC Building 151 rooftop. It was aligned to point at the sun by nulling both the pitch and yaw outputs and oriented so that the motion of the Earth would cause the sun to move in the pitch direction. Figure C-5 shows a comparison of the relative data predicted from the calculations and the observed output during the period of rooftop operation. Note that the slope of the curves is nearly the same for each case.

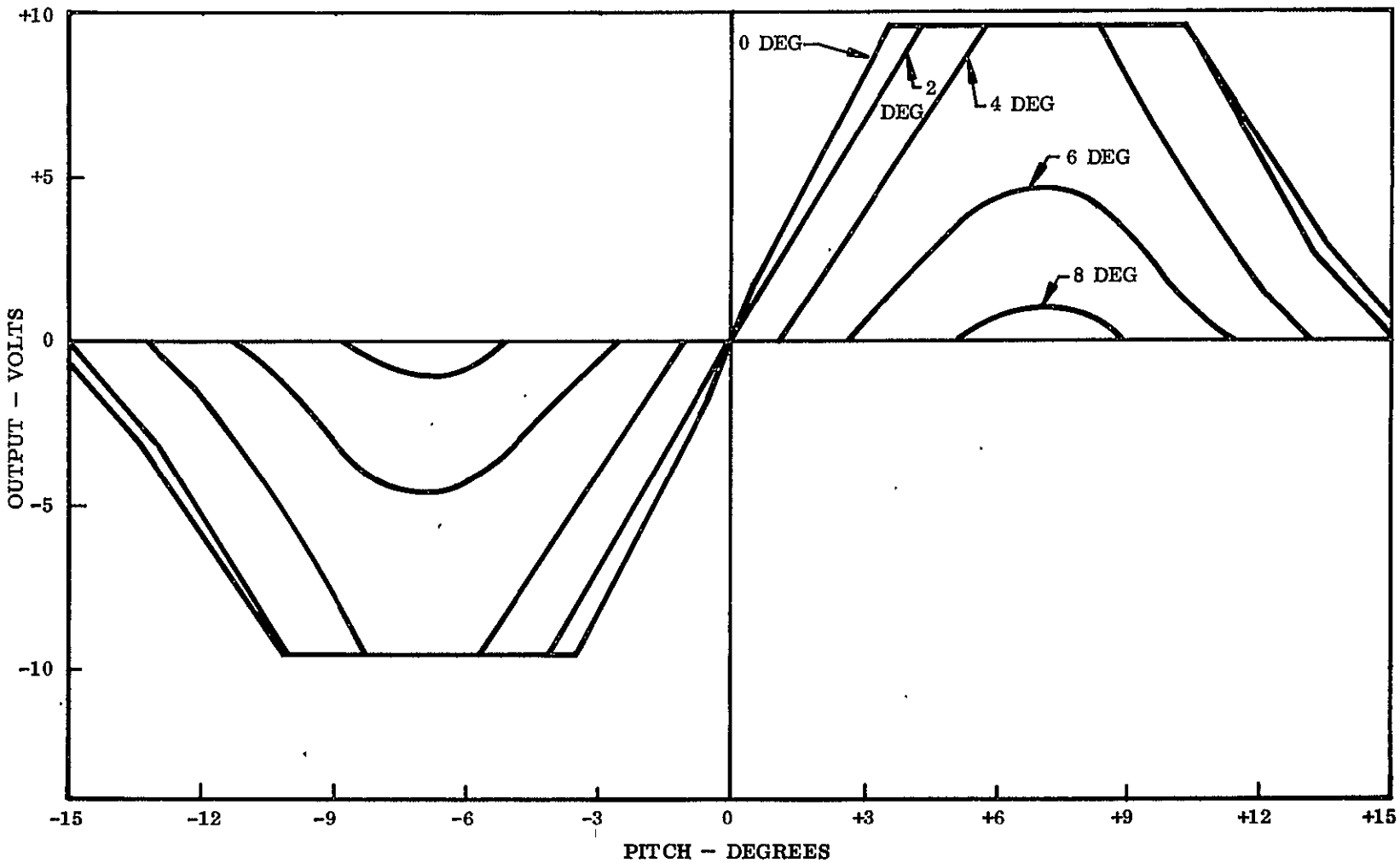

Fig. C-4 Pitch Output Versus Pitch Angle for Various Yaw Angles

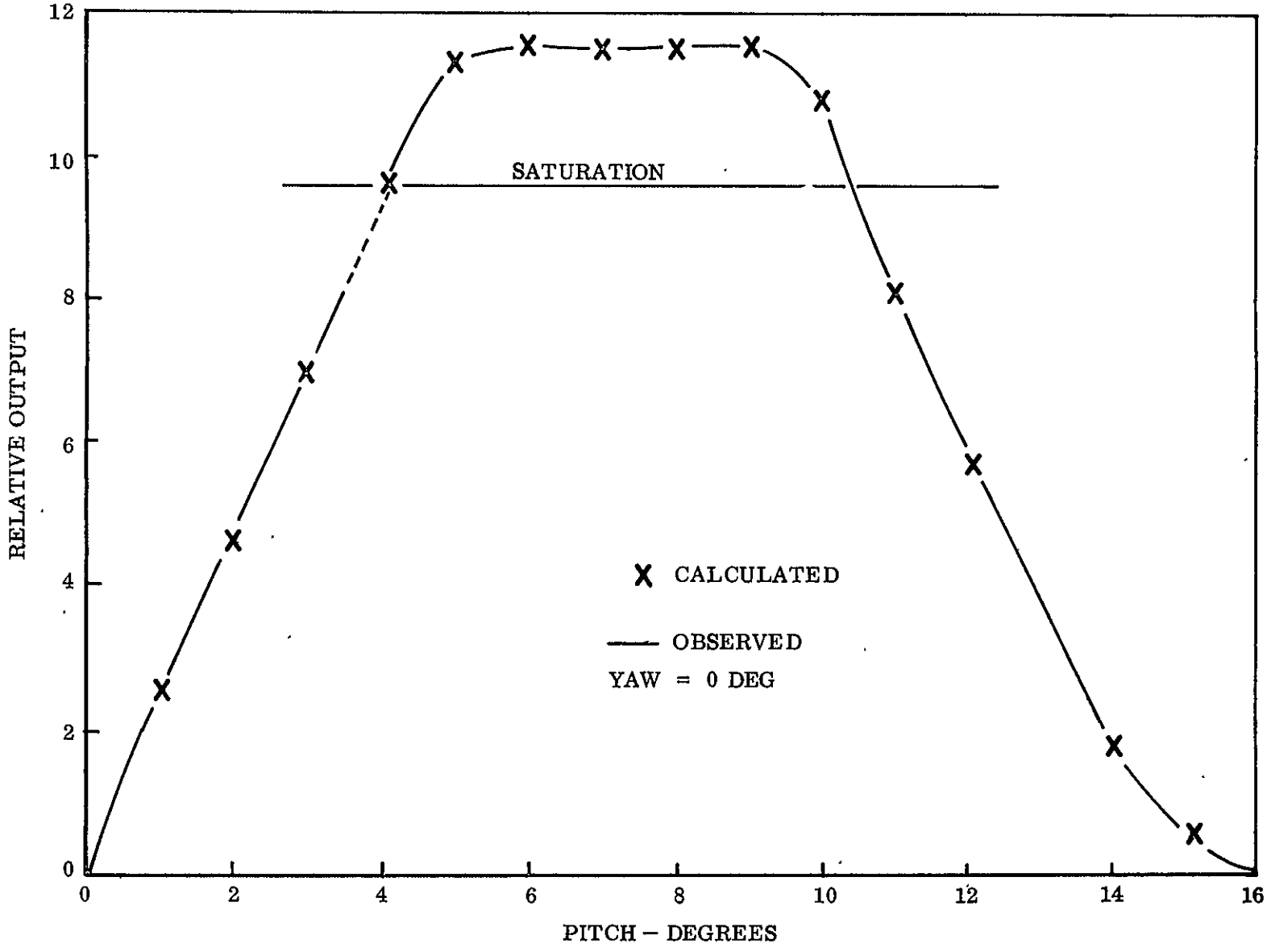

Fig. C-5 FSS Large Angle Characteristics

C.2.4 Mode Sensor Analysis

The basic geometry of an optical sensor with a small field-of-view is shown in Fig. C-6. The angular relationships are given by

$$\tan (A + \alpha) = (R2 - R1)/L$$
$$\tan (B - \alpha) = (R2 + R1)/L$$

where

- α = the half-angle of the sun at mean distance = 0.00465 radian
- R1 = the radius of the detector aperture
- R2 = the radius of the angle limiting aperture
- L = the distance from the detector aperture to the angle limiting aperture
- A = the angle (maximum) at which the detector is fully illuminated
- B = the angle (minimum) at which the detector is fully darkened

If the angle $(B + \alpha)$ is less than about 10 deg, the tan of the angle can be assumed equal to the angle and:

$$A = (R2 - R1)/L - \alpha \quad \text{(C1)}$$

$$B = (R2 + R1)/L + \alpha \quad \text{(C2)}$$

$$(B - A) = 2R1/L + 2\alpha \quad \text{(C3)}$$

Thus, the transition angle $(B - A)$ is approximately independent of R2.

Initially, the mode sensor was to have angle A = 1.5 deg and angle B = 2.5 deg. Two apertures with radii of 0.005 inch (R_1) and 0.050 inch (R_2) were procured for this configuration. Subsequently, the limits were changed to A = 9 deg and B = 11.5 deg.

Solving Equation (C3) for L and substituting that value into Equation (C1) leads to:

$$(B - A) = (2R_1/L) + 2\alpha$$
$$L = 2R_1/(B - A - 2\alpha) = 0.300$$
$$\text{and } A = [(R_2 - R_1)/L] - \alpha$$
$$R_2 = L(A + \alpha) + R_1 = 0.0535$$

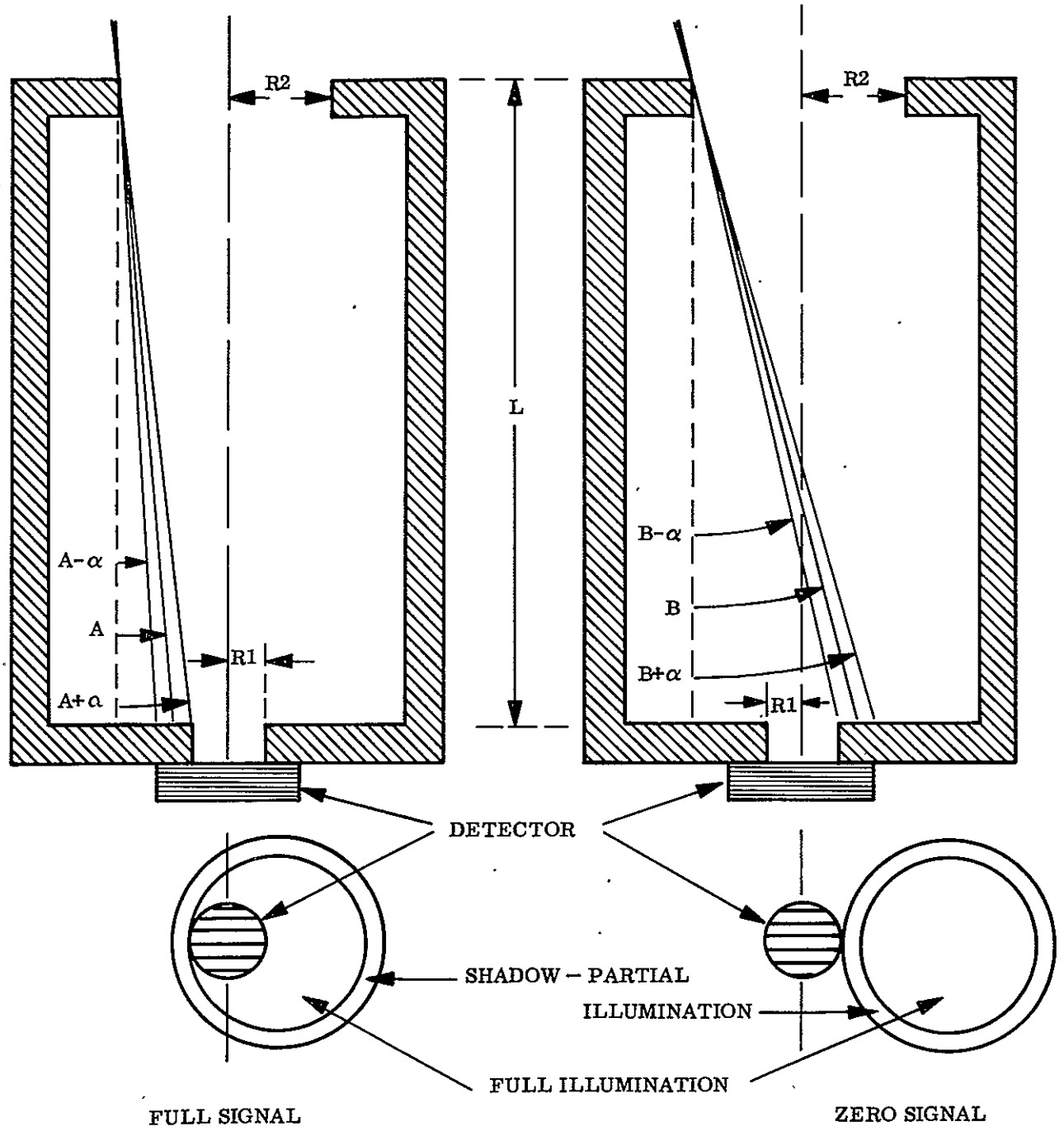

Fig. C-6 Small-Field Sensor Geometry

Because of mechanical limitations in the already designed FSS housing and availability of drill sizes to enlarge the aperture hole in the wafer for R_2, values of L and R_2 were made 0.270 inch and 0.050 inch, respectively. This made angle A 9.2 deg and angle B 12.1 deg; tolerance on these angles is ±1.0 deg. These values met the project requirements and were therefore used in the FSS design.

C.2.5 Detector Assembly

The detector assembly consists of four 0.5 x 0.5-inch n-on-p silicon cells arranged in a quadrant array and connected as shown below.

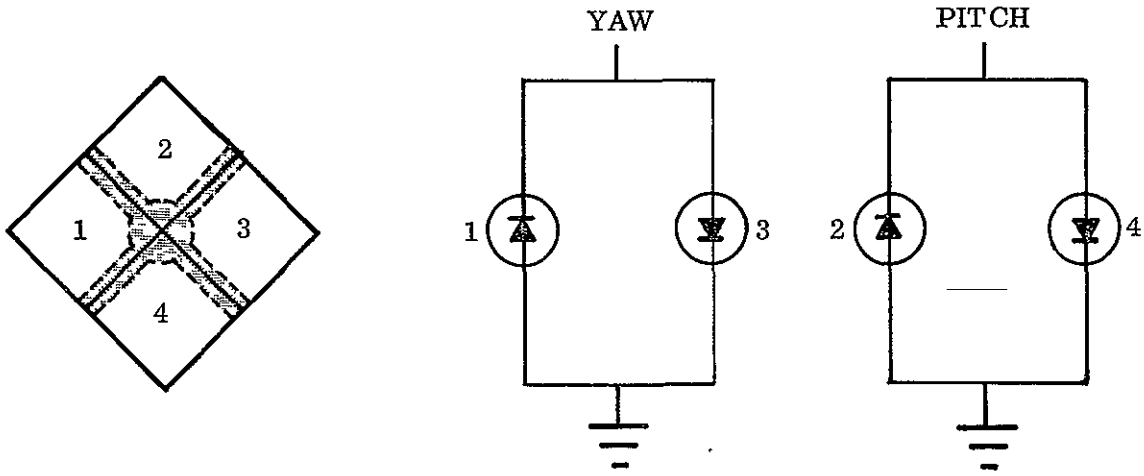

The cells are mounted on a substrate of beryllium oxide which serves both as a good thermal conductor and electrical insulator. Nonlinearities caused by edge effects are eliminated by covering the intersections of the cells with an opaque mask, as indicated by the shaded area in the figure above.

To reduce the error caused by drift in the individual cells, the exposed areas of the detector are covered with a glass mask to reduce the amount of light reaching each cell. This has the effect of increasing the ratio $\Delta i/i$,

where

Δi = change in current for a 1-arc-sec error angle ($|i_3 - i_1|$ for yaw, $|i_4 - i_2|$ for pitch)

$i \approx i_1 \times i_2 \approx i_3 \approx i_4$ = output from one detector quadrant near null

because it reduces the magnitude of i without reducing Δi . For the value $\Delta i/i = 0.01$, a 1 percent change in the output of a single detector results in a 1-arc-sec error, whereas for $\Delta i/i = 0.001$, the error is 10 arc sec; consequently it is desirable to make the ratio $\Delta i/i$ as large as possible. For the FSS with a 3-inch distance between the aperture and the detector, the ratio is 0.0016.

The detector assembly specification for the FSS requires that each cell of a pair be matched within 1 percent of the other, and that the yaw pair be matched within five percent of the pitch pair, under solar simular radiation and tungsten ($\sim 2800^{\circ}$K) radiation. An aperture filter similar to that used in the FSS is placed over the cells for the matching.

Drift was also measured under the solar simulator for a 50°F temperature change. All cell pairs had less than a 1 percent change, with 90 percent of the cell pairs changing less than 0.5 percent. Flight data indicate that the temperature of the detector assembly, as measured by a thermistor on the detector substrate, changed less than 3°F ; detector drift should therefore be less than 0.5 arc sec.

C.2.6 Filter Analysis

When silicon solar cells are heated, they exhibit an increased responsivity and shift in the peak spectral response toward the infrared (see Fig. C-7). If both cells of a pair shift equally, the only apparent change in the output of a pair connected differentially is a gain change on the order of 1 percent per 25°F . However, matching pairs

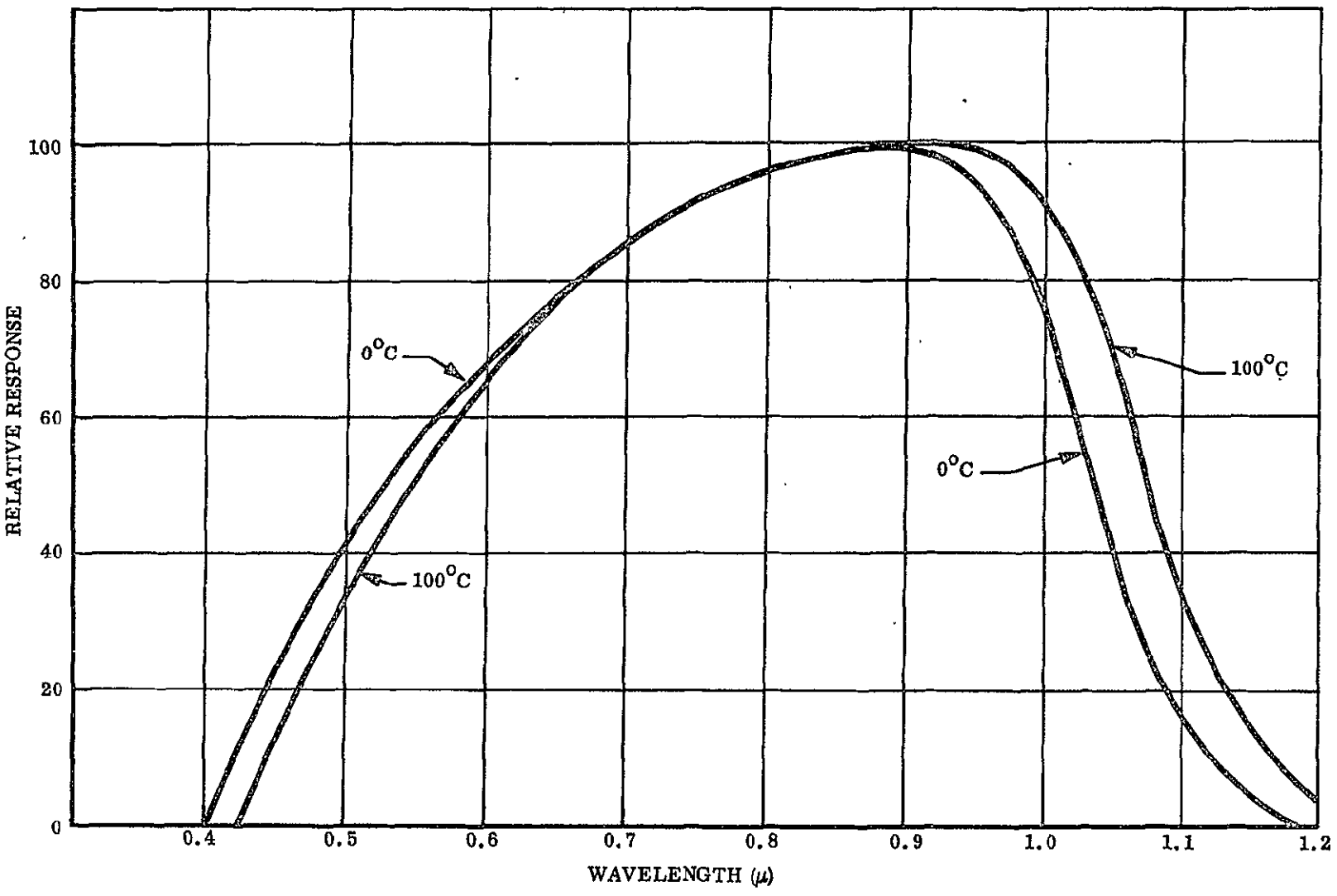

Fig. C-7 Variation of Spectral Response Versus Temperature

of cells for absolute spectral response requires that the spectral response of each cell be measured individually and cell pairs be selected from these data. The supplier indicated that approximately 50 individual cells were required to select 12 pairs of cells matched to within 1 percent in absolute response to tungsten and solar radiation. If this tolerance were required for absolute spectral response as well, over 100 individual cells would be required, and the cost would be prohibitive. To solve this problem, a filter was placed between the detector and the radiation to elimate the areas on the ends of the curve where the effect is greatest.

Ideally, a narrow filter centered around 0.75 μ should be used, but this would require very high gain amplifiers which also amplify the system noise. The majority of the spectral shift occurred below 0.55 μ and above 0.9 μ. Because the total radiation from tungsten (which was the source selected for the solar simulator) is much lower than solar radiation, it was advantageous to use as much of the upper end of the spectrum as possible. The selected filter has a bandpass between 0.6 μ and 0.9 μ, with less than 2 percent average transmission below and above these limits and more than 85 percent within bandpass. A curve of a typical filter is shown in Fig. C-8. An undesirable filter leak occurs at 0.46 μ, but the total area under the curve is small and the response of silicon is down to about 40 percent of its peak response at this point.

The opaque mask which defines the 0.3-inch FSS aperture (see Fig. C-3) is deposited on one side of the filter. Transmission through the opaque portion of the aperture filter is less than 0.5 percent.

C.2.7 Aperture Positioning and Alignment

The alignment of the electrical null axis to the reference optical surface is accomplished by positioning the aperture holder containing the aperture filter. The position of this aperture is critical, i.e., a 0.000015-inch movement (crosswise) of the aperture with respect to the detector causes a 1-arc-sec error. During alignment, the FSS is held in a fixture and aligned with an autocollimating solar simulator. Pins are then used to position the aperture filter, and room-temperature curing epoxy is used to secure the aperture in position when the pins are removed.

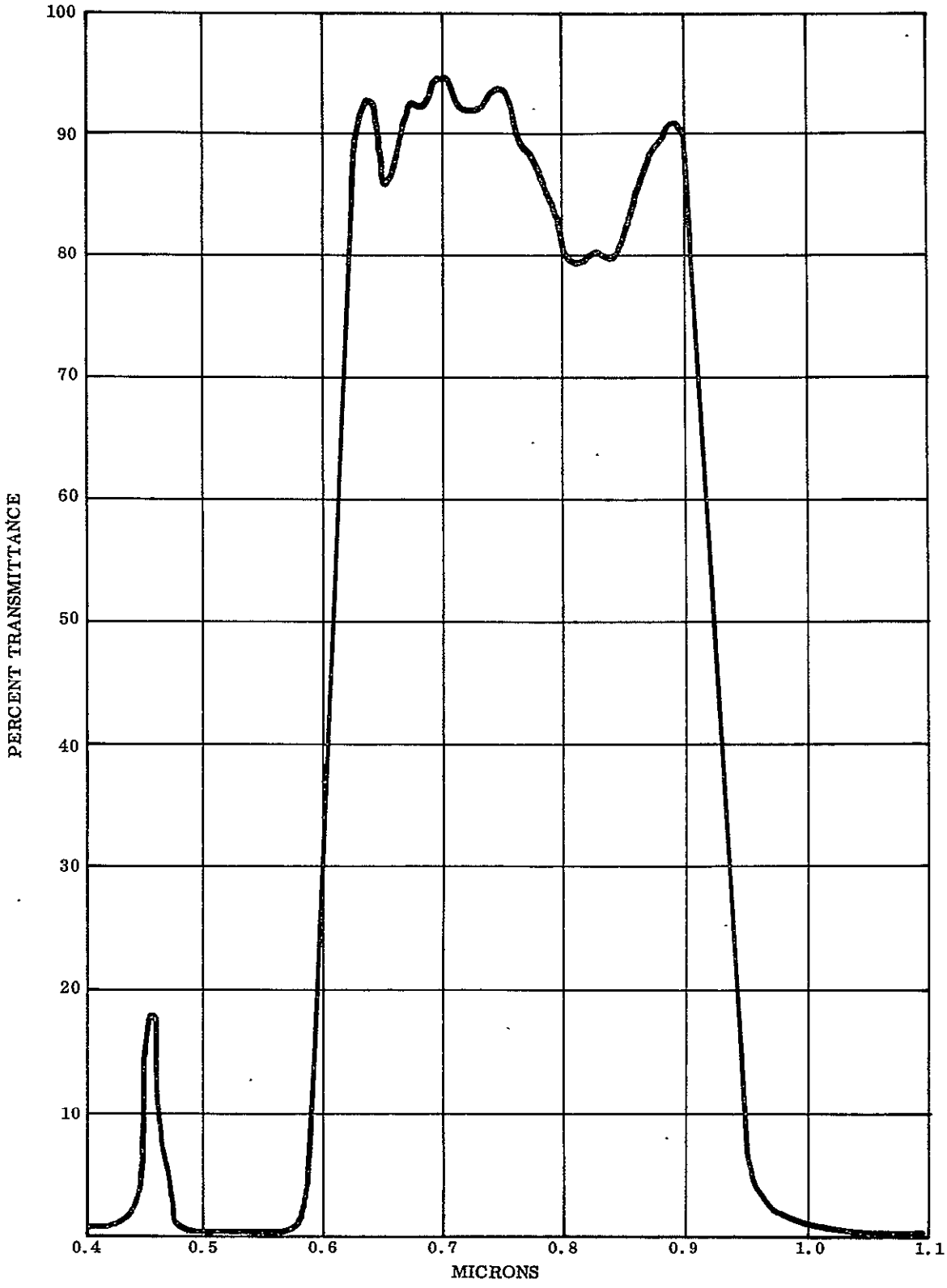

Fig. C-8 FSS Filter Response

Several methods were considered for adjusting and retaining the aperture filter. Counter rotating cams were the first means considered. However, the design complexity and cost were major disadvantages. Steel pins were not feasible because of the difference in coefficients of expansion between aluminum and steel. Epoxy was selected as being a simple, inexpensive method. Epoxy is forced into the cavity surrounding the aperture filter, giving uniform support on all sides. Alignment changes of 1 to 4 arc sec during temperature and vibration environments are attributed to the epoxy, but these changes are well within specification.

C.2.8 Reference Optical Surface

The contract specification requires that the electrical null axes of the FSS be aligned to an FSS mechanical reference surface (base mounting pads) to within 15 arc sec. Aligning the electrical null to this surface within the specified accuracy requires the use of optical equipment and a transfer mirror. To simplify these operations, a reference optical surface (ROS) was designed into the front surface of the FSS (see Fig. C-2). The electrical null axes for pitch and yaw are aligned to this surface and the base mounting pads are lapped to within 15 arc seconds of it. This surface can also be used as the reference plane during payload alignment, simplifying the alignment procedure.

Several methods for manufacturing the ROS were considered during the design phase. The method selected for the qualification unit was to coat the aluminum housing surface with copper, plate over the copper with rhodium, polish the rhodium, and deposit a thin aluminum layer which was then overcoated. This method gave a flat mirror surface; however, the appearance of the mirror surface was poor, the reflectivity was approximately 30 percent, and some of the plating leaked into the aperture retainer threads and other areas. The housing was usable in this state but a better method was deemed desirable.

The ROS on the remaining seven units was obtained by polishing the aluminum surface directly. A vendor was found who could meet the flatness requirement at a reasonable price; however, the reflectivity specification had to be lowered to 20 percent.

The mirrored surfaces on the first three housings had reflectivities which varied between 30 percent and 50 percent. Reflectivities of the last four units averaged about 65 percent. With an SiO protective coating, this method has proven to be satisfactory.

C.2.9 Electronics Design

The FSS electronics schematic is shown in Fig, C-9. The components are packaged into three cordwood soldered modules, divided as indicated in the illustration. Each module forms a 120 deg portion of an annular package which mounts around the main housing. The modules are not potted because the spacers have sufficient strength to support the components, and this arrangement facilitates the removal of components for testing and replacement. Power dissipation in each module is approximately equal, thereby equalizing thermal gradients.

The module on the left side of Fig. C-9 is the reference amplifier. It consists of an amplifier for the mode sensor photo diode (FPM200) and the bias potentiometers for the pitch and yaw amplifiers. The diodes on the input power leads are for protection against inadvertent power lead reversal. The bias potentiometers are used to offset the pitch and yaw outputs electrically to compensate for alignment errors of up to ±45 arc sec.

The two amplifier modules on the right side of Fig, C-9 are the pitch/yaw amplifiers. They are identical, with the exception of the feedback resistors which are lab set during FSS alignment and calibration. All three amplifiers use a Fairchild μA709 operational amplifier integrated circuit. The series resistors on the outputs (100 ohm on the pitch/yaw module and 750 ohm on the reference module) are to protect the integrated circuit against inadvertant grounding of the output.

The 1.0-uf capacitors in parallel with the 2K-lab set resistor in the feedback of the pitch and yaw amplifiers set the 3-dB roll-off point at approximately 80 Hz, whereas the FSS specification sets the minimum roll-off point at 10 Hz. As designed, however,

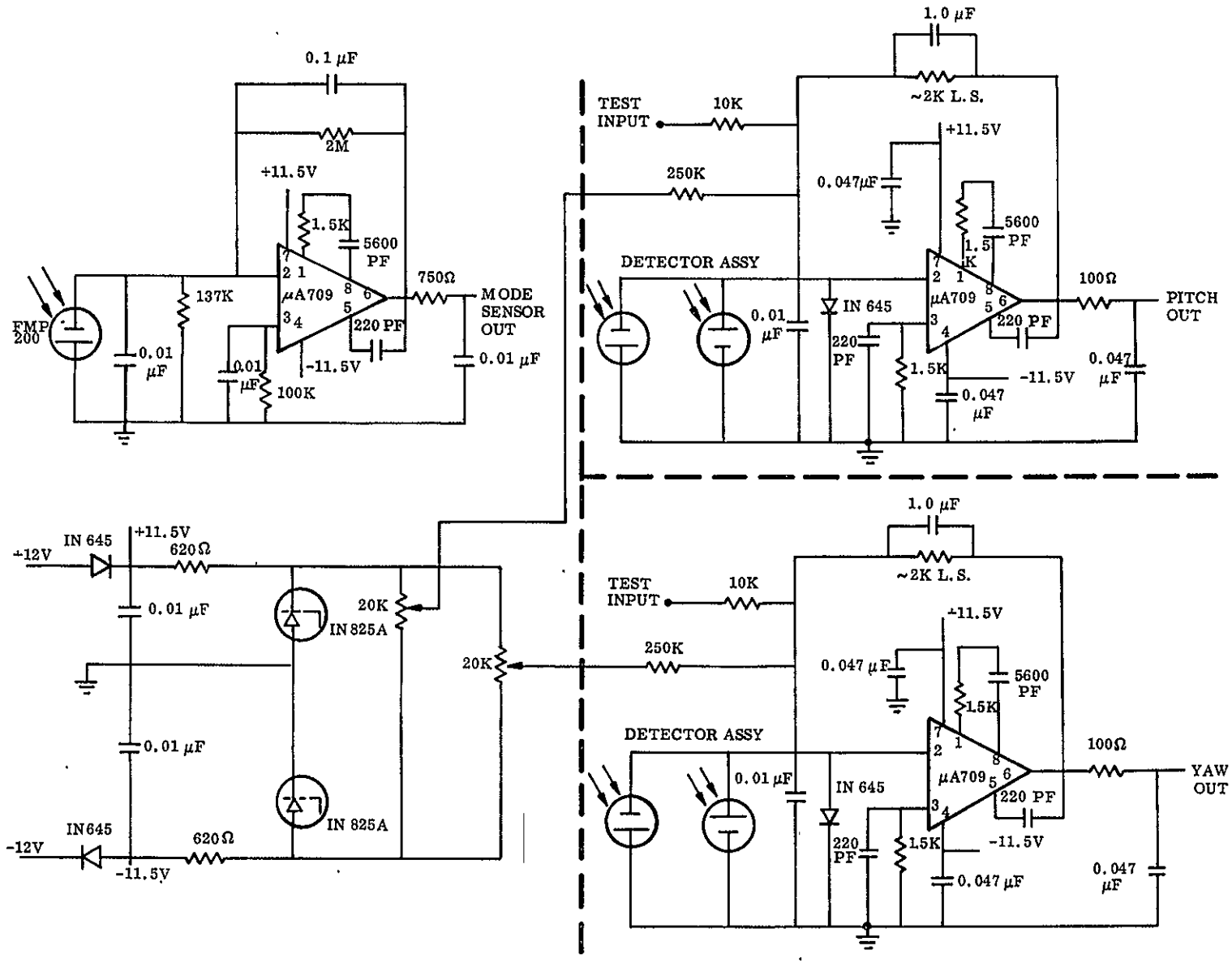

Fig. C-9 FSS Electronics Schematic

the noise on the output of the FSS meets the goal (less than 0.1 arc sec) for this parameter. To lower the roll-off point, it would be necessary to increase the capacitance and consequently the physical size of the capacitors; this could not be done without increasing the size of the FSS beyond the maximum limit.

C.2.10 Mechanical Design

The main housing of the FSS is a one-piece design to reduce internal stresses as much as possible. During fabrication, the housing is stress-relieved three times so that the reference optical surface will remain parallel to the base mounting pads during vibration and thermal environmental tests. All fabricated metal parts in the FSS are made from 2017 aluminum because of its low coefficient of expansion.

Three base mounting pads are used to provide 3-point support between the FSS and the payload section. To ensure that the specification requirement of 15 arc sec is met after testing, the plane of the pads is lapped to within 5 arc sec of the ROS. The FSS is positioned in roll to within 0.5 deg of the roll reference plane by accurately positioning the mounting screw holes. The detector assembly is located in roll with respect to the FSS housing to within less than 0.1 deg by means of a dowel pin and secured with a retaining ring.

Baffles are machined into the inner surface of the housing, which is then painted with 3M, 400 series, "black velvet" paint. This is to reduce the reflection of stray light rays, including the rays from the sun, when the FSS is at null. The shape of the earth-shine shield was governed by this same requirement.

The cover over the electronics is secured to the housing with three screws at the bottom of the cover, near the base of the FSS. (Testing on the first sun sensor showed that the ROS warped approximately 5 arc sec when screws were used at both top and bottom.) The cover is gold plated to reduce radiation absorption from surfaces, such as vehicle walls, which may be heated during launch. The Earth-shine shield is painted white because it is exposed primarily to solar radiation during fine pointing, and flat white paint has a lower absorption coefficient than gold for solar radiation.

C.2.11 Thermal Considerations

The most exacting performance requirement (par. C.1) proved to be the drift requirement. With the present design, a 1-arc-sec change is equivalent to a lateral translation of the aperture with respect to the detector of only 15×10^{-6} inches, or a differential change in detector pair output of only 0.15 percent.

Some of the methods of reducing mechanical drifts due to temperature have been previously discussed. These methods include symmetrical design of the housing, stress-relieving during fabrication, placement of the electronic modules around the housing to equalize power dissipation, and thermal coatings on the electronics cover and sunshade. All of these methods either reduce heating or allow all parts to expand or contract uniformly.

The second area to be considered was the electronics drift in the detectors and amplifiers. For a temperature change of $100^{\circ}F$, the amplifiers drift less than 0.5 arc sec, which is substantially lower than the design requirements. The detectors were far more critical because a pair is connected differentially and it is desirable to have individual detectors give a constant output with temperature change, or to have both detectors change equally so that the differential output remains constant.

Figure C-10 presents detector performance data typically obtained with the type of solar cell used in the FSS. In the short circuit mode (output voltage always zero), the output increases with increasing temperature. This effect does not change even after accelerated aging of the detector by electron bombardment (see lower curves of Fig. C-10). Table C-2(A) shows calibration data for the FSS detectors as a function of temperature, and Table C-2(B) shows calibration data for a similar sun sensor designed by LMSC. In both cases, the data show that output decreases with increasing temperature, in direct contrast to the result typically predicted for this type of detector.

Current vs. Voltage Curves for N/P 10 Ohm-Cm Silicon Solar Cells at Various Cell Temperatures Before and After 1 MeV Electron Irradiation (ϕ) . Measured in Simulated M=0 Sunlight.

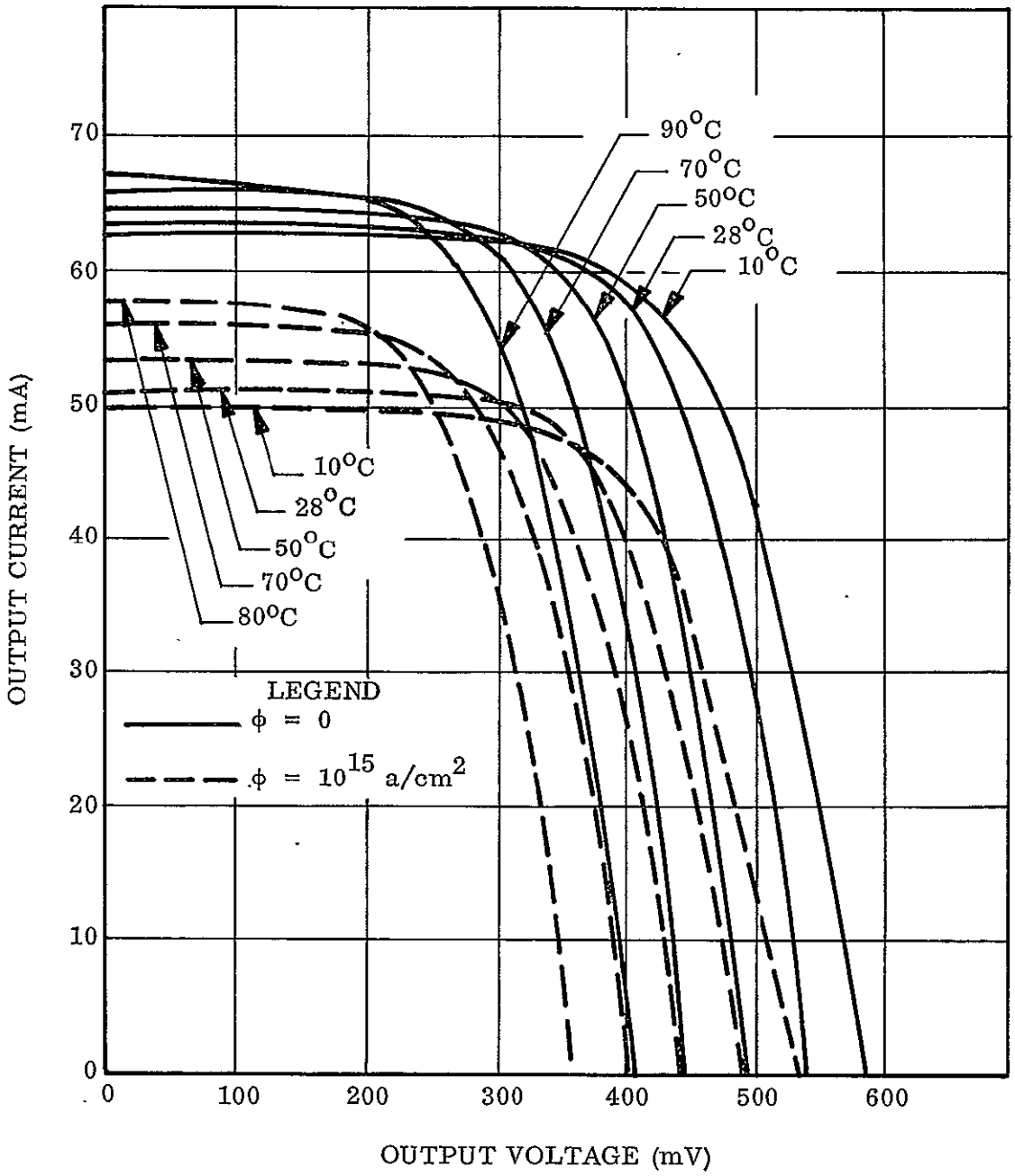

Fig. C-10 FSS Temperature Effects

Table C-2

CALIBRATION DATA

(A) FINE SUN SENSOR (FSS)

Unit	Cell	Temp (°F)	I_{sc}	Temp (°F)	I_{sc}	Temp (°F)	I_{sc}	Temp (°F)	I_{sc}
1	1	37	34.83	70	32.94	111	30.54	151	28.04
	3	37	36.08	71	33.81	114	31.28	151	28.80
	2	37	35.83	73	33.67	110	31.44	112	28.88
	4	37	36.48	72	34.57	110	32.25	113	29.59
2	1	54	33.38	72	31.85	108	29.44	147	26.91
	3	53	34.52	72	32.87	108	30.63	149	27.81
	2	53	34.95	73	33.23	110	30.68	146	29.90
	4	54	36.00	72	34.44	112	31.83	147	29.13

(B) SOLAR ARRAY SUN SENSOR (SASS)

Cell	Temp (°C)	I_{sc}	Temp (°C)	I_{sc}	Temp (°C)	I_{sc}	Temp (°C)	I_{sc}
1	-50	51.3	0	44.3	25	40.0	50	33.4
2	-50	55.6	0	49.0	25	45.8	50	42.1
3	-50	62.1	0	54.4	25	49.4	50	45.5
4	-50	57.0	0	50.0	25	45.3	50	41.4
5	-50	56.5	0	49.4	25	46.4	50	42.3
7	-50	65.5	0	57.5	25	53.3	50	49.1
9	-50	64.7	0	56.7	25	50.9	50	48.5
14	-50	59.1	0	52.1	25	47.2	50	43.8
15	-50	58.7	0	51.2	25	47.0	50	43.3
11	-25	42.9	28	43.7				
12	-25	47.3	28	47.0				
13	-25	44.3	28	44.0				

Note: Readings are the I_{sc} output in milliamps at one solar constant.

A number of temperature tests were conducted using the FSS detector at different temperatures and for various intensities and colors of illumination. The FSS detectors were placed in a temperature chamber and illuminated through a transparent window. The light source, filters, and amplifier were kept outside the temperature chamber to preclude possible temperature effects other than those directly related to the detectors. These tests showed that for moderate levels of illumination the short circuit current, I_{sc} increased with temperature. However, when resistors were placed in series with the output, the output slope could be made flat or made to decrease with temperature. The change in slope was found to depend on illumination level and the value of the series resistor. As a result of these tests and discussions with the vendor, it was concluded that the large area of the FSS detectors caused them to behave differently from conventional solar cells which have grids to reduce internal impedance. During calibration, the entire area of the detector is illuminated and the high current generated causes some back-biasing of the cell. For small signals, the detector output would be expected to increase with increasing temperature, whereas for large signals the output will decrease with increasing temperature.

Because of the difficulty of matching cells well enough to guarantee low differential drift over a 50^{o}F temperature range, the amplifier modules were designed so that resistors could be placed in series with the detectors to permit trimming if necessary to reduce drift. The accuracy of this method is questionable because detector trimming must be done with a tungsten simulator which has a different spectrum than sunlight. Fortunately, calculations showed and flight results later verified that a 50^{o}F change in detector temperature was very pessimistic and detector trimming would not be required.

Appendix D
DESCRIPTION OF COMPONENTS

Appendix D

DESCRIPTION OF COMPONENTS

This appendix provides a comprehensive analysis of the SPARCS attitude control system mechanization and includes schematics and test data for the various sensors and circuits that make up the system, excluding the Fine Sun Sensor (FSS) which was discussed in detail in Appendix C.

A block diagram of the major components of the SPARCS attitude control system is shown in Fig. D-1 below. A diagram showing the location of the sensors and thrusters relative to the body axes is presented in Section 1, Fig. 1-4.

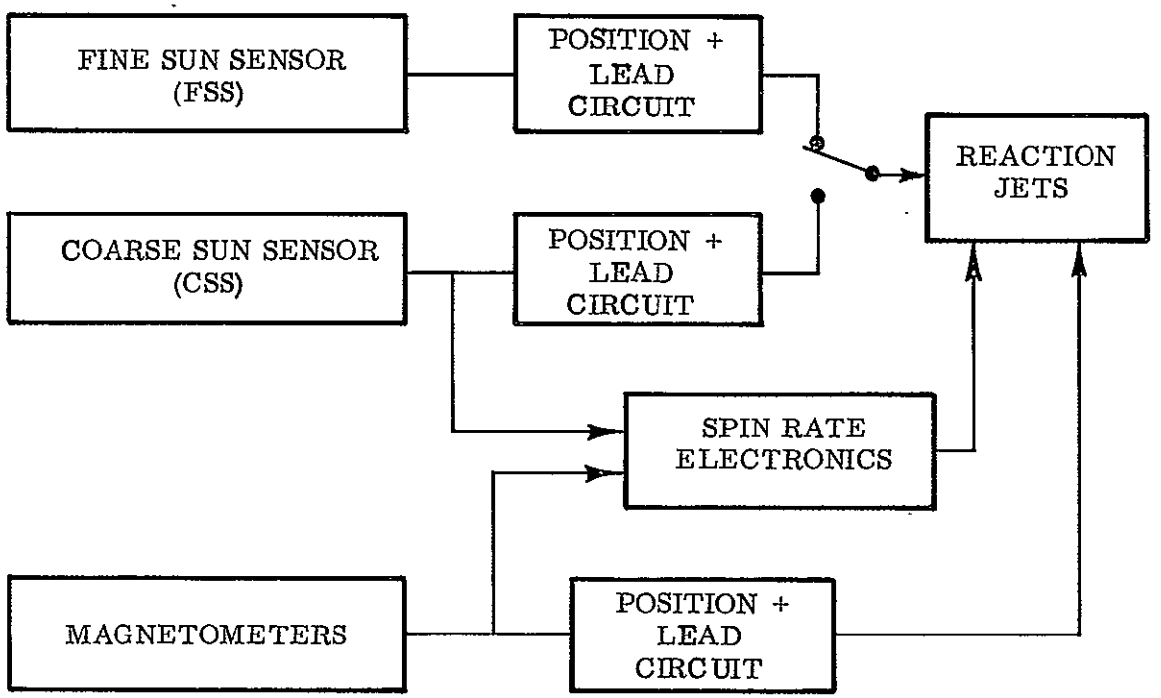

Fig. D-1 SPARCS Simplified Block Diagram

D.1 COARSE SUN SENSOR (CSS) SYSTEM

The coarse mode sensor system employs four sensors mounted with their normals along the transverse vehicle coordinate axes (see Section 1, Fig. 1-4). Each sensor consists of two solar cells, designated as main cell and bias cell, as shown in Fig. D-2. The bias cell is recessed in the mounting case and therefore has a restricted field-of-view (30 deg to 165 deg) from the vehicle's solar pointing axis. Because of this restricted field-of-view, the bias cell cannot see the sun when the vehicle's pointing axis is within a 30-deg half-cone angle from the direction of the sun. Thus, for this condition, the output of the cell is caused only by Earth shine irradiation (the bias cell is therefore sometimes referred to as the Earth shine sensor). The output of the bias cell is first attenuated 15 percent and then subtracted from the main cell output. Thus all but a small portion of the Earth shine signal is subtracted from the primary cell's output (see Fig. D-3). The secondary (bias) cell's output is attenuated slightly to guarantee positive control for large initial solar pointing error when both primary and secondary sensors see the sun.

The main and bias solar cells are connected to the control system as shown in Fig. D-4. The pitch and yaw channel circuits are identical up to and including the main channel amplifier, so only a diagram of the yaw circuit is presented. The yaw axis main cell outputs are summed together and then passed through the high-gain signal conditioning amplifier, designated AR1. This amplifier provides a gain factor and attenuates frequencies above 5.3 rad/sec. The output of AR1 goes to a lead network which adds a signal proportional to $\dot{S}_{12_m}$ to S_{12_m}. The bias cell amplifier provides a gain factor and attenuates frequencies above 0.6 rad/sec. The ratio of bias to main channel gain is approximately 0.866. Because of the discontinuous behavior of bias cell output, the rate proportional signal was derived from the main cell's output only.

D.1.1 Solar Sensing Element

The solar sensing element of the CSS system consists of a silicon photovoltaic cell attached to a TO-5 transistor case (Fig. D-5). The cell's active surface is protected against handling, dust, and humidity by a hermetically sealed glass bubble on top of the case. Because the solar cells are exposed to aerodynamic heating of 300°F, a high-temperature adhesive and a heat sink have been incorporated in the design.

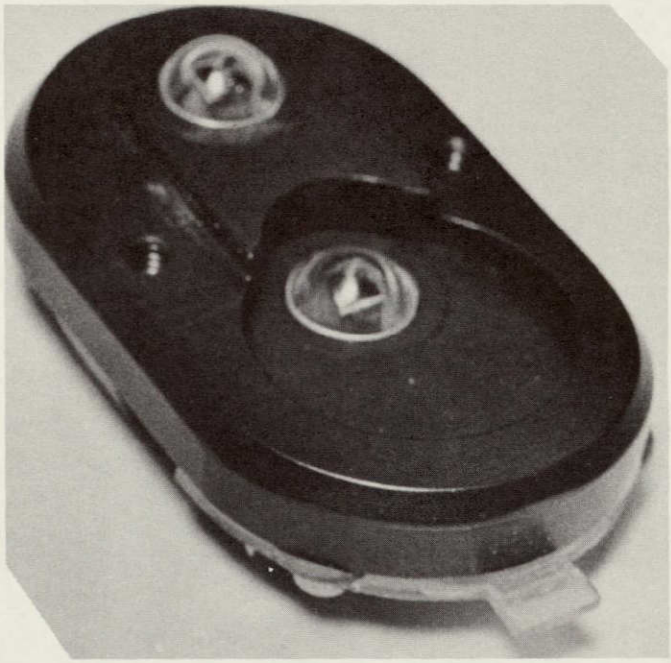

Fig. D-2 Coarse Sun Sensor (CSS)

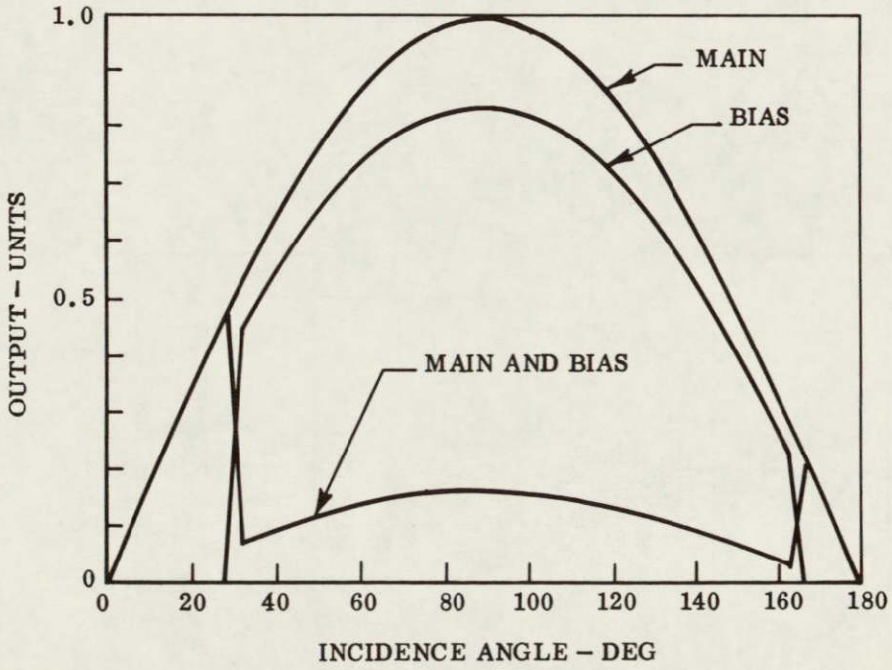

Fig. D-3 CSS Main, Bias, and Combined Cell Outputs

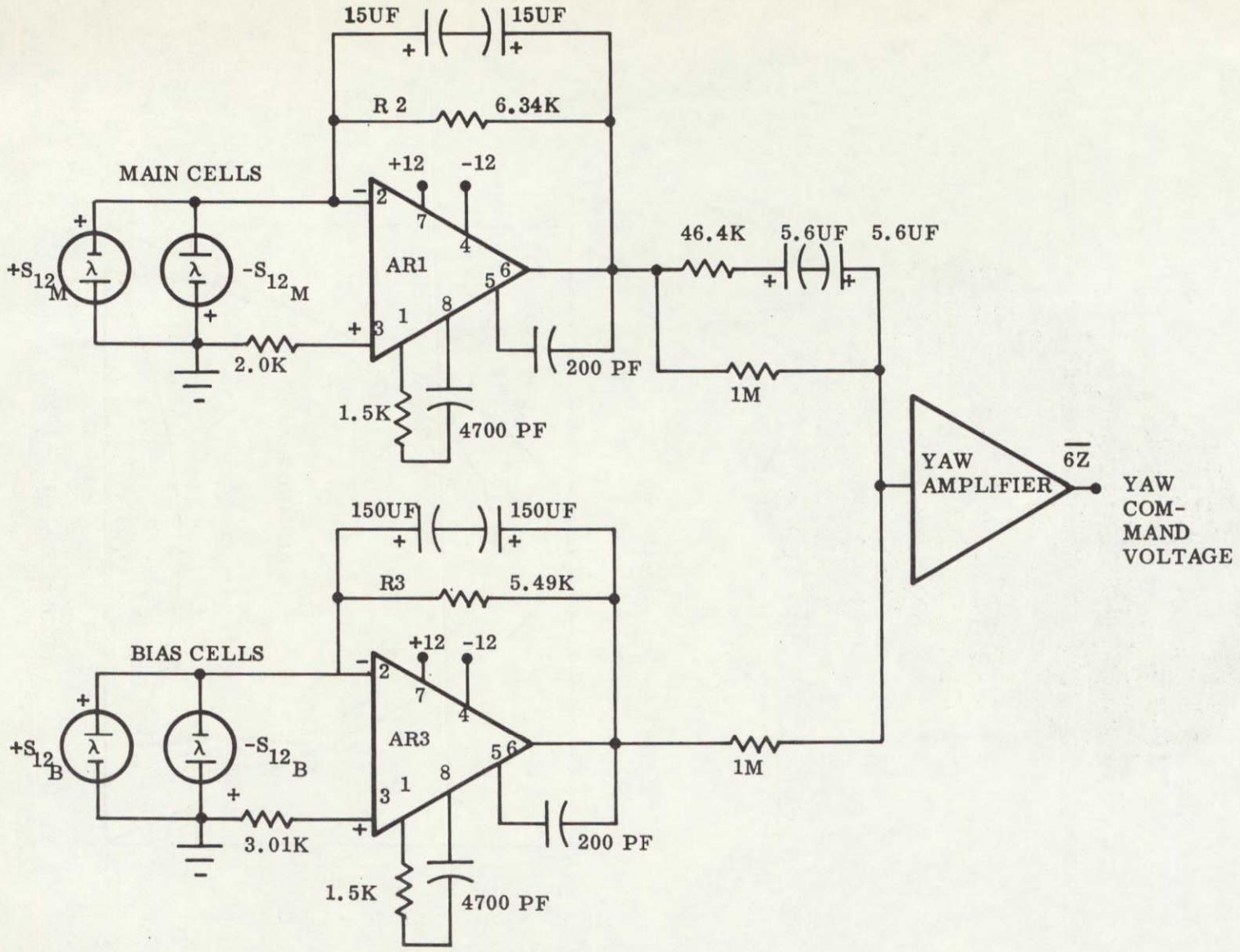

Fig. D-4 CSS Schematic (Yaw Channel)

The spectral response of silicon solar cells and the relative spectral distribution of radiation from the sun and a tungsten source are shown in Fig. D-6. These curves illustrate the problems associated with testing the solar cells with a tungsten light source, as compared to the flight environment where the solar energy is zero air mass. Since the sunlight and the tungsten spectral response is so different, some care must be used in comparing results where great precision is required. A good discussion of the problem is contained in Chapter 16 of Ref. 9.

The output current versus voltage for a typical solar cell is shown as follows:

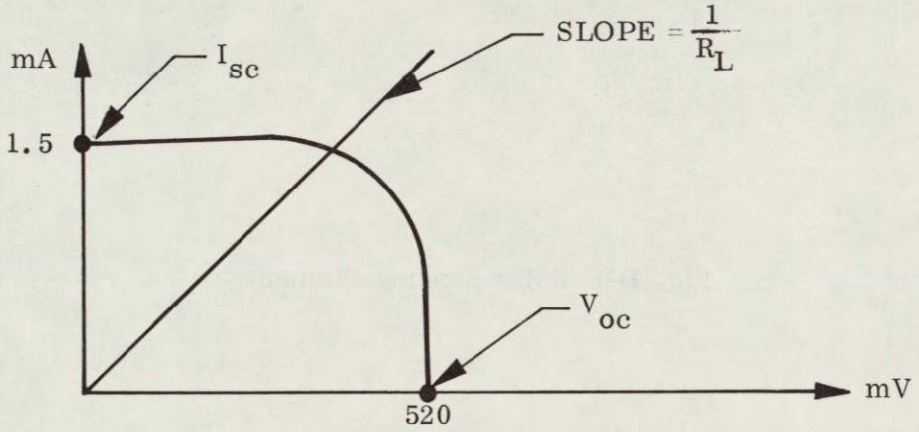

where

I_{sc} = short circuit current

V_{oc} = open circuit voltage

R_L = load resistance

The behavior of the cell depends upon the value of the load resistance, R_L . For large values of R_L, the cell operates as a voltage source (photovoltaic mode) and is highly temperature-sensitive. In this mode the output voltage is relatively independent of illumination, but it can vary ±20 percent over a temperature range of $-10^{o}C$ to $+70^{o}C$. For small values of R_L, the cell operates as a current source (photoconductive mode), with the current output proportional to the illumination. In this mode, which is used for the CSS, the output change with temperature is typically less than ±1.5 percent from $-10^{o}C$ to $+70^{o}C$.

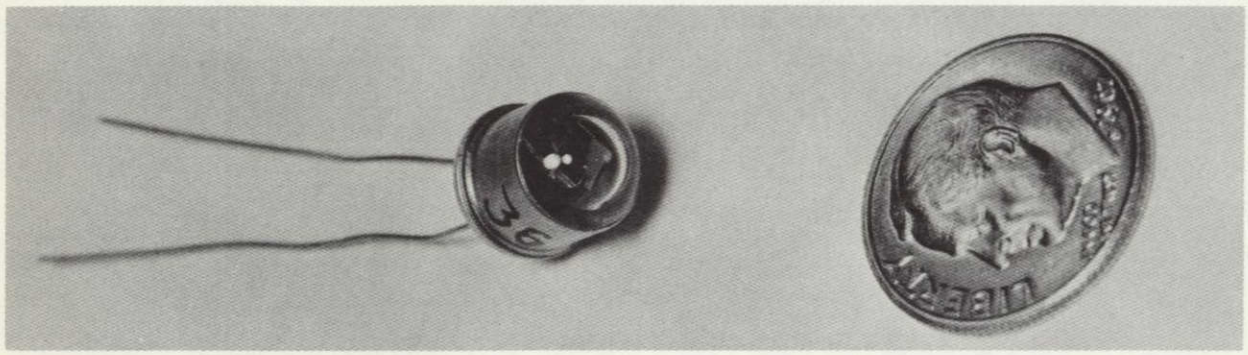

Fig. D-5 Solar Sensing Element

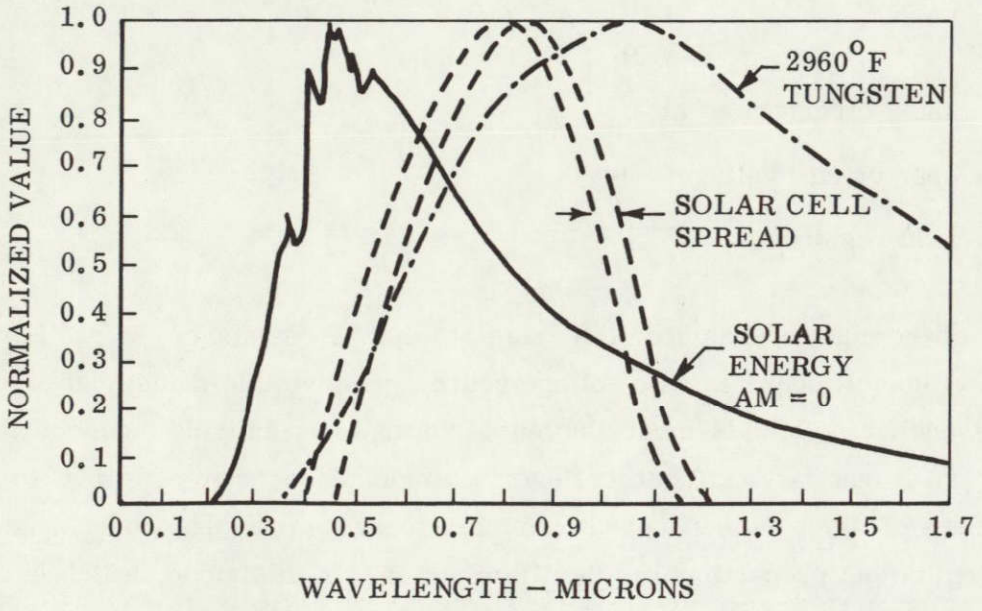

Fig. D-6 Solar Cells Spectral Response and Distribution

D.1.2 Signal Conditioning Amplifiers

The signal conditioning amplifiers (i.e., AR1 and AR3 shown in Fig. D-4) connected to the solar sensor elements are current amplifiers. They have very low input and output impedances. Their gain is $(I_s)\,R_f$, where I_s is the sensor short circuit current and R_f is the feedback resistor as shown below.

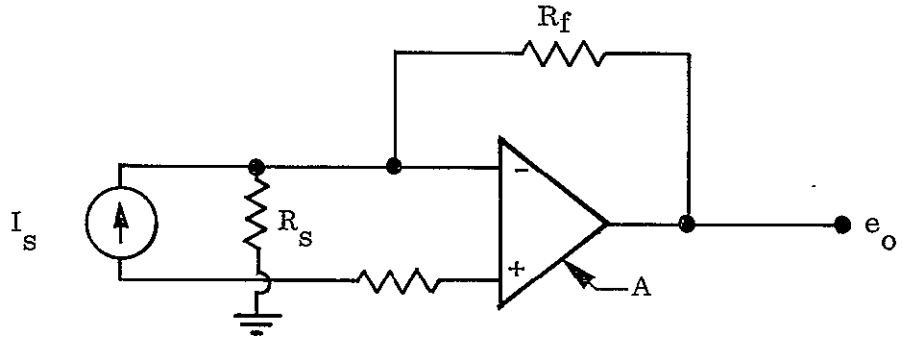

The resistance, R_s, is the equivalent solar cell source resistance. In order to maintain low offsets, the source resistances at the amplifier inputs were made equal by making $R = (R_s\,R_f)\,(R_s + R_f)$. The amplifier input impedance is approximately equal to R_f/A, where A is the amplifier open loop gain, and is typically less than 0.2 ohm since R_f is on the order of 6K ohms and A is typically 30K ohms.

D.1.3 Solar Cell Equivalent Circuit Analysis

The equivalent circuit for a solar cell is shown below.

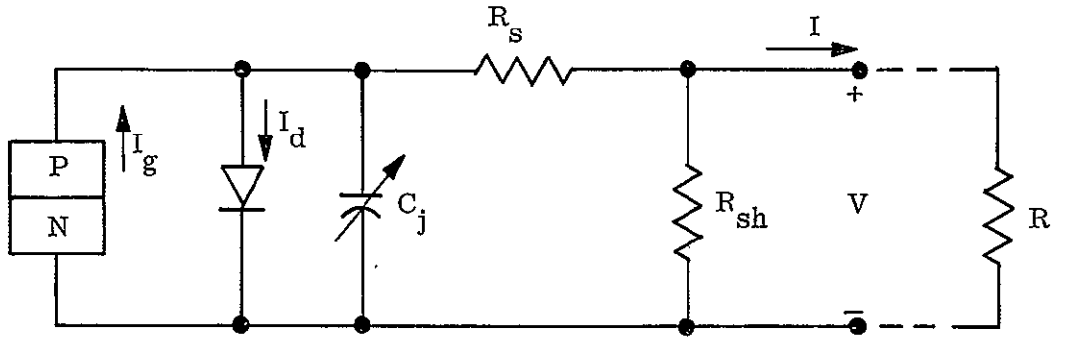

The steady-state descriptive equation is

$$I = I_g - I_o \left[\exp \frac{q(V + IR_s)}{ART} - 1 \right] - \frac{V}{R_{sh}}$$

where

I_g = light generated current

I_o = junction saturation current

I = device terminal current, 1 mA to 3 mA max

q = electron charge, 1.6×10^{-19} coulomb

k = Boltzmann constant, 1.38×10^{-23} joule/^{o}K

T = absolute temperature, 300^{o}K

V = device terminal voltage, 520 mV max

R_s = series resistance

R_{sh} = shunt resistance, 100K ohms minimum

R = external load resistance

A = an empirically derived constant, 1 to 2

C_j = junction capacitance

Thus the current into the load is a function of the voltage across the terminals. The equation consists of three terms describing the current delivered by the generator, i.e.:

$$I = I_g - (I_d + I_{sh}),$$

where

I_d = diode junction current $= I_o \left[\exp \frac{q(V + IR_s)}{ART} - 1 \right]$

I_{sh} = current through the shunt resistance $= \frac{V}{R_{sh}}$

If a current amplifier is used, V is approximately zero and the above equation reduces to

$$I = I_g - I_o \left(\exp \frac{qIR_s}{ART} - 1 \right)$$

For the following parameter values

$I = 1.5$ mA

$R_s = 200$ ohms

$A = 1$

$T = 300^{o}K$

the exponential term has the value

$$\exp \frac{qIR_s}{ART} = 1.0078$$

and consequently, the second term on the right in the above expression is negligible compared to the first. This demonstrates that for short circuit operation, the terminal current is directly proportional to the light generated current.

D.1.4 Angle of Incidence Analysis

The projected area of the solar cell in a plane perpendicular to the incoming light rays is proportional to the cosine of the angle of incidence, as illustrated on the following page.

As a consequence, the solar cell current output, which is proportional to the incident flux, is also proportional to $\cos \theta$ if reflected radiation is neglected.

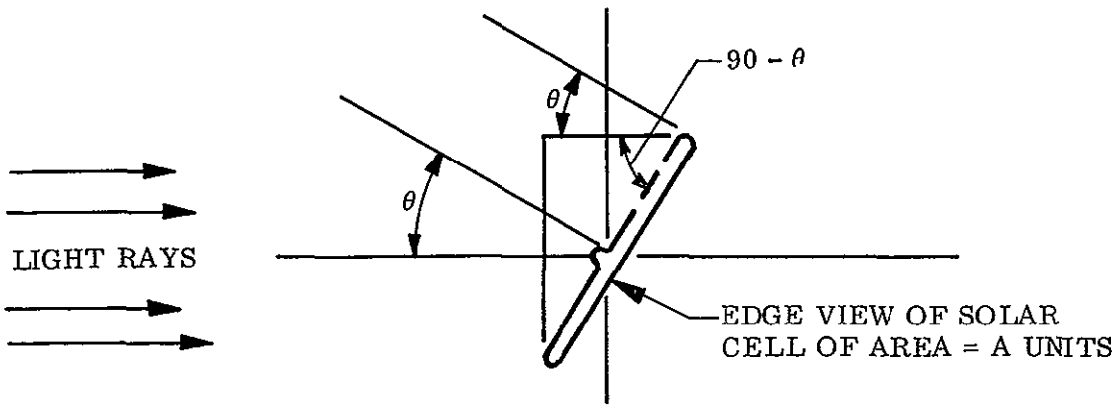

D.1.5 Error Analysis

The CSS output has errors associated with the signal conditioning amplifier and the solar cell. The error sources in the amplifier (see par. D.1.2) can be divided into five parts:

1. Computing accuracy
2. Part aging
3. Supply voltage change
4. Temperature change
5. Amplifier offset

Computing accuracy is defined as the error between the actual gain and the value calculated with the following approximate theoretical equation (see Ref. 10):

$$e_o = - i_s R_f \frac{1}{1+\frac{1}{A\beta}}$$

where

A = open loop voltage gain (μA709)

i_s = input current

R_f = feedback resistor

$\beta = 1 + \frac{R_f}{R_{in}}$.

R_{in} = shunt resistance at amplifier input

e_o = output voltage

The error due to the finite gain A can be ignored. The computing error is ±3.6 percent, due only to uncertainty in resistor R_f for a worst-on-worst environment.

Part aging is defined as the change in amplifier output due to permanent component change. The amplifier aging error is not given by the manufacturer and no data is readily available. Aging between a prelaunch calibration and launch can be estimated at 100 μV/day voltage offset and 5 nA current offset maximum (Ref. 10), and the amplifier output error can be found from the following equation (Ref. 10):

$$e_o = e_d \frac{(R_s + R_f)}{R_s} \pm i R_f$$

where

e_d = voltage drift

i_d = current drift

R_s = source resistance = 100K minimum

R_f = feedback resistance (= 6.34K for the main cells)

The maximum drift is less than ±120 μV per day calculated from the above expression. For a ±5-V range, the error is 0.0025 percent per day of full scale.

The supply voltage change error is defined as the ratio of the change in input offset voltage to the change in supply voltage producing it. This error is typically 25 μV/V with a maximum 150 μV/V for the μA709 amplifier. The supply voltage is 12 ± 0.12 V,

and the maximum offset is $150 \times 0.12 = 18\ \mu V$. The output is found from the above equation to be $18.5\ \mu V$, which is 0.37×10^{-3} percent of full scale.

The temperature change error is defined as the change in the output voltage due to the input temperature drift coefficient averaged over the temperature range of interest. For the μA709 amplifier, the input voltage offset versus temperature is typically $6\ \mu V/^{o}C$ and maximum $11\ \mu V/^{o}C$, while the input current offset versus temperature is typically $0.4\ nA/^{o}C$ and maximum $9\ nA/^{o}C$. These values can be converted into output drift using the above equation to yield a maximum drift of $41.2\ \mu V/^{o}C$. The temperature range of interest is from $25^{o}C$ to $66^{o}C$, and consequently the maximum output voltage change is 1.7 mV or 0.034 percent for full scale output.

The amplifier offset error is defined as the change in output voltage from zero with zero input voltage. For the μA709 amplifier, the input offset voltage is 5 mV maximum, and the input offset current is 200 nA maximum. The output offset of the amplifier circuit is ± 5.8 mV or 0.12 percent of full scale.

The sum of the signal conditioning amplifier errors discussed above is 3.8 percent worst-on-worst. The root sum of the squares (RSS) is close to 3.6 percent, since the resistor error is more than ten times the sum of the other errors.

Solar cell errors are due to:

1. Temperature change
2. Solar constant variation
3. Manufacturing variation
4. Angle of incidence response

The temperature change error is defined as the change in short circuit current over a specified temperature range. For a typical silicon solar cell, the change is less than 2 percent over the temperature range from $0^{o}C$ to $165^{o}C$ (see Fig. D-7). Reference 10, par. 3.4.2, restricts the variation to 20 percent between all cells and 10 percent between matched pairs.

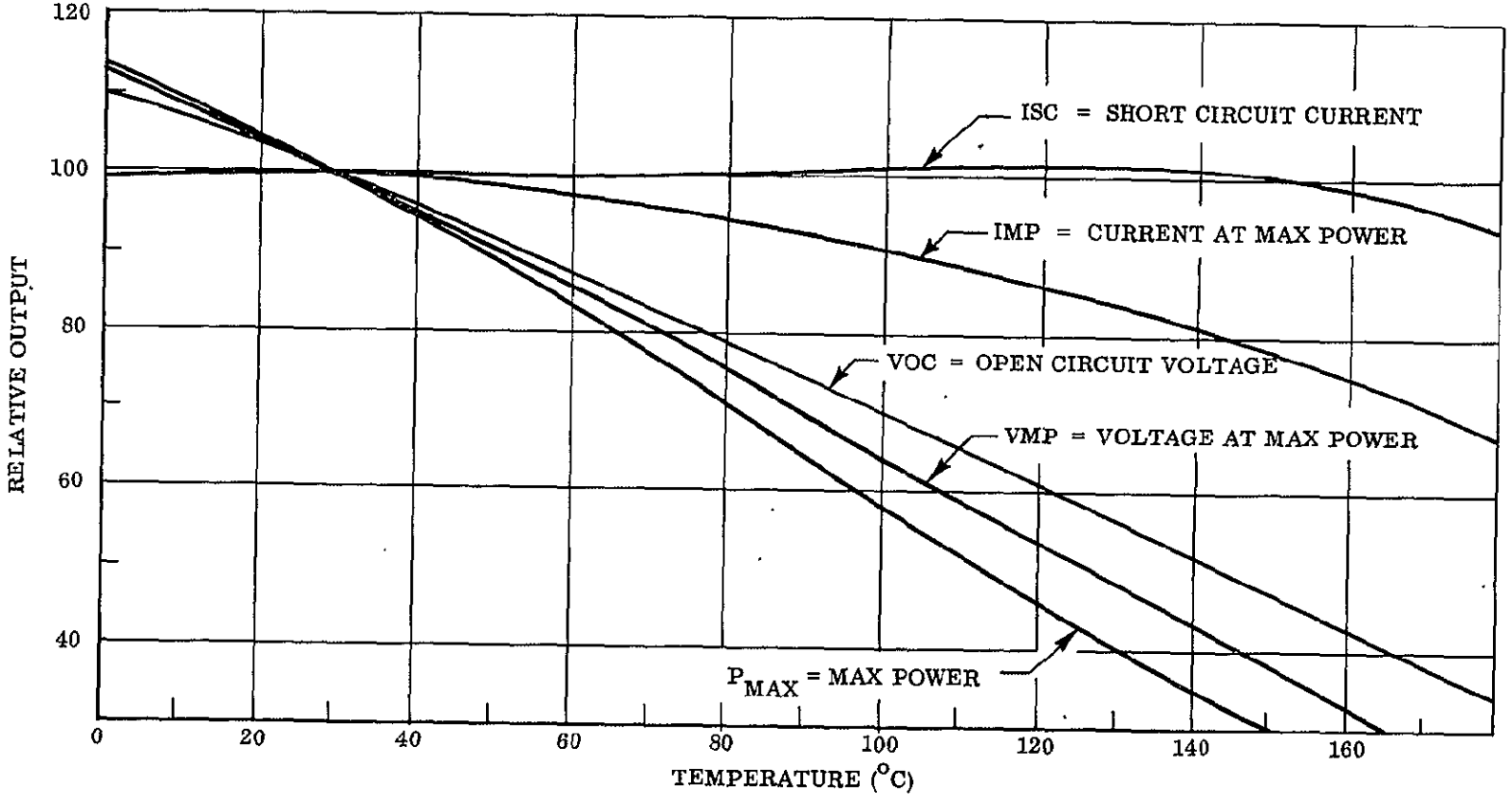

Fig. D-7 Temperature Characteristics of Hoffman N/P Soldered Ti-Ag Solar Cells

The solar constant has variations of ±3.5 percent because of the Earth's elliptical orbit and ±1.5 percent because of solar disturbances (Ref. 9).

The allowable manufacturing variation is controlled by the detail specification. The allowable variation in circuit current is 5 percent between all cells and 2 percent between matched pairs.

The short circuit current versus the angle of illumination incidence is controlled by the detail specification. For angles near 90 deg, which is the important operating point, the slope is controlled to ±15 percent for all cells and ±5 percent for matched pairs.

The sum of the solar cell errors discussed above is 17 percent worst-on-worst and 8.9 percent RSS for matched pairs. The combined solar cell and amplifier error is 20.8 percent worst-on-worst and 9.6 percent RSS.

D.1.6 Test Results

Temperature characteristics of Hoffman N/P solar cells are shown in Fig. D-7. The angle-of-incidence characteristics of the Hoffman N210CG-12 solar cell are shown in Fig. D-8. For angles of more than 70 deg, the output is seen to deviate significantly from a cos θ response. The angle-of-incidence characteristics for a Hoffman 55C cell are shown in Fig. D-9. Cells with three different surface conditions were tested: no cell cover (no lens), a clear cell cover (clear lens), and a sand-blasted cover (frosted lens). Note that the curves for the no lens and clear lens conditions show nearly the same response for small incidence angles, whereas the frosted lens has a response that is well below both of the other two.

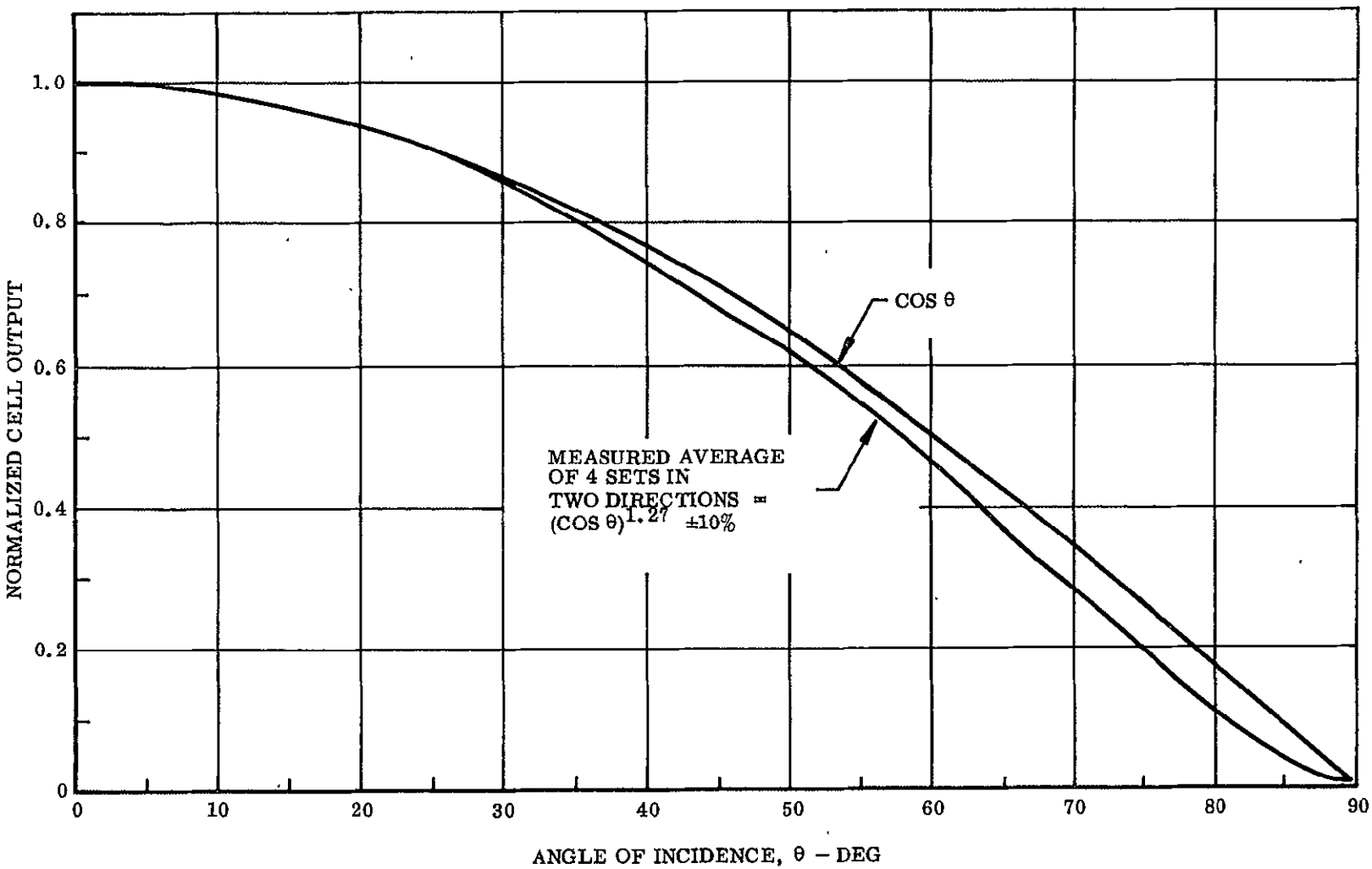

Fig. D-8 Angle of Incidence Characteristics Versus Desired Response for Hoffman N210CG-12 Solar Cells

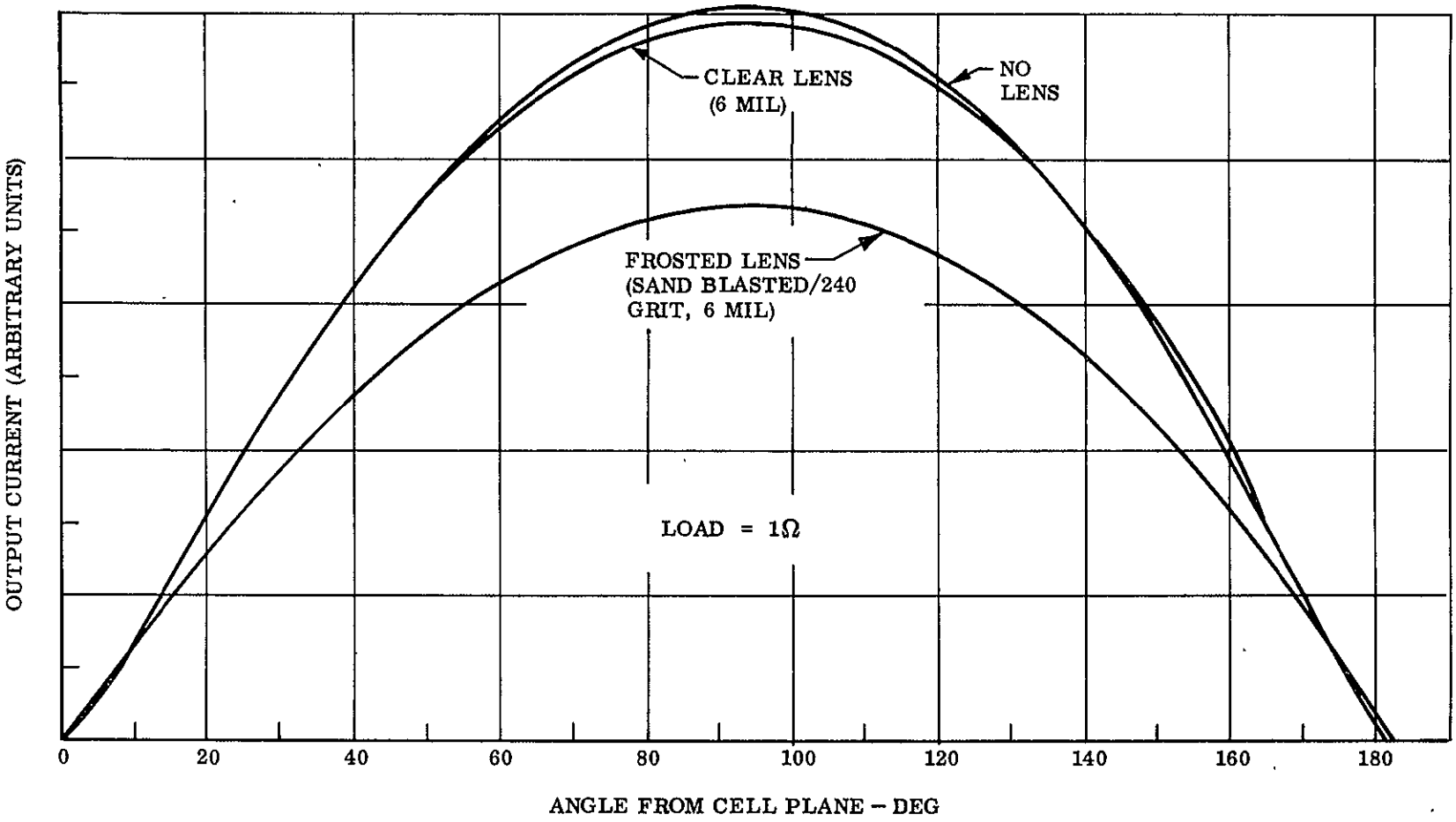

Fig. D-9 Angle of Incidence Characteristics Versus Output Current for Hoffman 55C Solar Cells

D.2 MODE SENSOR

The mode sensor, which consists of a single commercial photodiode, serves as a sun presence indicator for the Fine Sun Sensor (FSS) described in Appendix C. Its output characteristics are shown below as a function of the angle between the sun and the sensor axis.

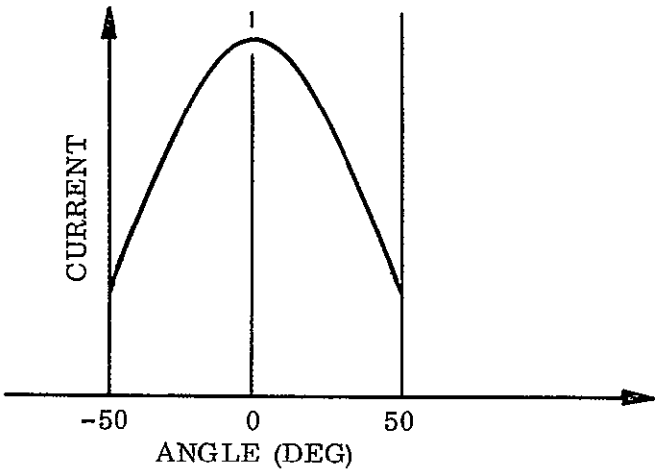

The mode sensor is mounted in the FSS at the base of a tube which restricts its field-of-view to approximately 10 deg about the center line (see Fig. C-1), and the normal to the mode cell is aligned with the FSS electrical null axis to within ±0.5 deg. It is operated as a current source, and its output is fed through a current amplifier to a mode switch logical network (discussed in par. D.4) to determine the time for switching from the coarse to the fine mode. Additional information on this sensor is provided in Appendix C, pars. C.2.4 and C.2.9.

D.3 MAGNETOMETERS

Two magnetometer sensors are used to establish the rocket's roll attitude with respect to the Earth's magnetic field. They are mounted on the Recovery Package structure to minimize the effect of payload magnetic components on the magnetometers. (The Recovery Package has been modified to eliminate magnetic components.) Provisions have been made for aligning the individual probe axes at right angles with the transverse vehicle axes.

The magnetometers are Type RAM-5 magnetic aspect sensors, manufactured by the Schonstedt Engineering Company. They incorporate the Schonstedt electronics package, which has the following performance characteristics:

Input Voltage	24 to 32 VDC
Input Current	11 mA
Range of Field	0 to ±9.6 oersteds
Sensitivity	0.004 VDC per millioersted
Stability of Sensitivity	±3% from 0^{o}F to ±165^{o}F
Null at Zero Field (biased at 2.4 VDC)	2.4 ±0.02 VDC
Operating Temperature Range	-50^{o}F to +185^{o}F (reduced accuracy)
Linearity	±3% of full scale
Output Impedance	Less than 20K ohms
Output Load	100K ohms
Weight	5 ounces

The Type RAM-5 magnetometer is the classical flux-gate type with a probe which consists of a permeable magnetic core surrounded by an excitation winding (primary) and a signal pickup winding (secondary). An alternating current is passed through the primary winding, producing an alternating magnetic field of sufficient strength to drive the core to saturation each half-cycle. If there is no external magnetic field acting on the core, the flux produced by the core will be identical in wave shape, but opposite in polarity, during the positive and negative half-cycles. However, if an external field exists having a component in line with the longitudinal axis of the core, the flux produced by the core is no longer symmetrical and contains even-order harmonics of which the second is the largest. The signal pickup winding is sensitive to the even harmonic flux but insensitive to odd harmonic flux. The output signal is detected from the second harmonic which is proportional to the component of the external field in line with the longitudinal axis of the core, as shown in the following sketch.

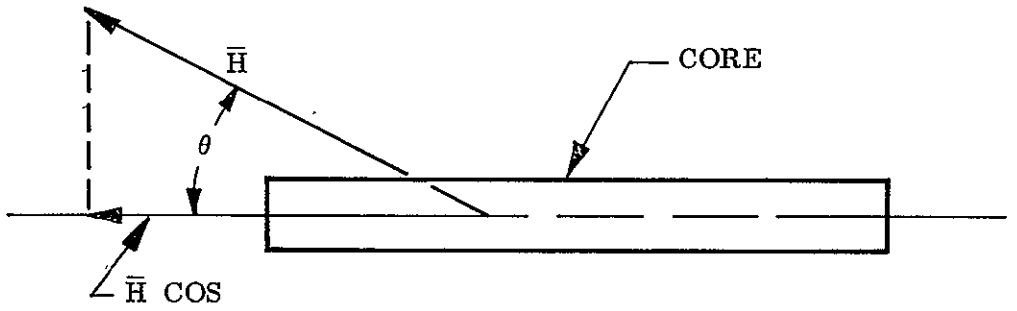

The voltage output of the magnetometer circuit is given by

$$E = KH \cos \theta$$

where

H = magnetic field intensity
θ = angle between field direction and input axis of probe
K = proportionality constant
E = voltage

D.4 SWITCHING SIGNAL CIRCUITS

The switching signal circuits produce signals that activate field effect transistor (FET) switches which perform the following functions:

1. Switch between the coarse and fine sensor circuits
2. Modify the fine mode forward loop electrical gain
3. Modify the thruster chamber pressure (i.e., thrust level)

The sequence and magnitude of these changes in mode and gain have varied during the various stages of development of the SPARCS vehicle; however, these changes have always been produced by two switching signals designated F and G. For SPARCS I, two additional switching signals, designated G′ and G″, were defined as time delayed

versions of G. The mode changes caused by the F and G switching signals are shown in Fig. D-10 for SPARCS 0 and I. The delay between the switch to low thrust and to high FSS gain in both systems is to allow the control gas trapped in the valve lines to be reduced to the low thrust level prior to switching to high gain.

D.4.1 F Switch Signal

The polarity of the F signal switches when the sun has been constantly in the mode sensor's field-of-view for a specified length of time (6 sec for SPARCS 0, 5 sec for SPARCS I). The input to the F switch (see Fig. D-11) is provided by the mode sensor. For SPARCS 0 systems, an additinal input from the roll rate signal (ω_x) is used to inhibit an F switch prior to despin by preventing the mode signal (if present) from charging the 10-μf capacitor. The ω_x input was deleted from SPARCS I because the F switch does not cause switching to low pressure, as in SPARCS 0. A switch to low pressure prior to completion of despin would be detrimental to sun acquisition.

A 6-V holding signal is imposed on the positive input terminal of the differential amplifier (MC 1519) which saturates the $\overline{F}$ and F outputs at +12 V and -12 V, respectively, without a mode switch input. A source follower unit gain amplifier (not shown in Fig. D-11) is used on the negative MC 1519 input signal to match the impedance of this signal to the amplifier.

When the sun enters the field-of-view of the mode sensor, the 10 μf capacitor begins to charge through an 8-sec delay network until the amplifier negative input signal voltage exceeds the 6-V holding signal by 0.5 V. At this time the amplifier quickly saturates in the opposite sense, making the output signals $\overline{F}$ and F equal to -12 V and +12 V, respectively. Should the sun pass out of the field-of-view of the mode sensor, the 10 μf capacitor is allowed to rapidly discharge through the diode across the 6.4K resistor, thus causing the $\overline{F}$ and F switching signals to return to their original polarities.

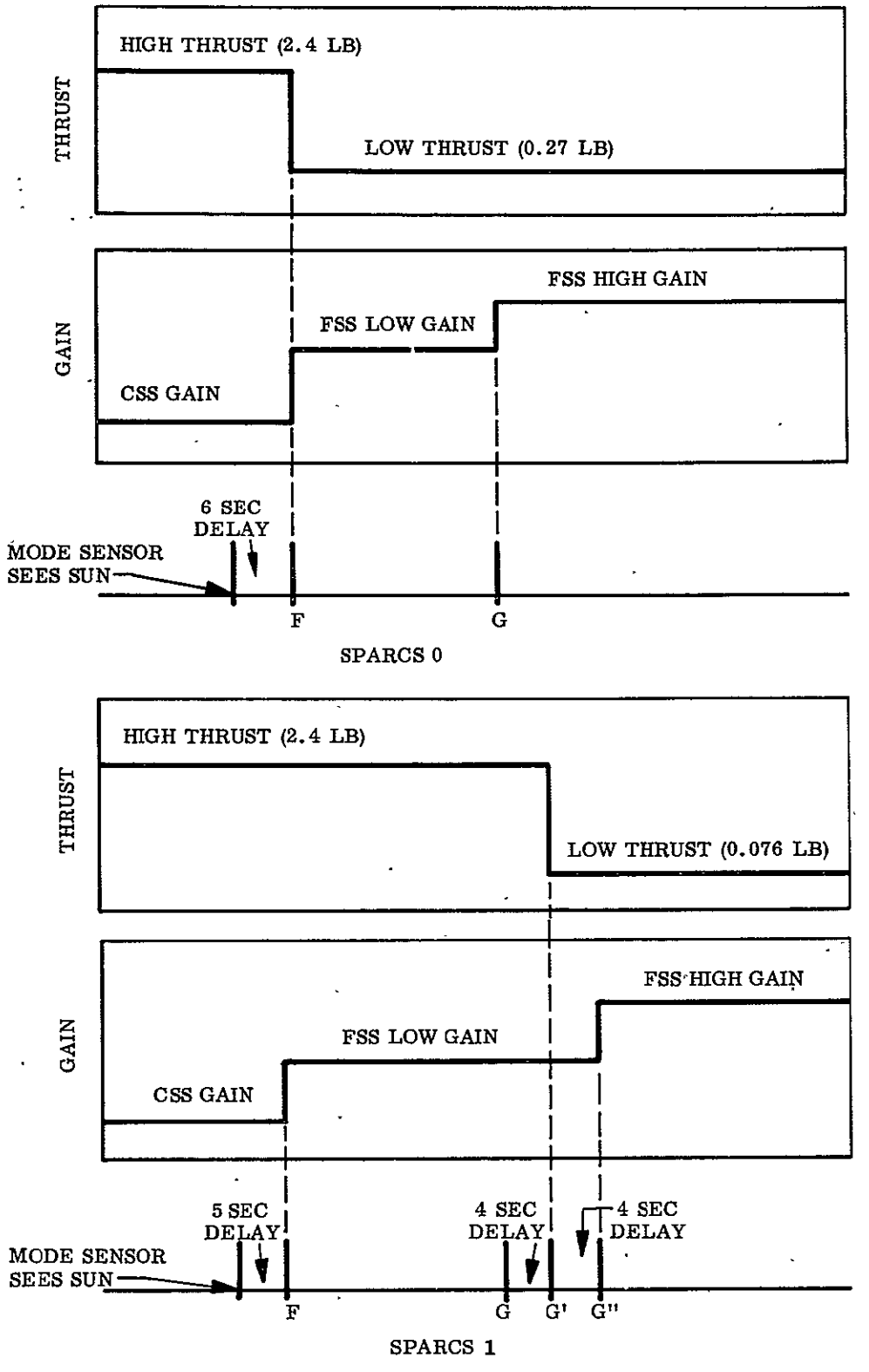

Fig. D-10 Mode, Gain, and Thrust Changes Caused by F and G Signals

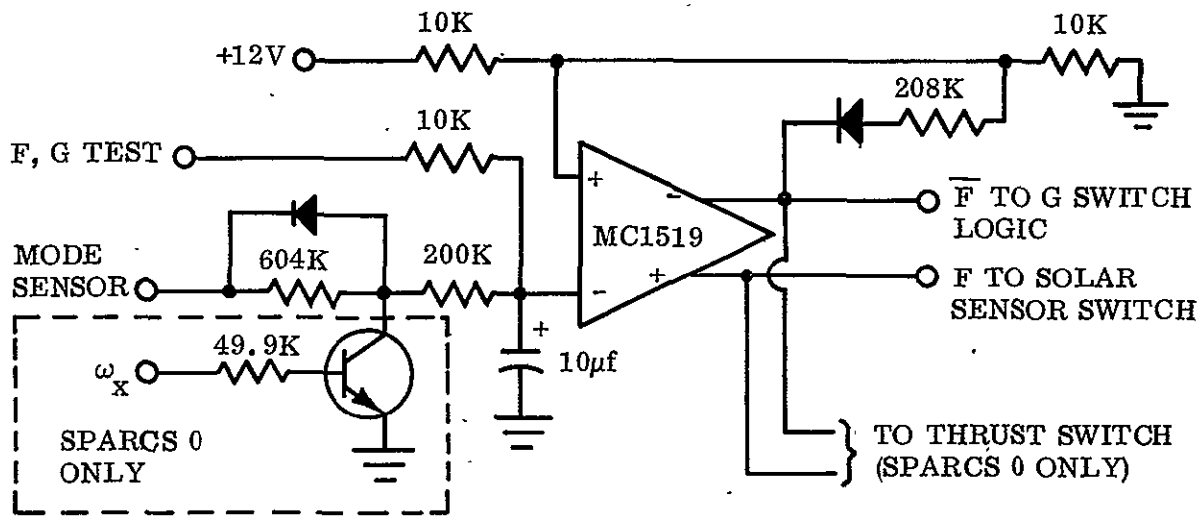

Fig. D-11 F Switch Schematic

D.4.2 G Switch Signal

Both SPARCS 0 and SPARCS I require a G switch signal as the final step prior to fine pointing. As a result of the G switch, the pitch/yaw loop gain and the thrust level are set for good fine pointing performance. For G to occur, two conditions must be satisfied:

1. $\overline{F} \leq 0.5$ V, indicating that the F switch has occurred
2. $S_{12f} + S_{13f} \leq 0.5$ V, indicating that the FSS is pointed to within 400 arc sec of the radiometric center of the sun

Conditions 1 and 2 must both be met because an erroneous null state could occur when the sun is outside the FSS field-of-view (this condition is sensed by $\overline{F}$ and F). This logical "AND" test is performed by the G switch logic circuit (Fig. D-12). When these conditions are met, a 6-V signal is applied to pin 8 of differential amplifier AR3, which overrides a + 4-V holding signal placed on pin 4 and causing the output signals

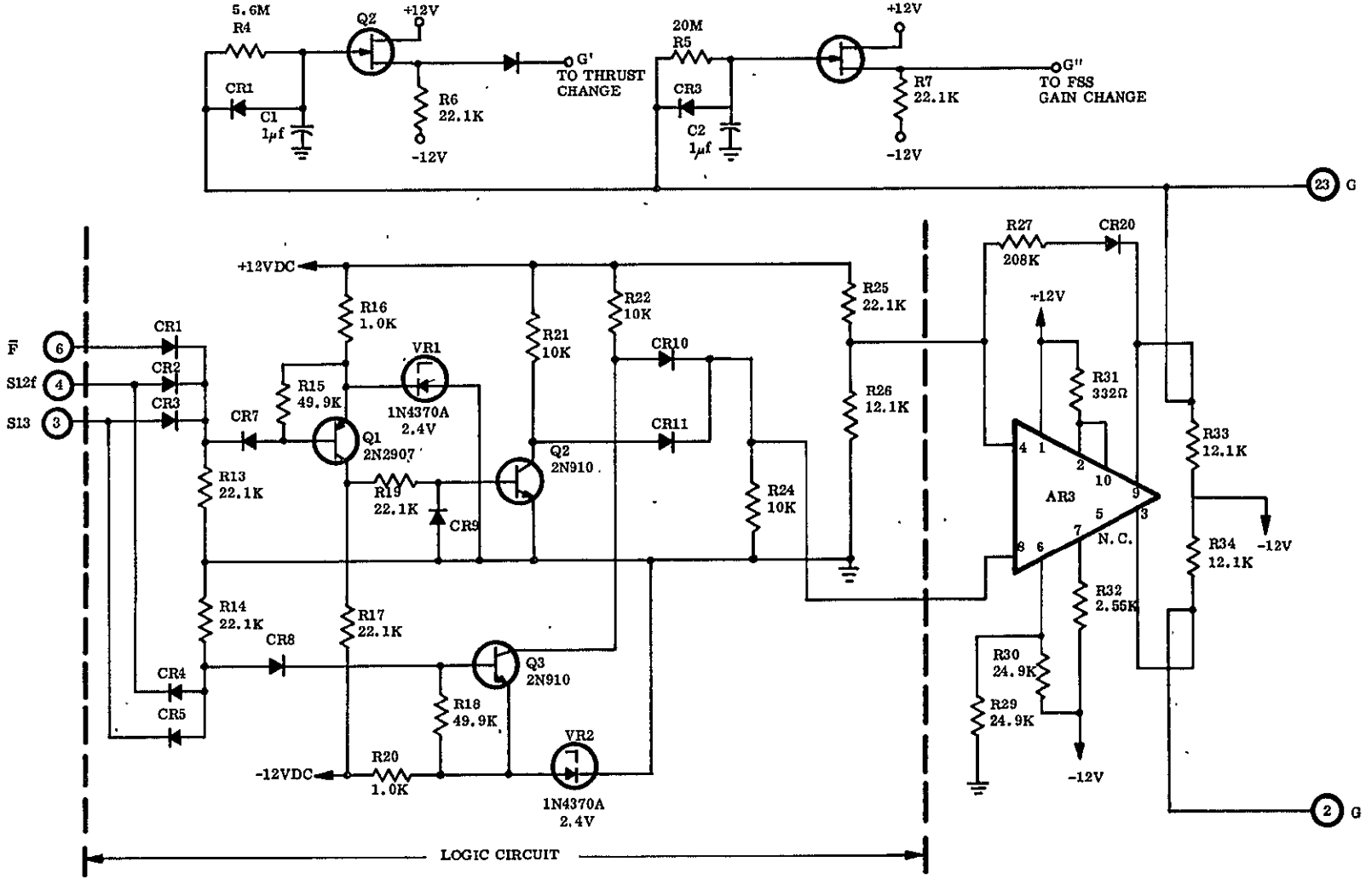

Fig. D-12 G Switch Schematic

(pins 9 and 3) to change polarity and saturate. Thus the $\bar{G}$ and G signals change polarity at this time. Should either condition 1 or condition 2 not be satisfied after $\bar{G}$ and G change state, the logic circuit removes the 6-V signal from pin 8 causing the outputs of AR3 ($\bar{G}$ and G) to revert to their original polarities.

In SPARCS 0, G is used to increase the gain of the FSS pitch/yaw channels for fine pointing.

In SPARCS I, G is used to trigger two delay circuits. G' follows G by 4 sec and G'' by 8 sec. At G', the valve pressure is lowered to the fine pointing level and the system enters a coarse limit cycle of approximately ±3 arc min. At G'', the FSS pitch/yaw gain is increased for arc-second fine pointing. Since in SPARCS I the low thrust level was significantly less than SPARCS 0, the switch to low thrust had to be delayed until SPARCS was near the fine pointing null. This occurs at G' when the system is in the coarse limit cycle.

D.5 PITCH AND YAW SCAN CIRCUITS

The pitch and yaw scan circuits allow the experimentor to scan the face of the sun at a preset rate and amplitude. The scan motion consists of a simultaneous oscillatory pitching and yawing of the vehicle from the null pointing direction. Figure D-13 depicts the scan motion on a plane containing the projected image of the sun. The maximum scan parameters are given below; these maximums are adjustable to zero in either axis.

	Maximum Displacement	Maximum Rate	Time for One Traverse of the Sun
Pitch	±650 arc sec	350 arc sec/sec	36 sec
Yaw	±650 arc sec	18 arc sec/sec	77 sec

The pitch and yaw scan circuits are identical, expect that resistor RG in the yaw circuit has a value of 1 MΩ to provide a lower range of selectable yaw scan frequencies.

The pitch scan amplifier is shown schematically in Fig. D-14. It consists of a square-wave oscillator (AR1 and its associated circuitry) which drives an integrator (AR2). The output of the integrator consists of a triangular wave train which is fed back to the oscillator to govern its frequency. The rate and output amplitude of the integrator may be adjusted with two separate potentiometers (R9 and R15, respectively) at the input terminal of the integrator. The scan amplifier is initially disabled with N channel FETs Q2A and Q2B. When scan operation is desired, a negative 12 VDC is applied to the gate of Q2A and Q2B, ungrounding the output. This turns off Q2A and Q2B and allows the scan signal to pass to the pitch amplifier. The FET Q2A controls oscillator turn-on and turn-off, whereas Q2B shorts the output signal of the scan element.

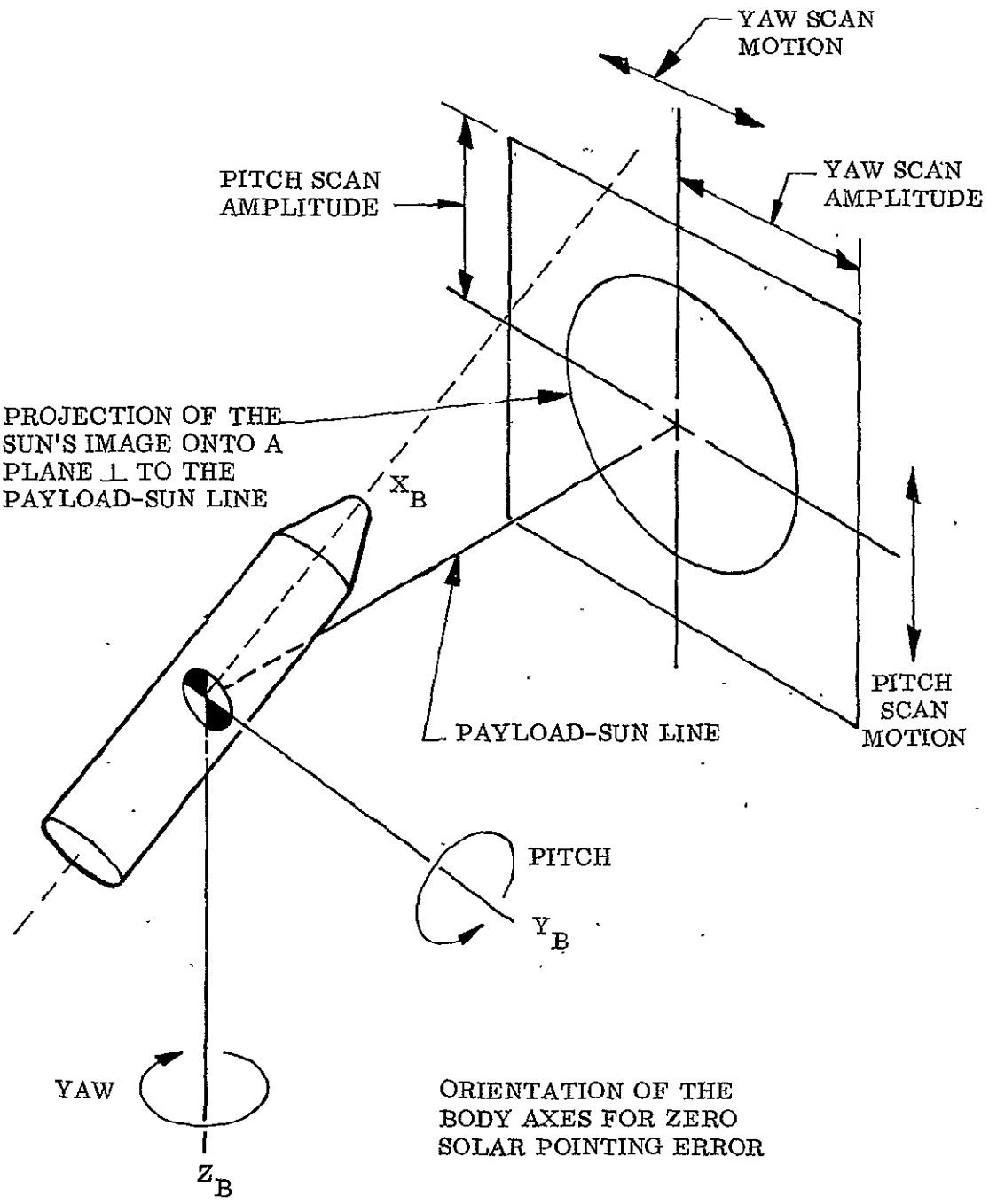

Fig. D-13 Pitch-Yaw Scan Motion

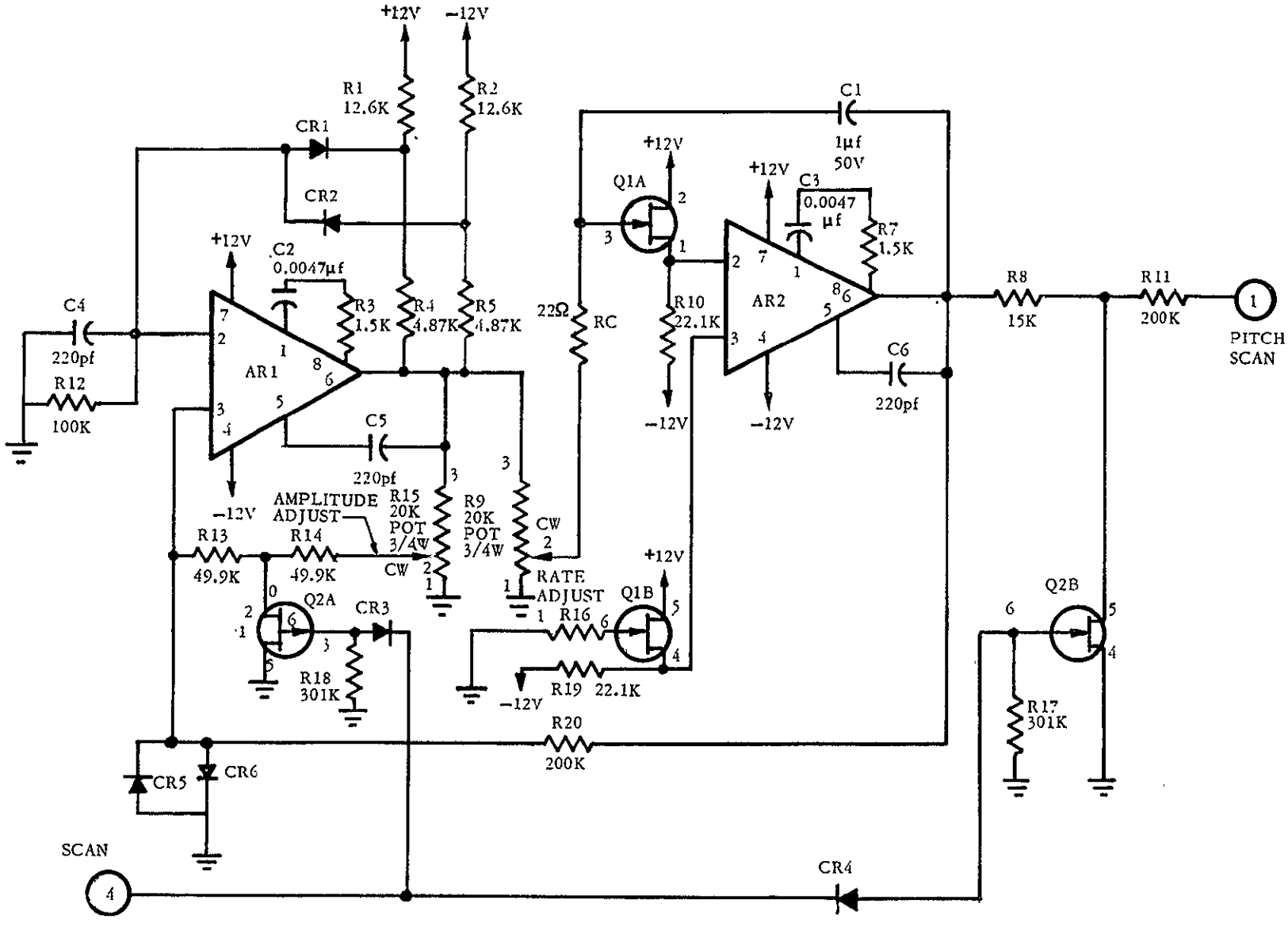

Fig. D-14 Pitch Scan Amplifier Schematic

D.6 PITCH AND YAW CHANNEL AMPLIFIERS

The yaw amplifier has five signal inputs and two control inputs, as shown in Fig. D-15. Inputs are from the FSS circuit (S_{12_f}), the CSS main and bias cell circuits (S_{12_m} and S_{12_B}), the yaw scan circuit, and the pitch rate compensation circuit ($\dot{S}_{13_n}$). These signals are controlled by the F and G control signals. The double FET switch determines which of these signals are connected to the input of the yaw channel amplifier. When no signal or a positive signal is applied to the switch gate, the switch is in the closed position. A negative signal opens the switch. The control values of the F and G signals are as follows:

	Original State	Switched State
F	-12 V	+12 V
$\overline{F}$	+12 V	-12 V
G	-12 V	+12 V
$\overline{G}$	+12 V	-12 V

All of the signal inputs have been defined in circuit discussions in previous sections, except the pitch rate compensation signal ($\dot{S}_{13_n}$). The circuit which produces this signal is shown in Fig. D-16. This circuit has a nonzero output only when $\omega_x \neq 0$. For a zero spin rate signal, both forward paths from S_{13_n} are grounded. A positive ω_x signal ungrounds the lower path which bypasses the high gain amplifier, and a negative signal ungrounds the upper path. Thus the compensation depends on the sense of the roll rate signal ω_x.

The sequence of events for the yaw amplifier is as follows. While in the coarse mode, $\overline{F}$ is +12 V and G is -12 V; thus S_{12_f} is grounded and the signals S_{12_B}, S_{12}, and yaw scan are connected to the amplifier input (the yaw scan signal should not be commanded until the fine mode has been achieved). After $\overline{F}$ changes state (but before G does), S_{12_B} and S_{12} are disconnected by switch No. 1, and S_{12_f} is ungrounded by the opening of switch No. 3. The impedance of the S_{12_f} signal path for this condition is shown below.

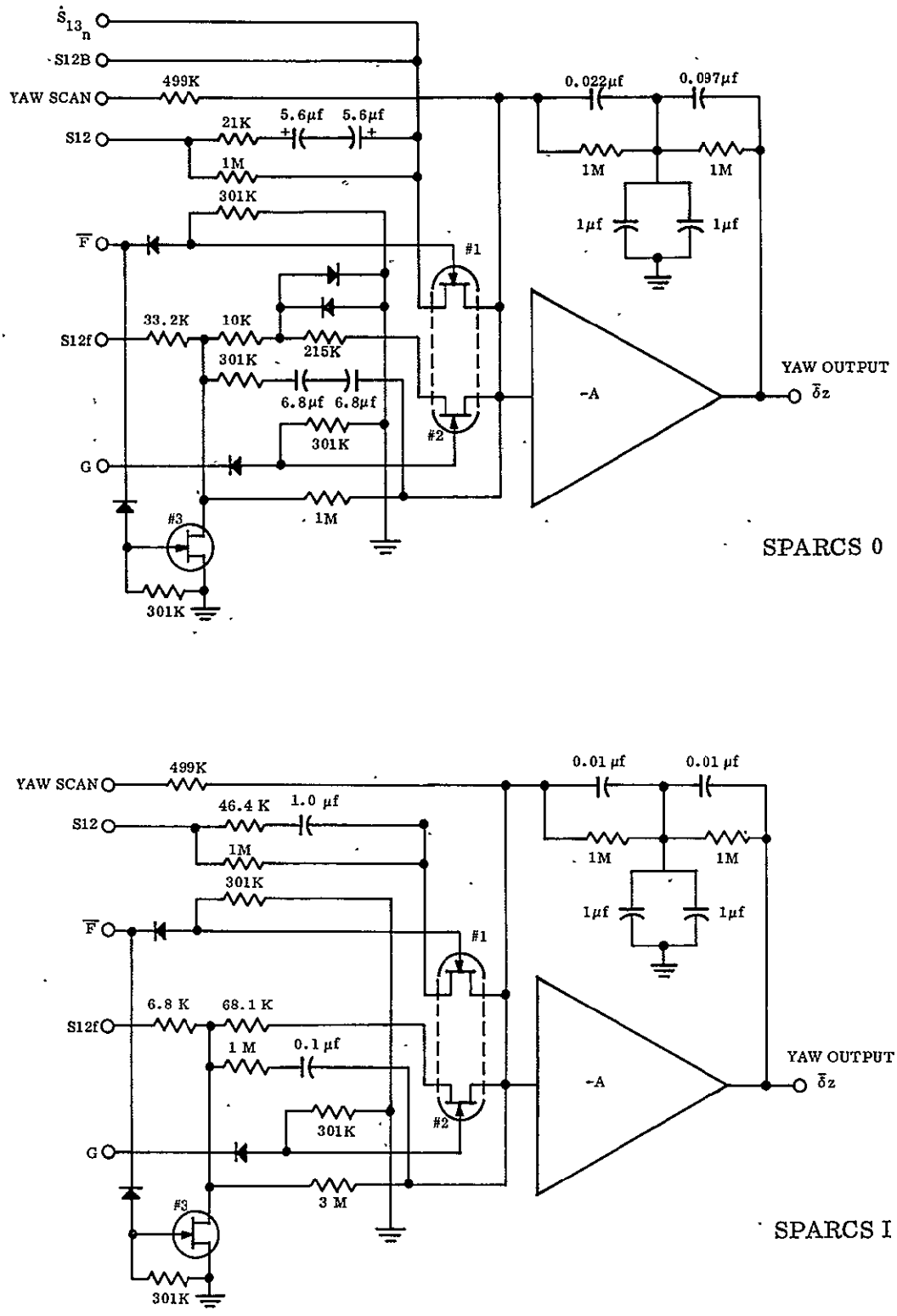

Fig. D-15 Yaw Amplifier Schematic

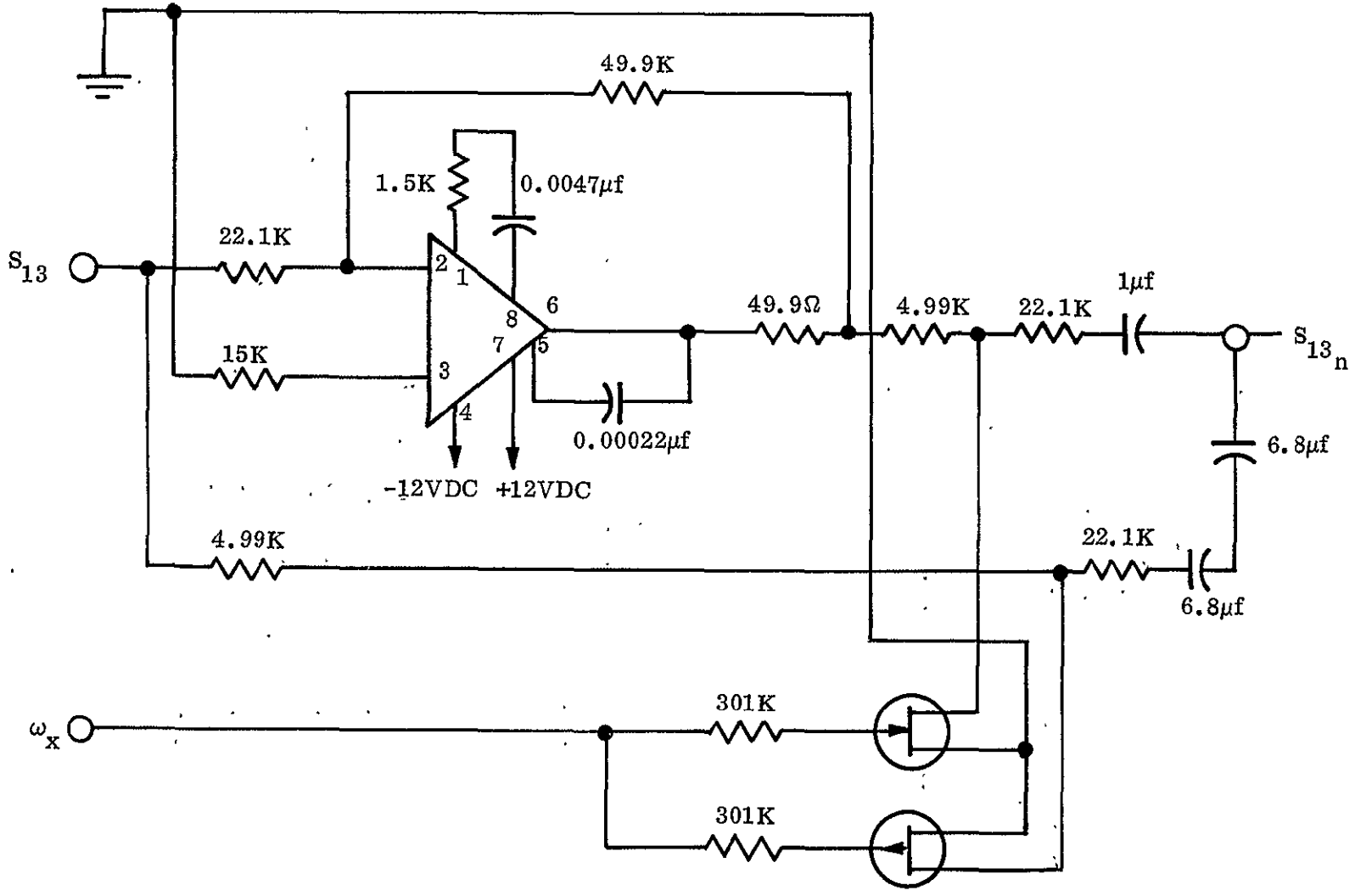

Fig. D-16 SPARCS 0 Pitch Rate Compensation Network for Yaw Channel

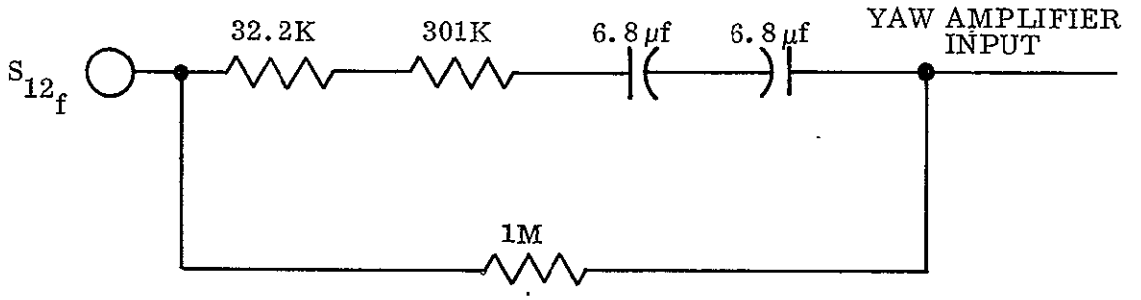

When G changes state to +12 V, switch No. 2 closes giving the following impedance to the S_{12_f} network.

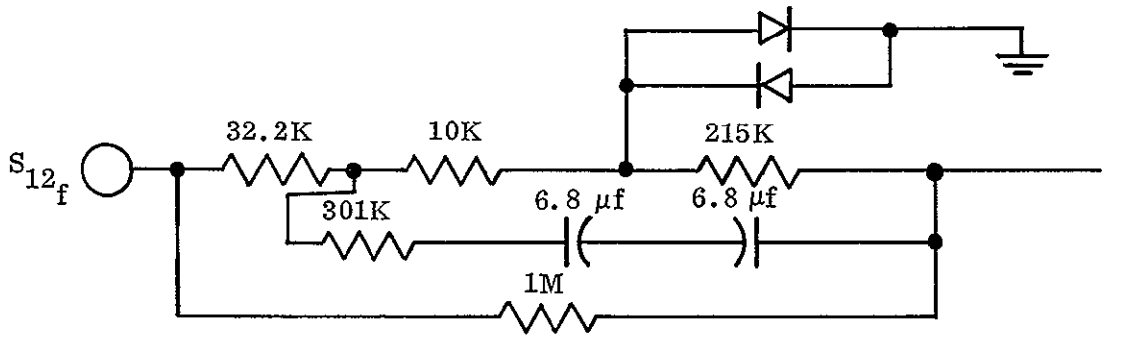

The fine mode high gain circuit is voltage-limited by the two diode paths connecting ground. Whenever the signal between the 10K and the 215K resistor exceeds ±0.5 V one of the diodes will break down, grounding the circuit.

The transfer functions between each of the primary control signal inputs and the yaw channel output were determined. Plots of yaw channel gain versus frequency for the scan, main cell coarse, and fine mode large and small signal inputs are shown in Fig. D-17; the corresponding phase versus frequency plots are presented in Fig. D-18.

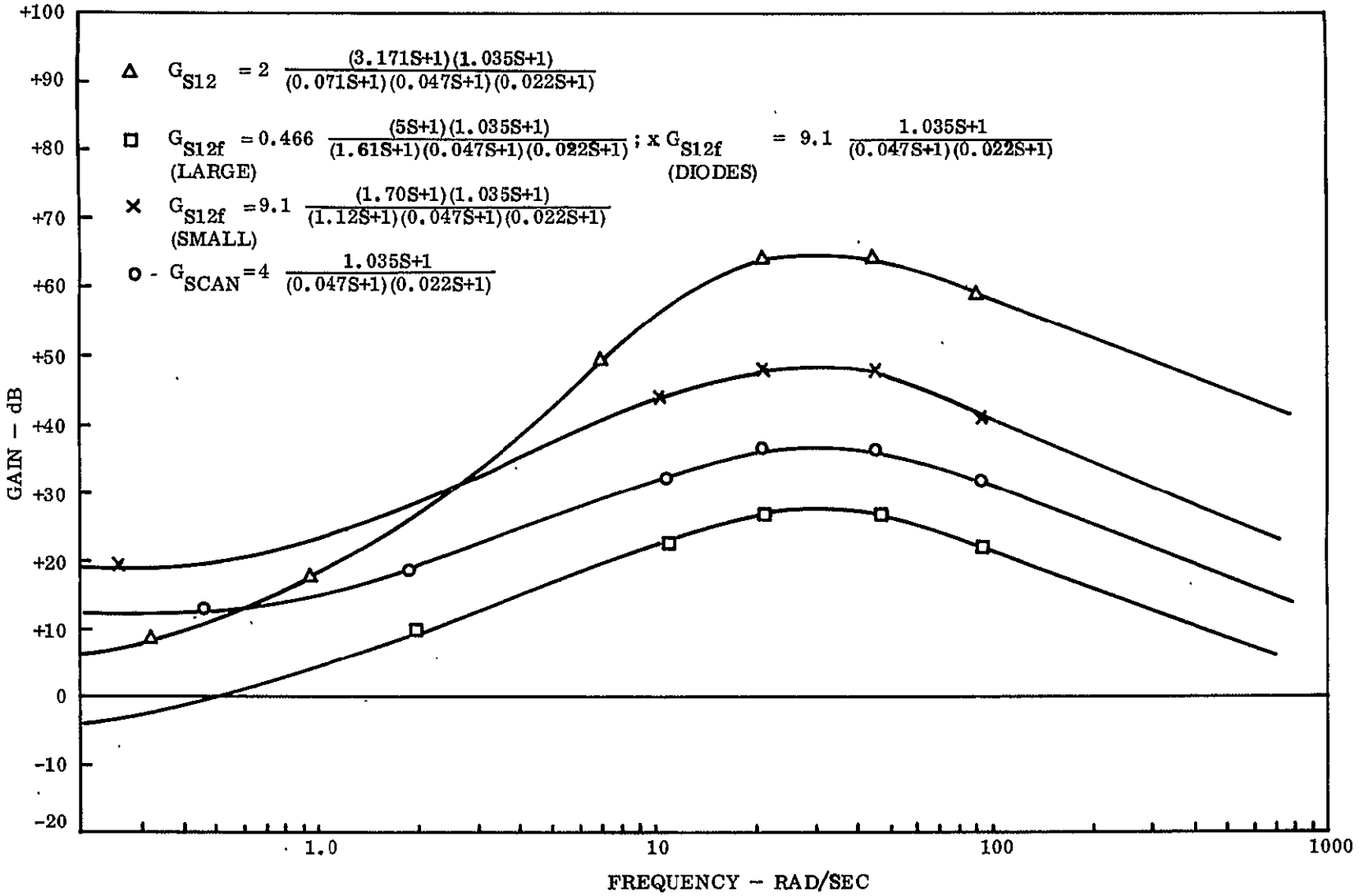

Fig. D-17 SPARCS I Yaw Amplifier Frequency Response – Gain Versus Frequency

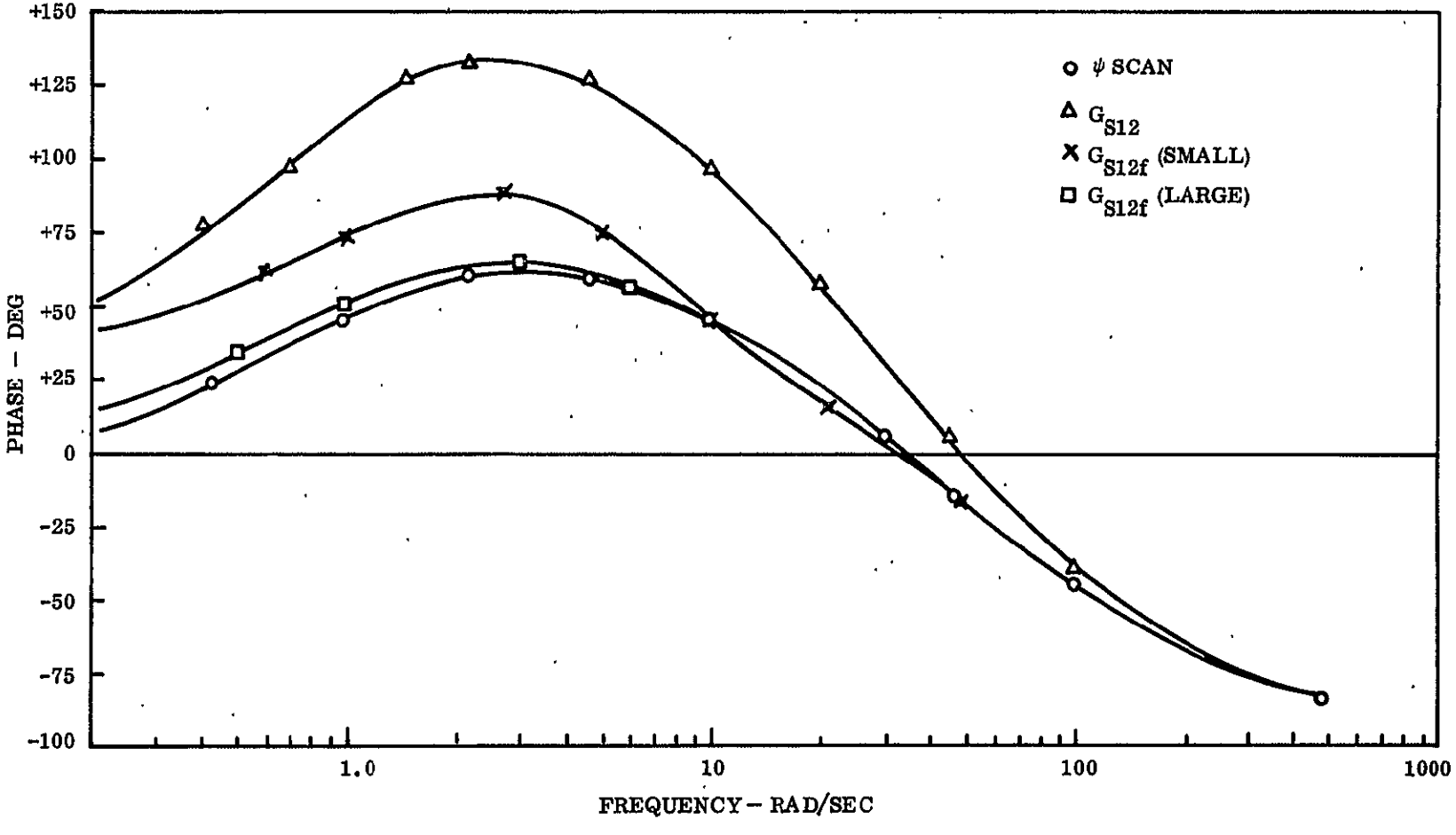

Fig. D-18 SPARCS I Yaw Amplifier Frequency Response – Phase Versus Frequency

The pitch amplifier circuit, shown schematically in Fig. D-19, is identical to the yaw amplifier circuit except for the value of one resistor in the coarse mode main cell circuit (S_{13}) and one capacitor in the amplifier feedback impedance network. Also, no yaw rate compensation network is used during despin.

Gain versus frequency plots for the pitch channel for scan, main cell coarse, and fine sun sensor inputs are presented in Fig. D-20; the corresponding phase versus frequency plots are presented in Fig. D-21.

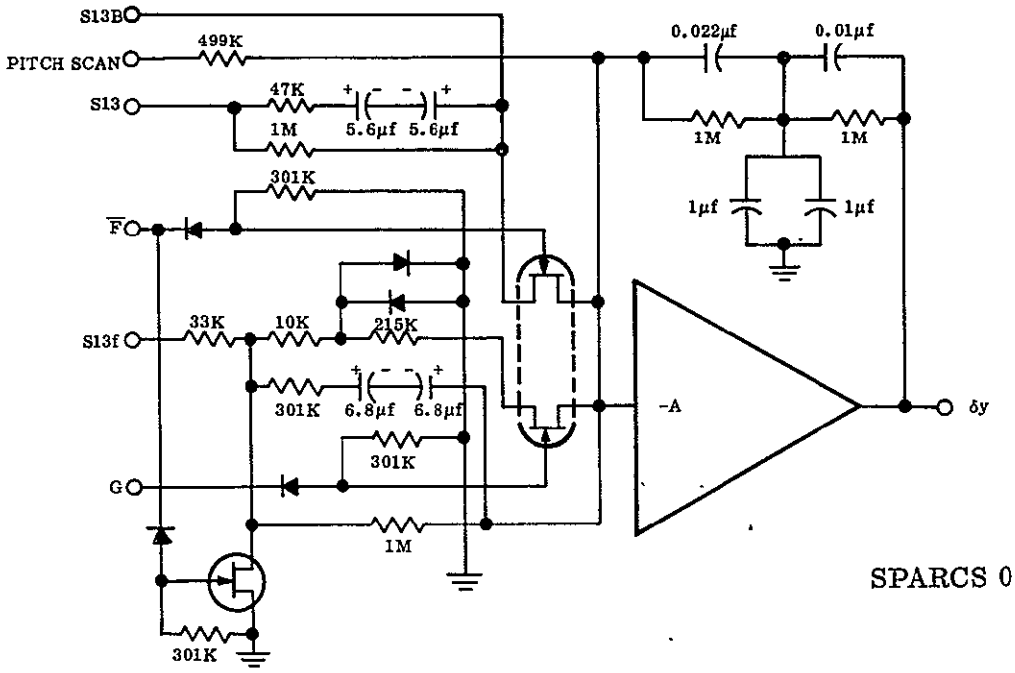

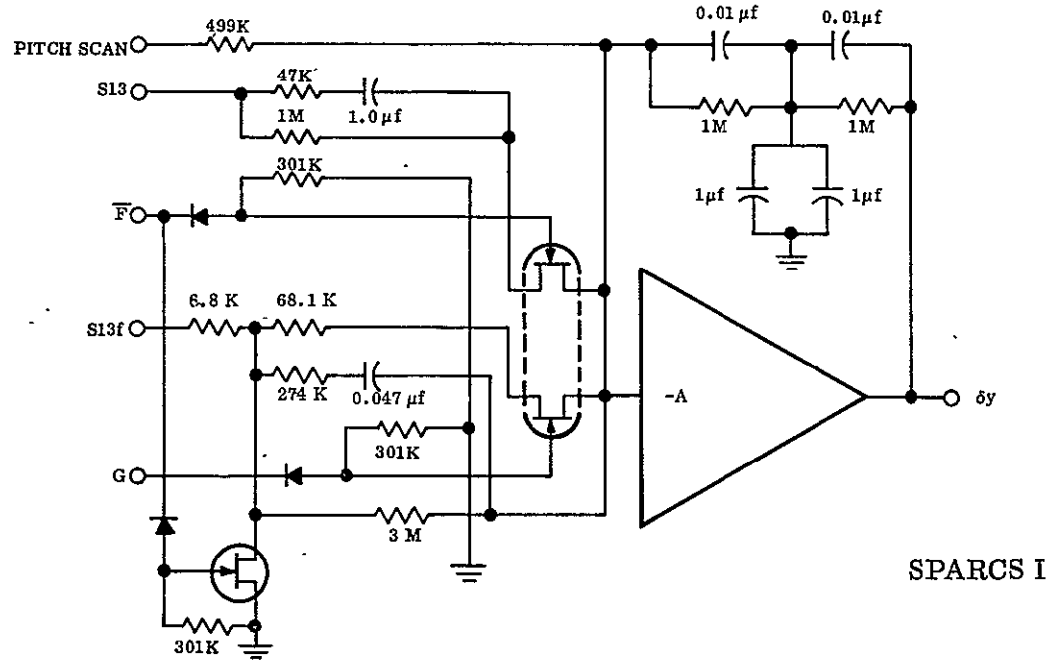

Fig. D-19 Pitch Amplifier Schematic

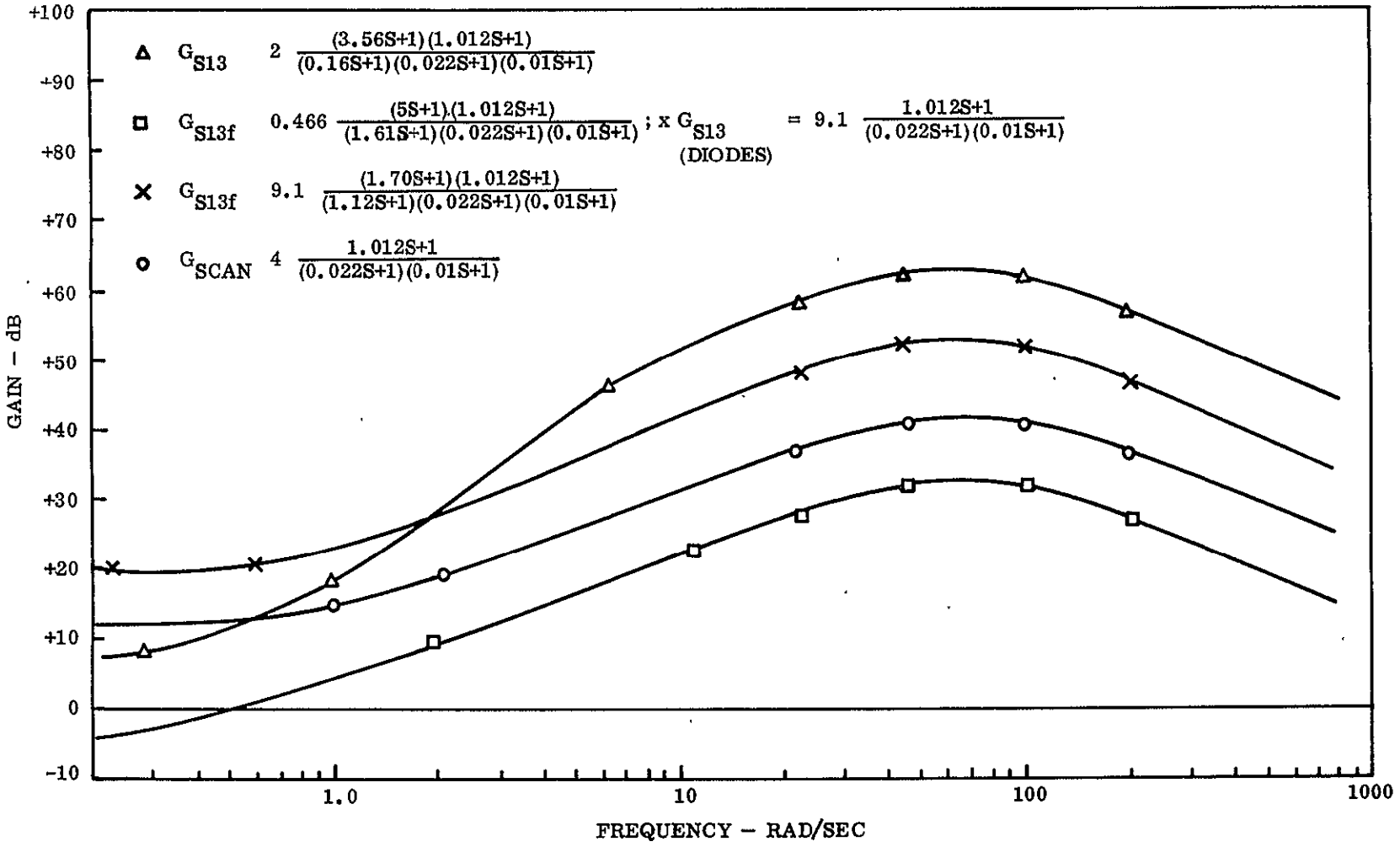

Fig. D-20 SPARCS I Pitch Amplifier Frequency Response — Gain Versus Frequency

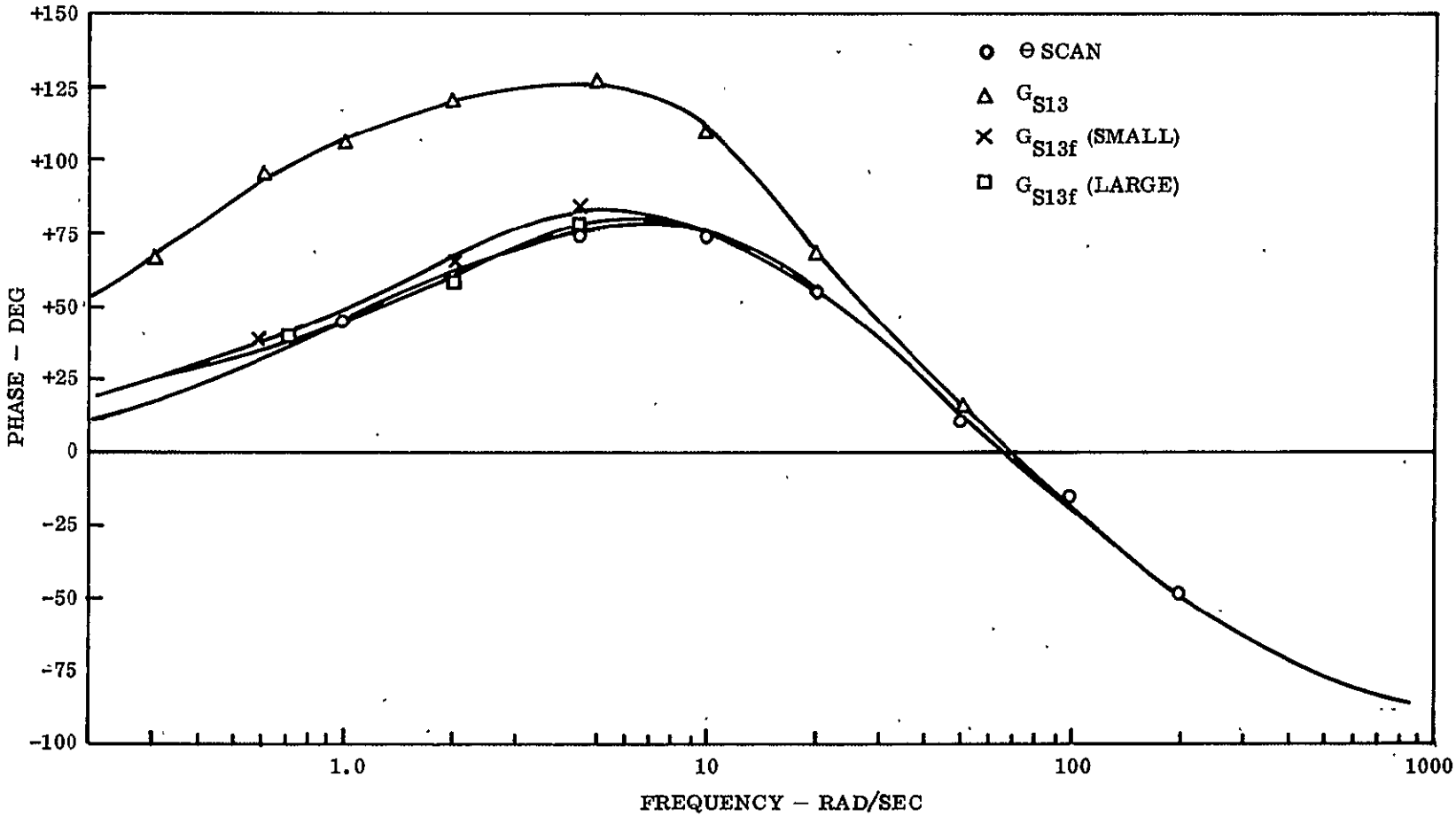

Fig. D-21 SPARCS I Pitch Amplifier Frequency Response – Phase Versus Frequency

D.7 ROLL AMPLIFIER

The roll amplifier is used in despinning the vehicle and in maintaining stabilization of the roll axis. It sums the roll rate signal, ω_x, the roll range correction signal, and the magnetometer signals; the output is then fed into the pulse width-pulse frequency modulation circuit.

Prior to amplification by the roll amplifier, the magnetometer signals are fed through a dual resolver as shown below.

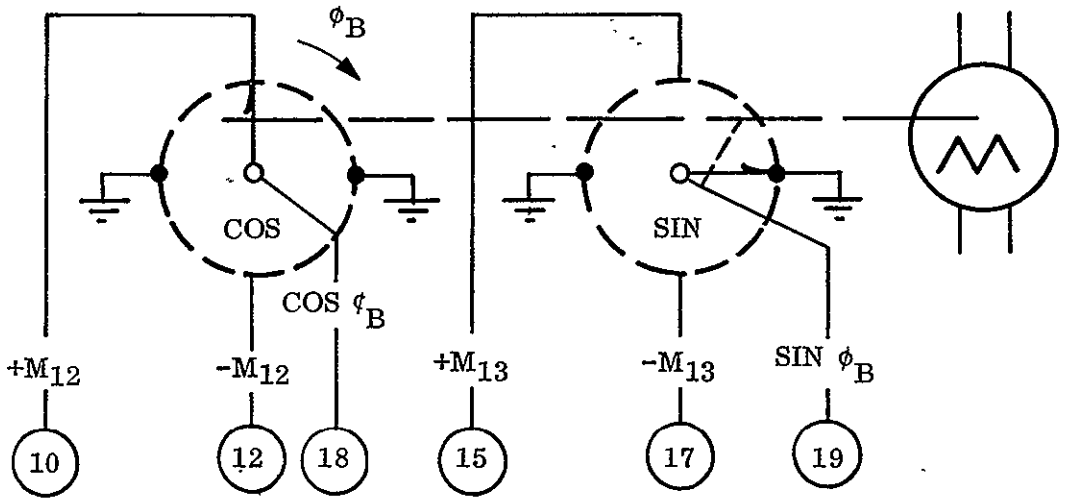

The dual resolver is an integral unit consisting of a stepper motor, gear train, and the dual potentiometer quads which are connected together at the wipers and are mechanically separated by 90 deg. The resolver allows the experimenter to set a payload roll axis null position, according to his needs, with the AGE Test Control Unit.

A schematic of the roll channel amplifier is shown in Fig. D-22. Two levels of circuit gain, depending on the signal level, are provided by the two diodes across the resistor R13 in the feedback path of AR6. For large signals one of the diodes breaks down, shorting out R13 and thus reducing the gain. The output signal of δ_x from the roll amplifier is given by the following equation:

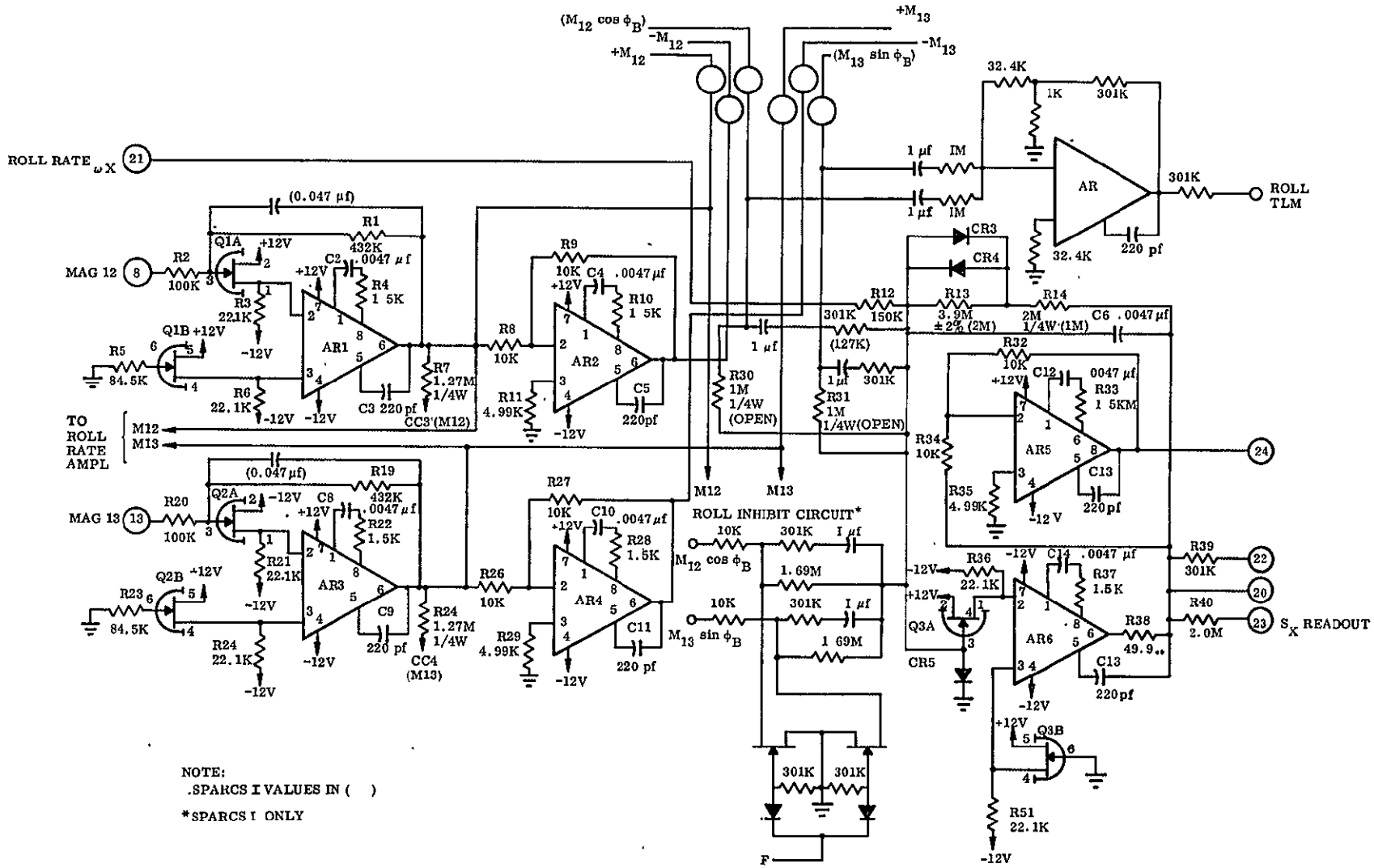

Fig. D-22 SPARCS Roll Amplifier Schematic

$$\delta_x = M_{12} \cos \phi_B - M_{13} \sin \phi_B + \omega_x$$

Gain and phase versus frequency plots for the roll amplifier circuit are presented in Figs. D-23 and D-24. They include both large and small input signals from the roll rate circuit and the resolvers.

The addition of the roll position inhibit circuit to SPARCS I increased the probability of sun acquisition over a greater range of η (angle between magnetic field and sun line) than SPARCS 0. The position signal is shorted to ground through two FET switches until the F switch indicates sun acquisition. At this time, F becomes positive and roll position becomes part of the roll error signal. Thus the payload rolls about the sun line to the roll null position. Prior to the F switch, the roll error signal was responsive only to ω_x. When ω_x was large, the pitch/roll valves were saturated for despin; after despin, ω_x is smaller and the pitch/roll valves are responsive primarily to the pitch error signal for sun acquisition. The ω_x input is used to prevent a roll-rate buildup.

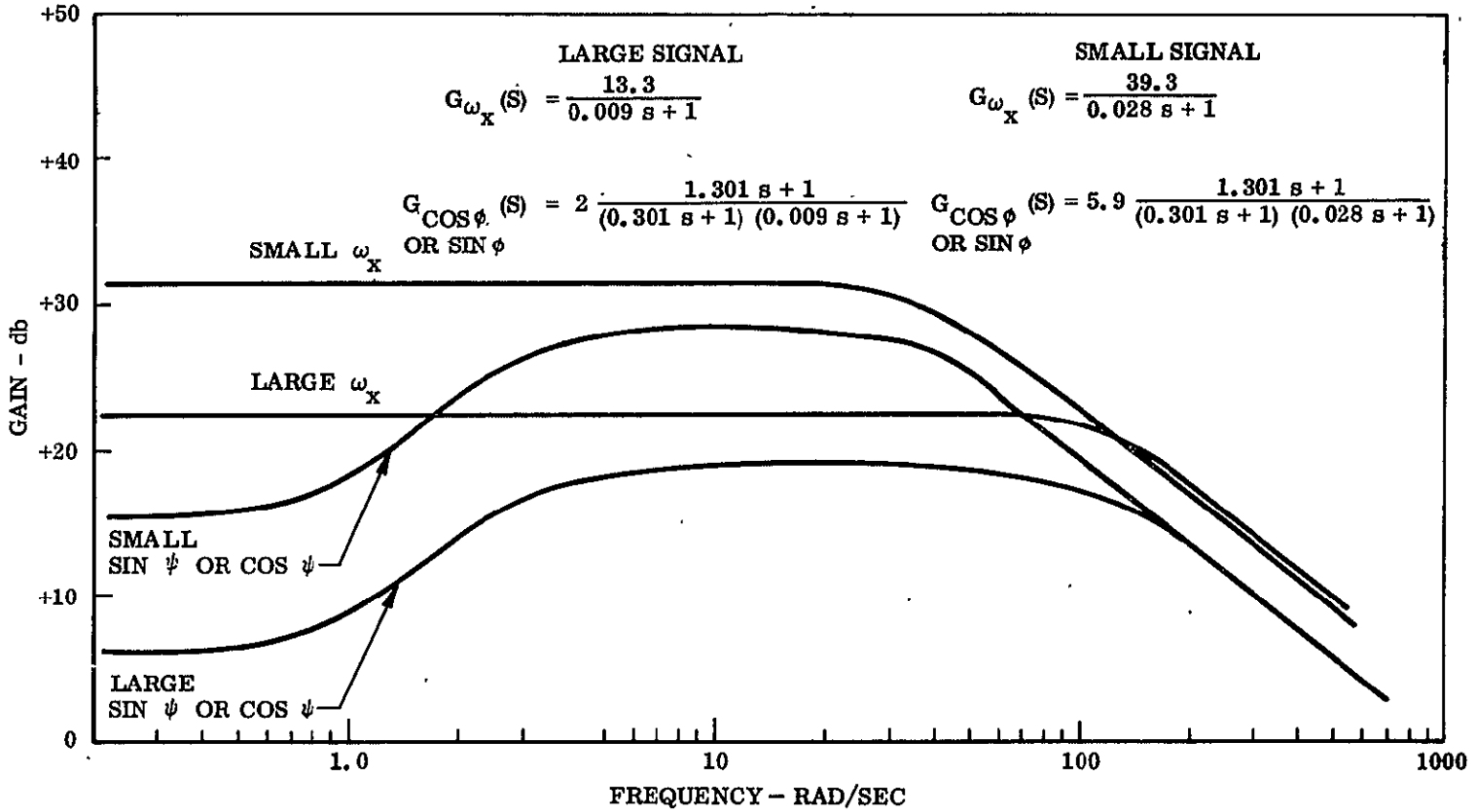

Fig. D-23 SPARCS I Roll Amplifier Frequency Response – Gain Versus Frequency

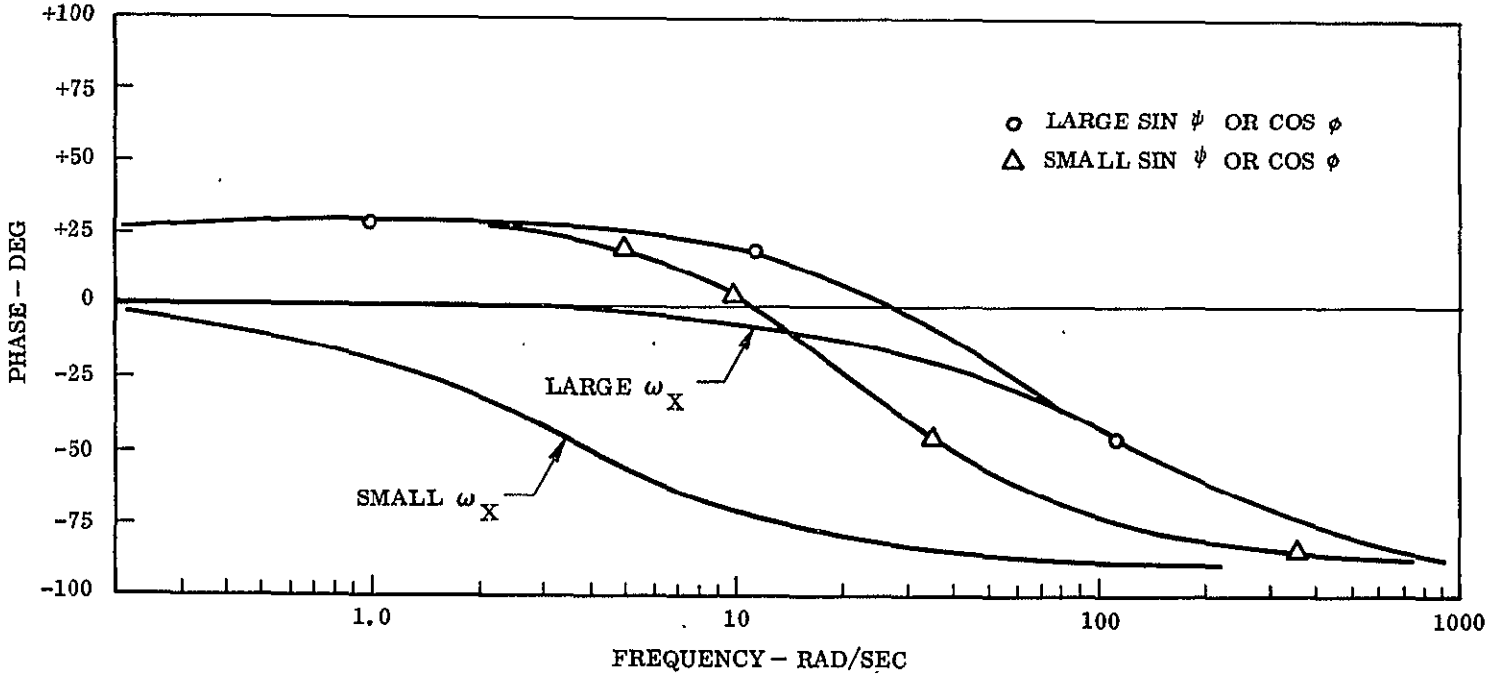

Fig. D-24 SPARCS I Roll Amplifier Frequency Response – Phase Versus Frequency

D.8 ROLL RATE CIRCUIT

The roll rate circuit, which consists of an array of bipolar switches and amplifiers, was designed to produce a signal proportional to vehicle roll rate by solving equations.

It has been shown (Appendix A) for a pencil shaped vehicle spinning about its minimum moment of inertia axis that

$$\dot{S}_{12} \cong P S_{13}$$
$$\dot{S}_{13} \cong P S_{12}$$
$$\dot{m}_{12} \cong P m_{13}$$
$$\dot{m}_{13} \cong P m_{12}$$

where

S_{ij} , m_{ij} = direction cosine between ith pointing axis and the jth body axis
$\dot{S}_{ij}$, $\dot{m}_{ij}$ = direction cosine rate
P = body roll rate

To remove roll rate sign ambiguity, the following expression was solved:

$$\dot{S}_{12} \ (\text{sign } S_{13}) - \dot{S}_{13} \ (\text{sign } S_{12}) + \dot{m}_{12} \ (\text{sign } m_{13})$$
$$- \dot{m}_{13} \ (\text{sign } m_{12}) \cong P \left[\left| S_{13} \right| + \left| S_{12} \right| + \left| m_{13} \right| + \left| m_{12} \right| \right]$$

Signals proportional to the direction cosine rates are produced by the 1-μf capacitors shown in Fig. D-25. The sign of each rate signal is controlled by a solid-state bipolar switch (Q1, Q2, Q3, Q4). Since each of the four switching circuits operates on the same principle, only a description of the S_{12} rate circuit is given here.

Consider a positive signal S_{13} applied to pin 4 of amplifier AR5. A positive voltage input to pin 4 drives the output of AR5 positive at pin 9 and negative at pin 3. The opposite output polarities result for a negative voltage at pin 4. A positive or zero voltage applied to the gate of the bipolar switch allows the input signal to pass. Since S_{13} has been assumed to be positive, the output at pin 9 is positive and the output at pin 3 is negative. Thus the pin 3 and pin 6 gate signals of Q3 are positive and negative,

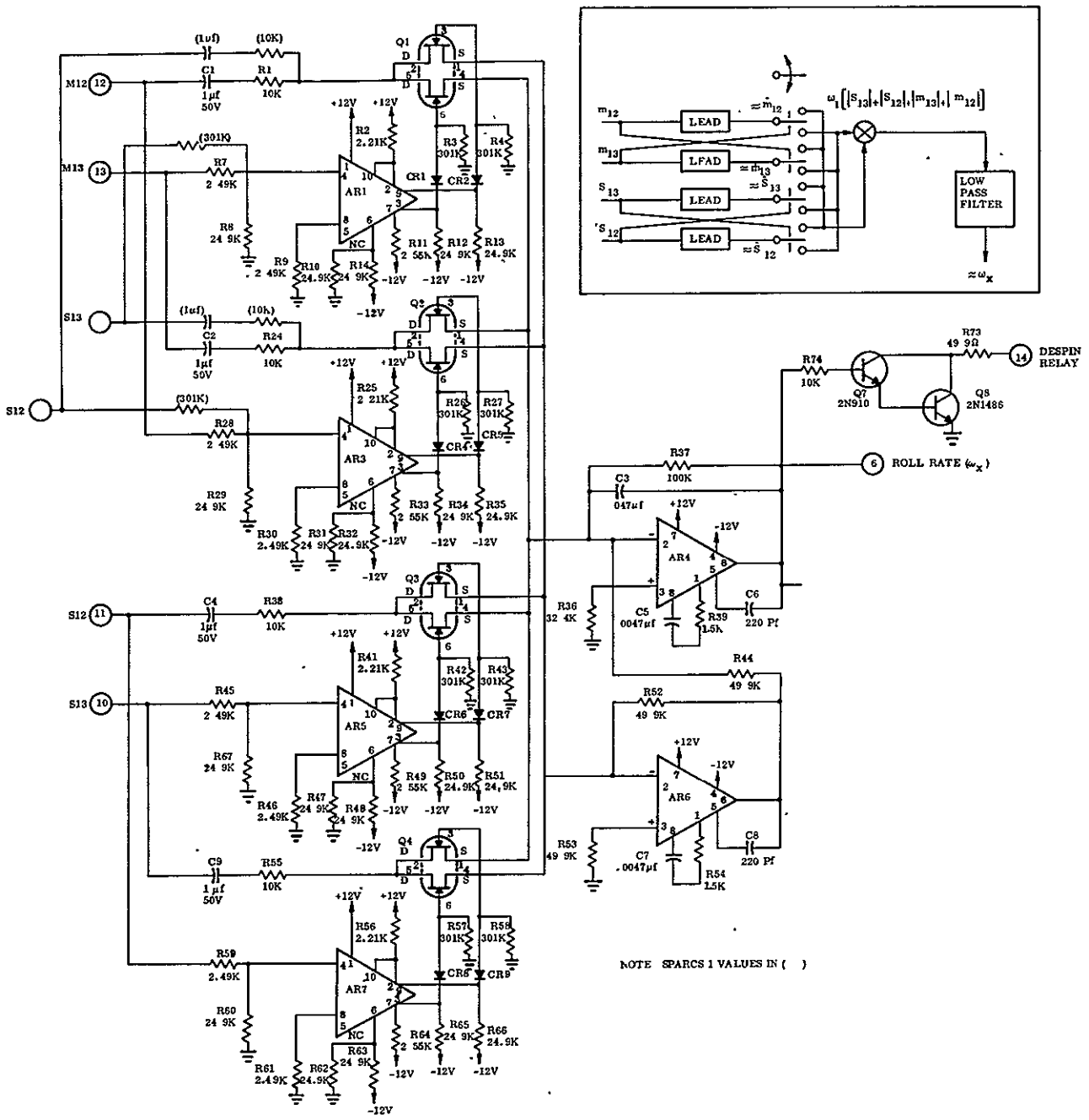

Fig. D-25 SPARCS Roll Rate Circuit

respectively. This means that the output of Q3 at pin 4 is disconnected from the rate signal; however, the rate signal is allowed to pass through pin 1.

Amplifiers AR4 and AR6 are sign inverting differential amplifiers. The signal that passes through pin 1 goes through both AR6 and AR4, and consequently it will have the same sign as the rate signal for S_{13} positive. When S_{13} is negative, the signal out of pin 1 of Q3 will be interrupted and the signal will pass out through pin 4. This signal bypasses AR6 and thus the output of AR4 will have the opposite sign as the signal coming from pin 4 of Q2, i.e., the rate signal S_{12}.

Amplifier AR4, in addition to performing sign inversion, acts like a low pass filter to the signal (due to capacitor C3), thus guaranteeing that none of the high frequency switching transient signals propagate into the roll channel circuit.

Figure D-26 shows the outputs of AR5, AR7, Q3, Q4, and AR6 for typical time histories of S_{13} and S_{12}. The responses due to m_{12} and m_{13} would be identical and therefore have not been shown. The case shown is for the S_{13} signal leading S_{12} in phase by 90 deg. This corresponds to a positive roll rate and resulted in a positive total output from AR4. A negative roll rate would cause the S_{12} signal to lead S_{13} by a phase angle of 90 deg. and the resulting output of AR4 would be negative.

For SPARCS I, the roll rate signal was improved by the addition of the CSS terms to the magnetometer portion of the circuit. The addition was made experimentally by analog computer tests and improved acquisition when η was greater than 160 deg.

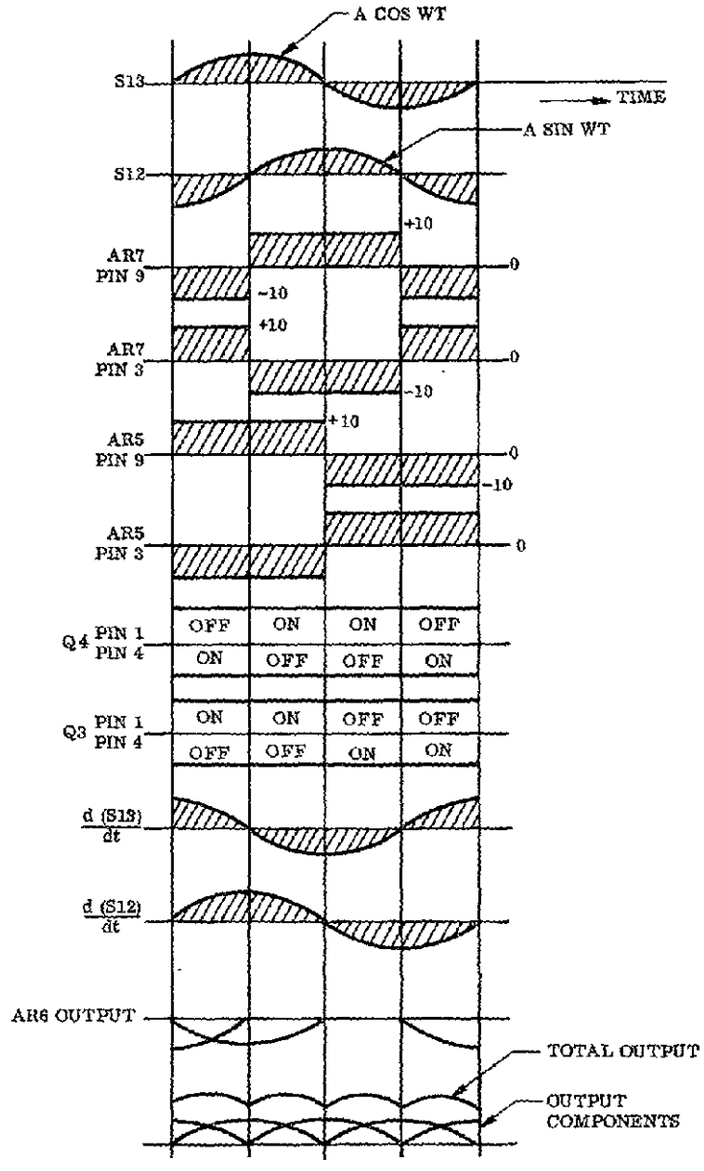

Fig. D-26 Roll Rate Output Waveform

D.9 ROLL RANGE CORRECTION CIRCUIT

An exponentially decaying signal is available in the roll channel to correct part of the errors due to a change of the Earth's magnetic field direction as the payload travels downrange (Appendix B contains a description of the requirement). The input voltage levels are ±8 V and the time constant is 300 sec. The signal is initiated when the umbilical is disconnected from the SPARCS insert. A schematic of the roll range circuit is shown in Fig. D-27. The roll range correction works as follows:

The roll bias angle is determined from the experimenter according to Appendix B, Fig. B-9, as

$$\phi'_B = \phi'_D - \phi'_N$$

but since ϕ'_N is actually range- and time-dependent, ϕ'_B must change accordingly to maintain ϕ'_D. ϕ'_N is determined for the end of the desired experiment time, from the predicted impact range and the time of launch, and ϕ'_B is set accordingly. Now ϕ'_D is satisfied only at the end of the experiment time. Therefore to the roll position signal is added the roll range correction voltage of a magnitude and sign required to yield ϕ'_D at liftoff, and

$$\phi'_B + V^{(t)}_{\text{roll range}} = \phi'_D - \phi'^{(t)}_N$$

After liftoff, $V^{(t)}_{\text{roll range}}$ decreases exponentially. The result is an approximation to ϕ'_D which is accurate within 1 deg at liftoff and at the end of the experiment time.

D.10 PULSE WIDTH-PULSE FREQUENCY CIRCUIT

The pulse width-pulse frequency circuit (PWPF) converts the DC error signals from the channel amplifiers into a saw-tooth waveform biased according to the polarity of the input signal (i.e., a positive input produces a positively biased output signal). The PWPF circuit output commands the thruster valves to turn on and off at a given frequency. The rate, duration, and duty cycle vary as a function of the variation in the input error signal.

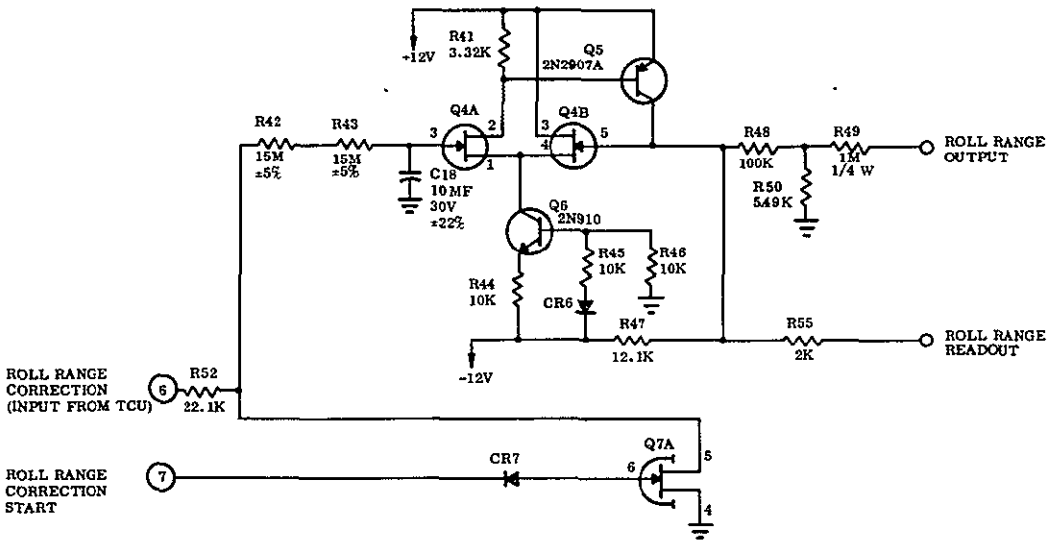

Fig. D-27 Roll Range Correction

The PWPF circuit consists of an integrator which drives threshold switches that turn a pair of solenoid valves full on and full off. A simplified block diagram of the PWPF circuit is shown in Fig. D-28.

The integrator amplifier (AR2) is a high-gain integrated circuit operational amplifier. With appropriate feedback, the amplifier is converted to a pulse width-pulse rate modulator. There are two negative feedback loops. Since the PWPF circuits are identical for the roll, pitch, and yaw channels, a schematic of only the yaw channel circuit is shown in Fig. D-29.

The threshold switches are two integrated circuit differential comparators with hysteresis which is a function of the positive feedback. When the input exceeds a predetermined level, the output switches. When an input signal is applied, the signal is integrated until a predetermined threshold level is reached. The inverted output of the integrator is a ramp which rises or falls at a rate that is directly proportional to the input signal, either positive or negative.

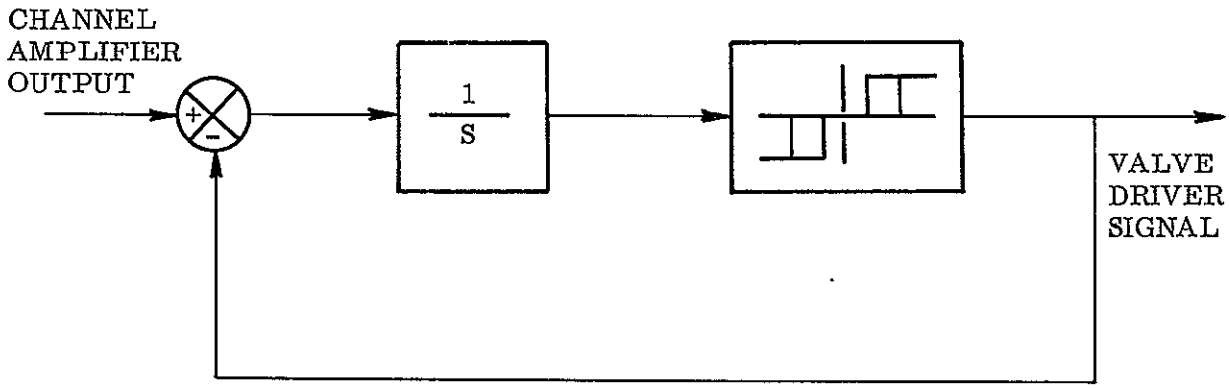

Fig. D-28 PWPF Simplified Block Diagram

A positive and a negative reference voltage is applied to threshold switches AR1 and AR3, respectively. With a positive input signal applied, threshold circuit AR3 switches when the output of the integrator reaches the AR3 threshold. The output of AR3 turns off transistor Q3 which causes a voltage of opposite phase to appear at the input summing junction. This causes the integrator output to reverse direction. The output pulse stays on until the integrator output goes below the threshold trigger point. Because of threshold hysteresis, the output pulse can be made to stay on some predetermined length of time. Operation of threshold switch AR1 is identical to AR3 except that inverting the AR1 output is not necessary.

Diodes CR1 and CR6 are reversed biased under no-signal conditions, thus preventing a negative voltage from the outputs of AR1 and Q3 from appearing at the summing junction leading to the input of AR1; for positive voltages, the diodes stabilize the circuit by producing dead zones in the feedback paths. Input-output relationships of the driver are shown in Fig. D-30.

For SPARCS I the gain of the PWPF was increased by 3, which is partly responsible for the improved fine-pointing stability of SPARCS I over SPARCS 0.

	INPUT 1	$\overline{gnd}$	I_y	I_y
	INPUT 2	$\overline{I_z}$	I_x	$\overline{I_x}$
SPARCS 0	R_1	49.9K	100K	100K
	R_2	100K	49.9K	49.9K
SPARCS 1	R_1	12.1K	22.1K	22.1K
	R_2	22.1K	5.1K	5.1K

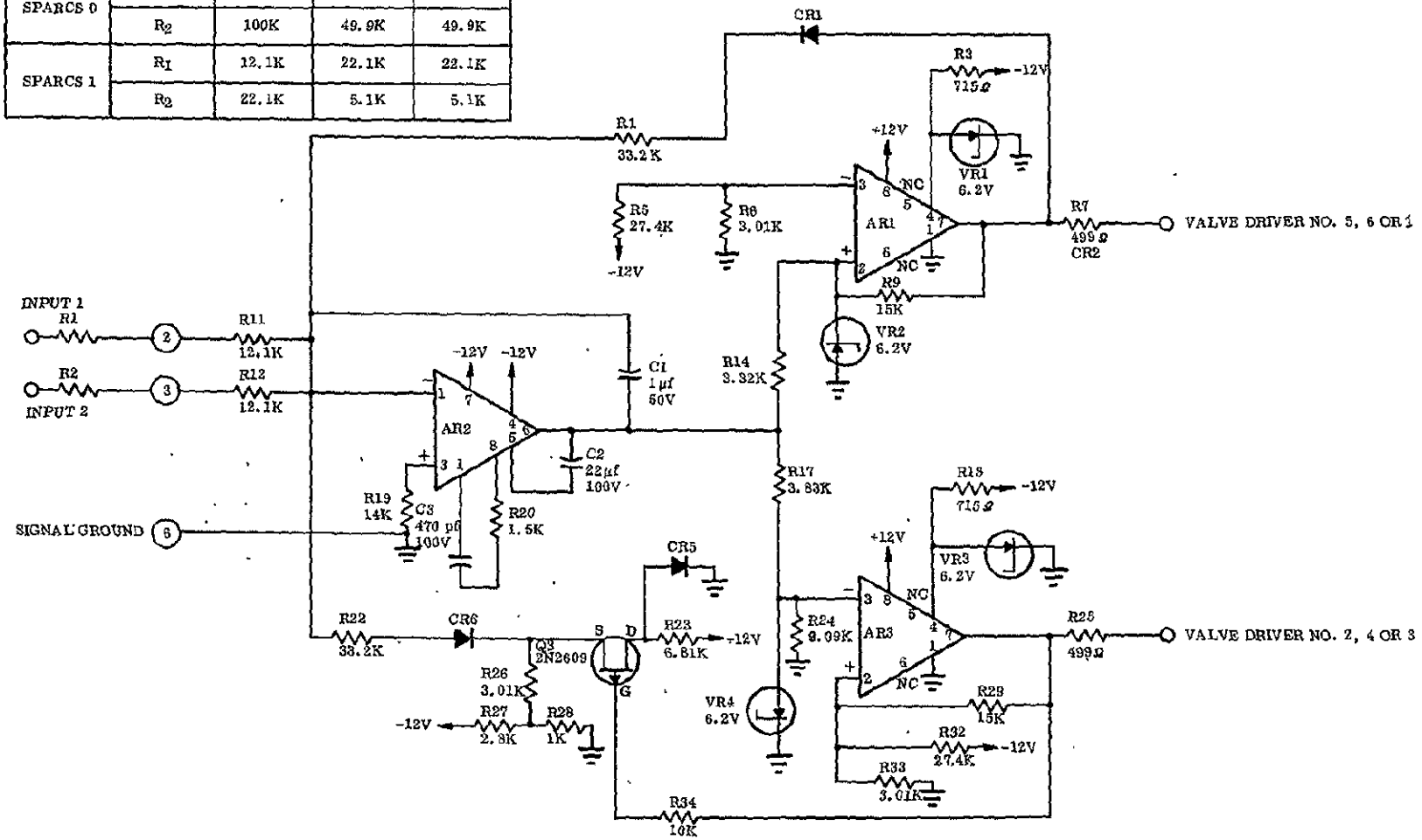

Fig. D-29 Pulse Width-Pulse Frequency Circuit Schematic

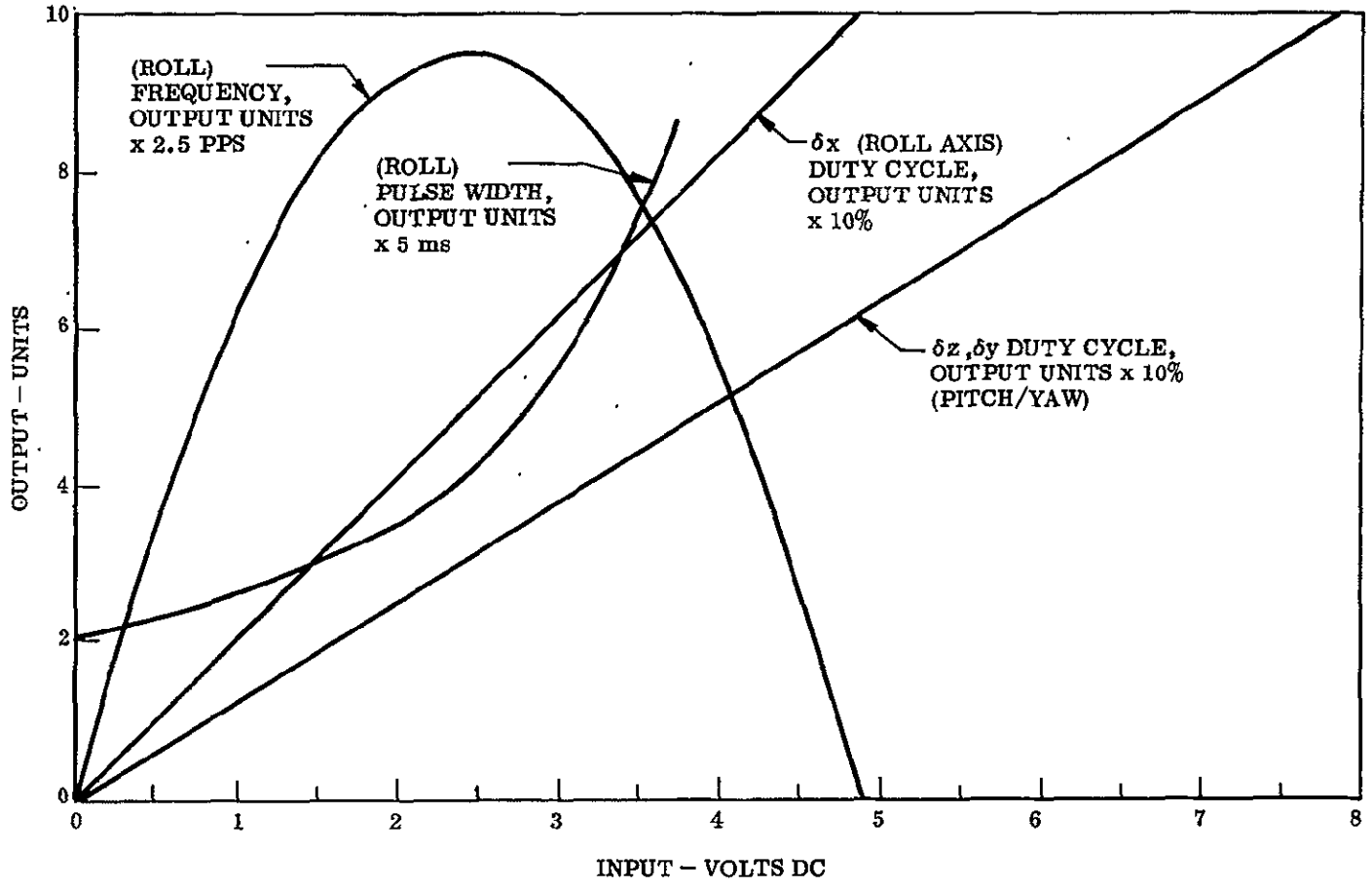

Fig. D-30 Pulse Width-Pulse Frequency Output Versus Input

D.11 VALVE DRIVER CIRCUIT

The valve driver circuit operates the cold gas thrust solenoids in response to commands from the pulse width-pulse frequency control circuit. The design investigation started with consideration of the valve load specifications and system requirements for minimum impulse. To meet the latter requirement, the valve coil turn-off transient voltage should be reduced as rapidly as possible; however, this rapid discharge causes secondary breakdown and possible permanent damage to the controlling power transistors. Because of the minimum impulse requirement, it was not desirable to use diode clamping of the valve coils to prevent secondary breakdown; consequently the effect of secondary breakdown on the circuit was studied.

D.11.1 Circuit Description

The valve driver circuit for a single axis is shown in Fig. D-31. The valve inhibit function, provided by the transistor Q3, prevents the valves from operating prior to SPARCS enable. The base drive to transistors Q_1 and Q_4 is shunted to the ground through the diodes CR_1 and CR_2 and through Q_3 when the inhibit voltage is present. This input is decoupled from the other inhibit inputs in the control system by the diode CR_3.

Both Q_1 and Q_2 are turned off for a negative or zero-V input command. No valve current flows and the valve does not operate. With a positive input command voltage of more than 1 V, both Q_1 and Q_2 turn on. The valve current increases to approximately 1 A and the valve turns on. The current through the valve increases exponentially with a 10-ms time constant. Transistors Q_4 and Q_5 turn on in response to a command signal for thrust in the opposite direction.

A simplified valve driver circuit and inductive load line is shown in the accompanying sketch. With the transistor off, the voltage and current are at point 1. When the transistor is turned off abruptly, the voltage induced across the inductor keeps the collector current flowing. The voltage and current increase clockwise around the load line

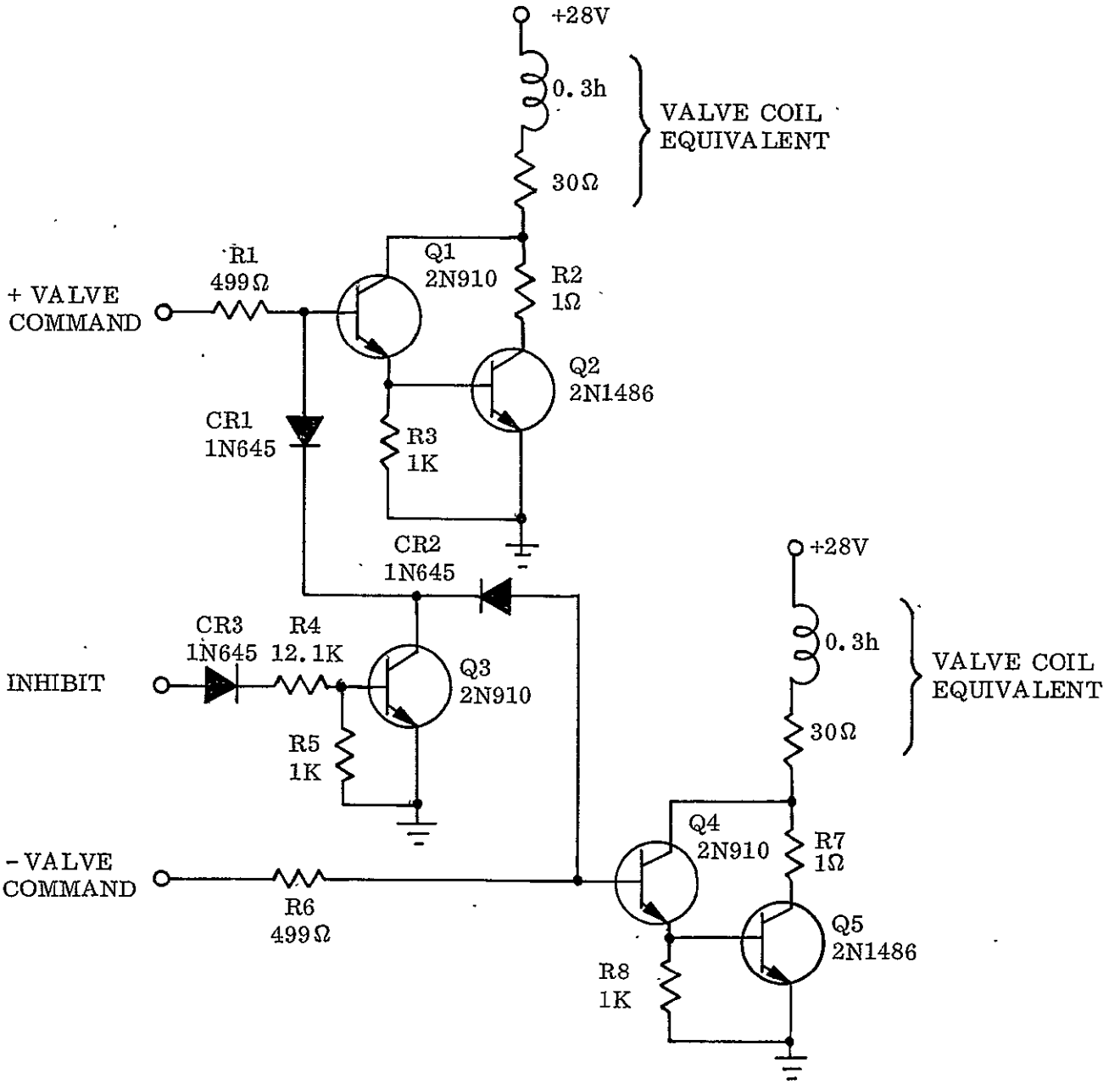

Fig. D-31 Valve Driver Circuit Schematic

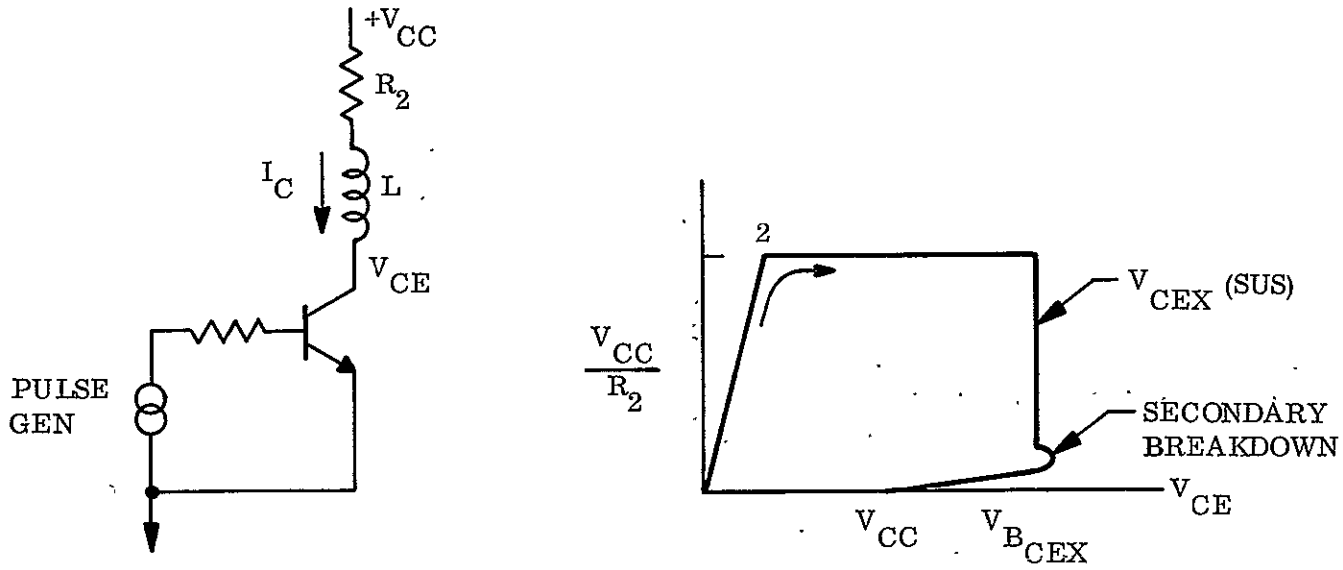

to point 1 and, in the process, the transistor goes into avalanche (charge carrier multiplication) and high power dissipation occurs. The time relationship between the collector voltage, the collector current, and the transistor power dissipation during turn-off is shown in Fig. D-32.

D.11.2 Secondary Breakdown

Secondary breakdown is a condition in which the output impedance of a transistor changes almost instantaneously from a large value to a small limiting value. It may be distinguished from normal transistor operation by the fact that once it occurs, the base no longer controls normal collector characteristics. Physically, secondary breakdown is caused by very localized current concentrations, resulting in the uncontrollable generation and multiplication of carriers, with a sudden reduction of the collection impedance. As the duration of this phenomenon exceeds the thermal time constant of this minute area, the transistor is irreversibly damaged. A more complete discussion is contained in Ref. 11.

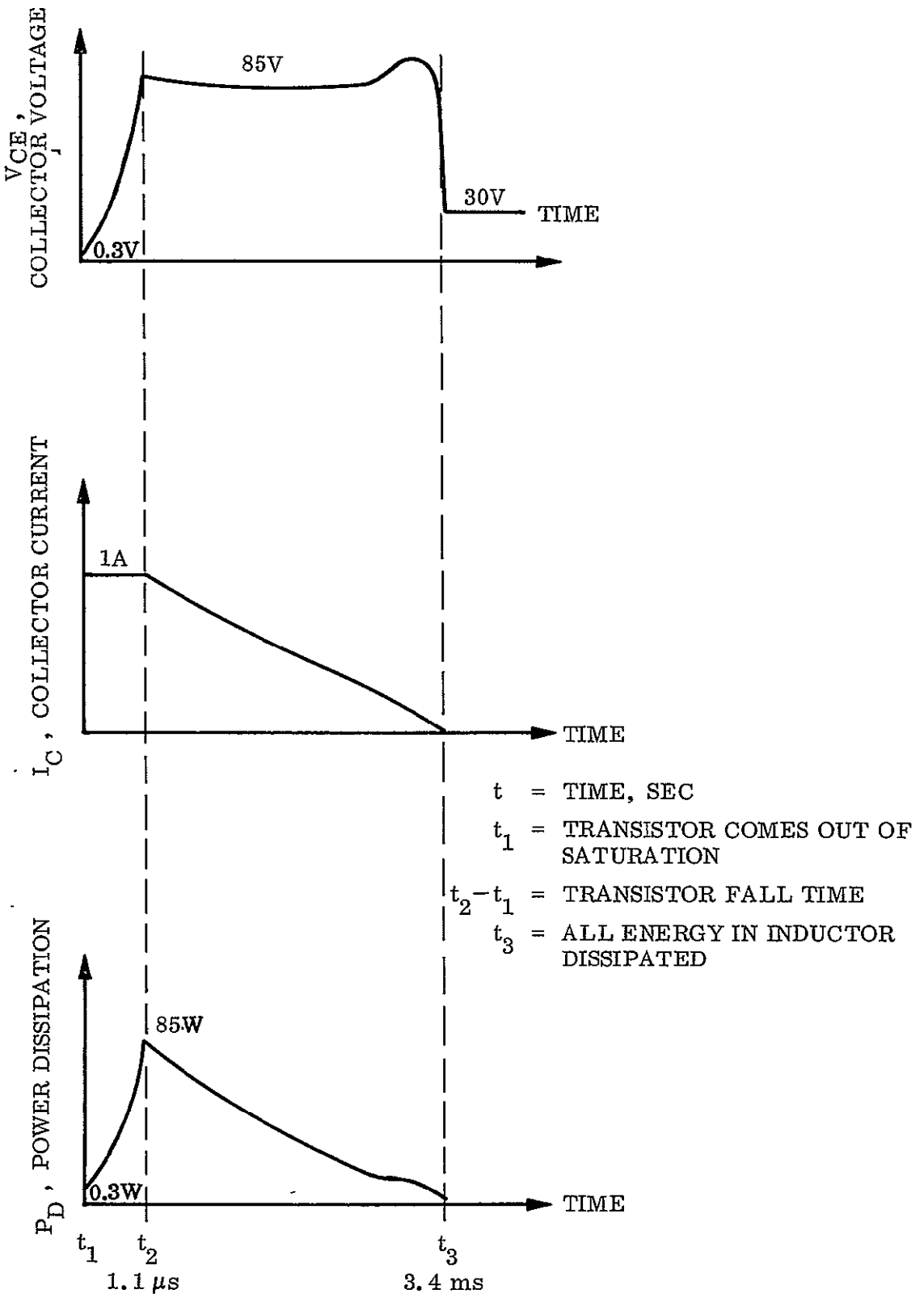

Fig. D-32 Valve Driver Current, Voltage, and Power Versus Time

Although the power transistors encounter secondary breakdown during their duty cycle, no permanent damage is done to them because enough heat energy is dissipated to prevent the occurrence of thermal instability.

D.11.3 Power Dissipation Requirements

The power transistor (2N 1486) is rated to handle an average power of 2 W in free air. Based on the worst-case duty cycle and the power curve shown in Fig. D-32, the power transistor must dissipate an average power of 4.3 W. To keep from overheating, the power transistors were mounted on a black anodized aluminum plate which acted as a heat sink and increased the operating rating above the 4.3-W requirement.

D.11.4 Thermal Stability

Thermal runaway is a condition in which the collector base leakage current increases with temperature and causes a regeneration effect on junction temperature. This could cause a valve to remain turned on if the quiescent collector current of the valve driver was more than the valve dropout current. A detailed analysis has shown that the circuit is stable.

D.12 PNEUMATICS SUBSYSTEM

The SPARCS pneumatics subsystem consists of a propellant tank, high and low pressure regulators, thrust valves, and nozzles. The thrust valves are activated by signals from the valve driver circuit.

D.12.1 Pneumatics Design

Starting with the range of mass properties of the Aerobee vehicles to be controlled, representative values of the jet, c.g. distances, and SPARCS performance requirements, computer simulations were conducted to determine thrust and impulse requirements. The parameter values originally established are tabulated below.

	Thrust Valve Output (lb)	Maximum Impulse Bit Per Valve Pulse (lb-sec)	Total Impulse (lb-sec)
Despin and Coarse Mode	2.45	0.035	150
Fine Mode	0.01	0.00012	

However, as a result of extensive air bearing vehicle testing, the fine mode thrust level was increased for the SPARCS 0 test flights. The thrust level was set to 0.7 lbf for the first test flight (4.201) and to 0.265 lbf for the second test flight (4.202). The 0.7-lbf level was too high, due to an error in calculating the thrust at altitude with Freon, and would have resulted in an unstable fine pointing mode. This did not occur during flight because the fine pointing mode was never achieved. For SPARCS I, the low pressure regulator is adjusted for approximately 0.08 lbf; the actual thrust is set so that the acceleration in the fine mode is 0.2 deg/sec. The capability of adjusting the low pressure regulator over this range (155 psi for 0.7 lbf to 20 psi for 0.08 lbf) is inherent in the regulator design.

For coarse mode operation, the thrust valve inlet pressure is set at the relatively high level of 525 psig to minimize the temperature drop across the regulator and prevent freezing of any condensed moisture. The thrust valve inlet pressure is throttled to a chamber pressure of 80 psig and then expanded isentropically through

the convergent-divergent nozzle where most of the temperature drop will occur. Since the nozzle has no moving parts, it is insensitive to low temperature.

D.12.2 Tankage Requirements

The pneumatic subsystem operates satisfactorily, and with the same functional hardware, when using any one of the following gases: nitrogen, Freon CF_4, argon, and helium. A 165-cu-in. off-the-shelf supply tank was originally selected on the basis of using CF_4 and a total impulse requirement of approximately 200 lb-sec with the tank pressurized to 3600 psia at 70°F. Additional supply volume is required when using any of the alternate gases, as indicated in the table below, and will be located in the payload section of the Aerobee vehicle.

	Density at 300 psia and 70°F (lb/cu ft)	Gas Weight (lb)	I_{sp} (sec)	Total Impulse (lb-sec)	Extra Volume Required for 227 lb-sec Impulse (cu in.)
CF_4	60.9	5.82	39.1	227	0
Nitrogen	17.7	1.69	65.3	110	175
Argon	26.0	2.48	50.4	125	135
Helium	2.25	0.215	160.0	34.1	925

Should data from actual flight experience indicate that 150 lb-sec is adequate impulse capability, the supply tank pressure could be increased when using nitrogen and argon and thereby eliminate the need for additional volume. The use of helium, however, will always require additional volume, as indicated in the following table.

(165-cu-in. tank at 70°F)

	I_{sp} (sec)	Required Impulse (lb-sec)	Pressure (psia)	Gas Weight (lb)
Nitrogen	65.3	150	4880	2.30
CF_4	39.1	150	1700	3.83
Argon	50.4	150	4210	2.98
Helium	160.0	150	*12000+	0.938

*Far exceeds proof pressure of 5400 psia

The tank operating pressure is 5000 psig, and the rated proof pressure is 5400 psig. The high pressure regulator, which is designed for only 3600 psia operation, was tested at 5000 psia pressure; its performance was found to be relatively unaffected by the pressure increase. Both the flight pressure transducer and AGE pressure transducer will survive over pressurization up to a limit of 6000 psig, which is the unit proof pressure. The pneumatic umbilical, however, is rated for only 3200 psia operation. Therefore a check valve has been placed in series with the umbilical valve for leakage protection.

D.12.3 Vacuum Thrust Levels

The thrust nozzles have a relatively low expansion ratio of 6.1:1 because they protrude outside the vehicle skin and must therefore be limited in size for aerodynamic considerations. The thrust coefficient, C_F, and specific impulse for this expansion ratio are as follows:

	C_F (N/D)	I_{sp} (sec)
Nitrogen	1.605	65.3
CF_4	1.646	39.1
Argon	1.553	50.4
Helium	1.553	160.0

The thrust valves are designed to provide a nominal vacuum thrust of 2.51 lb in the coarse mode with nitrogen as the propellant. This thrust level varies somewhat with alternate gases, as indicated below.

	Coarse Mode Thrust, lb	SPARCS 0 Fine Mode Thrust, lb	SPARCS I Fine Mode Thrust, lb
Nitrogen	2.45	0.27	0.08
CF_4	2.51	0.27	0.08
Argon	2.37	0.27	0.08
Helium	2.37	0.27	0.08

The valve flow area is designed to provide a nozzle chamber pressure of 0.161 times the regulated inlet pressure. A plot of thrust versus inlet pressure is shown in Fig. D-33.

D.12.4 Pneumatics Operation

A schematic of the pneumatic subsystem is shown in Fig. D-34. The system is charged through the fill valve, and the gas flows into the tank through a port on the flow controller housing until a tank pressure of 5000 psig maximum is reached. (The gas charging envelope for CF_4 is shown in Fig. D-35.) The gas will flow through the high pressure regulator seat until the downstream lockup pressure (600 psig maximum) is reached, at which time the high pressure regulator poppet will shut off further gas flow. Flow will resume when a thrust valve is actuated, or if the isolation valve solenoid is repeatedly actuated, creating small flow demands.

The flow controller has two outlet pressures: one for coarse mode operation and the other for fine mode operation.

> Coarse Mode. With the isolation valve open, the high pressure regulator output is fed directly to the thrust valves at a nominal 525 psig, through outlet No. 2.
>
> Fine Mode. With the isolation valve closed, the high pressure regulator output is fed through outlet No. 1 to the low pressure regulator and then to the thrust valves.

The high and low pressure regulators are sized to maintain output pressure levels of 525 (±25) psig and 85 psig, respectively, when as many as three thrust valves are firing.

The vent lines from the high and low pressure regulators, the low pressure relief valve, and the flow controller isolation solenoid terminate at the vent port on the skin of the SPARCS control insert.

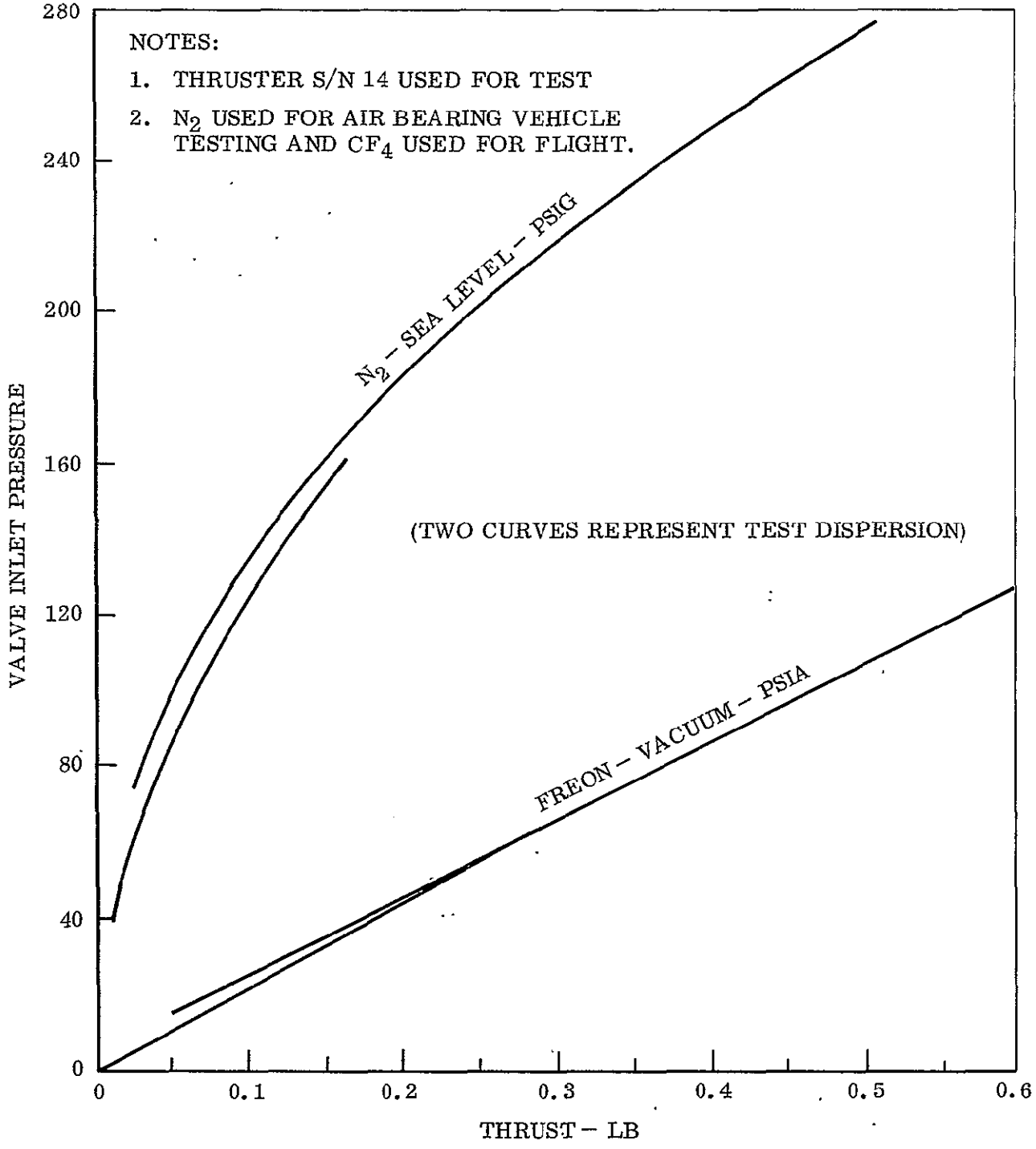

Fig. D-33 Thruster Input Pressure Versus Thrust

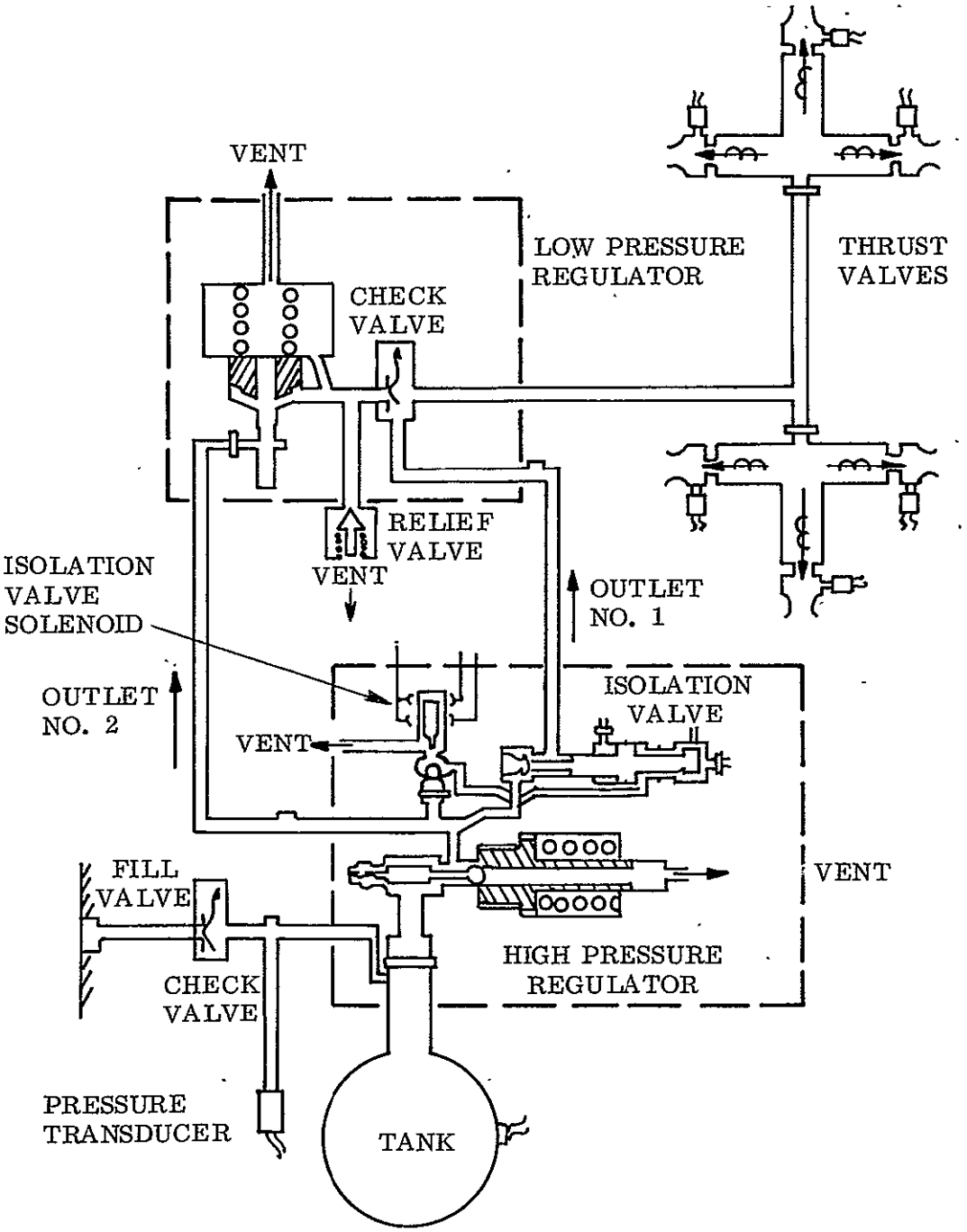

Fig. D-34 Pneumatics Subsystem Schematic

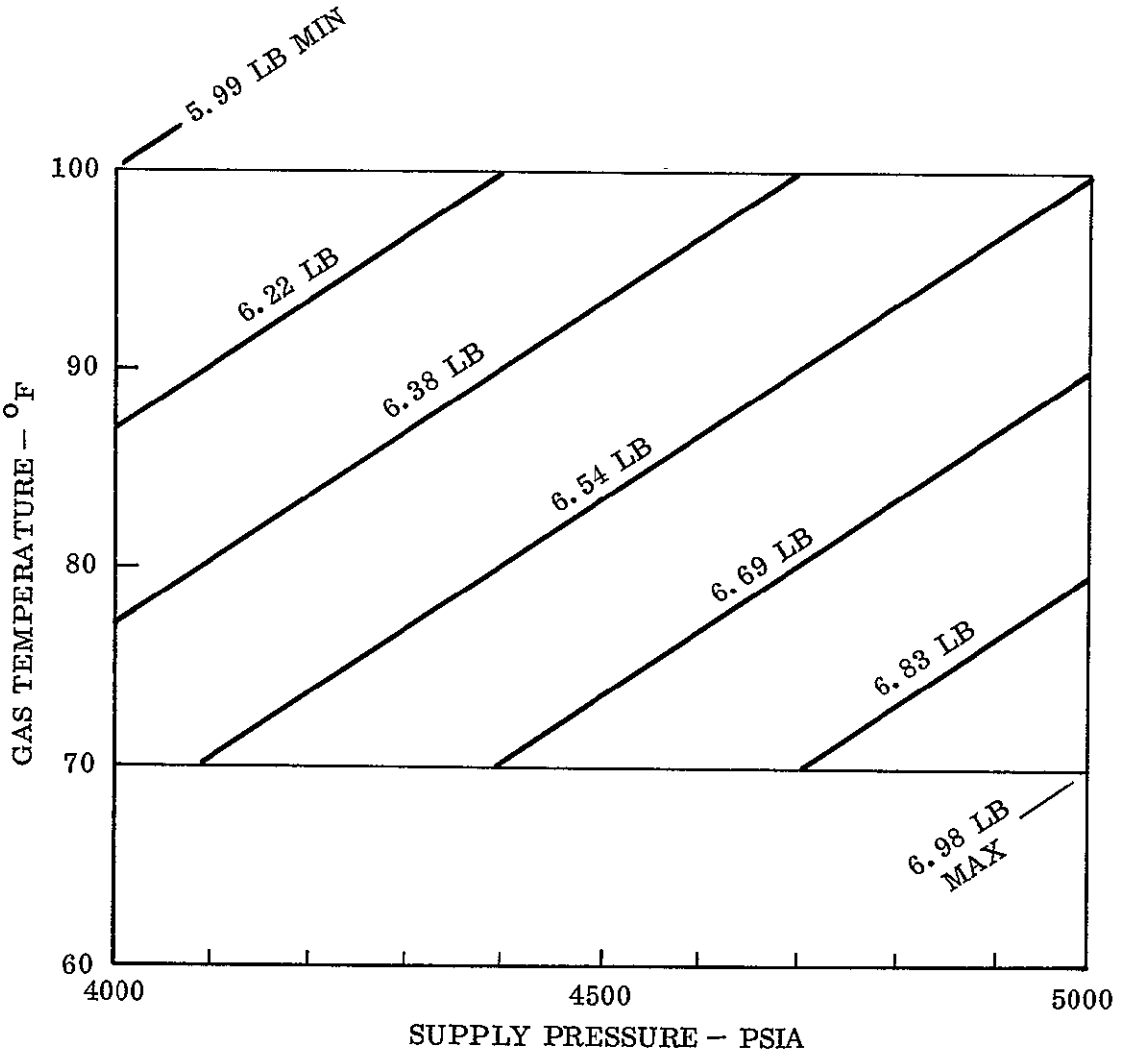

Fig. D-35 Gas Charging Envelope for CF_4

D. 12. 5 Pneumatics Instrumentation

Tank temperature and pressure are monitored by transducers. The temperature transducer is used during the fill operation to limit the charging rate so that the tank temperature does not reach 150°F. Readings from both transducers are used to accurately determine the weight of the control gas in the tank.

D. 13 POWER SUPPLY SUBSYSTEM

The SPARCS power supply subsystem consists of a 28-V battery pack and positive and negative regulation.

D. 13. 1 Battery-Magnetometer Electronics (BME) Assembly

This assembly, which is shown in Fig. D-36, consists of an electronics package for the magnetic aspect sensor assembly, a battery pack with nickel-cadmium cells, two terminal boards, and a single connector which provides the system interconnects between the control electronics, sensors, pneumatics, telemetry and AGE. The nickel-cadmium cells are insulated with heat shrink tubing (Raychem No. CR-9205) and bonded to the cell trays with epoxy adhesive. To reduce magnetic field distortion, the ferromagnetic batteries are enclosed in a Mu-metal magnetic shield.

D. 13. 2 Battery Description

The battery pack consists of 24 nickel-cadmium rechargeable cells connected in series with a nominal voltage of 1. 2 V per cell. The nominal capacity of the cells is rated at 1. 0 A-hr. Figure D-37 is a plot of the load on the battery during flight (based on a computer run) versus the battery voltage. The chart is based on a nominal voltage of 1. 2 V per cell; however, laboratory tests showed that the nominal voltage per cell was between 1. 27 V and 1. 32 V when fully charged. The SPARCS AGE Test Control Unit has the capability of recharging the battery pack and also maintaining a trickle charge to ensure peak capacity. A breakdown of the power load is shown in Table D-1; the resulting battery drains are given in Table D-2.

The nickel-cadmium battery has a minimum capacity of 1000 mA-hr at 68°F; consequently, a launch at 68°F would use only 27. 49 percent of the battery's capacity, leaving a 72. 51 percent reserve. At 150°F, the battery has a capacity of 700 mA-hr. At this temperature 39. 4 percent of the battery's capacity would be used in flight, leaving a 60. 6 percent reserve.

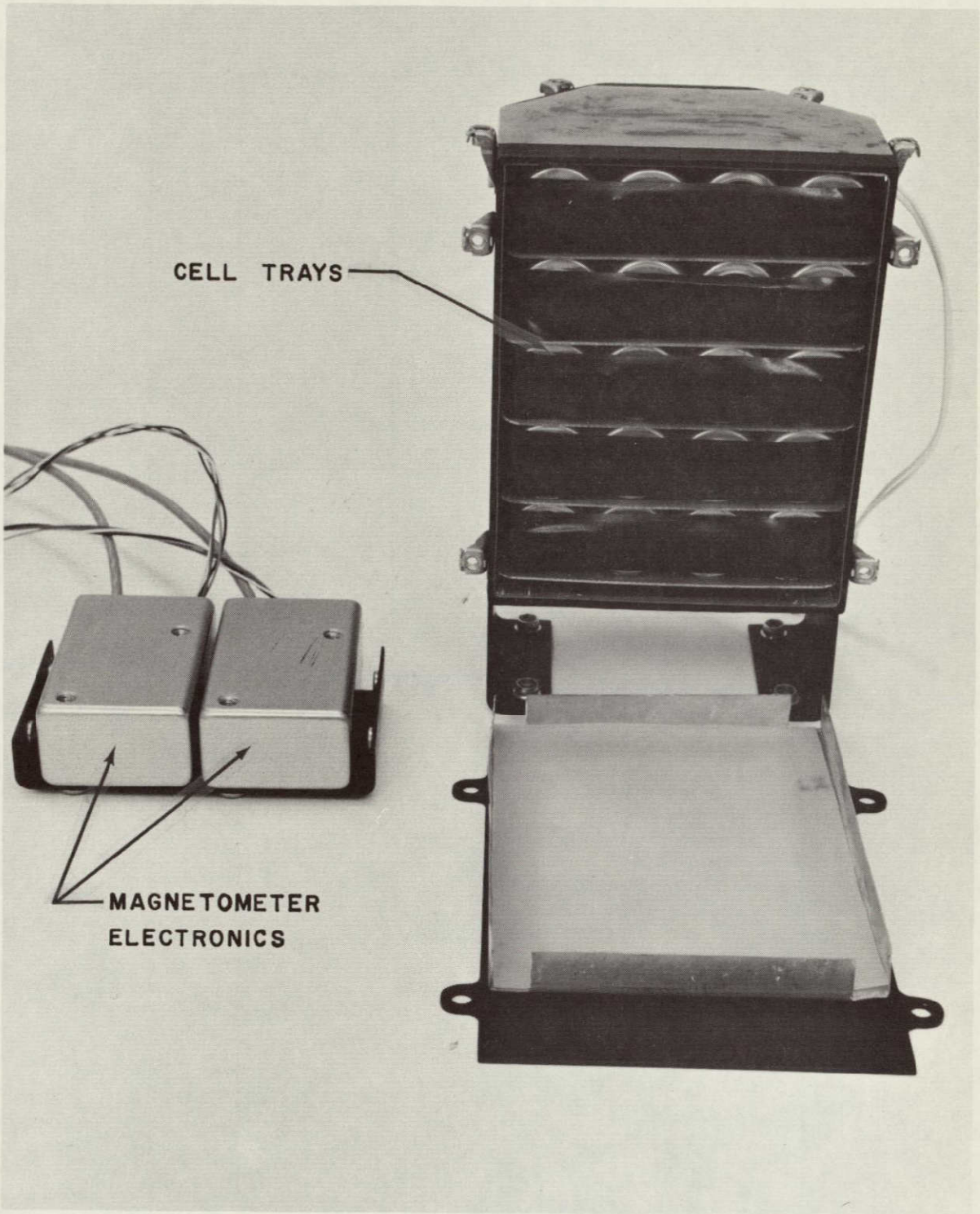

Fig. D-36 Battery-Magnetometer Electronics (BME) Assembly

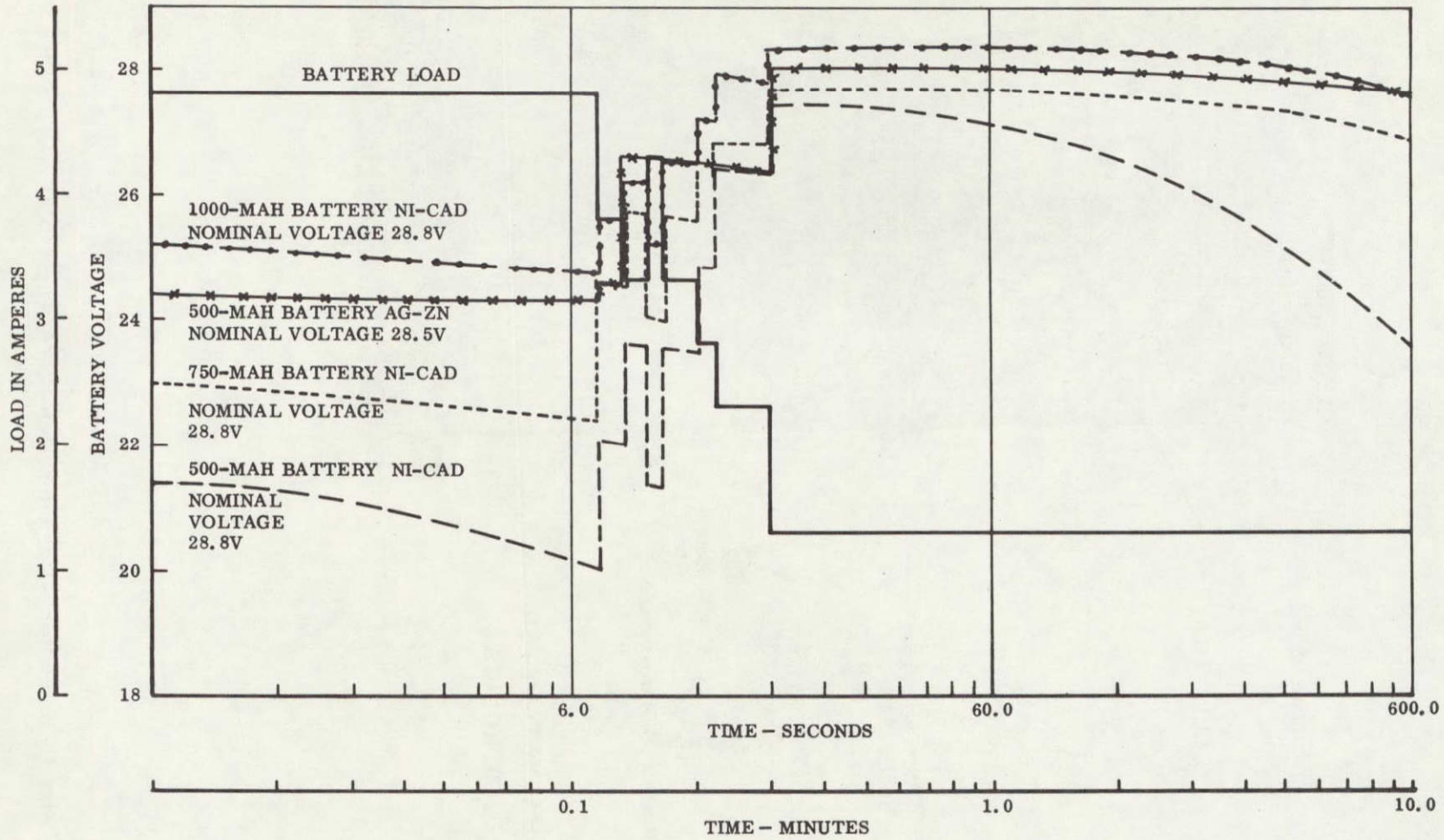

Fig. D-37 SPARCS Battery Load Versus Time

Table D-1

SPARCS POWER REQUIREMENTS

Parameter	SPARCS Power Supply Current Requirements (mA) 28.5 V	+12 V	-12 V
Total Power for Electronics Package = 13.7 W (28.5 V, 480 mA)			
34 each μA709		136	136
6 each μA710		24	24
6 each MC1519		30	30
Discrete Circuits		60	30
DC-DC Converter	75		
Commutator	90		
+12 V Reg Power Supply		20	
-12 V Reg Power Supply			20
Signel Conditioner		30	30
Pneumatics:			
Pressure Transducer		1	
Temperature Transducer		6	
Valve Drivers			
Acquisition 40 sec	(4000)		
Fine Pointing 6 min	(1000)		
Fine Sun Sensor		20	20
TOTAL STEADY CURRENT (mA)	165	327	290
PEAK CURRENT (mA)	5000		

Table D-2

BATTERY DRAINS

Steady Drain

at 28.5 V	165 mA x 10 min x $\frac{1 \text{ hr}}{60 \text{ min}}$	=	27.5 mA-hr
at +12 V	327 mA x 10 min x $\frac{1 \text{ hr}}{60 \text{ min}}$	=	54.5 mA-hr
at -12 V	290 mA x 10 min x $\frac{1 \text{ hr}}{60 \text{ min}}$	=	48.4 mA-hr

Additional Coarse Mode Drain

4000 mA x 40 sec x $\frac{1 \text{ hr}}{3600 \text{ sec}}$ = 44.5 mA-hr

Additional Fine Mode Drain

1000 mA x 6 min x $\frac{1 \text{ hr}}{60 \text{ min}}$ = 100.0 mA-hr

Total Drain 274.9 mA-hr

D.13.3 Battery Selection

Silver-zinc and nickel-cadmium batteries were both evaluated for the SPARCS primary power source. A comparison of the two candidates is shown in Table D-3. Although silver-zinc batteries offer a tremendous weight saving advantage, their optimum operating temperature range, operating life, and number of acceptable recharge cycles are not favorable. In addition, silver-zinc batteries require careful handling and special attention in the field prior to launch. Since battery weight was not a significant parameter in the SPARCS design, nickel-cadmium batteries were a clear-cut choice because of their superior operating characteristics.

D.13.4 Battery Arming Link

The battery arming link is a copper screw which is used as a positive shutoff for the SPARCS power supply. This positive link eliminates dependence upon a silicon-controlled rectifier for battery protection during nonoperational handling. The link is installed only when it is desired to operate SPARCS on internal power, since the SPARCS standby battery drain (although small) will deplete the battery charge in a few weeks.

Table D-3

NICKEL-CADMIUM AND SILVER-ZINC BATTERY COMPARISON

Parameter	Units	Silver-Zinc 500-mA-Hour Capacity	Nickel-Cad 500-mA-Hour Capacity	Nickel-Cad 750-mA-Hour Capacity	Nickel-Cad 1000-mA-Hour Capacity
Nominal Discharge Voltages					
C*	VDC	28.5	28.8	28.8	28.8
2C	VDC	28.2	28.0	28.0	28.0
5C	VDC	27.0	25.2	25.2	25.2
6.5C	VDC	26.0		23.0	
10C	VDC	24.4	21.4		
Charge-Discharge					
Charging Rate	mA	70	40-50	35-75	80-100
Charging Time	hr	10	5	20	5
Charge-Discharge Cycles	cycles	10-15	5000	5000	5000
Operating Life	months	6-9	years	years	years
Dry Storage Life	years	5	indefinitely	indefinitely	indefinitely
Charge Reduction		85% after one year			
Optimum Operating Temperature	^{o}F	+50 to +165	-20 to +140	-20 to +140	-20 to +140
Unit Cost		$109.75	$64.08	$120.00	$128.16
Physical Size					
Weight (1)	oz	15.2	28.8	54.0	57.6
Volume (2)	cu in.	17.4	16	31	35
Height	in.	1.56	3.4	3.1	3.4
Width	in.	2.2	3	4.5	4.5
Depth	in.	5.0	3.5	5.2	5.2

*C denotes nominal hour discharge rate

(1) 25 percent increase for packaging

(2) 20 percent increase for packaging

D. 14 TELEMETRY SYSTEM

Signals required to evaluate SPARCS performance may be monitored during flight. The SPARCS telemetry system consists of signal conditioners for scaling the monitored signals, a commutator, and buffer amplifiers. After conditioning and commutating, the signals are sent to the telemetry system in the Aerobee payload section for transmission. They are also available through the umbilical connector for communication with the AGE Test Control Unit while on the ground.

The following functions are telemetered on SPARCS:

Continuous	Valves 1 and 3	
	Valves 2 and 5	
	Valves 4 and 6	
	S12f, S13f	fine pointing (limit cycle) signals
Commutated	(refer to Table D-5)	

The SPARCS telemetry system has the following performance characteristics:

Bandwidth	0-20 cps
Over-range Limit	-0.5 V to +5.4 V
Accuracy	±2 percent of full scale
Output Impedance	10 K maximum

D. 14. 1 Telemetry Signal Conditioning

The telemetry signal conditioning section scales the various error and control signals to the proper amplitudes for telemetry data. It provides a high input and a low output impedance to minimize loading of input signals and related telemetry equipment. The continuously monitored signals are fed into emitter follower or operational amplifier circuits to effect the high input, low output impedance conditions. The various conditioners are discussed in the following paragraphs.

D. 14. 1. 1 FSS Temperature Conditioning Circuit. A thermistor has been placed on the Fine Sun Sensor (FSS) detector plate to measure the detector temperature during flight. The FSS temperature conditioner, which consists of a two-transistor emitter follower, is shown schematically in Fig. D-38. The relationship between telemetry output voltage and FSS temperature is shown in Fig. D-39.

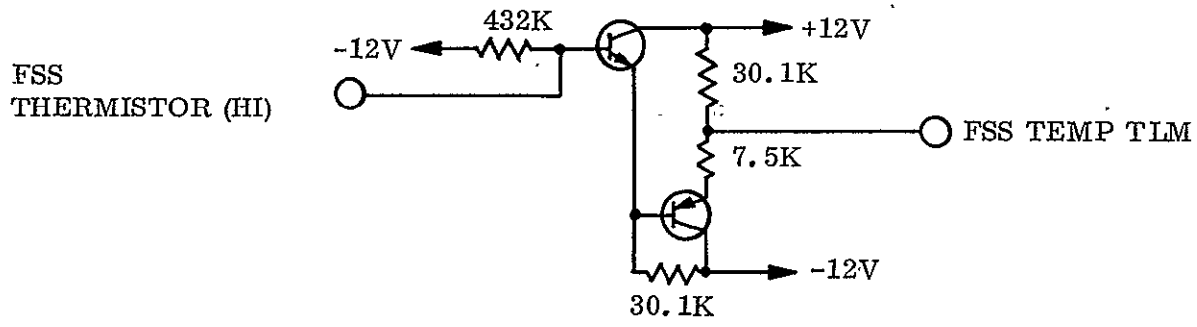

Fig. D-38 FSS Temperature Conditioning Schematic

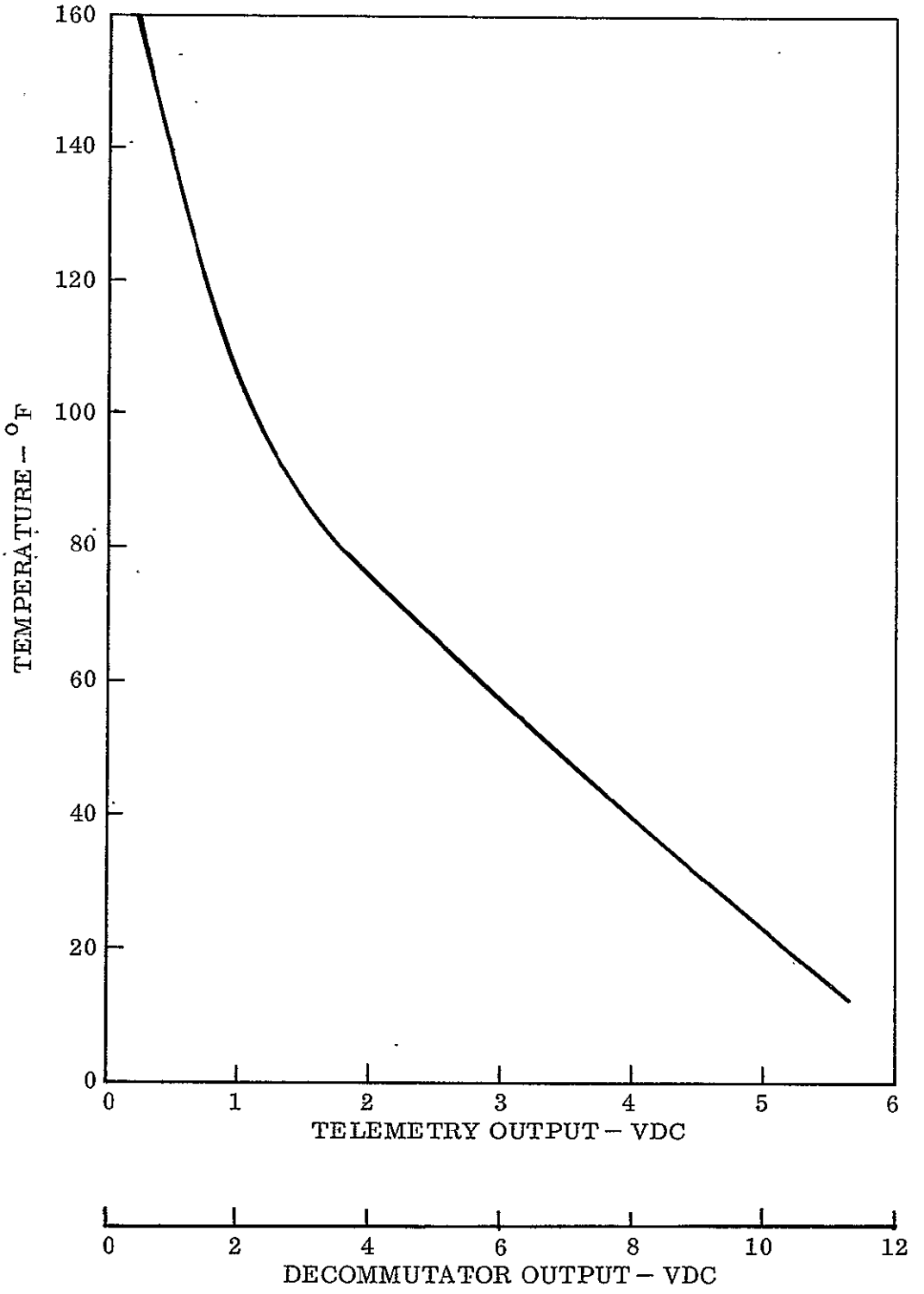

Fig. D-39 FSS Temperature Scaling

D. 14. 1. 2 Pneumatic Tank Temperature Conditioning Circuit. A thermistor is located on the pneumatic tank for temperature indication. The tank temperature buffer amplifier, which is similar to the FSS temperature amplifier, is shown schematically in Fig. D-40.

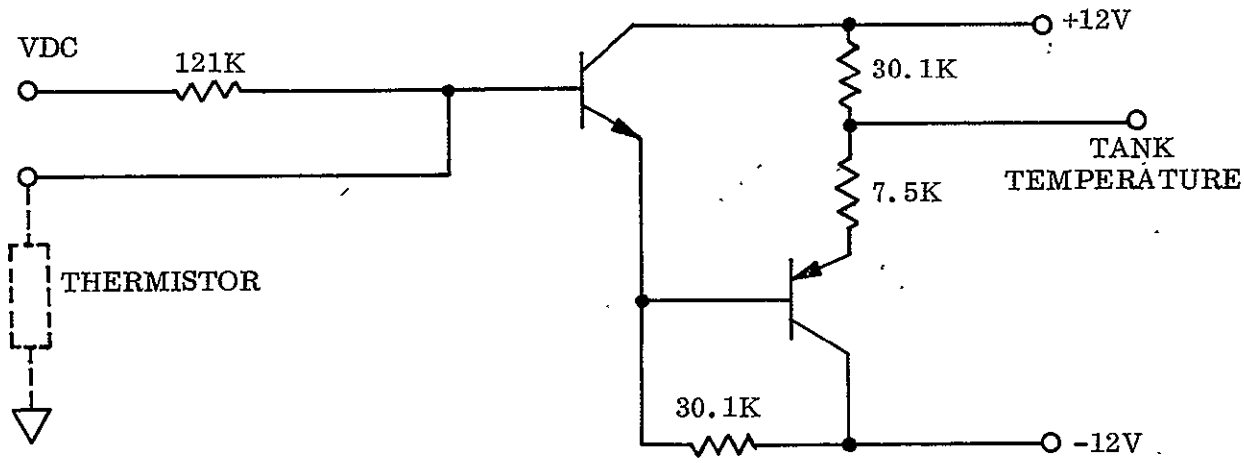

Fig. D-40 Tank Temperature Conditioning Schematic

The pneumatic tank temperature telemetry signal is a nonlinear function of temperature and is shown in Fig. D-41.

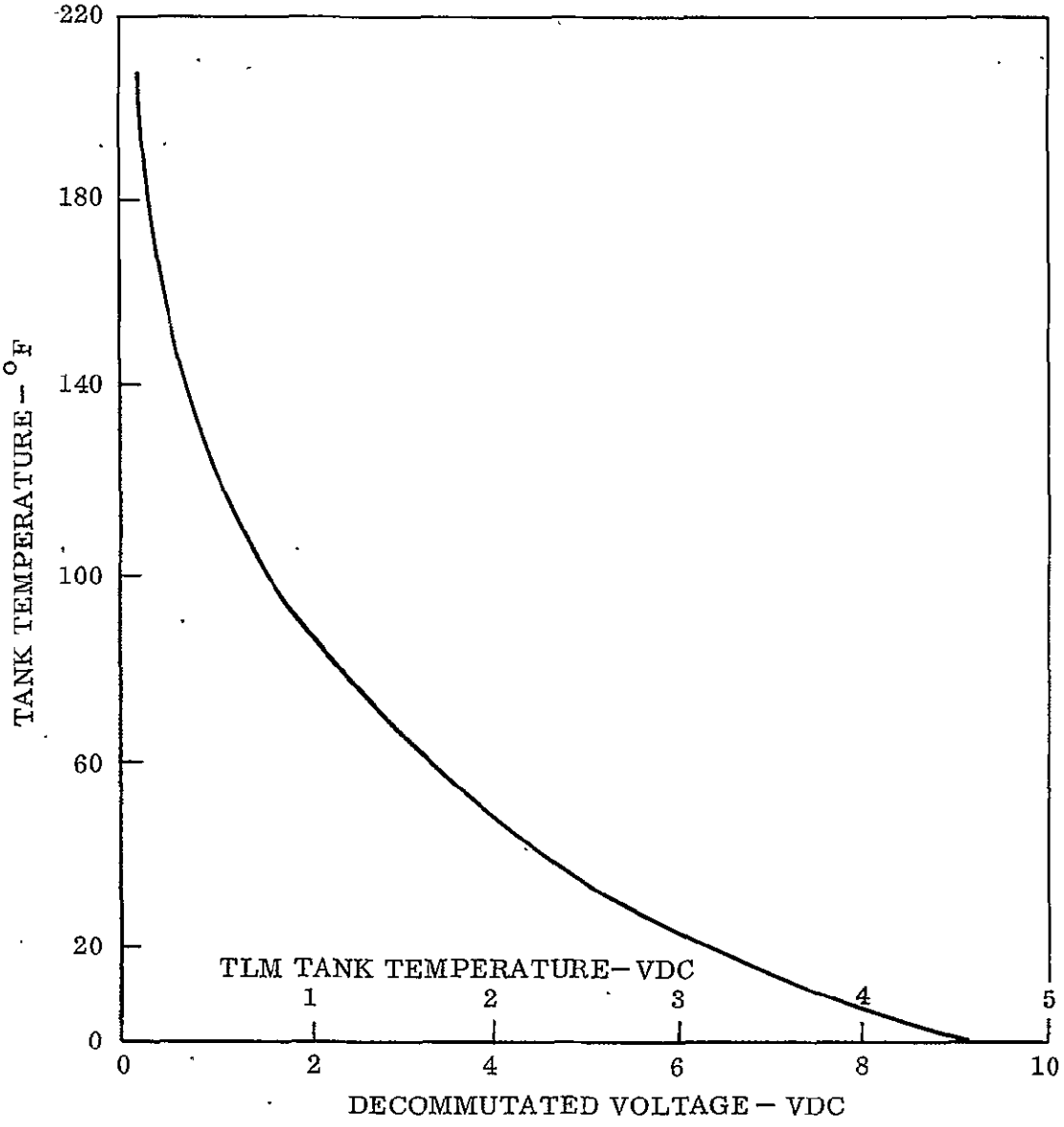

Fig. D-41 Tank Temperature Scaling

D. 14. 1. 3 FSS Output Conditioning Circuit. Since payload stability (jitter) information is of prime importance to the experimenter in evaluating system performance, pointing information is available for full-time monitoring. This pointing information is derived from the FSS-output signals which are amplified and limited for easy interpretation. Figure D-42 is a schematic of the pitch channel (S_{13_f}) conditioning electronics (identical to yaw channel). The zero or null level is +2.50 ±0.2 VDC. Scaling for the SPARCS 0 systems was 36.75 arc sec/V (28.8 mV/arc sec), and scaling for SPARCS I was 17 arc sec/V (58.8 mV/arc sec). The increased sensitivity was required for SPARCS I because of improved performance.

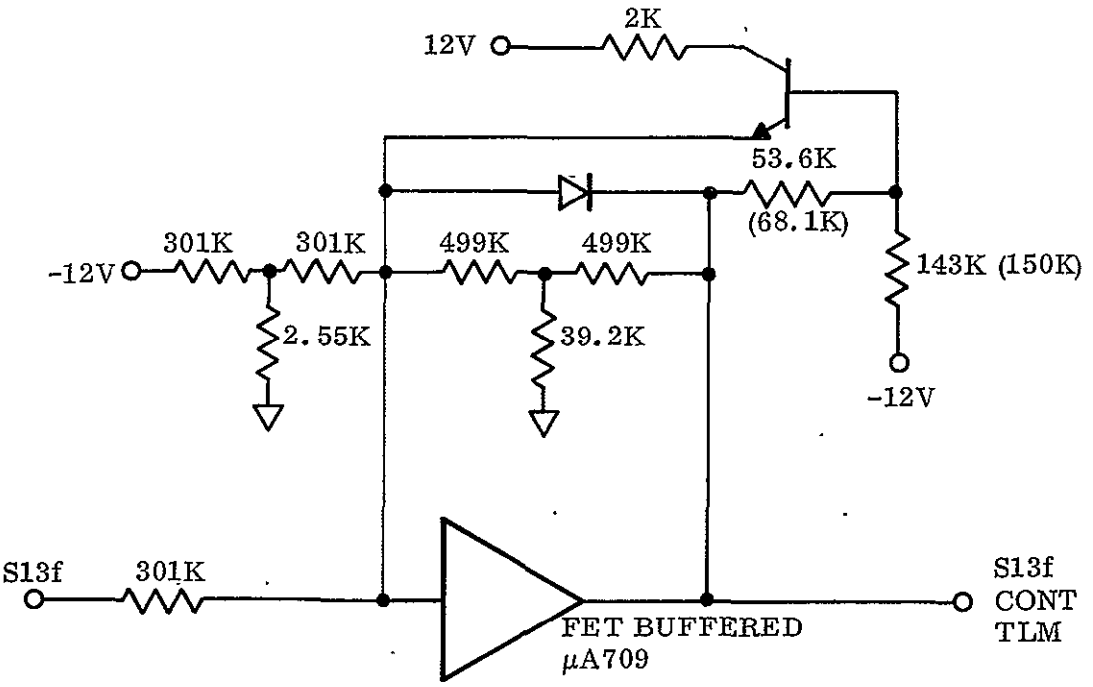

NOTE: SPARCS I VALUES IN ( )

Fig. D-42 S_{13_f} Signal Conditioning Schematic

D.14.1.4 Valve Thrusters Conditioning Circuit. Three continuous telemetry channels are provided to determine which valve thrusters are firing during flight. Conditions of the valves are indicated by logic levels at the telemetry valves output, as shown in the following table. The circuit is shown in Fig. D-43.

Telemetry Valve Voltage	Valve Condition					
	1	3	2	5	4	6
+5.0 ±0.5 VDC	OFF	OFF	OFF	OFF	OFF	OFF
+2.1 ±0.5 VDC	OFF	ON	OFF	ON	ON	OFF
0 ±0.5 VDC	ON	OFF	ON	OFF	OFF	ON

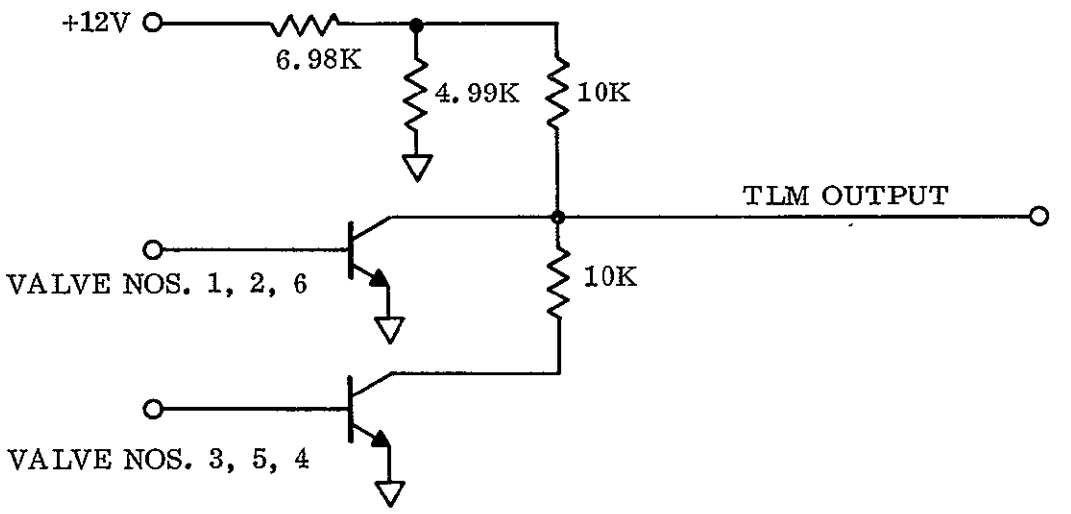

Fig. D-43 Valve Thrusters TLM Conditioning Schematic

D.14.1.5 $\overline{F}$, $\overline{G}$, Start Conditioning Circuit. The $\overline{F}$, $\overline{G}$, and start functions are conditioned for telemetry outputs through the circuits shown in Fig.D-44. Table D-4 shows the buffer amplifier output voltage for the various conditions for the $\overline{F}$, $\overline{G}$, and start signals. Following is a list of the possible status of the control signals:

Start	inhibit +7.8 V	noninhibit +0.0 V
$\overline{F}$	initial state +10 V	switched state -10 V
$\overline{G}$	initial state +10 V	switched state -10 V

Table D-4

$\overline{F}$, $\overline{G}$, START TELEMETRY LEVELS

Start	$\overline{F}$	$\overline{G}$	Buffer Amplifier Output	Decom Output	Remarks
+7.8	+10	+10	-0.1 V	-0.2 V	Normal Sequence
0	+10	+10	+1.47 V	+2.94 V	↓
0	-10	+10	+3.53 V	+7.06 V	↓
0	-10	-10	+4.96 V	+9.92 V	Normal Sequence
+7.8	-10	+10	+1.97 V	+3.94 V	Abnormal Condition
+7.8	-10	-10	+3.40 V	+6.80 V	↓
+7.8	+10	-10	+1.32 V	+2.64 V	↓
0	+10	-10	+2.90 V	+5.80 V	Abnormal Condition

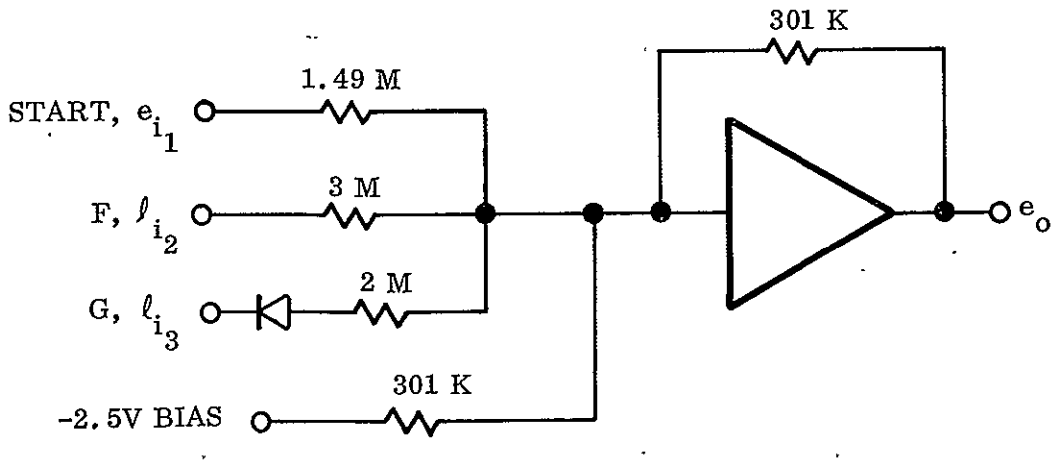

Fig. D-44 $\overline{F}$, $\overline{G}$, and Start TLM Conditioning Schematic

D. 14. 2 Telemetry Commutator

The conditioned signals to be commutated are connected to the commutator through load resistances. The commutator output is fed to a single-stage buffer amplifier, as shown in Fig. D-45. This amplifier has a transistor limiter to maintain the output voltage at a level compatible with telemetry requirements. The telemetered functions and their scale factors are shown in Table D-5.

A survey was made to determine the most suitable commutator for SPARCS; the results are summarized in Table D-6. The Fifth Dimension electromechanical unit was selected, primarily because of its low cost. Its performance was judged to be equal to that of the other units.

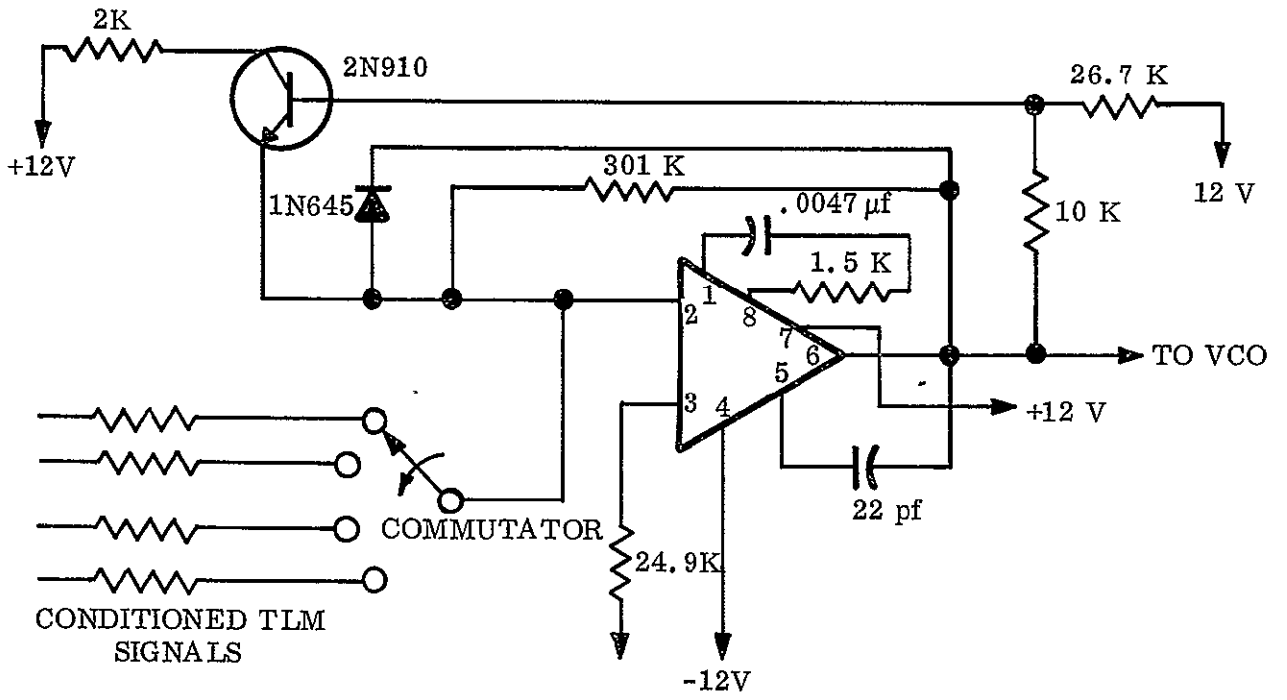

Fig. D-45 Telemetry Commutator Circuit

Table D-5

SPARCS TELEMETRY FUNCTIONS AND SCALE FACTORS

Channel		Sig TLM Load, R	Zero Sig Output, V	Output Input, V/V	Input Output, V/V	Input for Limit, V	Output Scale Factor	Input Scale Factor
1	Zero Calibration	—	+1.0	—	—	—	—	—
2	Full-Scale Calibration	—	+5.0	—	—	—	—	—
3	Magnetometer M12	1.27M	+2.5	-0.237	-4.22	±10.56	4.09 mV/mg	244 mg/V
4	Magnetometer M13	1.27M	+2.5	-0.237	-4.22	±10.56	4.09 mV/mg	244 mg/V
5	Fine Sun Sensor Temp	301K	Fig. D-39					
6	S_{13_f} TLM 6 and 11	1.27M	+2.5	-0.237	-4.22	±10.56	0.284 mV/$\widehat{\text{sec}}$	3520 $\widehat{\text{sec}}$/V
7	S_{12_f} TLM 7 and 12	1.27M	+2.5	-0.237	-4.22	±10.56	0.284 mV/$\widehat{\text{sec}}$	3520 $\widehat{\text{sec}}$/V
8	S_{13_f} Cont TLM SPARCS 0	301K	+5.0	+24	+0.0417	+0 −0.208	28.8 mV/$\widehat{\text{sec}}$	34.75 $\widehat{\text{sec}}$/V
	SPARCS I	301K	+2.5	+49	+0.0204	+0 −0.208	58.6 mV/$\widehat{\text{sec}}$	17.0 $\widehat{\text{sec}}$/V
9	Tank Pressure	301K	0.0	+1.25V/1000 lb	+800 lb/V	4000 lb	1.25 V/1000 lb	800 lb/V
10	Tank Temperature	301K	Fig. D-41					
11	see TLM 6	301K	+2.5	-1.0	-1.0	±2.5	1.2 mV/$\widehat{\text{sec}}$	833 $\widehat{\text{sec}}$/V
12	see TLM 7	301K	+2.5	-1.0	-1.0	±2.5	1.2 mV/$\widehat{\text{sec}}$	833 $\widehat{\text{sec}}$/V
13	S_{12_f} Cont TLM SPARCS 0	301K	+5.0	+24	+0.0417	+0 −0.208	28.8 mV/$\widehat{\text{sec}}$	34.75 $\widehat{\text{sec}}$/V
	SPARCS 1	301K	+2.5	+49	+0.0204	+0 −0.208	58.6 mV/$\widehat{\text{sec}}$	17.0 $\widehat{\text{sec}}$/V
14	S_{12}	1M	+2.5	-0.301	-3.32	±8.3	0.14 V/deg	7.17 deg/V
15	Regulated +12 V	30K	+2.5	-3.33	-0.3	±0.75	3.33 V/V	0.3 V/V
16	S_{13}	1M	+2.5	-0.301	-3.32	±8.3	0.14 V/deg	7.17 deg/V

Table D-5 (Cont.)

Channel		Sig TLM Load, R	Zero Sig Output, V	Output Input, V/V	Input Output, V/V	Input for Limit, V	Output Scale Factor	Input Scale Factor
17	Error Signal $\bar{S}x$	301K	+2.5	-1.0	-1.0	±2.5		
18	Regulated -12 V	30K	+2.5	-3.33	-0.3	±0.75	3.33 V/V	0.3 V/V
19	Error Signal $\bar{S}y$	604K	+2.5	-0.498	-2.02	±5.0		
20	Torque Signal $\bar{S}z$	499K	+2.5	-0.604	-1.658	±4.1		
21	Mode Sensor	1M	+5.0	-0.301	-3.32	+16.6 -0	0.301 V/V	3.32 V/V
22	Role Rate	1M	+2.5	-0.209	-4.78	±11.97		
23	Roll	301K	+2.5	+10	+0.1	±0.25	1.44 V/deg	0.695 deg/V
24	$\bar{F}$, $\bar{G}$/Start Command	3M 2M 1.4M	–	–	–	–	–	–
25	+28 V Circuit Power	100K	+2.87	-0.312	-3.2	+9.2 -6.8	0.312 V/V	3.2 V/V
26	Scan	375K	+2.5	-0.1994	-5.02	±12.5	–	2.4 step
27	Spare	–	+2.5	–	–			
28	Spare	–	+2.5	–	–			
29	Sync Pulse	–	5.0	–	–			
30	Sync Pulse	–	5.0	–	–			

Table D-6

COMMUTATOR COMPARISON

Company	Type	1-Pole, 30 Segments	RPS	Volume (cu in.)	Weight (oz)	Cost ($)	Buffer Amp	+28V Current (ma)	Remarks
Fifth Dimension	EM* SS**	√	30 100	6.0 6.0	9 12	600-900 1500-2500	No Yes	90 40	Speed ±5%; standard item Speed ±1%; long lead time
Lind Instruments	EM	√	30	5.0	8	900	No	90	Speed ±5%; local company
Datametrics	EM	√	30	5.3	10	900	No	90	High current capacity
EMR	SS	√	120	43.0	24	1200	Yes	280	Includes signal conditioner as one unit
R. M. Parsons	SS	√	1000	9.6	12	1175	Yes	40	Includes −1.0 V pedestal
Vector or LMSC	SS	√	100	5.0	6	3000 2500	Yes	60	IC; Transistor switching, Mosfet switching

*Electromechanical
**Solid State

SUMMARY:

(1) Both EM and SS have low noise, little bounce.
(2) SS has advantage of high sampling rate.
(3) EM is lower in cost and size (generally) and weight.
(4) EM power consumption is higher.
(5) EM life is 200 hr min; SS life is 5000 hr min.

D. 15 AEROSPACE GROUND EQUIPMENT (AGE)

The SPARCS AGE consists of a tower junction box, the PAGE portable pneumatics unit, a blockhouse Test Control Unit (TCU), a decommutator, and special umbilical cables on the tower and in the blockhouse. The launch base equipment furnished by the experimenter includes a recorder and commercial laboratory instruments, and also umbilical pullaway lanyards and springs if necessary. A diagram showing how the various pieces of AGE equipment connect to SPARCS is shown below.

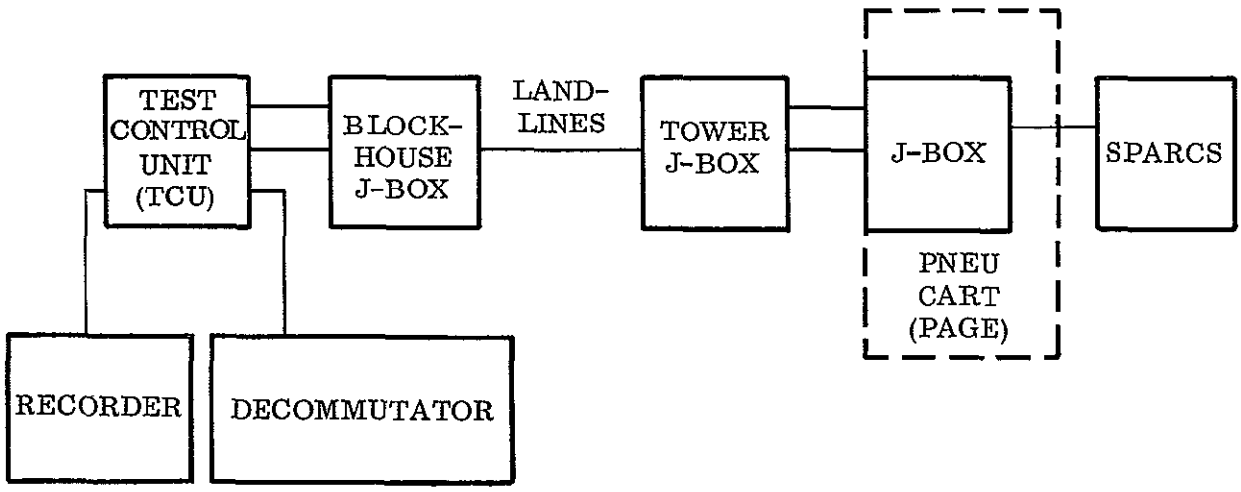

Fig. D-46 AGE-SPARCS Hookup Diagram

The AGE is used for checkout of the control system during integration of the payload, qualification and acceptance tests, and preflight and postflight tests. It is not required for complete calibration during qualification and acceptance tests, but is used to detect degradation in performance. Only go-no-go checks are required in the launch tower, except for automatic roll setting through the umbilical.

A detail description of AGE components and operating instructions is contained in the SPARCS manual.

D.15.1 Test Control Unit (TCU)

The TCU, shown in Fig. D-47, is used to check the SPARCS functions by providing simulated inputs and monitoring the outputs. It is self-contained, portable, and powered by 110 V, 60 cps. Communication with the control system is by direct lines and through the decommutator. Oral communication between personnel on the launch tower and at the TCU is also provided.

The simulated inputs provided by the TCU include the following:

a. A constant current source to excite the magnetometer electronics
b. A voltage source to simulate FSS and CSS inputs
c. A sine wave input for roll spin simulation and frequency response tests
d. A pulse generator system to position the dual resolvers for the proper roll bias
e. A roll range correction input
f. Control signals for inhibiting valve drivers and scan, and simulating coarse acquisition and fine pointing
g. Means of switching from external to internal power
h. Means of charging the nickel-cadmium battery pack
i. Means of actuating the pneumatic functions for charging SPARCS gas tank
j. Means of monitoring commutated telemetry data when used with a decommutator

D.15.2 Pneumatic Aerospace Ground Equipment (PAGE)

The primary function of the SPARCS PAGE is to charge the gas storage tank with propulsive gas. When used with the TCU, PAGE can be installed at the launch tower and operated remotely. PAGE accomplishes the following tasks:

a. Pressurization to automatic shutoff (3600 to 4800 psi)
b. Venting as required to 0 psi
c. Manually controlled pressure adjustment for pressurization above automatic shutoff

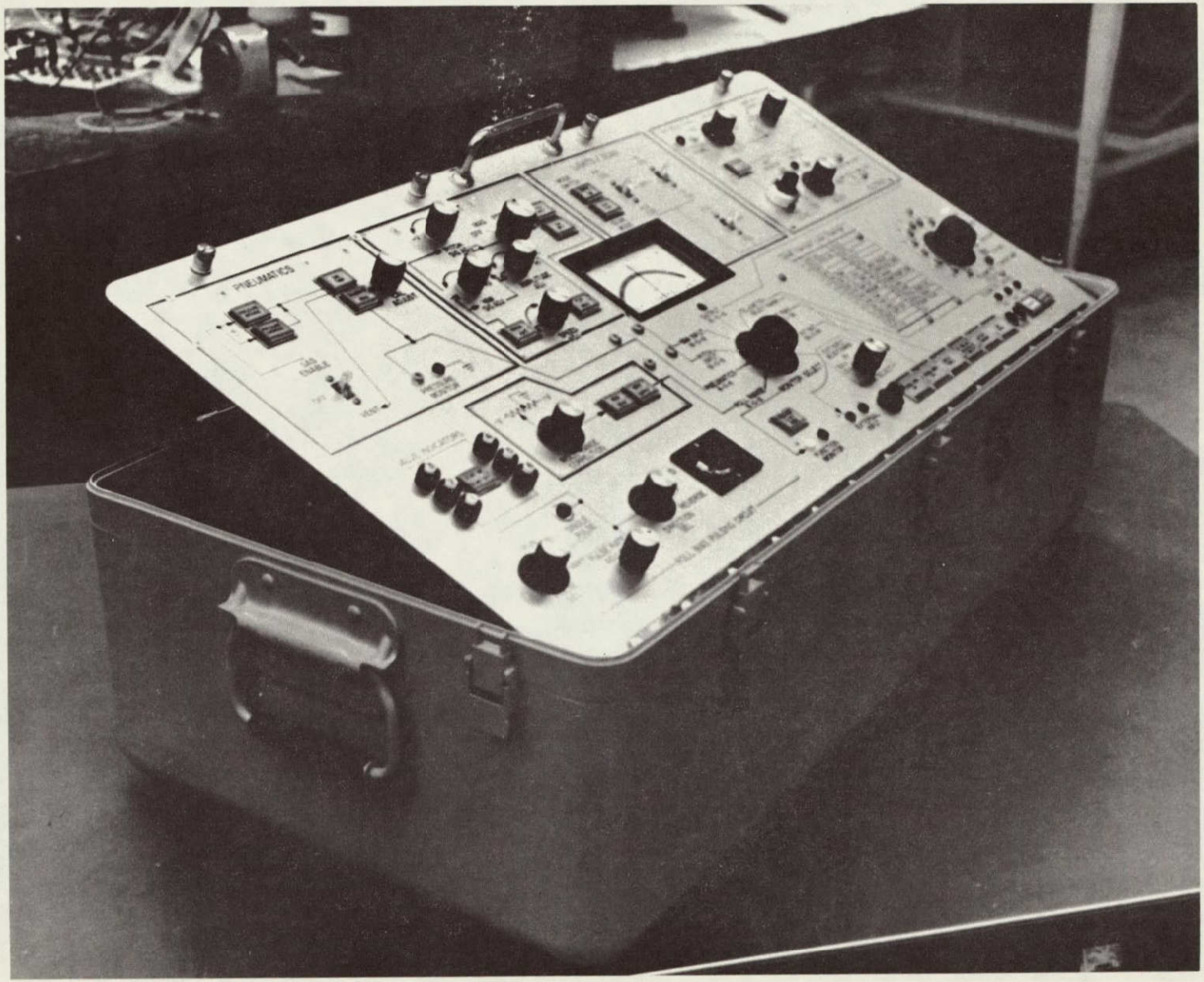

Fig. D-47 TCU Panel and Case

PAGE is self-contained and portable. It provides gas loading with a pressure boost from the low level (400 to 2200 psi) available from commercial gas storage bottles to the pressure level (above 3600 psi) needed for flight, and it is compatible with Freon, nitrogen, helium, and argon. A pressure regulator controls the stored gas output pressure (booster input pressure) to 400 psi. A pressure transducer (0 to 5000 psi range) monitors the SPARCS pneumatic tank pressure with readout available at the blockhouse. All equipment is proof-tested to more than 5400 psi.

PAGE is available in two forms: A portable PAGE cart, which contains the gas charging bottles (Fig. D-48), and a PAGE suitcase (Figs. D-49 and D-50).

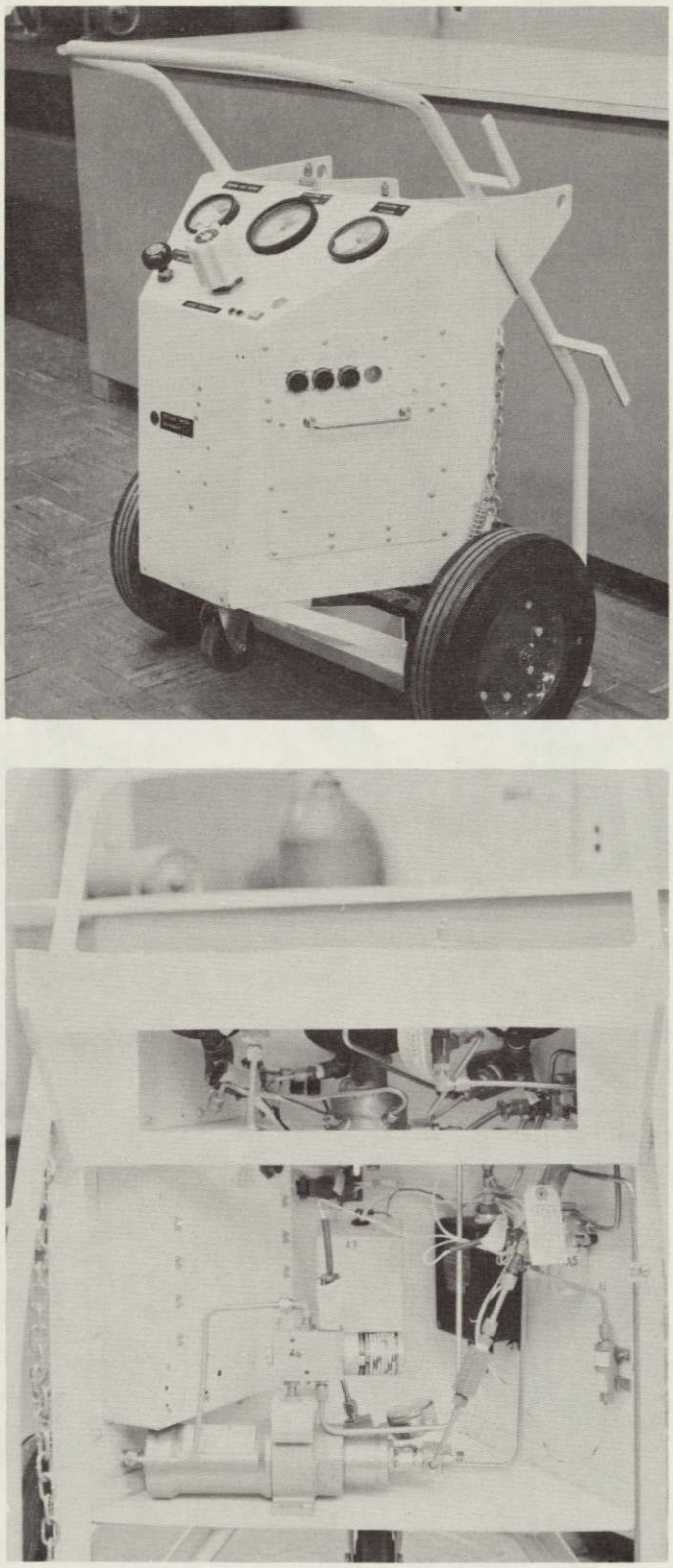

Fig. D-48 PAGE Cart

Fig. D-49 PAGE Suitcase, Showing Control Panel

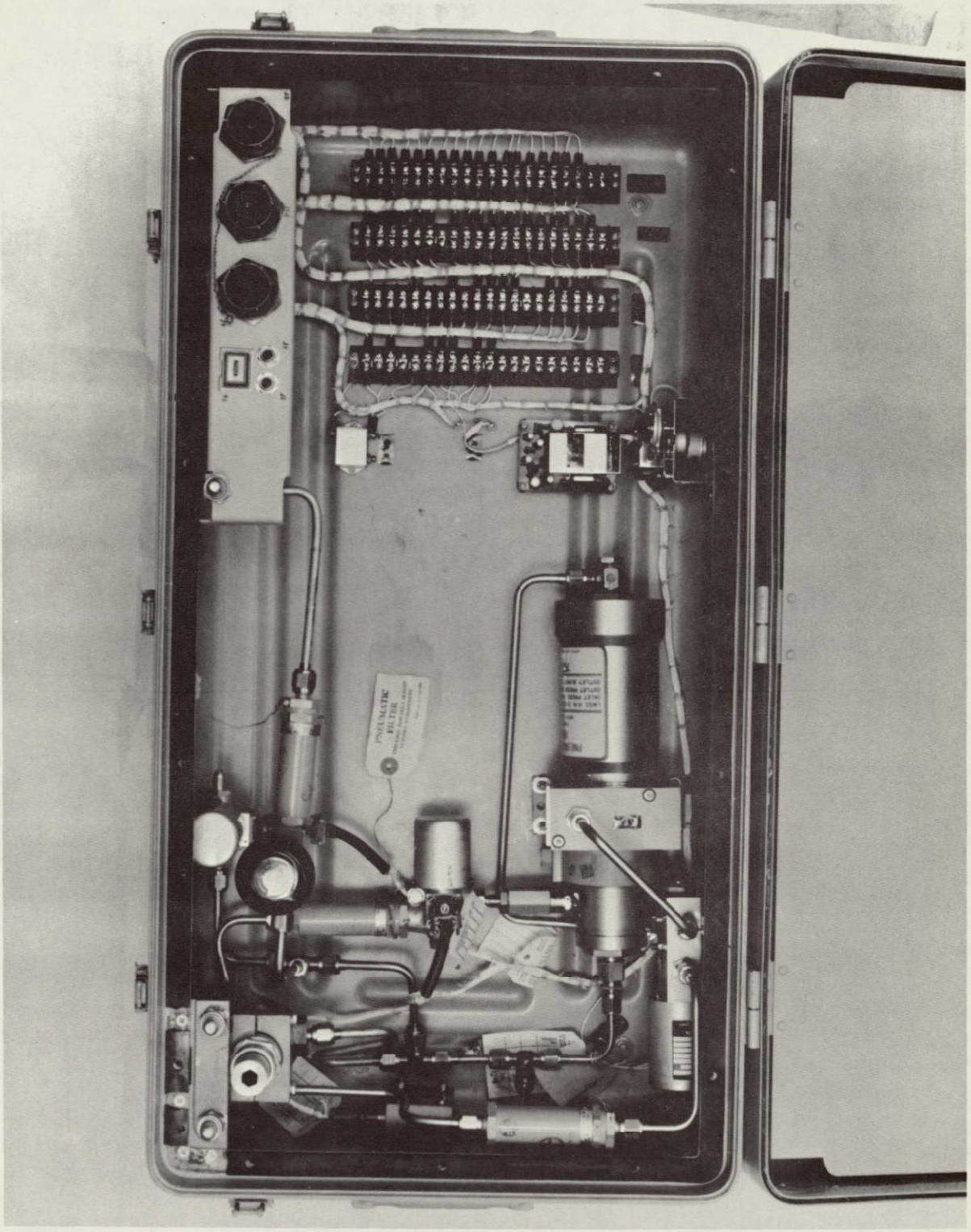

Fig. D-50 PAGE Suitcase, Internal View

Appendix E
RELIABILITY ANALYSIS

Appendix E
RELIABILITY ANALYSIS

E.1 ASSUMPTIONS

In deriving the equipment reliability estimates given in this Appendix, the following assumptions were made:

a. Equipment functional failures result from independent part failures that are both random and catastrophic.

b. The probability of component failure is a direct function of operating time. If a component is subject to duty cycling, it is further assumed to have a zero failure rate in its nonoperation condition. The system and equipment reliability is thus described by the exponential distribution $R = e - \lambda t$.

c. Subsystem and equipment interface reliabilities are taken as unity unless otherwise noted.

d. A mission time of 0.1 hour is assumed for all subsystems.

e. The analysis was not restricted to only those equipments whose failure could result in a mission failure; the telemetry subsystem, which is not essential to primary mission success, was also considered.

E.2 METHODOLOGY

With the exception of the magnetic aspect sensors (magnetometers), all subsystems and their respective subassemblies have been evaluated by assigning failure rates to each component. Subsystem failure rates were then summed and multiplied with a mission time of 0.10 hour. The final subsystem reliability prediction, $R \simeq 1 - \lambda t$, was then calculated. Capacitors, resistors, diodes, transistors and integrated circuits were evaluated by means of Ref. 12. Batteries, resolver, commutator, and solar sensors were evaluated based on similarities to parts listed in Ref. 13. The cold-gas tank, pressure regulators, isolation valves, and thrust valves are similar to parts used on Agena programs. All components used are either standard parts from Ref. 14 or individual parts approved by ARC.

E.3 SYSTEM RELIABILITY

The overall SPARCS vehicle reliability estimate is calculated to be the product of the major subsystems reliabilities. Reliability blocks are developed for each subsystem by combining the reliability estimates for each of its constituent components. These equipment reliability estimates are based on currently available information on each particular equipment item and may include reliability stress and failure rate data, part-count analyses, or a combination of these sources. In this section, the reliability estimates derived from test and flight data will be at a confidence level of 50 percent or higher.

References 12, 13, and 15 were used as failure data sources. The basis for reliability estimates of SPARCS subsystems are given in par. E.4. An illustration of the Aerobee rocket and its major components is presented in Fig. 1-1 of Section 1.

A summary of the reliability estimates and goals for the individual subsystems is given below. As shown, the estimated reliability for the over-all vehicle is 0.92.

Subsystem	Reliability Estimate	Reliability Goal
R-1 Power Supply	0.99	0.99
R-2 Control Electronics	0.99	0.99
R-3 Sensors (Including FSS)	0.98	0.97
R-4 Telemetry	0.99	0.99
R-5 Valve Driver Electronics	0.99	0.99
R-6 Pneumatics	0.99	0.99
R-7 Structures	0.99	0.99
Over-all Vehicle Reliability	0.92	0.90

E.4 SUBSYSTEM RELIABILITY

A SPARCS subsystem block diagram is shown in Fig. E-1. Brief discussions of each subsystem are presented in the following paragraphs. In subsystems containing more than one constituent, where one or more have estimated reliabilities of 0.999 or less, the estimates have been calculated using the formula

$$R = \frac{N}{\pi R_i}$$

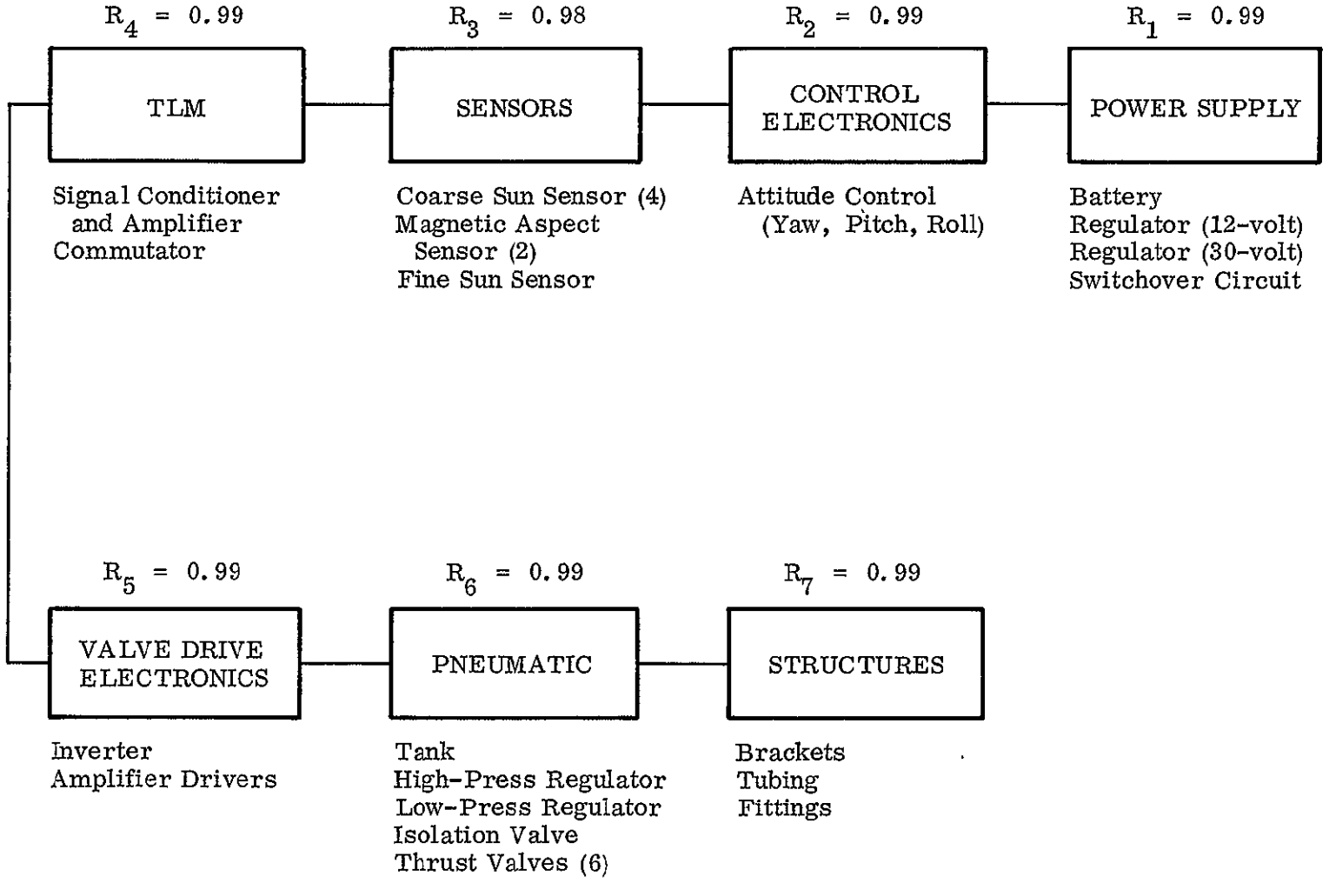

Fig. E-1 SPARCS Subsystem Block Diagram

where

R = total reliability index

N = number of constituents

R_i = reliability of individual constituent

The reliability index R is defined as the probability of successful operation throughout the required operating time.

E.4.1 R-1 – Power Supply

This subsystem consists of 24 1.2-V nickel-cadmium batteries (connected in series and providing a total voltage of 28.8 VDC) and associated regulator circuits. The subsystem supplies continuous power throughout the flight to all the electrical circuits in each of the subsystems. The reliability index is estimated to be

$$R = 0.99989 \text{ (goal } 0.99)$$

E.4.2 R-2 – Control Electronics

This subsystem receives signals from the attitude sensors (FSS, CSS, and magnetic aspect sensors), which are being amplified and conditioned for pulsing (square wave) of the valve driver circuits. The reliability index is estimated to be

$$R = 0.99998 \text{ (goal } 0.99)$$

E.4.3 R-3 – Sensors

This subsystem monitors and passes on flight data to the control system so despin and coarse and fine alignments with the sun can be obtained. The thermistor is not essential for mission success and is not included in these calculations. The electronic components are derated 50 percent or better. The mission time is 6 minutes. Based on evaluation of vendor data, computations, and sound engineering judgment, the reliability index for the sensors is estimated to be

$$R = 0.98 \text{ (goal } 0.97)$$

E.4.4 R-4 – Telemetry

This subsystem receives, conditions, and passes on signals representing vehicle attitudes, thrust valve operation, power supply voltages, and cold-gas tank pressure and temperature. The reliability index is estimated to be

$$R = 0.9995 \text{ (goal } 0.99)$$

Total reliability of the telemetry subsystem is somewhat less than the other subsystems, but is well above the established goal of 0.99. The main reason for this is the commutator, which has an assumed failure rate of 5000 per 10^6 hours.

E.4.5 R-5 – Valve Driver Electronics

This subsystem obtains and controls pulsed signals from the control subsystem. It activates one or more of the thrust valves as required, acquiring coarse or fine alignment with the sun. The reliability index is estimated to be

$$R = 0.99999 \text{ (goal } 0.99)$$

E.4.6 R-6 – Pneumatics

This subsystem is operated whenever adjustments are required to obtain proper coarse or fine alignment with the sun. These changes take place when one or more of the six solenoid-operated thrust valves are activated by pulses via the valve driver circuits. Failure rates are based on similarities to Air Force Agena and NASA Agena pneumatic parts. Temperature and pressure transducers are not included in this prediction, since they are not essential to success of the primary mission. The reliability index is estimated to be

$$R = 0.99988 \text{ (goal } 0.99)$$

E.4.7 R-7 – Structure

Brackets, supports, tubing, and fittings are made of solid material with no moving parts. Material fatigue is very unlikely to occur, due to the short mission time. It should also be noted that this hardware design is not unique. All items, such as the tank and valves, were developed or used in similar flight circumstances. Based on the simplicity of this system, it is safe to assume

$$R = 0.9999 \text{ (goal } 0.99)$$

E.5 CONCLUSION

Based on the conditions and calculations discussed in the foregoing paragraphs, it is concluded that the SPARCS system will meet or exceed the reliability goal of 0.90.

Appendix F
RELATED HARDWARE STUDIES

Appendix F
RELATED HARDWARE STUDIES

Several SPARCS-related hardware items were developed during the course of the SPARCS program but, for various reasons, were not included in the final SPARCS design. The three most significant of these items were an integrated circuit thin-film magnetometer, an Intermediate Sun Sensor (ISS), and an adjustable mount for the Fine Sun Sensor (FSS).

F.1 INTEGRATED CIRCUIT THIN-FILM MAGNETOMETER

The magnetometers were included among the "buy" items in the SPARCS contract. Due to quality control requirements, the cost of the SPARCS magnetometers is more than twice the list price for an equivalent off-the-shelf item. This motivated an examination by LMSC of a low-cost, thin-film magnetometer.

The thin-film magnetometer (TFM) selected for study was a state-of-the-art integrated circuit design which has the advantages of being compact, lightweight, and requires no chokes and transformers to facilitate tuning of the magnetometer. Also, the circuit components lend themselves readily to microminiaturization.

F.1.1 Theory of Operation

Operation of the TFM is based on the second harmonic magnetic fluxgate principle. The thin-film sensor consists of an alumina substrate on which a Permalloy material is vacuum deposited in the presence of a magnetic field. The sensor is then surrounded by a pumping coil and a pickup coil which are mutually perpendicular. The pumping coil is driven by an AC signal which is derived from a crystal oscillator; the pickup coil is tuned to the second harmonic of the pumping frequency to obtain the output signal.

The output signal is maximum when the applied magnetic field is parallel to the pickup coil axis, the polarity of the output signal depending on the direction of the applied magnetic field. When the applied magnetic field is perpendicular to the pickup coil axis, a null output results.

Since the amplitude of the output signal is a function of the applied magnetic field, the variation of the output signal may be expressed as

$$E = H \cos \theta$$

where H is the applied magnetic field and θ is the angle between the applied field and the pickup coil axis.

A schematic diagram of the TFM is shown in Fig. F-1. A magnetic thin-film sensor of this type can be used for direct measurement of fields in the range of 1 to 5000 gamma. The range can be extended by means of feedback. The sensitivity of the TFM is greater than 0.25 V per millioersted.

F.1.2 Flight Evaluation

Aerobee 150 Flight 4.294 carried an assembly of two prototype TFMs and their associated electronics mounted in the recovery package between the parachute container can and the external shell. One of the TFMs was aligned with the longitudinal axis of the payload and provided a third axis of magnetic reference. The second unit was aligned parallel to the SPARCS M_{13} magnetometer and at right angles to the first TFM. The outputs from the magnetometers were fed into the experimenter's telemetry system for recording during the flight. Significant flight test results are given in the following paragraphs.

F.1.2.1 Roll Axis Position. During the fine pointing phase of SPARCS controlled payloads, the X axis (roll axis) is in line with the sun line. The η angle (angle between the sun line and the local magnetic vector) has been tabulated for the date and time of each flight. The longitudinal TFM gave an output that was a function of the cosine of the η angle. A calculation of the η angle, as indicated by the TFM, shows the angle to be 157.3 deg. The computed η angle supplied for the time of the

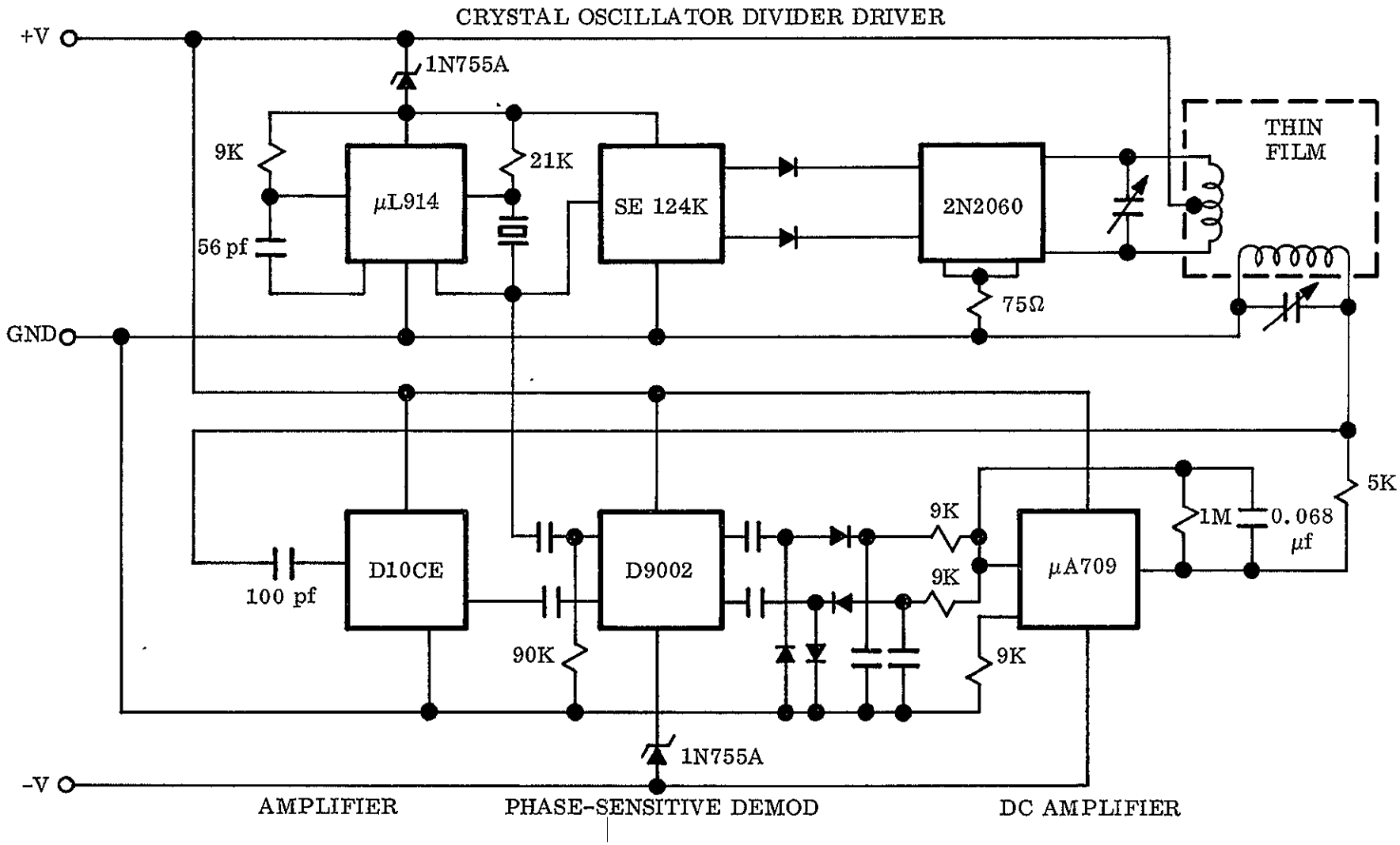

NOTES:
1. All capacitors are 0.01 μf unless otherwise specified.
2. All diodes are 1N645
3. All active elements are ICs, with the exception of 2N2060 which is a dual NPN transistor.

Fig. F-1 Schematic of IC Thin-Film Magnetometer

flight was 157 deg. However, TFM data accuracy is limited by lack of an inflight calibration to about ±0.05 V. When this tolerance is applied to the data obtained, the actual η angle as observed by the TFM might differ from 157.3 deg by ±4.3 deg.

F.1.2.2 Roll Position. A secondary function of the TFM prototype was to provide a comparison between it and the standard SPARCS M_{13} magnetometer. These two magnetometers were aligned to read the magnetic field parallel to the SPARCS Z axis. During the fine pointing portion of the flight, the corrected TFM output was 0.35 V. The output of the SPARCS M_{13} magnetometer for the same period was 0.37 V. This 0.02-V difference is equivalent to about one degree and is well within the expected error of ±0.05 V due to variations in telemetry outputs. The error due to misalignment of the magnetometers is an order of magnitude less than this.

F.1.2.3 Flight Anomalies. The longitudinal TFM output as recorded by telemetry showed some disturbances during the first 90 seconds of the flight and again after SPARCS was disabled. These disturbances evidently originated in the telemetry section. The output of the magnetometer was connected directly to the experimenter's commutator operating on IRIG channel 16, segments 3, 12, and 21. This disturbance did not occur during the fine pointing portion of the flight. The output of the lateral TFM showed a continuous oscillation which begain with the shock of the parachute deployment and continued until loss of the telemetry signal. This effect has not been observed during post-flight tests and is tentatively attributed to an intermittant connection on the printed circuit board connector.

F.1.2.4 Condition of the Recovered TFM Assembly. The TFM prototype system operated properly in a post-flight functional test. The post-flight alignment of the TFM assembly could not be checked in the field. Post-flight examination of the removed TFM assembly revealed that one of the two nylon screws holding the TFM to the adjusting shaft was broken, but the remaining screw had not shifted and the original alignment appeared unchanged. Portions of the TFM housing that were in contact with the recovery package showed signs of heat deformation around some of the screw holes. The material used for the mounting was Lexan, which has a heat-distortion temperature of 264°F at a stress of 260 psi. A Tempilabel temperature

sensor applied to the TFM electronics package indicated that the temperature did not exceed 150°F in that area. Other temperature sensors installed on the skin adjacent to the TFM assembly were destroyed by impact on recovery and could not be read.

F.1.3 Development Plan

Improvement of the TFM mounting assembly will be performed to provide higher heat resistance tolerance. In addition, the alignment adjustment will be modified to eliminate the nylon screws and allow greater ease in alignment adjustment after installation in the recovery package.

F.2 INTERMEDIATE SUN SENSOR

The Fine Sun Sensor (FSS) for SPARCS was originally planned as a subcontract item, but this plan was changed early in the subcontract and resulted in a slow start on FSS development. In order to prevent subsequent schedule delays, a critical angle prism sensor was fabricated for use as a substitute FSS during design studies on the air bearing vehicle. The prism sensor, shown in Figs. F-2 and F-3, is attractive because it provides identical system stability (jitter amplitude) as the FSS but is much smaller, simpler and less costly, and has significantly less coupling between axes. Laboratory tests indicate no difference in electronic performance of the prism sensor and the FSS. The prism sensor has been designated an Intermediate Sun Sensor (ISS), referring to intermediate accuracy, because its ability to achieve absolute pointing comparable to the FSS has not been established. The sensor shown in Figs. F-2 and F-3 requires an amplifier package to mate with the existing SPARCS.

F.3 FINE SUN SENSOR ADJUSTABLE MOUNT

Early in the FSS development program, it was believed that precise alignment of the FSS with respect to the rocket axis was necessary. An FSS adjustable mount, shown in Fig. F-4, was designed, manufactured, and shock tested to determine if FSS alignment could be preserved during the SPARCS shock environment.

A dummy sensor, with mass properties approximating the FSS, was used for the shock test. The FSS mount assembly was adjusted so that the plane of the top of the mount was nearly parallel to the base mount. Two mirrors were mounted, one on the top and one on the base, so that they overlapped each other when viewed from a point perpendicular to them. The alignment bolts were tightened to about 35-in.-lb torque, and the mount assembly was then subjected for 6 ms to a single-axis shock of 35 g's in the same plane as the assembly mounting plate. The angular error was measured and recorded as shown below.

	Before Shock	After Shock	Change
X Axis	0^{o} 5' 40.1"	0^{o} 5' 39.7"	0^{o} 0' .4"
Y Axis	0^{o} 1' 23.7"	0^{o} 1' 19.5"	0^{o} 0' 4.2"

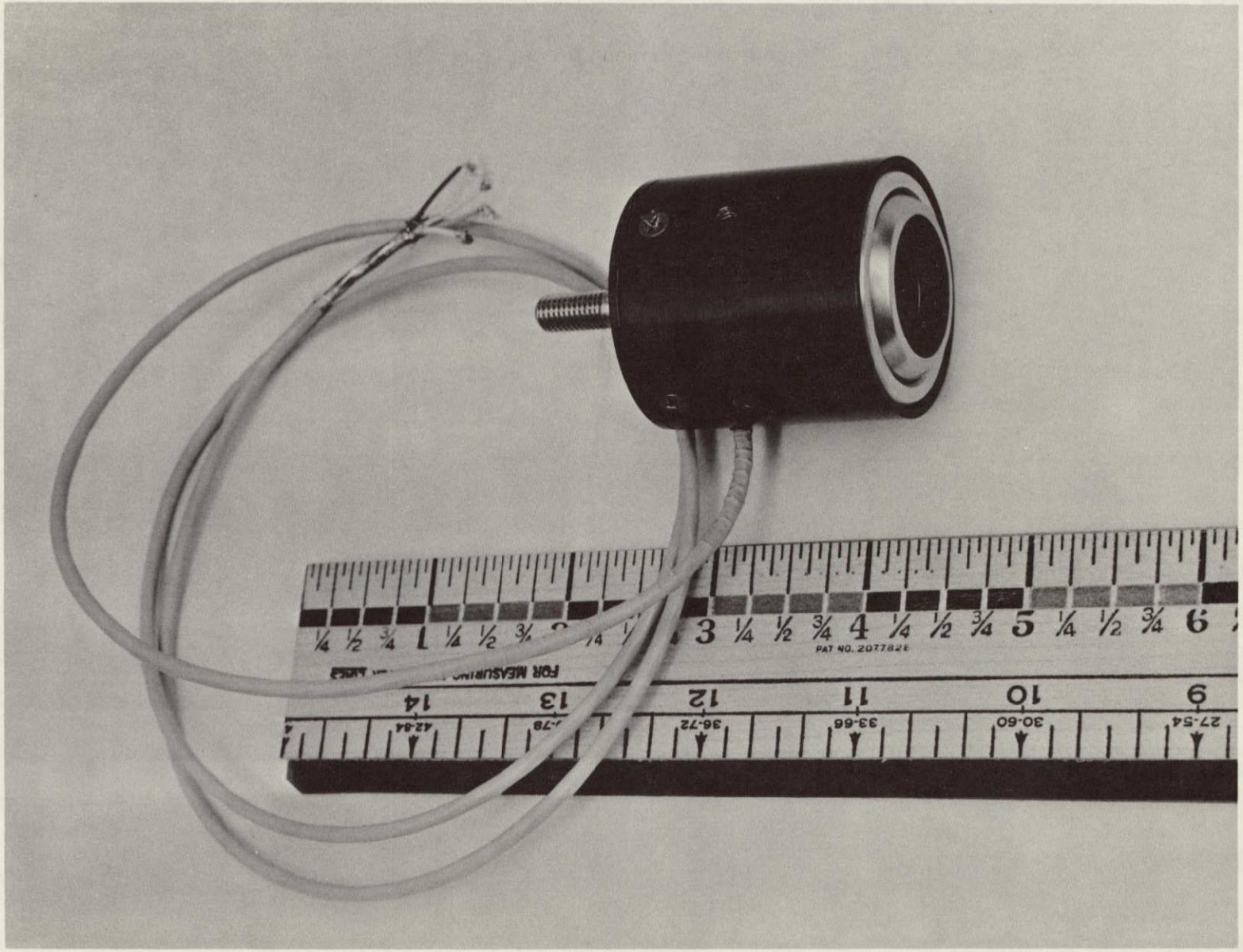

Fig. F-2 Prism Sensor

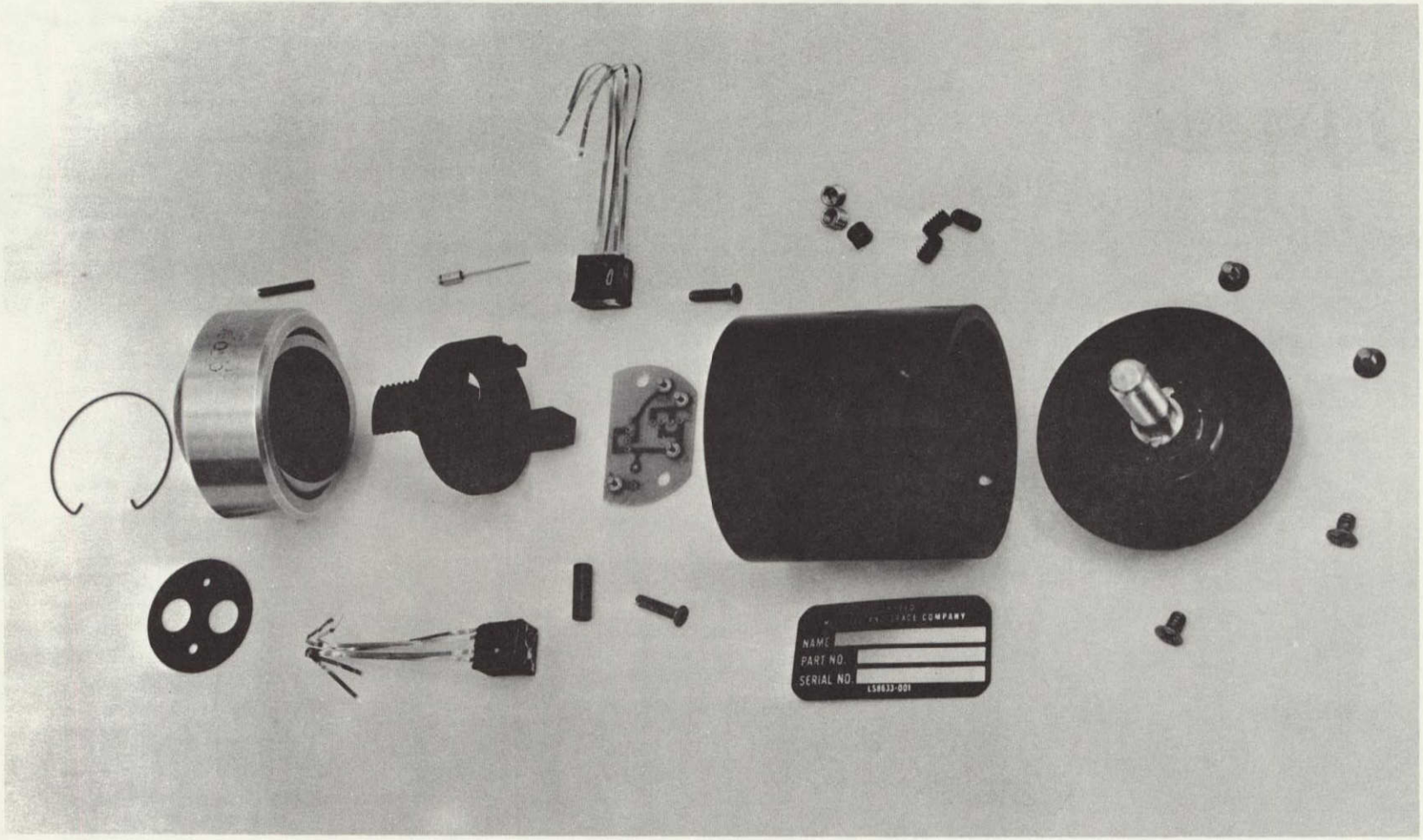

Fig. F-3 Prism Sensor Components

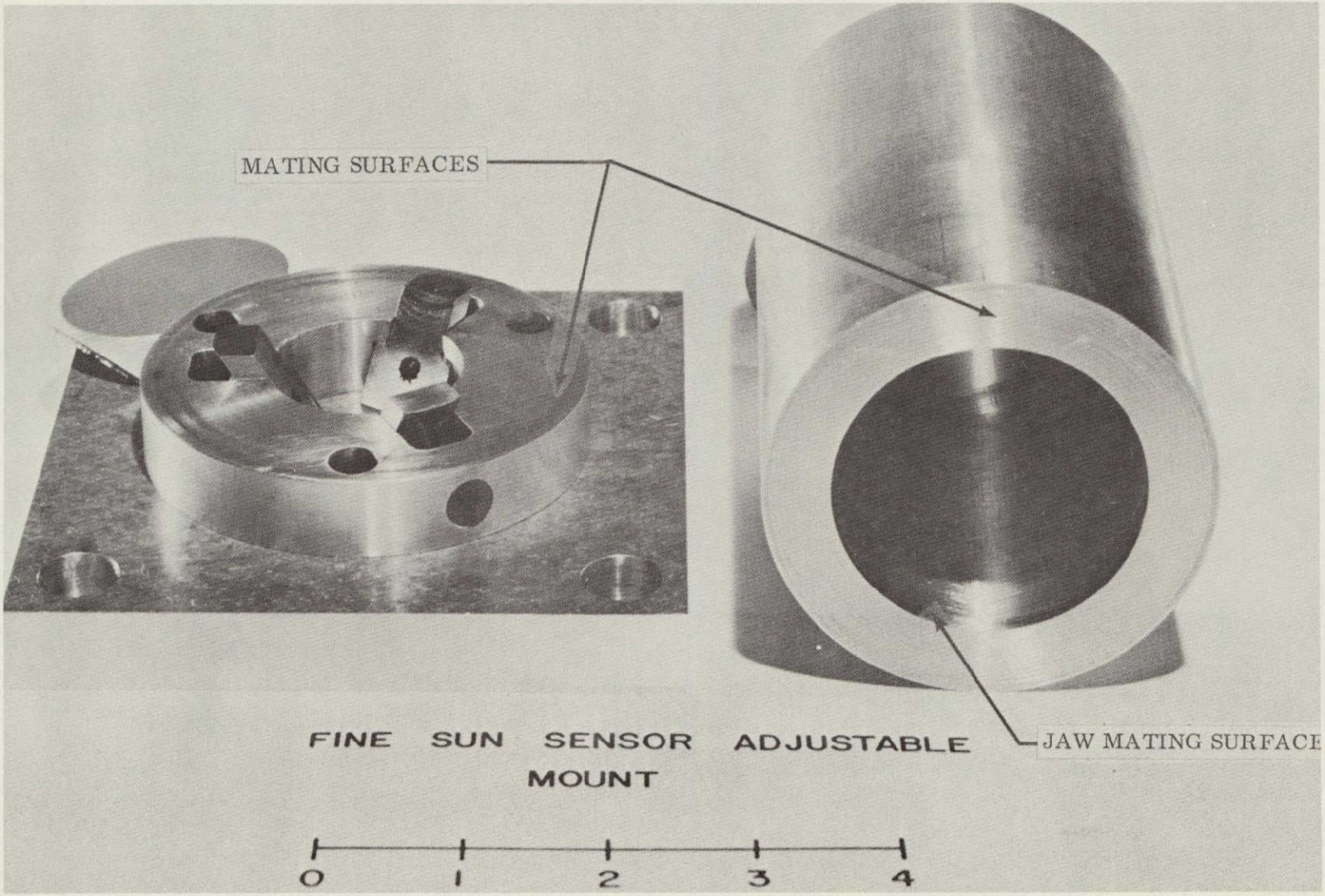

Fig. F-4 FSS Adjustable Mount

Appendix G
REFERENCES

Appendix G

REFERENCES

G.1 CITED REFERENCES

1. "Aerobee 150 – SPARCS Vehicle, Description and Nominal Trajectories," P. J. Douglas, SPARCS Memo No. 3, LMSC/582463, Sunnyvale, Calif., 1 July 1966.

2. "Lift on Inclined Bodies of Revolution in Hypersonic Flow," G. Grimminger, E. P. Williams, G. B. Young, Journal of the Aeronautical Sciences, Vol. 17, No. 11, p. 675, November 1960.

3. "Aerobee-SPARCS Vehicle, Payload Separation Study," P. J. Douglas, SPARCS Memo No. 5, LMSC/582469, Sunnyvale, Calif., 1 July 1966.

4. "Free Molecule Flow Theory and Its Application to the Determination of Aerodynamic Forces," L. H. Sentman, LMSC/448514, Sunnyvale, Calif., 10 October 1961.

5. "Theory and Application of Radiation Forces," Lyle E. Wiggins, LMSC/A384055, Sunnyvale, Calif., 25 September 1963.

6. "The Equations of Rotational Motion for a Satellite Containing Control Moment Gyros," V. P. Peline, TM 57-15-01, LMSC/A074835, Sunnyvale, Calif., 1 June 1962.

7. "Satellite Environmental Handbook," Francis S. Johnson, Stanford University Press, First Edition, Palo Alto, Calif.

8. "A Survey of Geomagnetism," Francis Glover and Francis Heyden, Georgetown Observatory Monograph No. 16, Washington, D. C., December 1960.

9. "Solar Cell and Photocell Handbook," 5th printing, International Rectifier Corporation, March 1964.

10. "Operation Amplifiers," R. Stata, Analog Devices Application note in four parts.

11. "Second Breakdown in Transistors under Conditions of Cutoff," P. Schiff, RCA Application note SM4-30.

12. MIL-HDBK-217

13. FARADA

14. ARC Standard 203, NASA Approved Parts

15. Agena (SSD and NASA), LMSC reliability data

G.2 UNCITED REFERENCE

"A Gyroless Solar Pointing Attitude Control System," Hansen, Gabris, Pearson and Leonard, paper presented at AIAA, Sounding Rocket Vehicle Technology Specialist Conference, Williamsburg, Va., 27 February – 1 March 1967